Vysoké učení technické v Brně
Fakulta elektrotechniky a komunikačních technologií
Ústav fyziky

HABILITAČNÍ PRÁCE

Dielektrická spektroskopie kompozitů a piezokeramických materiálů

Brno, 2020 Ing. Vladimír Holcman, Ph.D.

PODĚKOVÁNÍ

Nejprve bych chtěl vyjádřit velké díky za cenné rady a nezištnou pomoc nejen při řešení výzkumných problémů mému školiteli doc. Karlu Liedermanovi, který mne uvedl do problematiky dielektrické spektroskopie a nedestruktivního testování. Můj veliký dík také patří prof. Aloisi Loidlovi, od něhož jsem získal neocenitelné znalosti a zkušenosti týkající se měření a vyhodnocení v moderních materiálech.
Dále bych chtěl poděkovat mým kolegům z ústavu fyziky za vytvoření tvůrčího a inovativního prostředí k mé práci a zejména doc. Vlastě Sedlákové, Dr. Jiřímu Majznerovi, prof. Lubomíru Grmelovi, prof. Pavlu Koktavému, doc. Petr Sedlákovi, Dr. Pavlu Toflovi za inspirativní poznatky a pomoc při řešení dané problematiky.
A na závěr (nikoliv na posledním místě) bych chtěl poděkovat mé ženě Veronice a dětem Sofii, Julii a Klaudii za jejich podporu, porozumění a trpělivost.

KLÍČOVÁ SLOVA

Kompozitní soustavy, komplexní permitivita, ztrátové číslo, dielektrické vlastnosti, piezoelektrické materiály, bezolovnatá keramika.

KEYWORDS

Composite systems, complex permittivity, loss number, dielectric properties, piezoelectric materials, lead-free ceramics.

OBSAH

VYBRANÉ VaV VÝSLEDKY AUTORA PRÁCE

ABSTRAKT

Tato práce se věnuje problematice dielektrické spektroskopie kompozitních systémů a analýze systému směsných vztahů pro dielektrické materiály, v druhé části následuje charakterizace dielektrických a piezoelektrických parametrů v piezoelektrických materiálech.

Habilitační práce je předkládána jako komentář k souboru vědeckých prací publikovaných většinou v impaktovaných časopisech a ve sbornících mezinárodních konferencí, a představuje přehled významných výsledků dosažených od odevzdání mé disertační práce v roce 2008. Celá dosavadní vědecká práce je spojena s dielektrickou spektroskopií v prvních letech zejména polymerních materiálů, v posledních letech zejména piezokeramických materiálů.

Jelikož průmyslová praxe žádá stále lepší materiály s výhodnějšími elektrickými, tepelnými a chemickými vlastnostmi, a dále žádá materiály umožňující přípravu tvarově složitějších, přesnějších a hlavně levnějších výrobků, je jednou z možností vývoje nových materiálů zkoumání a výroba kompozitních systémů. Proto se hledají nové možnosti v oblasti dielektrických a magnetických složených soustav – kompozitů. Nedílnou součástí přípravy kompozitních systémů jsou také empirické matematické funkce sloužící k predikci výsledných parametrů nového kompozititu. Analýzou těchto funkcí a návrhem nové funkce se věnuje první část předložené práce.

Dielektrická spektroskopie (DS) nebo impedanční spektroskopie, také známá jako elektrochemická impedanční spektroskopie, se často používá ke studiu odezvy dielektrických materiálů vystavených elektrickému poli. Elektrické pole může být stejnosměrné, častěji ovšem střídavé. DS popisuje dielektrické vlastnosti materiálu jako funkci frekvence a následné analýzy mohou popsat chování molekul a charakteristické vlastnosti elektrických dipólů.

V této práci je prezentována metoda analýzy dielektrických spekter podle nejběžnějších empirických vztahů. Následně je v předkládané práci studována záležitost týkající se rozborů dosud známých směsných vztahů pro predikci elektrických parametrů a návrh nového směsného vztahu pro kompozitní systém polymer-kovové plnivo s unikátním koeficientem reprezentující velikost dopantových částic.

V druhé části jsou prezentované výsledky analýzy dielektrických a piezoelektrických spekter u olovnaté a bezolovnaté keramiky a vliv různých dopantů na tyto struktury.

Bezolovnatá piezoelektrická keramika je široký pojem, který obsahuje v zásadě dvě obecné skupiny. Z nichž jedna skupina soutěží o podobné aplikace jako PZT a druhá se zabývá vlastnostmi, které jsou mimo rozsah aplikací PZT. Do první skupiny patří materiály označené KNN, BCZT a BNT-BT. Do druhé skupiny pak materiály zkráceně označeny BZT, respektive BNKT, jejichž piezoelektrické vlastnosti mohou být horší než u materiálových systémů PZT. Piezoelektrická keramika je použitelná v širokém spektru odvětví, například ve fotolitografii (mikroelektronika prostřednictvím polohovacích prvků), ultrazvukovém zobrazování (lékařská diagnostika), senzorech, akčních členech atd. Bezolovnatá piezoelektrická keramika, jako je BCZT, má sice většinu vlastností srovnatelných s PZT, ale přesto je v mnoha ohledech stále horší než běžné PZT. Jedná se zejména o parametry vysoká teplota zpracování a slinování a velká velikost zrn, což snižuje možnost miniaturizace, proto je hlavní myšlenkou většiny současných prací studium strukturálních změn keramiky pomocí dopovaní různými prvky. Jelikož se jedná o dielektrických systém, je dielektrická spektroskopie vhodný nástroj pro vyhodnocení změn elektrických vlastností dopovaných materiálů.

ABSTRACT

This work deals with the problem of dielectric spectroscopy of composite systems and analyzes of the system of mixed relations for dielectric materials, in the second part follows the characterization of dielectric and piezoelectric parameters in piezoelectric materials.

The habilitation thesis is presented as a commentary on a set of scientific papers published in impact journals and proceedings of international conferences, and presents an overview of significant results of clothing and dissertations in 2008. All scientific work is associated with dielectric spectroscopy in the first years, especially polymeric materials in recent years especially piezoceramics.

As industry practice demands ever better materials with more advantageous electrical, thermal and chemical properties, materials enabling the preparation of more complex, more accurate and especially cheaper products, one of the possibilities of developing new materials is to research and manufacture composite systems. Therefore, look for new possibilities in the field of dielectric and magnetic composite systems - composites. An integral part of the preparation of composite systems are also mathematical empirical functions used to predict the resulting parameters of a new composite. The analysis of these functions and the proposal of new functions are devoted to the first part of the presented work.

Dielectric spectroscopy (DS) or obstacle spectroscopy, known as electrochemical obstacle spectroscopy, often used to study the response of dielectric materials exposed to electric fields. The electric field can be direct current, more often alternating. The DS describes the dielectric properties of a material as a function of frequency, and the analysis can describe the behavior of molecules and the key properties of electrical dipoles.

In this work, the method of analysis of dielectric spectra according to the most common empirical relations is presented. Subsequently, a matter concerning the analysis of hitherto known mixing relations for the prediction of electrical parameters and the design of a new mixing relationship for a polymer-metal filler composite system with a unique factor representing the size of dopant particles is studied.

The second part presents the results of the analysis of dielectric and piezoelectric spectra in lead and lead-free ceramics and the influence of various dopants on these structures.

Lead-free piezoelectric ceramics is a broad term that basically contains two general groups. One group competes for similar applications as PZT and the other focuses on features that are outside the scope of PZT applications. The first group includes materials marked KNN, BCZT and BNT-BT. In the second group, the materials are abbreviated BZT or BNKT, respectively, the following piezoelectric properties may be worse than in the case of PZT material systems. Piezoelectric ceramics can be used in a wide range of industries, such as photolithography (microelectronics via positioning elements), ultrasound imaging (medical diagnostics), sensors and actuators, etc. Lead-free piezoelectric ceramics such as BCZT have several properties comparable to PZT, but still is in many ways a hall worse than a regular PZT. These are mainly the parameters of high processing and sintering temperature and large grain size, which requires the possibility of miniaturization, so the main idea is to conduct current studies to study the structural changes of ceramics using doped active elements. As these are dielectric systems, dielectric spectroscopy is a suitable tool for evaluating changes in the electrical properties of doped materials.

1 DIELEKTRICKÁ SPEKTROSKOPIE KOMPOZITNÍCH SYSTÉMŮ

Kompozitní materiály jsou v dnešní době na popředí výzkumů a rozšiřují obzory konstruktérů ve všech oborech. Společnost nevidí za lesklý exteriér nebo závodní výkon jachty GRP1, ani necítí složitost struktury kompozitního listu rotoru vrtulníku nebo moderní tenisové rakety CFRP2, přesto za každým zvýšením byť jednoho parametrů těch struktur stojí roky výzkumu a vývoje. [1]

Moje dosavadní práce v oblasti kompozitních systémů byla zejména v době po obhajobě disertační práce zaměřena na analýzu dielektrických spekter a nalezení nových směsných vztahů charakterizující dané materiály. [A1-A8]

V kompozitech jsou materiály kombinovány takovým způsobem, který nám umožňuje lépe využívat jejich předností a do určité míry minimalizovat dopady jejich nedostatků. Tento proces optimalizace může designéra osvobodit od omezení spojených s výběrem a výrobou konvenčních materiálů či tvarů. Může využívat tvrdší a lehčí materiály s vlastnostmi, které lze přizpůsobit konkrétním požadavkům na design. Vzhledem ke snadnosti, s jakou lze vyrábět složité tvary, může úplné přehodnocení zavedeného designu z hlediska kompozitů často vést k levnějším i lepším řešením.

Koncept „kompozitů“ není lidským vynálezem. Dřevo je přírodní kompozitní materiál sestávající z jednoho druhu polymeru - celulózových vláken s dobrou pevností a tuhostí - v pryskyřičné matrici jiného polymeru, polysacharidu ligninu. Příroda dělá design a výrobu mnohem lépe než my, i když si člověk uvědomil, že způsob překonání dvou hlavních nevýhod přírodního dřeva - velikosti (strom má omezený příčný rozměr) a anizotropie (vlastnosti se výrazně liší v axiálním a radiálním směru) je vyrobit kompozitní materiál, který nazýváme překližka. Kosti, zuby a skořápky měkkýšů jsou další přírodní kompozity, které kombinují tvrdé keramické výztužné fáze v matricích z přírodního organického polymeru. [2]

Jednoduchý termín „kompozity“ dává jen málo informací o široké škále jednotlivých kombinací, které jsou zahrnuty v této třídě materiálů. Zmínil jsem některé z těch známějších, ale diagram na obr. 1.1 poskytuje jasnější představu o rozsahu vynalézavosti, který má k dispozici materiálový inženýr či vědec a jeho zákazník, konstruktér.

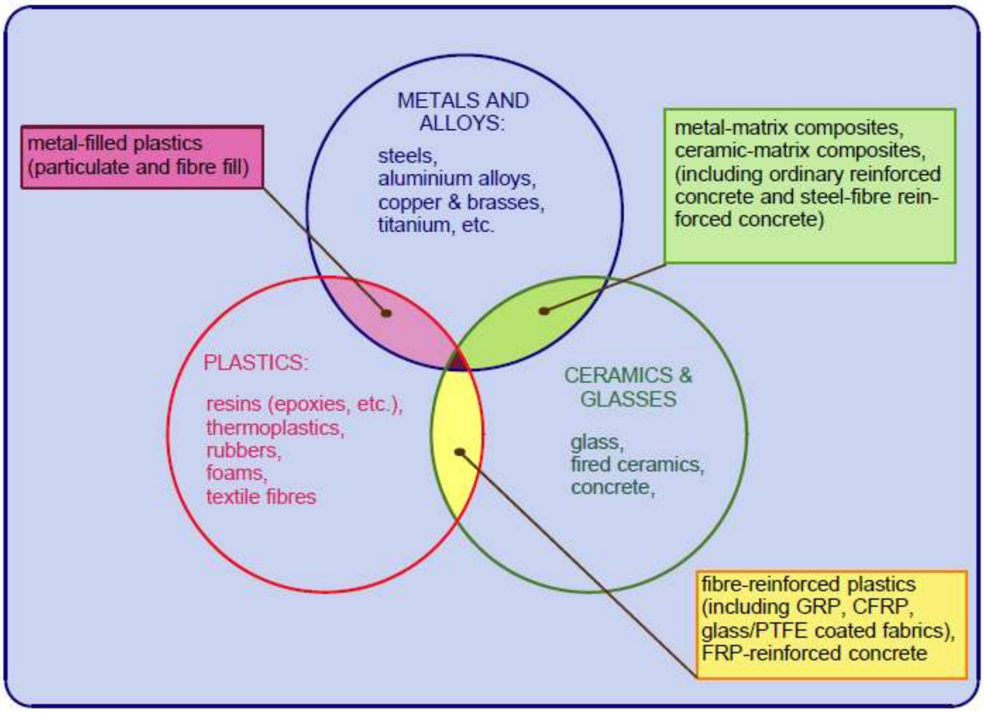

Obr. 1.1 Vztahy mezi třídami materiálů, ukazující vývoj kompozitů [2]

Kompozitní materiál „znamená jakýkoli materiálový systém, který se skládá z minimálně dvou složek, z nichž alespoň jedna je pevná, s makroskopicky rozeznatelným rozhraním mezi fázemi“ [2,3]. Kompozity lze označit jednoduše jako kombinaci několika materiálů dohromady, které musí získat jiné vlastnosti, než jaké mohou poskytnout některé ze složek samotné, nebo než jejich jednoduchý součet.

Kompozitní materiály se obecně klasifikují podle následujících kritérií [2,3]:

- matricovým materiálem (základní fáze):
  - polymer (termoplasty, termosety nebo elastomery)
  - keramika a jiné anorganické látky (obvykle silikát, síran vápenatý nebo báze).
- Podle struktury nebo geometrických charakteristik rozptýlených částic:
  - disperze (tvrdé kovy)
  - částice (částice, zrnitost)
  - částice pravidelných tvarů (koule, destičky)
  - plynné inkluze (pórovité polymery, pěnobeton)
  - vlákno (dlouhé, krátké, uspořádané, neuspořádané vlákna).

1.1 PLNIVA KOMPOZITŮ

Plniva jsou pevné látky, které se do polymerů přidávají v poměrně velkých objemech za účelem úpravy objemu, hmotnosti, nákladů, povrchu, barvy, chování při zpracování, mechanické pevnosti, elektrických vlastností a mnoha dalších parametrů. Ve většině průmyslových aplikací jsou obecně plasty smíchány s plnivy, aby se zlepšily jejich funkční vlastnosti (tuhost, houževnatost, tahové vlastnosti), zvýšila se trvanlivost gumových směsí a snížily se náklady na konečný produkt. Plniva lze obvykle klasifikovat do následujících kategorií [2,4]:

- ředidla nebo degradující plniva (neztužující): snižují jak mechanickou tak i elektrickou pevnost směsí, do nichž se přidávají, a přidávají se hlavně ke snížení výrobních nákladů zvýšením objemu a hmotnosti produktu (ve skutečnosti však neexistuje plnivo, které je plně neaktivní a snižuje pouze náklady), např. pigmenty, uhličitan vápenatý, mastek, síran barnatý;
- výplňová nebo částečně vyztužující plniva: mají malý vliv jak na mechanickou tak i elektrickou pevnost směsí, např. tvrdý jíl, vysrážený uhličitan vápenatý;
- vyztužující plniva: zvyšují mechanickou tak i elektrickou pevnost směsí a podstatně zlepšují jejich mechanické vlastnosti, např. srážený oxid křemičitý, pyrogenní oxid křemičitý, saze.

Výztuž lze definovat jako zlepšení mechanických vlastností sloučenin, ale také elektrických vlastností jako jsou elektrická pevnost, permitivita, průrazné napětí, schopnost zhášet el. oblouk a další.

Kromě klasifikací založených na jejich mechanickém či elektrickém účinku v polymerní matrici lze plniva rozlišit také na základě jejich struktury a různých rozměrů Obr. 1.2[5,7]:

- nulový rozměr (0D): nízký poměr stran, izotropní koule, kostky, mnohostěny, např. saze, uhličitan vápenatý, fulleren;
- jednorozměrné (1D): částice plniva, ve kterých je jeden rozměr podstatně větší než ostatní (tyče, dráty, trubky), např. uhlíkové nanotrubice s více stěnami, uhlíkové nanodráty, sepiolit;
- dvourozměrný (2D): částice plniva, ve kterých mají dva rozměry značnou délku (disky, hranoly, desky), např. vrstvený křemičitan, grafen, grafit;
- trojrozměrný (3D): částice plniva, ve kterých mají tři rozměry značnou délku, např. boehmit, diamant.

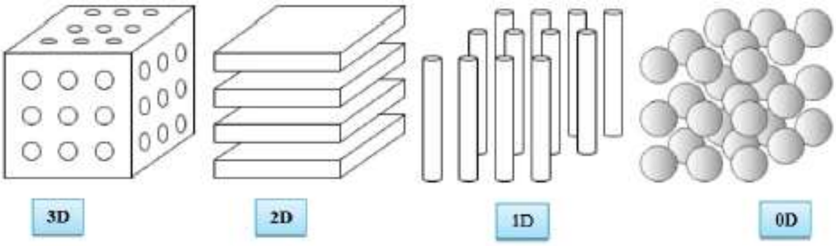

Obr. 1.2 Různé typy příměsí [6]

Hlavní kritéria ovlivňující výztuž

Rozhodujícími parametry, které určují účinek výplní na elektrické vlastnosti kompozitů a také na jejich predikci, jsou geometrie výplně (velikost, tvar, poměr stran) a interakce výplň-matice. [6]

Velikost částic

Průměrná velikost částic je obvykle první charakteristikou plniva, které je třeba vzít v úvahu. V reakci na důležitost malých částic při přípravě funkčních, vysoce výkonných kompozitů se sofistikovanou architekturou se objevila nová generace nano plnidel. Vliv výztuže se zvyšuje se zmenšováním velikosti částic, což přináší větší plochu rozhraní polymer-plnivo a tedy účinnější mezifázovou vazbu. Samozřejmě tento jev platí jen v určitém rozsahu objemového zastoupení plniva v matrici. Plniva mají obvykle průměry částic v rozmezí 10 nm až 200 µm. Velké částice v plnivu již omezují kontakt mezi matricí a povrchem plniva a působí jako místa iniciace poruchy, které vedou k předčasnému selhání materiálu[7].

Specifický povrch (SA) a pórovitost

Termín „měrný povrch“ (SA) se vztahuje k ploše / jednotkové hmotnosti a obvykle se vyjadřuje jako m^2/g. Specifický povrch přesně souvisí s velikostí částic. Snížení průměrné velikosti částic plniva a následné zvýšení SA, zvětšuje mezifázovou vazbu polymer / plnivo, a proto je žádoucí při navrhování elektrických kompozitů. Specifický povrch určuje celkový povrch plniva, které je v kontaktu s polymerem. SA je charakterizován měřením adsorpce specifických molekul. Nejčastěji používaná adsorpční technika je založena na metodě Brunauer-Emmett-eller (BET) adsorpce N2, která poskytuje „celkovou“ povrchovou plochu včetně pórovitosti. Dalším přístupem je metoda cetyltrimethylamoniumbromidu (CTAB) Obr. 1.3, která analyzuje vnější povrchovou plochu, která odpovídá efektivní ploše plniva resp. prakticky dosažitelné ploše rozhraní plnivo matrice. Jednoduchou metodou pro získání hodnot souvisejících se SA je stanovení adsorpce oleje. Prázdný prostor (prázdný objem) mezi agregáty a aglomeráty lze vyjádřit jako objem dibutylftalátu (DBP) absorbovaný daným množstvím plniva, což se odráží v hodnotě čísla DBPA [8].

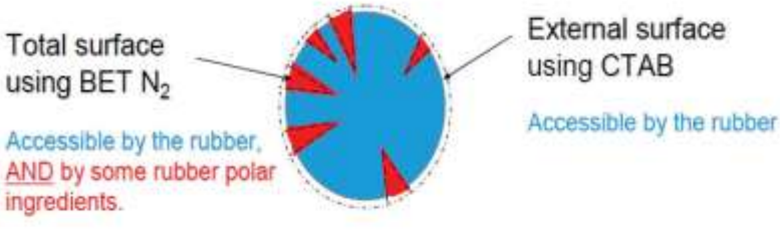

Obr. 1.3 Srovnání metod BET a CTAB [8]

Absorpce oleje DBPA je technika používaná ke kvantifikaci množství a strukturních charakteristik stupně plniva poskytováním informací o stupni pórovitosti a struktuře částic plniva. Vyšší čísla absorpce oleje DBPA odpovídají vyšším strukturám CB. Obecně platí, že zvětšení povrchu (zmenšení velikosti částic) poskytuje nižší odolnost a vyšší pevnost v tahu. U elektrických vlastností již velmi záleží na typu a velikosti plniva a je možné dosáhnou jak poklesu, tak i růstu elektrické vodivosti, průrazného napětí, permitivity atd. [8]

Teoretické řešení složené soustavy

Složené materiály představují složenou soustavu tvořenou makroskopickými útvary dvou nebo více materiálových složek. Podle [7] je složeným materiálem soustava vyhovující následujícím kritériím:

- soustavu tvoří spojení dvou nebo více materiálů rozdílného chemického složení se zřetelnou hranicí mezi geometrickými útvary složek,
- geometrické útvary jednotlivých složek jsou v soustavě spojeny v celém objemu,
- složená soustava musí mít vlastnosti odlišné od vlastností složek,
- složená soustava musí být vytvořena člověkem.

Vlastnosti složených materiálů jsou závislé na množství jednotlivých složek, geometrickém tvaru částic složek, jejich orientaci, uspořádání a rozložení v soustavě. Reakce na hranicích bývají nežádoucí, protože snižují mechanickou pevnost složených materiálů. Navíc vedou k vytvoření přechodových vrstev, které ztěžují matematicko-fyzikální analýzu složené soustavy.

Nejčastějším matematicky popisovaným případem složených soustav je soustava dvousložková. Matematický popis vychází z údajů o vlastnostech jednotlivých složek.

Často se řeší složené soustavy z hlediska relativní permitivity nebo relativní permeability. V obecném případě lze pro permitivitu vícesložkové soustavy psát:

$$\varepsilon_S = F(\varepsilon_1, \varepsilon_2, ...\varepsilon_n, v_1, v_2, ...v_n), \qquad (1.1)$$

kde v_1 až v_n jsou poměrné objemové díly jednotlivých složek soustavy, přičemž platí

$$\sum v_i = 1. \qquad (1.2)$$

Teoretické přístupy k řešení vztahu 1.1 vedou ke složitějším výrazům, nevhodným pro praktické aplikace. Za zjednodušujících předpokladů lze však z těchto složitých výrazů odvodit jednoduché vztahy pro dvousložkovou soustavu. Nejznámější jsou vztahy Maxwellův a Böttcherův [3,4]. Tyto vztahy popisují matriční složené soustavy s dispergovanými částicemi kulového nebo alespoň přibližně kulového tvaru.

Maxwellův vztah pro dvousložkovou soustavu s nízkou koncentrací dispergovaných částic má tvar

$$\frac{\varepsilon_s - \varepsilon_2}{\varepsilon_2} = 3v_1.\frac{\varepsilon_1 - \varepsilon_2}{\varepsilon_1 + 2\varepsilon_2}. \quad (1.3)$$

Böttcherův vztah pro dvousložkovou soustavu s kulovými částicemi lze psát ve tvaru

$$\frac{\varepsilon_s - \varepsilon_2}{\varepsilon_s} = 3v_1.\frac{\varepsilon_1 - \varepsilon_2}{\varepsilon_1 + 2\varepsilon_2}, (1.4)$$

a je vhodný pro soustavy s vyšší koncentrací dispergovaných částic.

V technické praxi velmi používaný je Lichteneckerův mocninový vztah; pro vícesložkovou soustavu platí

$$\varepsilon_s^k = \sum_{i=1}^{n} v_i.\varepsilon_i^k, \qquad (1.5)$$

kde *k* je empirický parametr závislý především na tvaru a orientaci částic a nabývající hodnot v intervalu <-1,1>.

Odvozením z (1.5) pro k→0 se získá Lichteneckerův logaritmický vztah, který má pro dvousložkovou soustavu tvar

$$\log \varepsilon_s = v_1.\log \varepsilon_1 + v_2.\log \varepsilon_2 , \qquad (1.6)$$

Empirické Lichteneckerovy směsné vztahy byly odvozeny pro poměr permitivit menší nebo roven 4. Experimentálně bylo zjištěno, že čím menší je poměr permitivit ε_1 a ε_2, tím tento vztah poskytuje lepší souhlas s experimentálními výsledky.

Další velmi používané směsné vztahy jsou uvedeny v tab. 1.1 [3,4].

Tab. 1.1 Používané směsné vztahy

Částice	Vzorec	Poznámky	Reference
kulové	$\varepsilon_1\left[1+3v_2\dfrac{\varepsilon_2-\varepsilon_1}{2\varepsilon_1+\varepsilon_2}\right]$	$V_2<0.05$	Wagner
kulové	$\dfrac{\varepsilon^{\frac{1}{3}}-\varepsilon_1^{\frac{1}{3}}}{\varepsilon_2^{\frac{1}{3}}-\varepsilon_1^{\frac{1}{3}}}=v_2$	$V_2<0.2$	Looyenga
vodivé kulové	$\varepsilon_1\dfrac{1+2v_2}{1-v_2}$	$\varepsilon_2<<\varepsilon_1$ $v_2<0.25$	Corcum
malé kulové	$\varepsilon_1\left[1+v_2\dfrac{\varepsilon_2-\varepsilon_1}{\varepsilon_1+A(\varepsilon_2-\varepsilon_1)}\right]$	$V_2<0.2$	Sillars
elipsoidy – náhodná orintace	$\varepsilon_1\left[1+\dfrac{1}{3}v_2\sum_i\dfrac{\varepsilon_2-\varepsilon_1}{\varepsilon_1+A(\varepsilon_2-\varepsilon_1)}\right]$	$V_2<0.2$	Fricke
válcový	$\varepsilon_1\dfrac{3\varepsilon_1+2v_2(\varepsilon_2-\varepsilon_1)}{3\varepsilon_2-v_2(\varepsilon_2-\varepsilon_1)}$	$V_2<0.2$	Rayleigh
zploštělé	$\varepsilon_2\dfrac{3\varepsilon_1+2v_2(\varepsilon_2-\varepsilon_1)}{3\varepsilon_2-v_2(\varepsilon_2-\varepsilon_1)}$		Bruggemann
vodivé elipsoidy	$\dfrac{\varepsilon_1}{1-\dfrac{1}{3}v_2\sum_i\left(\dfrac{1}{A_i}\right)}$	$\varepsilon_2>>\varepsilon_1$	Altschuller
libovolné	$\dfrac{\varepsilon-\varepsilon_1}{\varepsilon+K}=v_2\dfrac{\varepsilon_2-\varepsilon_1}{\varepsilon_2+K}$	K=empirický parametr	Wiener

1.2 DIELEKTRICKÁ SPEKTROSKOPIE

Slovo dielektrikum je odvozeno od předpony dia, původně znamená skrz nebo napříč. Dielektrická relaxační spektroskopie (DRS) představuje jednu ze styčných oblastí na pomezí fyziky, chemie, elektrotechniky a materiálového inženýrství s výraznými aplikačními výstupy. V obecném pojetí se DRS zabývá studiem molekulární dynamiky elektricky nabitých částic, resp. dipólů a je tvořena souborem teorií a metod k experimentálnímu zkoumání této dynamiky. Na rozdíl od polovodičů je zakázaný pás energií širší, takže tepelně generované nosiče náboje obecně chybí. V přítomnosti náboj elektrického pole neprotéká dielektrickým materiálem proud jako ve vodiči, ale pouze nastává pouze posun z jejich rovnovážných poloh „polarizace dielektrika“. [2,10]

Polarizace dielektrik je tedy pohyb vázaných elektrických nábojů pod účinkem elektrického pole a vysunutí těchto nábojů z jejich rovnovážných poloh na ohraničenou malou vzdálenost, stejně jako orientace polárních molekul. V průběhu dielektrické polarizace dochází buď ke vzniku indukovaných dipólů obr. 1.4, či k orientaci permanentních dipólů obr. 1.5, popřípadě k obojímu současně.

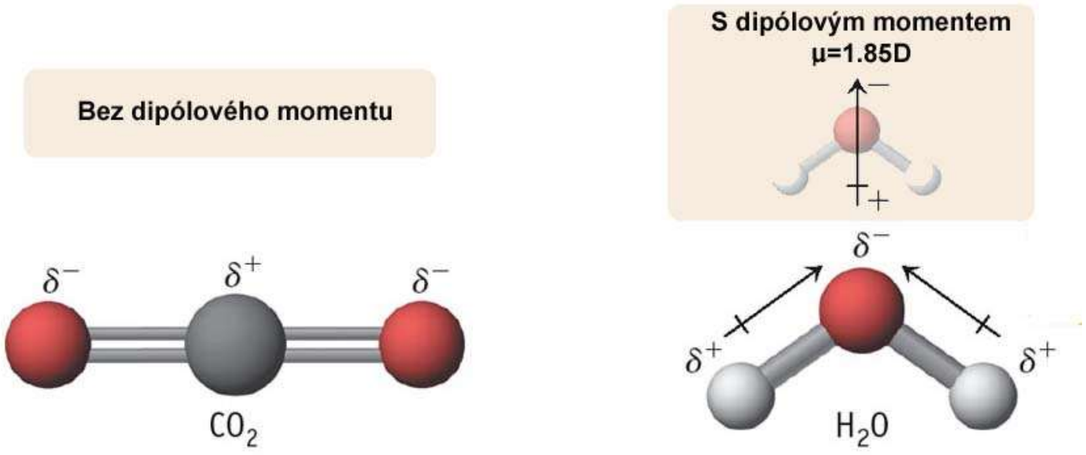

Obr. 1.4 Vznik dipólového momentu molekuly [10]

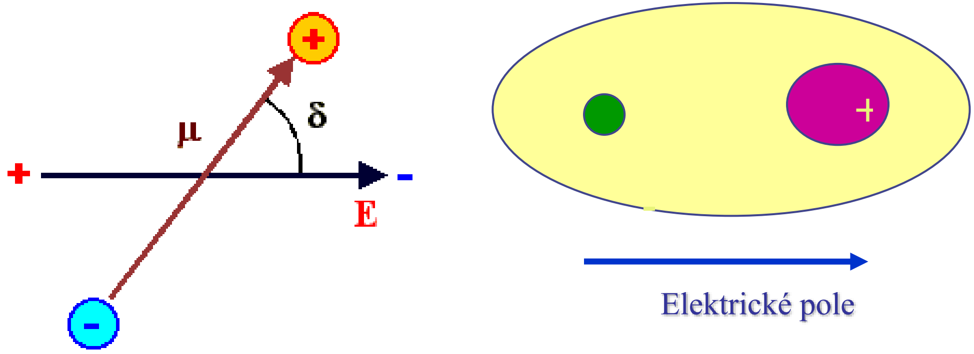

Obr. 1.5 Natáčení dipólu za působení elektrického pole [10]

Jak je patrno z obr. 1.4 a obr. 1.5 molekula, která má odlišné těžiště kladného a záporného náboje, se chová jako elektrický dipól. Dipól popisujeme veličinou zvanou elektrický dipólový moment a je zpravidla označována řeckým písmenem μ. Jeho hodnota je určena součinem elektrického náboje q a vzdáleností nábojů l. Jednotkou dipólového momentu je 1 D (debye) = $3{,}33564.10^{-30}$ C.m.

V následujícím obrázku je názorně uvedeno, jak se mění dipólový moment chlorovaného metanu v závislosti na počtu substitucí vodíku chlórem. Molekula metanu sama o sobě má molekulární dipólový moment roven nule (tj. molekula metanu je nepolární), poněvadž obsahuje čtyři slabé polární vazby C – H, které jsou umístěny v prostoru symetricky. Vektorový součet jejich dipólových momentů je tedy roven nule.

S postupným nahrazováním vodíku chlórem je symetričnost narušena a molekuly monochlórmetanu, dichlórmetanu a trichlórmetanu mají dipólový moment nenulový - tyto molekuly jsou tedy polární. Při poslední substituci vzniká molekula tetrachlórmetanu, který obsahuje čtyři silně polární vazby C – Cl, jež jsou ovšem rozmístěny v prostoru symetricky, takže výsledný dipólový moment molekuly tetrachlórmetanu je opět nulový [10].

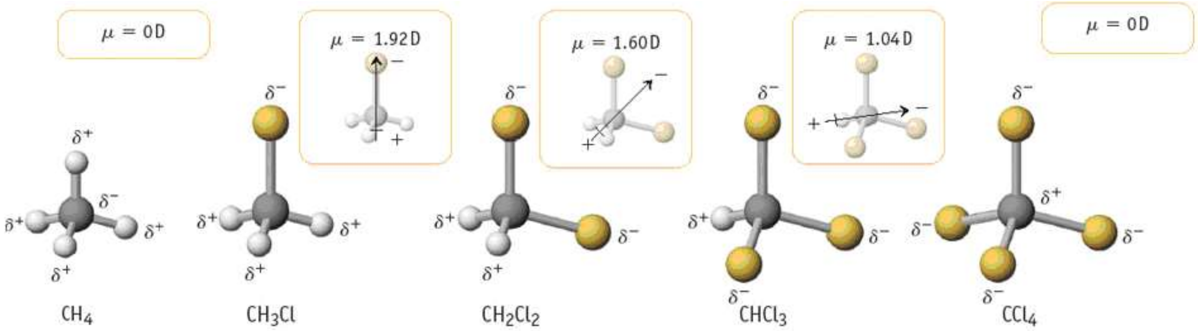

Obr. 1.6 Dipólový moment vícenásobně chlorovaného metanu [10]

Velikost indukovaného dipólového momentu je úměrná velikosti působící intenzity lokálního elektrického pole; platí

$$\mu_i = \alpha . E_l \quad (1.7)$$

kde α je polarizovatelnost.

Dielektrická polarizace představuje vektorový součet všech dipólových momentů molekul. Proto platí:

$$\vec{P} = \frac{\sum_i \vec{\mu}_i}{V} = n.\alpha.\vec{E}_l \quad (1.8)$$

kde *n* je koncentrace polarizovatelných částic.

Při vystavení dielektrických materiálů vnějším vlivům mechanické napětí, teplotní variace se objevují různé dielektrické jevy jako piezoelektřina, pyroelektřina a feroelektřina, které se využívají pro různé aplikace v kondenzátorech, akčních členech, měničích, aplikacích paměti senzorů atd.

Empirické funkce pro rozložení relaxačních dob molekul

Pro popis dielektrické relaxace bylo odvozeno několik, více či méně empirických funkcí. Stěžejním prvkem studia dielektrické spektroskopie je studium těchto empirických funkcí, resp. jejich parametrů v závislosti na vnějších faktorech. Mezi nejvýznamnější faktory patří teplota, intenzita elektrického pole, vlhkost a tlak. Jelikož reálné dielektrické systémy jsou nanejvýš pouhým přiblížením ke klasickému Debyeovu modelu, používají se v praxi pro dielektrický popis následující empirické funkce označované jako rozdělení. [12,13]

- Coleovo – Coleovo (CC) rozdělení
- Coleovo – Davidsonovo (CD) rozdělení
- Havriliakovo – Negamiho (HN) rozdělení

V následující části bude podrobněji rozebráno pouze HN rozdělení, neboť poskytuje nejhlubší fyzikální interpretaci jejich parametrů.

Toto rozdělení vzniklo na základě vyhodnocení rozsáhlého souboru experimentálních dat kombinací CC a CD rozložení relaxačních dob. Výraz pro komplexní permitivitu má tvar:

$$\varepsilon^* = \varepsilon_\infty + \frac{\varepsilon_S - \varepsilon_\infty}{\left[1 + \left(j\omega\tau_0\right)^\alpha\right]^\beta} \quad (1.9)$$

Z uvedeného vztahu 1.9 je zřejmé, že toto rozdělení musí postihovat řadu experimentálních souborů dat lépe, než CC a CD, protože obsahuje čtyři nezávisle volitelné parametry (α, β, $\varepsilon_s - \varepsilon_\infty$, τ_0), zatímco v Coleově – Coleově i Coleově – Davidsonově rozdělení jsou tyto nezávislé parametry pouze tři. Je však potřeba si uvědomit, že zvyšování počtu parametrů vede ke zvýšení shody příslušné závislosti s experimentem, není však zárukou dokonalejší fyzikální interpretace experimentálních dat. Havriliakovo – Negamiho rozdělení má významnou vlastnost, že v logaritmických souřadnicích je závislost $\varepsilon''(\omega)$ tvořena dvěma přímkami se směrnicemi α pro $\omega << 1/\tau0$ a $\alpha\beta$ pro $\omega >> 1/\tau0$. Z toho plyne, že parametry α a β mají názornou geometrickou interpretaci, a proto se Havriliakovo – Negamiho rozdělení velice často používá pro popis relaxace [13]. Na obr. 1.7 je znázorněn průběh HN rozdělení v souřadném systému log ε´´ - log ω. Na obr. 1.8 je pak uvedena závislost ztrátového čísla a relativní permitivity na frekvenci pro HN rozdělení.

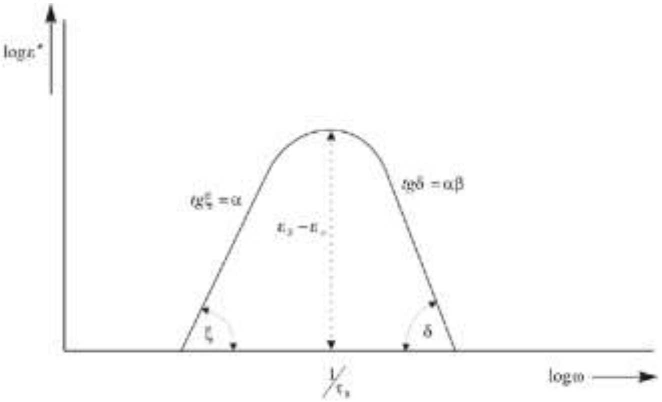

Obr. 1.7 Havriliakovo – Negamiho rozložení v souřadném systému log ε´´ - log ω

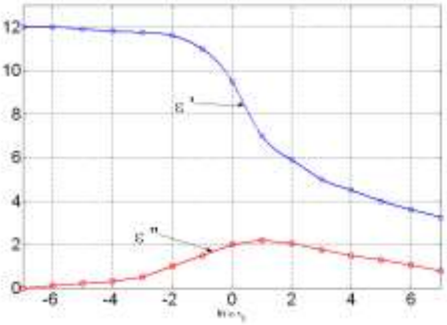

Obr. 1.8 Ztrátové číslo a relativní permitivita pro HN rozdělení
(α=0,33, β=0,14) - simulace

1.3 NOVÝ SMĚSNÝ VZTAH PRO KOMPOZITY S KULOVÝMI ČÁSTICEMI

Kompozitní materiály s kovovými plnivy představují dvousložkový nebo vícesložkový systém, jehož vlastnosti jsou ovlivňovány vlastnostmi polymerní matrice [7,8,11], vlastnostmi kovového plniva a jejich vzájemnou interakcí na rozhraní plnivo-polymer. Kompozity jsou často předmětem současného materiálového výzkumu, dopadu velikosti částic je však věnována jen malá pozornost. S rozvojem nanokompozitů se toto téma stává stále důležitějším. Tato práce byla zaměřena na experimentální studie a numerickou analýzu dopadu velikosti Ni plniva na dielektrické vlastnosti celého kompozitu, i když celkový obsah Ni zůstává konstantní. Na základě experimentálních zjištění byl vyvinut vzorec permitivity (dielektrická konstanta) kompozitu, který zohledňuje jak koncentraci, tak i velikost kovových částic plniva.

Cílem výzkumu bylo pozorování a následné vyhodnocení vlivu Ni kovového plniva v různých koncentracích na 5 různých velikostí částic v rozmezí 35 - 115 µm na jejich dielektrické vlastnosti. Uvedené výsledky jsem z velké většiny změřil na Institutu für Physik Universität Augsburg (Německo), některé dílčí části na UFYZ FEKT VUT v Brně. Výsledky byly publikována v A2-A4,A8. Jako matrice byl zvolen kopolymer ethylen - vinylacetát (PEVAc) se 45% (hmotn.) podílem vinylacetátu. Niklové práškové plnivo bylo použito v různých velikostech částic Ni (označované jako „frakce“) a koncentraci. Přehled studovaných frakcí a celkového obsahu Ni je uveden v následující tabulce:

Tabulka 1.2 – frakce připravovaných vzorků

Fraction	Range of sizes of 99.99 % of all particles from the fraction	Average particle size (diameter) parameter-*b*
1520	90-140 µm	115 µm
1320	45-125 µm	85 µm
1120	30-96 µm	63 µm
1020	20-71 µm	45 µm
1010	3-73 µm	35 µm

Měřicí zařízení

Měření byla prováděna pomocí různých impedančních analyzátorů - HP 4284A Precision LCR Meter, Alpha-Analyzer od Novocontrol a E4991A RF Impedance / Material Analyzer od Agilent. Vzorky měly kruhový tvar (d = 55 mm) a tloušťku 0,5 mm. Kromě toho byly při měření pomocí Alpha-Analyzer použity obdélníkové vzorky o rozměrech 15x15x1 mm. Zkušební vzorky byly měřeny při frekvencích 0,1 Hz - 10 MHz; tento příspěvek se však zaměřuje na závislost elektrických vlastností na koncentraci a velikosti částic. Proto jsou uváděny pouze výsledky při 1 kHz.

Měření na všech dostupných vzorcích přineslo výsledky, které jasně dokazují vliv velikosti přidaných sférických částic Ni na měřené elektrické i dielektrické vlastnosti. Obrázek 1.9 a) ukazuje relativní permitivitu ε' a ztrátové číslo ε'' jako funkci velikosti částic Ni při stejném obsahu Ni (tj. Počet větších částic je menší, aby byl zachován konstantní obsah Ni).

Rozdíl mezi měřenými vzorky lze také pozorovat na grafu rezistivity uvedeném na obr. 1.9 b). Plné čáry označují nejlepší shody s naměřenými hodnotami za předpokladu lineární závislosti.

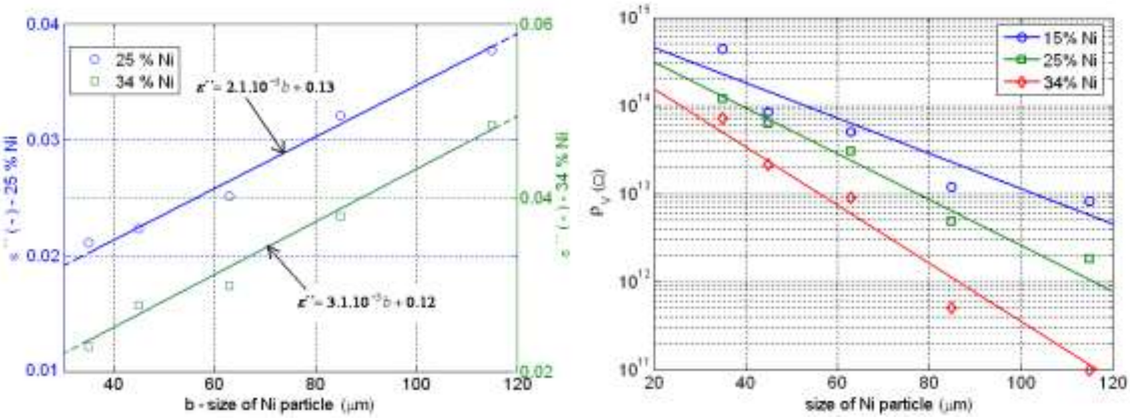

Obr. 1.9 a) relativní permitivita ε' a ztrátové číslor ε'' jako funkce velikosti dopantových částic

b) rezistivita v závislosti na velikosti dopantových částic pro 15 %, 25 % and 34 % hm zastoupení Ni [A3]

Obrázek 1.9 b) ukazuje pokles odporu s rostoucí velikostí částic Ni a také skutečnost, že rychlost tohoto poklesu (sklon křivky) roste se zvyšujícím se obsahem Ni v matrici. Rovněž velikost měrného odporu obecně klesá se zvyšujícím se obsahem Ni.

V další části se pokusím matematicky popsat vztah mezi odporem vzorku a velikostí kovových částic. Cílem je najít vhodný matematický vztah na základě zavedených směšovacích pravidel i číselných hodnot případných koeficientů.

V první části analýzy byla na výsledky měření Obr. 1.9 a tabulka 1.2 použita řada klasických směšovacích pravidel tab. 1.1. Střední kvadratická odchylka pro směsné vztahy a vzorky 1120 a 1520 je uvedena v následující tabulce:

Mixing rules	root-mean-square error	root-mean-square error
	Fraction 1120	Fraction 1520
my new rule	$1{,}8.10^{-1}$	$1{,}1.10^{-1}$
Maxwell	$1{,}3.10^{2}$	$5{,}3.10^{2}$
Lichtenecker log.	$5{,}8.10^{6}$	$8{,}1.10^{3}$
Lichtenecker exp. k=0.1	273,1	771,8
Botcher	$3{,}5.10^{3}$	$4{,}1.10^{3}$

Žádný z testovaných vzorců neobsahoval velikost částic, a proto žádný z nich nebyl shledán uspokojivým. Hlavní nevýhodou většiny směsných vztahů byla skutečnost, že byly platné pouze do 50% obsahu plniva. Dle výsledků Lichteneckerovo exponenciální směšovácí pravidlo s exponentem k = 0,1 nejlépe vyhovuje kompozitu Ni-PEVAc, a proto bylo Lichteneckerovo exponenciální pravidlo použito jako výchozí bod pro odvození nového směsného vztahu, který také zohledňoval velikost přidaných částic.

Lichteneckerův exponenciální vztah pro vnitřní měrný odpor vícesložkového kompozitního systému je následující:

$$\rho_{vs}^{k} = \sum_{i=1}^{n} v_i . \rho_{Vi}^{k} \quad (1.10)$$

kde *k* je empirický parametr, který závisí primárně na tvaru a orientaci částic, $\sum\rho_i$ jsou rezistivity a v_i jsou objemové podíly jednotlivých složek. Parametry leží v intervalu (-1, +1) [A1-4].

V našem případě se objemová koncentrace částic Ni v matrici pohybuje od 15% do 75%. Aby bylo možné ustanovit nové směšovací pravidlo, je nutné najít funkci, která by charakterizovala pokles křivek odporu s rostoucí velikostí částic směrem k nižším hodnotám odporu. Analýza naměřených křivek vedla k závěru, že příspěvek matice k vodivosti kompozitu musí být změněn s ohledem na velikost částic pomocí exponenciální závislosti:

$$\rho_m = \rho_{mm}.\exp(-0{,}035.b) \quad (1.11)$$

kde ρ_{mm} označuje experimentálně stanovenou hodnotu měrného odporu matice, *b* je průměr částic Ni v µm a ρ_m označuje měrný odpor částice vstupující do rovnice 1.10.

Křivky odporu nejenže s rostoucí velikostí částic klesají na nižší hodnoty odporu, ale jejich sklon se také mění v závislosti na obsahu Ni, jak je patrné z obr. 1.9. Proto bylo nutné zahrnout změnu sklonu do nového směšovacího pravidla. Nejlepším způsobem, jak zahrnout změnu sklonu, bylo vytvořit závislost koeficientu *k* na velikosti částic. Závislost byla analyzována a bylo zjištěno, že funkci vystihující uvedené proměnné je dána vztahem $k = -9{,}8.10^{-4}.b + 0{,}16$.

Jelikož nyní byly nalezeny všechny vlastnosti související se změnou velikosti částic Ni ve složeném systému, lze nově upravený Lichteneckerův vzorec navrhnout následovně:

$$\rho_{vs}^{k} = \frac{v_1.\rho_{Ni}^{k} + v_2.(\rho_{mm}.\exp[-0{,}035.b])^{k}}{v_1}$$

kde $k = -9{,}8.10^{-4}.b + 0{,}16$ a b označuje průměr rozptýlených sférických částic Ni [µm]. Po přeskupení lze výše uvedenou rovnici zapsat jako:

$$\rho_{vs} = \exp\left[\frac{\log(v_1^2 \rho_{Ni}^{k} + v_2(\rho_{mm} * (-0{,}035 * b))^{k})}{v_1.k}\right]$$

Toto nové směšovací pravidlo velmi dobře vyhovuje celé analyzované škále obsahu Ni a velikostí částic Ni. Grafická interpretace předloženého vzorce pro systém Ni-PEVAc je uvedena na obr 1.10. Grafická interpretace pro jiné směsné vztahy je obsažena [A5-A8].

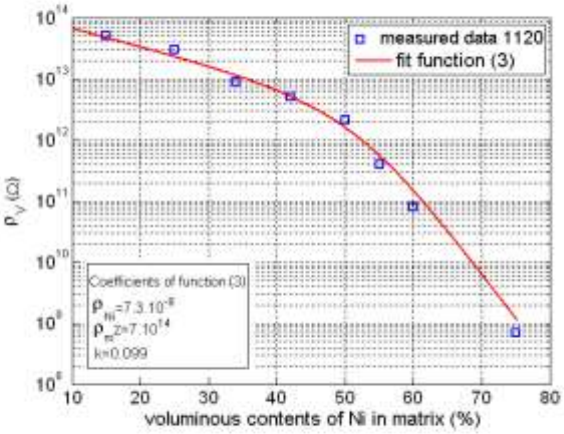

Obr. 1.10 Aplikace nového pravidla směšování pro frakce 1120

Přidání plniva Ni (sférické částice), s různými velikostmi, ale se stejnou koncentrací Ni, do polymerní matrice vede ke kompozitům s různými dielektrickými vlastnostmi. Nově navržené směšovací pravidlo popisuje chování Ni-polymerního systému v celém rozsahu dostupných koncentrací Ni, tj. v intervalu 0% - 75% obsahu Ni, a navíc obsahuje koeficient charakterizující velikost částic. Nový vzorec byl vytvořen a experimentálně ověřen pro systém Ni-PEVAc a Cu-PEVAc. [A5,A8] Je pravděpodobné, že toto nové směsné pravidlo bude, platí pro jiné systémy obsahující sférické částice v polymerní matrici, ovšem nebylo již ověřeno.

2 DIELEKTRICKÉ A PIEZOELEKTRICKÉ VLASTNOSTI PIEZOKERAMIKY

V dnešní době se elektrokeramika používá v mnoha aplikacích, jako jsou senzory, akční členy a piezoelektrická zařízení. Titaničitan-zirkoničitan olovnatý (PZT) je piezoelektrický materiál, který vykazuje vysoký piezoelektrický výkon vhodný pro použití v piezoelektrických aplikacích. PbO odpařený během vysokoteplotních procesů je však toxická sloučenina pro člověka a životní prostředí. Evropská unie (EU) schválila omezení používání těžkých kovů, jako je olovo (Pb), kadmium (Cd), chrom (Cr), rtuť (Hg), cín (Sn) a jiné těžké kovy [15,16]. Z těchto důvodů jsou místo PZT vyvíjeny bezolovnaté piezoelektrické materiály s podobnými vlastnostmi pro použití v piezoelektrických aplikacích.

Piezoelektřina

Podle definice je piezoelektrický materiál necentro-symetrický materiál, který se stane elektricky polarizovaným působením mechanické síly [17]. Název piezoelektrický je odvozen z řeckého slova piezen, což znamená stisknutí [18]. Tento efekt je lineární i reverzibilní, tedy velikost polarizace přímo souvisí s velikostí aplikovaného napětí, přičemž znaménko je závislé na směru napětí (v tahu nebo v tlaku). Všechny sloučeniny s necentro-symetrickou třídou krystalů kromě 432 jsou piezoelektrické, obrázek 2.1.

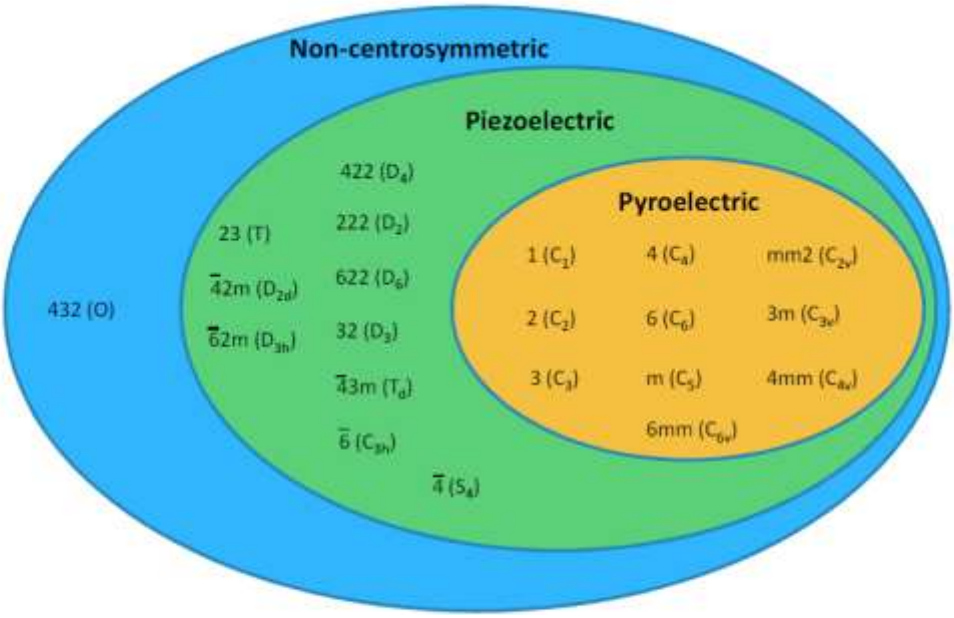

Obr. 2.1 Diagram ukazující vztah mezi fyzikálními vlastnostmi a třídou krystalů pro dielektrické materiály

Skutečnost, že polarizace a napětí spolu korelují, jak je popsáno výše, vede ke dvěma formálním definicím piezoelektřiny, známým jako přímí a nepřímí (reverzní, konverzní) piezoelektrický jev. Přímý piezoelektrický jev je pozorován, když fyzická deformace piezoelektrického materiálu, nebo na něj aplikované napětí indukuje polarizaci a odpovídající povrchový náboj v materiálu. Nepřímý piezoelektrický jev popisuje aplikaci elektrického pole na piezoelektrický materiál vedoucí k fyzické deformaci (přetvoření). Tyto dva efekty lze matematicky popsat pomocí rovnic 2.1 a 2.2 [19]:

$$\vec{D} = d_{ab}\vec{T} + \varepsilon^{T}\vec{E} \quad přímí\ jev \quad (2.1)$$

$$\vec{S} = d_{ab}\vec{E} + s^{E}\vec{T} \quad konverzní\ jev \quad (2.2)$$

Kde $\vec{D}$ je elektrická indukce, která přímo souvisí s polarizací materiálu, $\vec{T}$ je mechanické napětí, $\vec{E}$ je elektrické pole, $\vec{S}$ je povrchové napětí, *d* je piezoelektrický koeficient vztahující elektrické pole podél osy *a* k výslednému přetvoření podél osy *b*, *s* je materiálová konstanta (inverzní k modulu pružnosti) a *ε* je dielektrická konstanta (permitivita).

2.1 KŘIVKA DIELEKTRICKÉ HYSTEREZE.

Polarizace, která se obvykle označuje *P*, souvisí s elektrikou indukcí *D* lineárním výrazem:

$$D_i = P_i + \varepsilon_0 E_i$$

kde dolní index *i* představuje kteroukoli ze tří souřadnic x, y a z a ε_0 je permitivita vakua. Důsledkem odolnosti proti přepínání domén, ve feroelektrických materiálech je, že polarizace je hysterezní, což znamená, že *D* a *P*, jsou nelineární funkce *E* a mohou záviset na předchozím stavu materiálu. Konkrétně je polarizace *P* dvojitou funkcí aplikovaného elektrického pole *E*, a není tedy s polem přesně reverzibilní. Horní část obrázku 2.2 ukazuje vztah mezi *P* a *E* pro komerční feroelektrický materiál. Tato křivka je známá jako křivka dielektrické hystereze.

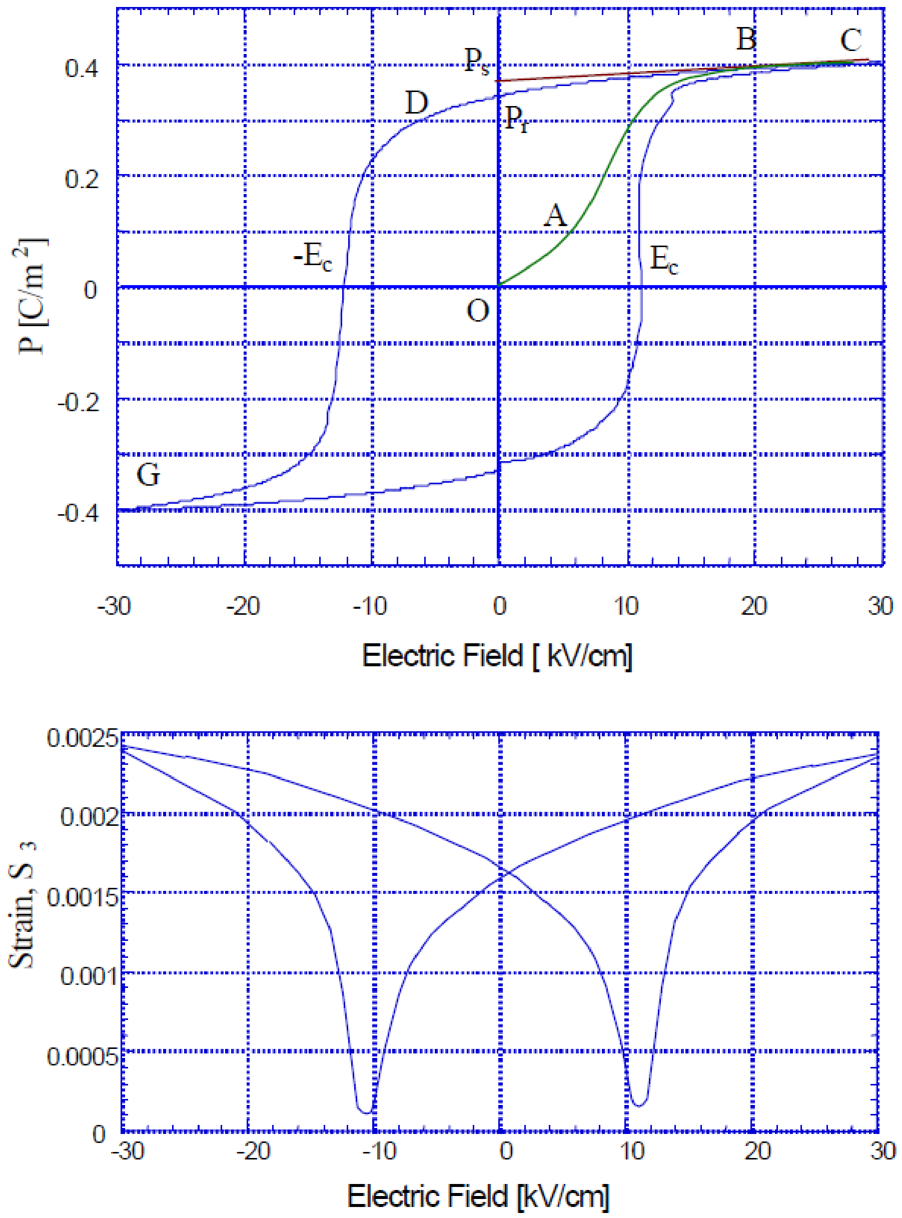

Obr. 2.2 (Horní část obrázku): Dielektrická hysterezní smyčka PZT-5
(Obrázek spodní): Deformační smyčka PZT-5 ve směru leštění S3

Pokud je zpočátku nepolarizovaný vzorek piezokeramiky vystaven rostoucímu elektrickému poli při teplotě mírně pod jeho *Tc* (Curieova teplota), dipóly se postupně natáčejí do směru el. pole a polarizace bude sledovat křivku zobrazenou v horní části obrázku.

Pokud je aplikované elektrické pole malé, je pozorován pouze lineární vztah mezi *P* a *E*, protože pole není dostatečně velké, aby natočilo jakoukoli doménu, a krystal se bude chovat jako normální dielektrický materiál. Tento případ odpovídá segmentu OA v horní části obrázku 2.2. Jak se zvyšuje elektrické pole, řada negativně orientovaných domén, které mají polarizaci opačnou ke směru pole, se postupně začne natáčet do směru el. pole a začne probíhat orientace domény. To má za následek prudce rostoucí *P* s rostoucím polem *E* a polarizace se bude rychle zvyšovat (segment AB), dokud nebudou všechny domény natočeny do směru elektrického pole (segment BC). Toto je stav nasycení, ve kterém se krystal jeví, že se skládá pouze z jedné domény, natočené do směru el. pole. Tento jev je označován jako saturace polarizace materiálu.

Jakmile poté intenzita el. pole klesá, polarizace se obecně snižuje, ale nevrací se zpět na nulu (bod D v horní části obrázku 2.2). Jakmile je el. pole sníženo na nulu, část domén zůstane napólována (natočena) ve směru el. pole a krystal bude vykazovat remanentní polarizaci P_r. Extrapolace lineárního segmentu BC křivky zpět na polarizační osu (v bodě E) představuje hodnotu spontánní polarizace P_S. Remanentní polarizaci v krystalu nelze odstranit, dokud aplikované pole v opačném směru nedosáhne určité hodnoty (v bodě F). Intenzita pole potřebná ke snížení polarizace P na nulu se nazývá koercitivní síla E_C. Pokud se el. pole dále zvětšuje v záporném směru způsobí úplné natočení elektrických dipólů v tomto směru a cyklus lze dokončit opětovným obrácením směru el. pole.

Tvar hysterezní křivky se liší u různých piezoelektrických materiálů, ale remanentní polarizace je u všech materiálů PZT obecně kolem 0,3–0,35 C/m2.

Dolní část obrázku 2.2 ukazuje odchylku relativní deformace vzorku S_3 (tj. ve směru polarizace) elektrickým polem a je vidět, že také vykazuje hysterezní charakter, který odpovídající přesně účinku pozorovanému pro polarizaci.

2.2 LINEÁRNÍ TEORIE PIEZOELEKTŘINY

Na Obrázek 2.2 zobrazuje hysterezní chování feroelektrických materiálů. Přesto je činnost feroelektrického materiálu omezena na takzvaný lineární rozsah, představovaný přibližně segmentem CD. Je vidět, že větší aplikace elektrického pole znamená větší nelinearitu. [20]

Chování piezoelektrických materiálů v lineárním rozsahu lze vysvětlit lineární teorií piezoelektriky, která je uvedena v této části. V případě neferoelektrických materiálů, jako je křemen, je tato teorie velmi přesná. V případě feroelektrických materiálů je nutné vzít v úvahu její omezení. Obecně platí, že aplikace lineární teorie piezoelektřiny je omezena a neplatí na rezonanci materiálů, jejich depolarizaci a na další nelineární efekty. [20]

Materiálové konstanty jsou standardní hodnoty určené na definovaných tělesech (odpovídající IEEE Standard on Piezoelectricity 1978)[25]. V souladu s touto konvencí se ortogonální osy X, Y a Z (také 1,2,3) obvykle používají jako základ pro identifikaci elasto-piezo-dielektrických koeficientů materiálu. Směr Z je určen jako směr polarizace. Čísla 4, 5 a 6 popisují mechanická smykové napětí, které působí tangenciálně k oblastem definujícím souřadný systém. Jak je znázorněno na obrázku 2.3, lze je chápat jako rotace kolem každé osy.

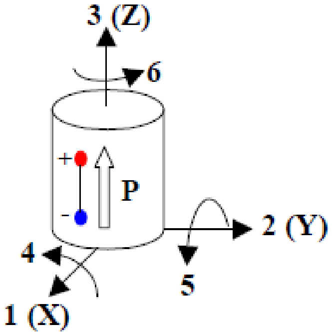

Obr. 2.3 Konvence pro osy.

2.2.1 Základní rovnice

Obecně lze přímý piezoelektrický efekt (tzv. Senzorový efekt), který se aplikuje na piezoelektrický materiál v jediném krystalu, popsat maticí, která vysvětluje polarizaci vyvinutou krystalem při vnějším napětí (normální, T_1 až T_3 a smykové, T_4 až T_6). [21]

Specifický případ přímého piezoelektrického jevu je, když je míra polarizace prováděna na vnějším elektrickém poli E = 0 V/m. V tomto případě je polarizace rovna volnému náboji q, který je na elektrodách, jak je dáno rovnicí (2.1).

$$P_i = q_i = d_{ij} \,.\, T_j \quad (2.3)$$

V rovnici (2.3) představuje q_i lineární volný náboj rozprostřený na povrchu ve směru i. Rovnici (2.3) lze také vyjádřit jako:

$$\begin{Bmatrix} q_1 \\ q_2 \\ q_3 \end{Bmatrix} = \begin{bmatrix} d_{11} & d_{12} & d_{13} & d_{14} & d_{15} & d_{16} \\ d_{21} & d_{22} & d_{23} & d_{24} & d_{25} & d_{26} \\ d_{31} & d_{32} & d_{33} & d_{34} & d_{35} & d_{36} \end{bmatrix} . \begin{Bmatrix} T_1 \\ T_2 \\ T_3 \\ T_4 \\ T_5 \\ T_6 \end{Bmatrix} \quad (2.4)$$

V rovnicích (2.3) a (2.4) se polarizační vektor rovná volnému náboji na elektrodách v důsledku nulového vnějšího elektrického pole.

Předchozí rovnice (2.3) platí plně pro monokrystaly a v takovém případě představuje polarizaci generovanou v materiálu při působení mechanického napětí. Piezoelektrické koeficienty d_{ij} indikují intenzitu polarizace v každém směru. [21]

Pokud vezmeme v úvahu lineární rozsah, ekvivalentní výraz pro feroelektrické materiály je dán vztahem

$$P_i = (P_s)_i + d_{ij} . T_j \quad (2.5)$$

V praxi se P_S uvažuje pouze ve směru pólování, protože v příčných směrech je zanedbatelný. Tedy $(P_S)_i = P_3$.

Nepřímý piezoelektrický efekt lze popsal pomocí napětí generovaného v piezoelektrickém materiálu, když je vystaven vnějšímu elektrickému poli E_i. Zejména pokud materiál není upnutý (podmínka volného posunu, $T_{ij} = 0$), lze konverzní efekt vyjádřit jako:

$$S_i = d_{ij}^{\theta,T} . E_j \quad (2.6)$$

nebo přesněji

$$\begin{Bmatrix} S_1 \\ S_2 \\ S_3 \\ S_4 \\ S_5 \\ S_6 \end{Bmatrix} = \begin{bmatrix} d_{11}^{\theta,T} & d_{12}^{\theta,T} & d_{13}^{\theta,T} \\ d_{21}^{\theta,T} & d_{22}^{\theta,T} & d_{23}^{\theta,T} \\ d_{31}^{\theta,T} & d_{32}^{\theta,T} & d_{33}^{\theta,T} \\ d_{41}^{\theta,T} & d_{42}^{\theta,T} & d_{43}^{\theta,T} \\ d_{51}^{\theta,T} & d_{52}^{\theta,T} & d_{53}^{\theta,T} \\ d_{61}^{\theta,T} & d_{62}^{\theta,T} & d_{63}^{\theta,T} \end{bmatrix} . \begin{Bmatrix} E_1 \\ E_2 \\ E_3 \end{Bmatrix} \quad (2.7)$$

V předchozích rovnicích (2.6) a (2.7) se $d_{ij}^{\theta,T}$ nazývá nábojový piezoelektrický koeficient. Tento koeficient udává intenzitu deformace ve směru *i*, S_i, když je elektrické pole aplikováno ve směru *j*, E_j. Indexy horního indexu se používají k označení veličin, které jsou udržovány konstantní nebo nulové. Piezoelektrický koeficient d_{ij} je tedy stejný jako u přímého efektu. [21]

2.3 KONSTITUTIVNÍ ROVNICE

Obecně může lineární dielektrikum odolat současně vnějším podmínkám teploty, mechanickému namáhání a elektrickému poli. V tomto případě je možné analyzovat mechanické a elektrické chování materiálu a následně spojit oba výsledky.

2.3.1 Mechanické chování piezoelektrického materiálu

Parametr ***S*** popisuje mechanické lineární chování (aproximace Hookova zákona) piezoelektrického materiálu vystaveného elektrickému poli ***E***, napětí ***T*** a změně teploty Δθ. Tento stav je zobrazen v následující matici:

$$\begin{Bmatrix} S_1 \\ S_2 \\ S_3 \\ S_4 \\ S_5 \\ S_6 \end{Bmatrix} = \begin{bmatrix} d_{11}^{\theta,T} & d_{12}^{\theta,T} & d_{13}^{\theta,T} \\ d_{21}^{\theta,T} & d_{22}^{\theta,T} & d_{23}^{\theta,T} \\ d_{31}^{\theta,T} & d_{32}^{\theta,T} & d_{33}^{\theta,T} \\ d_{41}^{\theta,T} & d_{42}^{\theta,T} & d_{43}^{\theta,T} \\ d_{51}^{\theta,T} & d_{52}^{\theta,T} & d_{53}^{\theta,T} \\ d_{61}^{\theta,T} & d_{62}^{\theta,T} & d_{63}^{\theta,T} \end{bmatrix} \begin{Bmatrix} E_1 \\ E_2 \\ E_3 \end{Bmatrix} + \begin{bmatrix} s_{11}^{E,\theta} & s_{12}^{E,\theta} & s_{13}^{E,\theta} & s_{14}^{E,\theta} & s_{15}^{E,\theta} & s_{16}^{E,\theta} \\ s_{21}^{E,\theta} & s_{22}^{E,\theta} & s_{23}^{E,\theta} & s_{24}^{E,\theta} & s_{25}^{E,\theta} & s_{26}^{E,\theta} \\ s_{31}^{E,\theta} & s_{32}^{E,\theta} & s_{33}^{E,\theta} & s_{34}^{E,\theta} & s_{35}^{E,\theta} & s_{36}^{E,\theta} \\ s_{41}^{E,\theta} & s_{42}^{E,\theta} & s_{43}^{E,\theta} & s_{44}^{E,\theta} & s_{45}^{E,\theta} & s_{46}^{E,\theta} \\ s_{51}^{E,\theta} & s_{52}^{E,\theta} & s_{53}^{E,\theta} & s_{54}^{E,\theta} & s_{55}^{E,\theta} & s_{56}^{E,\theta} \\ s_{61}^{E,\theta} & s_{62}^{E,\theta} & s_{63}^{E,\theta} & s_{64}^{E,\theta} & s_{65}^{E,\theta} & s_{66}^{E,\theta} \end{bmatrix} \begin{Bmatrix} T_1 \\ T_2 \\ T_3 \\ T_4 \\ T_5 \\ T_6 \end{Bmatrix} + \begin{Bmatrix} \alpha_1^{E,T} \\ \alpha_2^{E,T} \\ \alpha_3^{E,T} \\ \alpha_4^{E,T} \\ \alpha_5^{E,T} \\ \alpha_6^{E,T} \end{Bmatrix} \Delta\theta \quad (2.8)$$

Koeficient α je koeficient tepelné roztažnosti, definovaný jako [21,23]:

$$\alpha_i^{E,T} = \left[\frac{\partial S_i}{\partial \theta}\right]_{E,T=const} \quad (2.9)$$

2.3.2 Elektrické chování piezoelektrického materiálu

Elektrická odezva materiálu je popsána lineární polarizací *P* generovanou v materiálu v důsledku mechanické, elektrické nebo tepelné deformace a je dána rovnicí (2.10) [23]:

$$\begin{Bmatrix} D_1 \\ D_2 \\ D_3 \end{Bmatrix} = \begin{bmatrix} d_{11}^{E,\theta} & d_{12}^{E,\theta} & d_{13}^{E,\theta} & d_{14}^{E,\theta} & d_{15}^{E,\theta} & d_{16}^{E,\theta} \\ d_{21}^{E,\theta} & d_{22}^{E,\theta} & d_{23}^{E,\theta} & d_{24}^{E,\theta} & d_{25}^{E,\theta} & d_{26}^{E,\theta} \\ d_{31}^{E,\theta} & d_{32}^{E,\theta} & d_{33}^{E,\theta} & d_{34}^{E,\theta} & d_{35}^{E,\theta} & d_{36}^{E,\theta} \end{bmatrix} . \begin{Bmatrix} T_1 \\ T_2 \\ T_3 \\ T_4 \\ T_5 \\ T_6 \end{Bmatrix} + \begin{bmatrix} \varepsilon_{11}^{E,\theta} & \varepsilon_{12}^{E,\theta} & \varepsilon_{13}^{E,\theta} \\ \varepsilon_{21}^{E,\theta} & \varepsilon_{22}^{E,\theta} & \varepsilon_{23}^{E,\theta} \\ \varepsilon_{31}^{E,\theta} & \varepsilon_{32}^{E,\theta} & \varepsilon_{33}^{E,\theta} \end{bmatrix} \begin{Bmatrix} E_1 \\ E_2 \\ E_3 \end{Bmatrix} +$$

$$\begin{Bmatrix} p_1^{T,E} \\ p_2^{T,E} \\ p_3^{T,E} \end{Bmatrix} \Delta\theta \quad (2.10)$$

Koeficient *p* je pyroelektrický koeficient, definovaný jako:

$$p_i^{T,E} = \left[\frac{\partial D_i}{\partial \theta}\right]_{E,T=const} \quad (2.11)$$

2.3.3 Globální odezva: Spojení mechanického i elektrického chování

Piezoelektrické koeficienty, d_{ij}, jsou identické pro elektrickou i mechanickou odezvu. To znamená, že piezoelektřina zahrnuje interakci mezi elektrickým a mechanickým chováním materiálu. Z tohoto důvodu je možné vyjádřit globální výslednou maticí, která spojila obě chování. Tato matice se nazývá elasto-piezoelektrická matice a je uvedena v rovnici (2.12) [23].

$$\begin{Bmatrix} S_1 \\ S_2 \\ S_3 \\ S_4 \\ S_5 \\ S_6 \\ D_1 \\ D_2 \\ D_3 \end{Bmatrix} = \begin{bmatrix} s_{11}^{E,\theta} & s_{12}^{E,\theta} & s_{13}^{E,\theta} & s_{14}^{E,\theta} & s_{15}^{E,\theta} & s_{16}^{E,\theta} & d_{11}^{\theta,T} & d_{12}^{\theta,T} & d_{13}^{\theta,T} \\ s_{21}^{E,\theta} & s_{22}^{E,\theta} & s_{23}^{E,\theta} & s_{24}^{E,\theta} & s_{25}^{E,\theta} & s_{26}^{E,\theta} & d_{21}^{\theta,T} & d_{22}^{\theta,T} & d_{23}^{\theta,T} \\ s_{31}^{E,\theta} & s_{32}^{E,\theta} & s_{33}^{E,\theta} & s_{34}^{E,\theta} & s_{35}^{E,\theta} & s_{36}^{E,\theta} & d_{31}^{\theta,T} & d_{32}^{\theta,T} & d_{33}^{\theta,T} \\ s_{41}^{E,\theta} & s_{42}^{E,\theta} & s_{43}^{E,\theta} & s_{44}^{E,\theta} & s_{45}^{E,\theta} & s_{46}^{E,\theta} & d_{41}^{\theta,T} & d_{42}^{\theta,T} & d_{43}^{\theta,T} \\ s_{51}^{E,\theta} & s_{52}^{E,\theta} & s_{53}^{E,\theta} & s_{54}^{E,\theta} & s_{55}^{E,\theta} & s_{56}^{E,\theta} & d_{51}^{\theta,T} & d_{52}^{\theta,T} & d_{53}^{\theta,T} \\ s_{61}^{E,\theta} & s_{62}^{E,\theta} & s_{63}^{E,\theta} & s_{64}^{E,\theta} & s_{65}^{E,\theta} & s_{66}^{E,\theta} & d_{61}^{\theta,T} & d_{62}^{\theta,T} & d_{63}^{\theta,T} \\ d_{11}^{E,\theta} & d_{12}^{E,\theta} & d_{13}^{E,\theta} & d_{14}^{E,\theta} & d_{15}^{E,\theta} & d_{16}^{E,\theta} & \varepsilon_{11}^{E,\theta} & \varepsilon_{12}^{E,\theta} & \varepsilon_{13}^{E,\theta} \\ d_{21}^{E,\theta} & d_{22}^{E,\theta} & d_{23}^{E,\theta} & d_{24}^{E,\theta} & d_{25}^{E,\theta} & d_{26}^{E,\theta} & \varepsilon_{21}^{E,\theta} & \varepsilon_{22}^{E,\theta} & \varepsilon_{23}^{E,\theta} \\ d_{31}^{E,\theta} & d_{32}^{E,\theta} & d_{33}^{E,\theta} & d_{34}^{E,\theta} & d_{35}^{E,\theta} & d_{36}^{E,\theta} & \varepsilon_{31}^{E,\theta} & \varepsilon_{32}^{E,\theta} & \varepsilon_{33}^{E,\theta} \end{bmatrix} \begin{Bmatrix} T_1 \\ T_2 \\ T_3 \\ T_4 \\ T_5 \\ T_6 \\ E_1 \\ E_2 \\ E_3 \end{Bmatrix} \quad (2.12)$$

Předchozí matice je takzvaná konstitutivní rovnice d-formy a obvykle je reprezentována v kompaktní formě, jak je znázorněno rovnicí (2.13) v tabulce 2.1. Volba nezávislých proměnných je libovolná. Daná dvojice rovnic piezoelektrické matice odpovídá konkrétní volbě nezávislých proměnných. Rovnice (2.13) až (2.16) ukazují další možné konstitutivní maticové rovnice používající různé nezávislé proměnné.

Tabulka 2.1. Sada konstitutivních rovnic pro piezoelektrický materiál [23]

Nezávislé proměnné	typ	Piezoelektrický vztah	forma
T, E	Rozsáhlý	$\begin{Bmatrix} [S] \\ {[D]} \end{Bmatrix} = \begin{bmatrix} [s^E] & [d] \\ {[d]} & [\varepsilon^T] \end{bmatrix} \begin{Bmatrix} [T] \\ {[E]} \end{Bmatrix}$ (2.13)	d
S, D	Rozsáhlý	$\begin{Bmatrix} [T] \\ {[E]} \end{Bmatrix} = \begin{bmatrix} [c^D] & [-h] \\ {[-h]} & [\beta^S] \end{bmatrix} \begin{Bmatrix} [S] \\ {[D]} \end{Bmatrix}$ (2.14)	h
T, D	Směsný	$\begin{Bmatrix} [S] \\ {[E]} \end{Bmatrix} = \begin{bmatrix} [s^D] & [-g] \\ {[-g]} & [\beta^T] \end{bmatrix} \begin{Bmatrix} [T] \\ {[D]} \end{Bmatrix}$ (2.15)	g
S, E	Směsný	$\begin{Bmatrix} [T] \\ {[D]} \end{Bmatrix} = \begin{bmatrix} [c^E] & [e] \\ {[e]} & [\varepsilon^S] \end{bmatrix} \begin{Bmatrix} [S] \\ {[E]} \end{Bmatrix}$ (2.16)	e

[E] a *[D]* jsou tenzory prvního řádu; *[S]* a *[T]* jsou tenzory druhého řádu (matice 3x3); *[d]*, *[g]*, *[e]* a *[h]* (piezoelektrické koeficienty) jsou tenzory třetího řádu (matice 6x3); *[ε]*, *[β]* (dielektrické koeficienty) jsou tenzory druhého řádu (matice 3x3) a *[s]*, *[c]* (elastické koeficienty) tenzory čtvrtého řádů (matice 6x6). Ve výše zmíněných konstitutivních rovnicích nebyl uvažován tepelný účinek a musí být zahrnut, pokud jsou uvažovány pyroelektrické materiály[21,23].

2.3.4 Interpretace elasto-piezoelektrických koeficientů

Piezoelektrické koeficienty

Piezoelektrický koeficient d_{ij} je známý jako piezoelektrický napěťový koeficient. Protože koeficient d je ekvivalentní pro přímý a nepřímý efekt, je možné jej definovat pomocí dvou ekvivalentních výrazů, jak je znázorněno rovnicí (2.17).

$$d_{ij}^{\theta} = \begin{cases} \left[\frac{\partial S_j}{\partial E_i}\right]_{D,\theta} \quad [m/V] \ \text{přímý jev} \\ \left[\frac{\partial D_i}{\partial T_j}\right]_{S,\theta} \quad [C/N] \ \text{nepřímý jev} \end{cases} \qquad (2.17)$$

Protože piezoelektrický materiál může být anizotropní, jsou jeho fyzikální konstanty (pružnost, permitivita a piezoelektrické koeficienty) tenzorové veličiny a vztahují se jak ke směru působícího napětí, elektrickému poli atd., a také ke směrům na ně kolmým. Z tohoto důvodu jsou koeficienty obecně dány dvěma indexy. Dolní index, který odkazuje na směr dvou souvisejících veličin (např. napětí a pružnost). Horní index se používá k označení veličiny, která se udržuje konstantní.[24]

U piezoelektrických koeficientů, které odkazují na elektrickou a mechanickou veličinu, označuje první dolní index směr uvažované elektrické veličiny (posunutí nebo elektrické pole) a druhý dolní index označuje směr uvažované mechanické veličiny.

Další matice zobrazují strukturu z d-matice pro tři důležité případy piezoelektrických materiálů: monokrystalický křemen, feroelektrická keramika PZT a feroelektrický polymer PVDF.[24]

Monokrystalický křemen

$$\boldsymbol{d_{mono}} = \begin{matrix} \boldsymbol{d_{11}} & \boldsymbol{-d_{11}} & \mathbf{0} & \boldsymbol{d_{14}} & \mathbf{0} & \mathbf{0} \\ \mathbf{0} & \mathbf{0} & \mathbf{0} & \mathbf{0} & \boldsymbol{-d_{14}} & \boldsymbol{-2d_{11}} \\ \mathbf{0} & \mathbf{0} & \mathbf{0} & \mathbf{0} & \mathbf{0} & \mathbf{0} \end{matrix}, \quad \mathbf{(2.19)}$$

d_{11}=2,3.10^{-12} C/N; d_{14}=-0,7.10^{-12} C/N

BaTiO3, PZT, BCZT a další polykrystalická feroelektrika. (osa pólování = 3)

$$\boldsymbol{d_{PZT}} = \begin{matrix} \mathbf{0} & \mathbf{0} & \mathbf{0} & \mathbf{0} & \boldsymbol{d_{15}} & \mathbf{0} \\ \mathbf{0} & \mathbf{0} & \mathbf{0} & \boldsymbol{d_{15}} & \mathbf{0} & \mathbf{0} \\ \boldsymbol{d_{31}} & \boldsymbol{d_{31}} & \boldsymbol{d_{33}} & \mathbf{0} & \mathbf{0} & \mathbf{0} \end{matrix}, \quad (2.20)$$

PVDF piezoelektrický polymer

$$\boldsymbol{d_{PVDF}} = \begin{matrix} \mathbf{0} & \mathbf{0} & \mathbf{0} & \mathbf{0} & \boldsymbol{d_{15}} & \mathbf{0} \\ \mathbf{0} & \mathbf{0} & \mathbf{0} & \boldsymbol{d_{24}} & \mathbf{0} & \mathbf{0} \\ \boldsymbol{d_{31}} & \boldsymbol{d_{32}} & \boldsymbol{d_{33}} & \mathbf{0} & \mathbf{0} & \mathbf{0} \end{matrix}, \quad (2.21)$$

Zbytek piezoelektrických koeficientů má analogickou definici, jak je uvedeno v následujících rovnicích:[25]

Piezoelektrický napěťový koeficient

$$\boldsymbol{g_{ij}^{\theta}} = \left\{ \frac{\left[\frac{\partial S_j}{\partial D_i}\right]_{D,\theta=konst.} \quad [m^2/C] \;\; \textbf{nepřímý jev}}{\left[\frac{\partial E_i}{\partial T_j}\right]_{S,\theta=konst.} \quad [V.m/N] \quad \textbf{Přímý jev}} \right., \quad (2.22)$$

Piezoelektrický koeficient tuhosti

$$\boldsymbol{h_{ij}^{\theta}} = \left\{ \frac{\left[\frac{\partial T_j}{\partial D_i}\right]_{D,\theta=konst.} \quad [N/C] \;\; \textbf{nepřímý jev}}{\left[\frac{\partial E_i}{\partial S_j}\right]_{S,\theta=konst.} \quad [V/m] \quad \textbf{přímý jev}} \right., \quad (2.23)$$

Piezoelektrický e koeficient

$$\boldsymbol{e_{ij}^{\theta}} = \left\{ \frac{\left[-\frac{\partial T_j}{\partial E_i}\right]_{D,\theta=konst.} \quad [N/m/V] \;\; \textbf{nepřímý jev}}{\left[\frac{\partial D_i}{\partial S_j}\right]_{S,\theta=konst.} \quad [C/m^2] \quad \textbf{Přímý jev}} \right., \quad (2.24)$$

Elastické koeficienty

Pro vyjádření vztahu mezi mechanickým namáháním a napětím lze uvažovat dva elastické koeficienty: poddajnost a tuhost.

Poddajnost materiálu je definována jako přetvoření produkované na jednotku aplikovaného napětí. Může být měřeno při konstantě elektrického pole nebo při konstantě elektrického náboje, jak je uvedeno v následujících rovnicích:

Elastický koeficient poddajnosti s_{ij}:

$$S_{ij}^{E,\theta} = \left[\frac{\partial S_i}{\partial T_j}\right]_{E,\theta=konst.} \quad [m^2/N] \;\; Shoda\ při\ E = konst.\ nebo\ nula\ (SHORT), \quad (2.25)$$

$$S_{ij}^{D,\theta} = \left[\frac{\partial S_i}{\partial T_j}\right]_{D,\theta=konst.} \quad [m^2/N] \;\; Shoda\ při\ D = konst.\ nebo\ nula\ (OPEN), \quad (2.26)$$

První dolní index se vztahuje ke směru přetvoření, druhý ke směru napětí. Například: S_{23}^{E} je soulad pro normální napětí kolem osy 3 a doprovodné napětí ve směru osy 2 za podmínek konstanty elektrického pole.

Podobně je definován koeficient tuhosti jako:

Koeficient pružné tuhosti c_{ij}:

$$C_{ij}^{E,\theta} = \left[\frac{\partial T_j}{\partial S_i}\right]_{E,\theta=konst.} \quad [N/m^2] \quad Shoda\ při\ E\ =\ konst.nebo\ nula\ (SHORT)\ , (2.27)$$

$$S_{ij}^{D,\theta} = \left[\frac{\partial T_j}{\partial S_i}\right]_{D,\theta=konst.} \quad [N/m^2] \quad Shoda\ při\ D\ =\ konst.nebo\ nula\ (OPEN)\ , (2.28)$$

Dielektrické koeficienty

Permitivita je definována jako posun dielektricky vázaných nábojů na jednotku elektrického pole. Je reprezentován dvěma dolními indexy: první dolní index udává směr natočení dielektrických dipólů, druhý udává směr elektrického pole. Může být měřeno při volném posunutí (T = 0) nebo při blokovací síle (S = 0), jak je znázorněno v rovnici (2.29) [26].

$$\varepsilon_{ij}^{S,\theta} = \left[\frac{\partial D_i}{\partial E_j}\right]_{S,\theta=konst.} \quad \left[\frac{F}{m}\right] \quad Permitivita\ při\ D\ =\ konst.nebo\ nula\ (blokovací\ síla)\ , (2.29)$$

$$\varepsilon_{ij}^{T,\theta} = \left[\frac{\partial D_i}{\partial E_j}\right]_{T,\theta=konst.} \quad [F/m] \quad Permitivita\ při\ T\ =\ konst.nebo\ nula\ (volný\ posunutí), (2.30)$$

2.3.5 Omezení lineární teorie

Elektrostrikce

Obecně má odezva piezoelektrických materiálů kvadratickou složku, která je superponována na lineární chování. Tato složka závisí na elektrostrikčním koeficientu. U piezoelektrických materiálů je tento koeficient obvykle nižší než lineární piezoelektrický koeficient. Ovšem velmi výrazně se mění při zvýšení elektrického pole.

Depolarizace

Po pólování bude keramika trvale polarizována, a proto je třeba při každé další manipulaci věnovat pozornost tomu, aby nedocházelo k depolarizaci keramiky, protože by to mělo za následek částečnou nebo dokonce úplnou ztrátu jejích piezoelektrických vlastností[23].

- Elektrická depolarizace - Vystavení silnému elektrickému poli s opačnou polaritou než elektrické pole při pólování. Intenzita pole potřebná pro zahájení depolarizace závisí mimo jiné na druhu materiálu, době, kdy je materiál vystaven depolarizačnímu poli a teplotě pólování.
- Mechanická depolarizace - k mechanické depolarizaci dochází, když se mechanické napětí na piezoelektrickém prvku stane dostatečně vysoké, aby narušilo orientaci domén, a tím zničilo vyrovnání dipólů. Bezpečnostní limity pro mechanické namáhání se značně liší podle druhu materiálu.
- Tepelná depolarizace - pokud se piezoelektrický prvek zahřeje na teplotu T_c, domény se stanou neuspořádanými a prvek se úplně depolarizuje. Piezoelektrický prvek proto může fungovat po dlouhou dobu bez výrazné depolarizace pouze při teplotách hluboko pod Curieovým bodem. Bezpečná provozní teplota je za normálních podmínek přibližně v polovině intervalu i 0 - T_c.[26]

Frekvenční omezení

Všechny fyzikální systémy mají vlastní frekvenci kmitů. Pokud je systém vystaven vnějším harmonickým vlivům s frekvencí v blízkosti vlastní frekvence, bude se systém dostávat do oblasti rezonance. Pokud je však materiál piezoelektrický, lze dosáhnout elektrické rezonance, když je materiál namáhán mechanickou silou. Na druhé straně mohou být při elektrickém namáhání materiálu způsobeny vysoké mechanické deformace. Proto bude elektrický signál s frekvencí velmi blízkou mechanickým vlastním kmitům systému produkovat rezonanci.

Obrázek 2.4 ukazuje typickou frekvenční odezvu piezoelektrického disku, jedná se o frekvenční závislost absolutní hodnoty elektrické impedance. Jednotlivé elektrické rezonance ve spektru odpovídají mechanickým rezonancím (planární a tloušťkové) tohoto disku. Rezonanční frekvence bude záviset na charakteristikách piezoelektrického materiálu a mechanických a elektrických podmínkách prostředí[23].

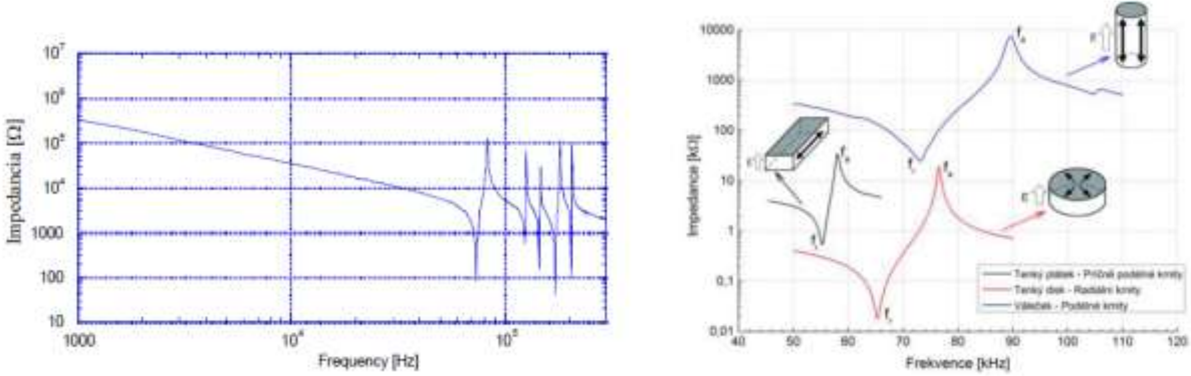

Obr. 2.4 Impedance PZT disku jako funkce frekvence (vlevo), Impedanční charakteristiky pro příčné a podélné kmity tenkého plátku, radiální kmity tenkého disku a podélné kmity válečku (vpravo)[27]

2.4 KOEFICIENT VAZBY K

Piezoelektrické materiály spojují elektrická a mechanická pole. Můžeme použít tento druh materiálů, kdy na ně aplikujeme elektrickou energii a získáme mechanickou energii, nebo naopak.

Poté je nutné mít koeficient pro měření účinnosti, s jakou se elektrická energie převádí na mechanickou energii nebo pro opačný případ. Spojovacím článkem je faktor k_{eff} (efektivní koeficient elektromechanické vazby) a je definován při frekvencích pod rezonanční frekvencí piezoelektrického tělesa jako[25]:

$$k_{eff}^2 = \frac{\textit{přeměněná energie}}{\textit{vstupní energie aplikovaná na materiál}}$$

Definice pro přímý a konverzní piezoelektrický jev:

Přímý piezoelektrický jev	**nepřímý piezoelektrický jev**
$\boldsymbol{k_{eff}^2 = \frac{\textbf{\textit{elektrická energie}}}{\textbf{\textit{mechanická energie}}}}$	$k_{eff}^2 = \frac{\textit{mechanická energie}}{\textit{elektrická energie}}$

Studium hodnot k_{eff} ukazuje, že pro moderní piezoelektrickou keramiku lze při nízkých frekvencích až 50% akumulované energie přeměnit. Hodnoty k_{eff}^2 uvedené v tabulkách jsou však obvykle teoretickým maximem založeným na přesně definovaných režimech (tj. nerealistických) materiálu. U praktických převodníků je vazební faktor obvykle výrazně nižší.

Vazební koeficient k_{eff} popisuje přeměnu energie ve všech směrech. Pokud se berou v úvahu pouze převody v konkrétních směrech, výsledný spojovací faktor je označen indexem. Například k_{33} je vazebný faktor pro podélné vibrace a velmi dlouhého a velmi tenkého válce (teoreticky nekonečně dlouhý, v praxi s poměrem délka / průměr > 10) pod vlivem podélného elektrického pole. Například k_{31} je vazebný faktor pro podélné vibrace dlouhého válce pod vlivem příčného elektrického pole a k_{15} popisuje smykové vibrace piezoelektrického tělesa.

Zvláštními případy vazebního faktoru jsou planární vazební faktor k_p a tloušťkový vazebný faktor k_t.

Planární vazebný faktor k_p tenkého disku představuje vazbu mezi elektrickým polem ve směru 3 (rovnoběžně s osou disku) a současnými mechanickými účinky ve směrech 1 a 2 (obrázek 2.6), které vedou k radiálním vibracím. Tento systém se nazývá radiální spojka[26].

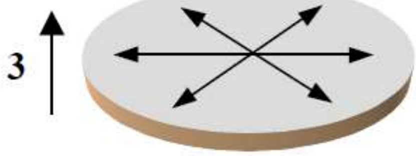

Obr. 2.5 Rovinné oscilace tenkého disku piezoelektrického materiálu

Faktor tloušťkové vazby k_t představuje vazbu mezi elektrickým polem ve směru 3 a mechanickými vibracemi ve směru 3 tenkého rovinného objektu libovolného obrysu (tj. Objektu, jehož povrchové rozměry jsou velké ve srovnání s jeho tloušťkou).

Tloušťková rezonanční frekvence tenkého rovinného objektu je mnohem vyšší než jeho příčná rezonanční frekvence.

Faktor vazby k_{eff} lze vyjádřit jako podíl energetických hustot[27]

$$k_{eff}^2 = \frac{\frac{1}{2}\varepsilon^T E^2 - \frac{1}{2}\varepsilon^S E^2}{\frac{1}{2}\varepsilon^T E^2}, \ (2.31)$$

V rovnici (2.31) představuje vztah $\frac{1}{2}\varepsilon^T E^2$ celkovou hustotu uložené energie pro volně se deformující piezoelektrické těleso (T = 0). Vztah $\frac{1}{2}\varepsilon^S E^2$ představuje hustotu elektrické energie, když je těleso omezeno (S = 0). Rozdíl mezi těmito dvěma členy se rovná uložené, převedené mechanické energii.[29]

Tuto energii lze často extrahovat a nepřeměněnou energii lze také získat zpět. Ačkoli je pro efektivní transdukci žádoucí vysoké k, neměl by se k^2 považovat za měřítko účinnosti (to je definováno jako poměr užitečně převedeného výkonu ke vstupu výkonu), protože nepřeměněná energie nemusí být nutně ztracena (převedena do tepla) a může být v mnoha případech využita.

Skutečná účinnost je poměr převedené užitečné energie k energii absorbované materiálem. Správně naladěný a dobře nastavený měnič pracující v jeho rezonanční oblasti může dosáhnout účinnosti přes 90%. Mimo jeho rezonanční oblasti by jeho účinnost však mohla být velmi nízká.[30]

2.5 PIEZOELEKTRICKÉ MATERIÁLY NA BÁZI PEROVSKITU

Mnoho z piezoelektrických materiálů, které se v současné době používá, je založeno na perovskitové struktuře, která je pojmenovaná po minerálu perovskit, $CaTiO_3$. Struktura ideálního perovskitu, sestává z kubické jednotkové buňky ABX_3. Prvek A umístěným na [½, ½, ½], prvek B-umístěn v [0,0,0] a kyslík umístěný v [½, 0,0], což vede k tomu, že prvek B tvořící sub-mřížku oktaedrů sdílejících vrchol a prvek A tvořící sub-mřížku cuboctahedra, obrázek 1.3.[31]

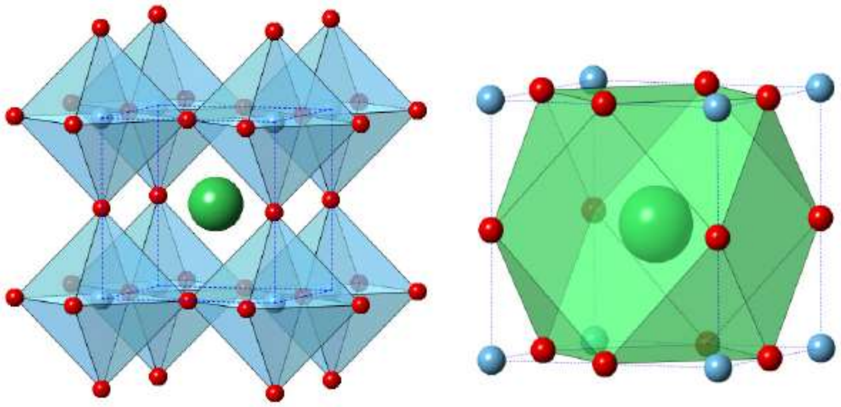

Obr. 2.6 Perovskitová jednotková buňka zobrazující oktaedru B-místa (vlevo) a A-místo cuboctahedron

Mnoho z piezoelektrických materiálů, které jsou rozsáhle studovány nebo používány, je pólováno (feroelektrická perovskitová keramika). Piezoelektrické vlastnosti v těchto materiálech vznikají v důsledku nesymetrického Jahn-Tellerova zkreslení oktaedru B-prvku což má za následek kooperativní posun kationtů vzhledem ke kyslíkovému aniontu v krystalové mřížce (obrázek 2.7), která vytváří polarizaci. [32-34] To vyžaduje, aby se jednotková buňka zkreslila ze své ideální kubické perovskitové struktury. Aplikace elektrického pole na materiál může dále podporovat vycentrování nebo mu bránit, v závislosti na směru aplikovaného pole vzhledem k centrujícím iontům. Výsledkem je fyzická deformace materiálu. Naopak, pokud je keramika stlačena nebo protažena pod napětím v tahu, je zkreslení jednotkové buňky buď zvýšeno, nebo sníženo, což má za následek změnu polarizace. [A11]

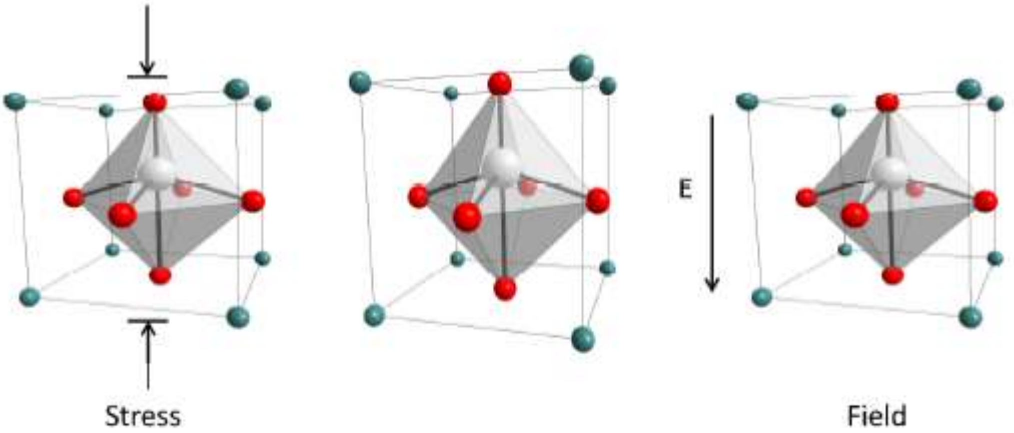

Obr. 2.7 Zkreslení piezoelektrického perovskitu napětím (vlevo) a aplikovaným elektrickým polem (vpravo); obojí způsobuje deformaci a změnu polarizace [35]

2.5.1 Olovo zirkoničitan titaničitý, PZT

Většina dnes používaných piezoelektrických zařízení je založena na směsi tuhého roztoku zirkoničitanu olovnatého a titaničitanu olovnatého sloučeniny ve formě $PbZr_xTi_{1-x}O_3$ (PZT), a% [$Pb(Mg_xNb_y) O_3$] - b% [$PbTiO_3$] (PMNPT), kvůli jejich příznivým piezoelektrickým vlastnostem včetně vysokých hodnot T_C, obvykle > 750 K s polarizacemi > 70 µC cm^{-2} [29] a piezoelektrický koeficient d_{33} hodnot až 590 pCN^{-1} ($PZT\text{-}5H^+$) [30].

Sloučeniny na bázi PZT se široce používají kvůli přítomnosti hranice morfotropní fáze, MPB. Morfotropní fázová hranice je definována jako náhlá změna v krystalografické struktuře [36]. Na takovéto fázové hranici mohou existovat dvě nebo více různé krystalografické fázové struktury s různou polarizací, ale s podobnými volnými energiemi. Každá z těchto fázových struktur může mít různé osy polarizace. Když je tedy aplikováno elektrické pole, existuje více různých os, které mohou být v souhlasném směru s vnějším elektrickým polem, což vede k vylepšeným piezoelektrickým vlastnostem. Změny struktury mají tendenci být v podstatě nezávislé na teplotě, takže je možné, aby MPB existoval v materiálu v širokém rozmezí teplot.

V PZT ve složení $PbZr_{0.46}Ti_{0.54}O_3$existuje MPB, přičemž materiál přijímá buď romboedrickou nebo tetragonální strukturu. V tomto případě je celkem 14 os polarizace, které mohou být schopny vyrovnat se s aplikovaným elektrickým polem, 6 z tetragonální fáze a 8 z romboedrické fáze. (obr. 2.8)

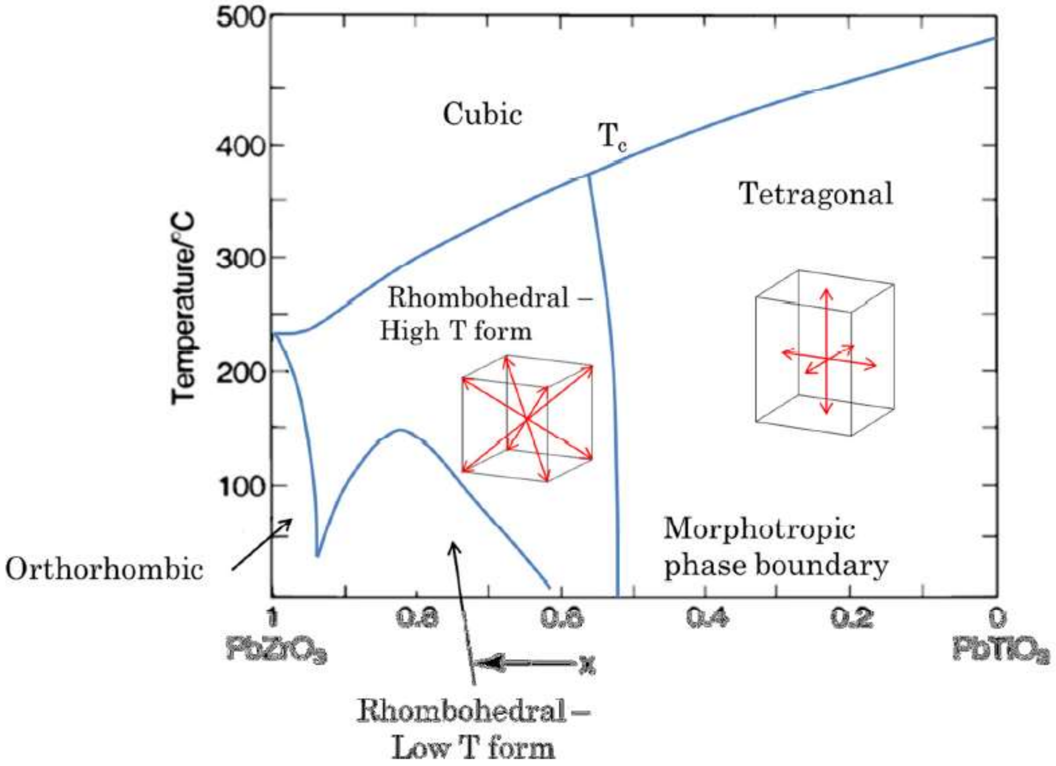

Obr. 2.8 Fázový diagram pro olovo zirkoničitan titaničitý [37]

Některé z vlastností jsou výrazně lepší na hranicích morfotropních fází. Jedná se zejména o relativní permitivitu ε_r a vazebný koeficient, k_p, což je míra účinnosti, s jakou je elektrická energie převedena na energii mechanickou (nebo naopak). Obrázek 2.9 zobrazuje variace těchto dvou parametrů pro různé kompozice PZT o jeho MPB.

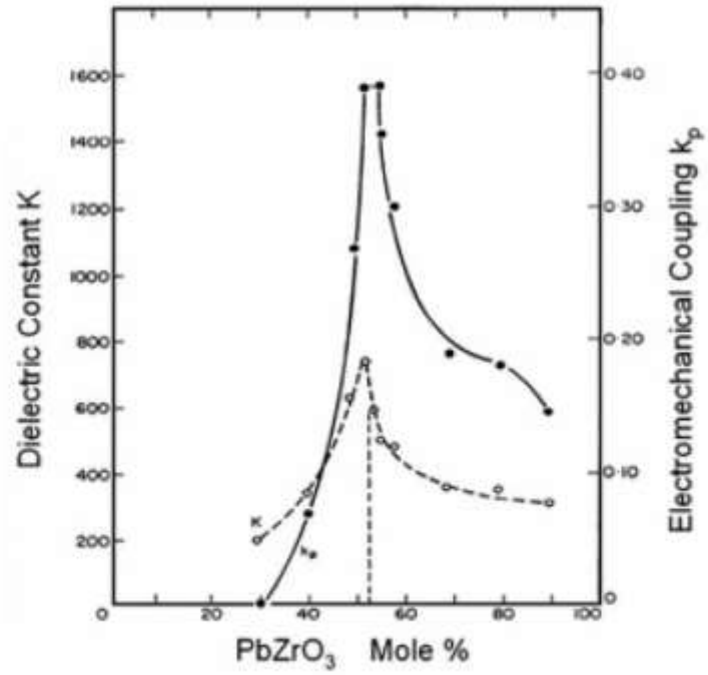

Obr. 2.9 Vylepšené dielektrické a piezoelektrické vlastnosti zobrazené v PZT kolem MPB [37]

2.5.2 Titaničnan barnatý

Titaničnan barnatý má perovskitovou strukturu s Ba^{2+} na místě A a Ti^{4+} na místě B. Byl objeven v roce 1941 uprostřed tajemství, které obklopovalo mnoho z vědeckých vývojů během válečné éry, a proto na něm pracovalo mnoho vědců včetně Thurnauera, Wainera a Salomona [35]. Kvůli válce začaly být publikovány patenty a články až v polovině 40. let [36–39], přičemž materiál byl vyvíjen jako kondenzátor s vysokým ε. V roce 1945 byl poprvé použit jako piezoelektrický měnič [25], když Robert B. Gray zjistil, že použití externího elektrického pole o vhodné síle způsobí, že se domény určité keramiky, včetně titaničitanu barnatého, vyrovnají a způsobí elektrickou odezvu.

Titaničnan barnatý má permitivitu za pokojové teploty $\varepsilon' \approx 1000–5000$ [40] a T_c 130 °C. Tato hodnota T_C je nižší než odpovídající hodnoty pro PZT [38], ale významně vyšší než jakékoli jiné materiály známé v době jejího objevu. To vedlo k jeho velkému komerčnímu využití v padesátých letech, zejména v kondenzátorech, kde nahradil TiO_2, který měl permitivitu za pokojové teploty 80-90 [31].

Struktura titaničitanu barnatého se mění s teplotou, ale je založena na jednom ze dvou systémů: neferoelektrická hexagonální struktura nebo kubická uzavřená struktura, která může být feroelektrická. Hexagonální forma existuje při teplotách nad 1460 °C [36]. Pod touto teplotou je kubický perovskit stabilnější. Formovaný perovskit může sám nabývat různých symetrií při různých teplotách, z nichž tři, rhombohedral, orthorhombic and tetragonal, jsou feroelektrické. Tyto formy existují při mnohem nižších teplotách nežli T_C 130 °C. Na každé fázové hranici je mnoho rozdílných elektronických vlastností včetně dielektrické permitivity, kapacity a piezoelektrických koeficientů.

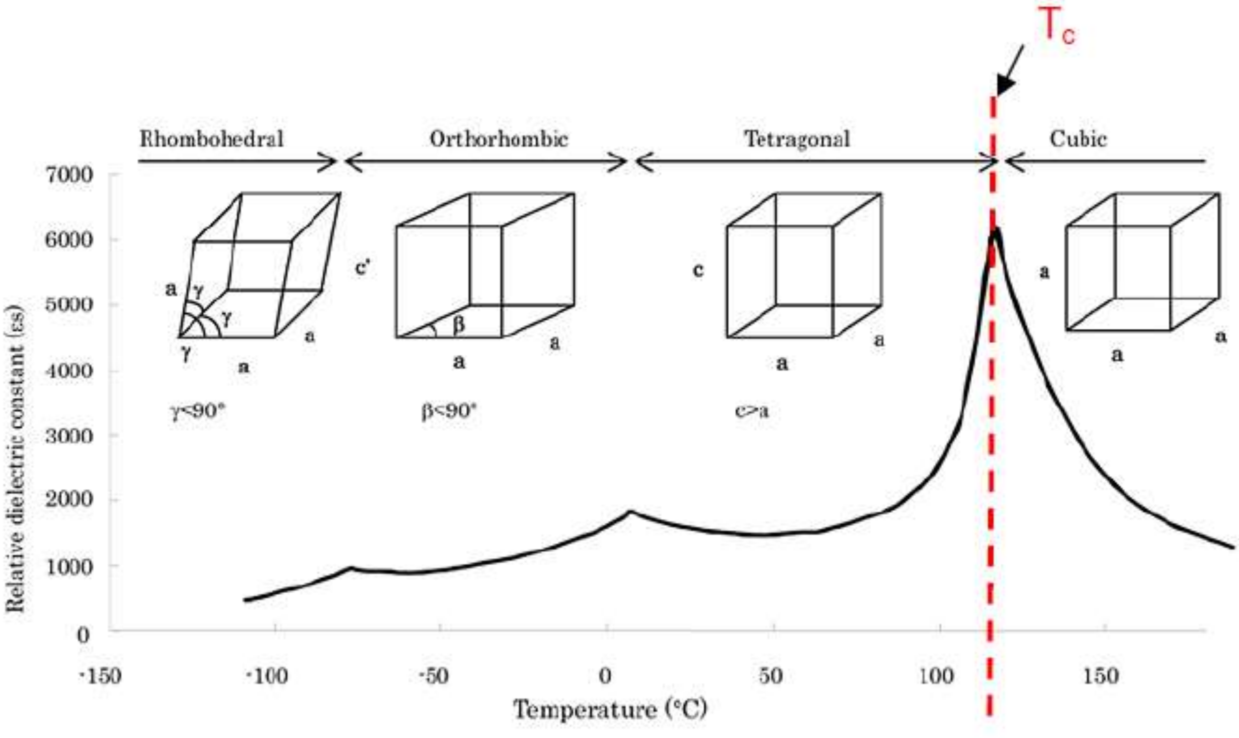

Obr. 2.10 Krychlové uzavřené perovskitové formy BaTiO3 ukazující přechod teploty, směr zkreslení doprovázející každý fázový přechod a doprovodná lokální maxima v dielektrické konstantě[36]

Nízkoteplotní rhombohedral, orthorhombic a tetragonal feroelektrické polymorfy titaničitanu barnatého jsou typické piezoelektrické perovskity. V tetragonální formě jsou ionty Ti^{4+} přemístěny podél osy c. V závislosti na orientaci jednotkové buňky v dané doméně tak vznikne 6 možných os polarizace, obrázek (2.11) [16, 21].

V ortorombické jednotkové buňce dochází k polarizaci podél čelní úhlopříčky, což vede ke 12 osám polarizace, zatímco v romboedrickém polymorfu k polarizaci dochází podél hlavní úhlopříčky. To dává 8 možných os polarizace [16, 21].

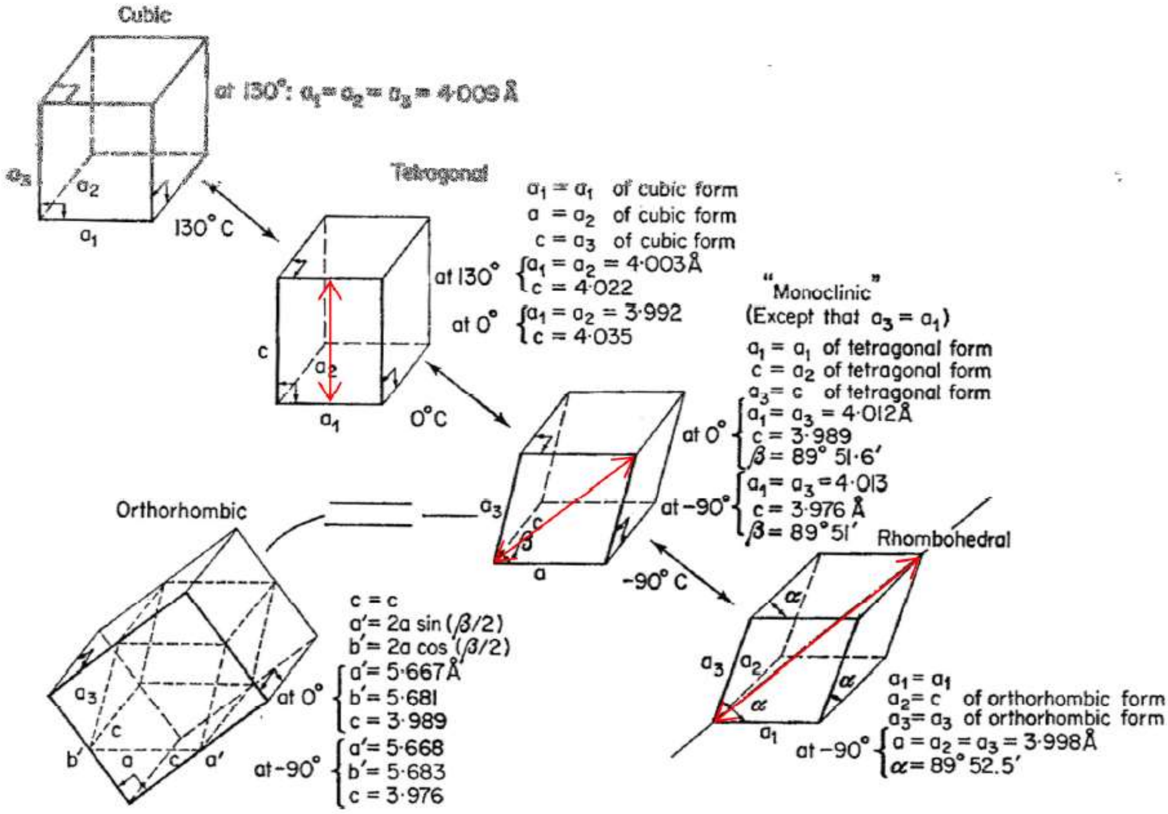

Obr. 2.11 Zkreslení jednotkových buněk pro každou z kubických forem perovskitu s orientací polarizace zobrazenou červeně

Přítomnost různých možných polarizačních os v polymorfní fázi vede ke složité struktuře domén v kompozicích na bázi barium titaničitanu a titaničitanu barnatého. Každá doména existuje jako oblast jednotkových buněk, z nichž všechny mají stejnou osu polarizace. Každá doména je obklopena dalšími doménami, které mohou mít jinou osu polarizace. Výsledkem je, že celková polarizace keramiky bude zanedbatelná kvůli rušivým účinkům konkurenčních náhodných domén.

Aplikace elektrického pole na feroelektrické perovskity, jako je $BaTiO_3$, zejména při teplotách pod nebo blízko Curieovy teploty, může vést k tomu, že domény, které jsou v souladu s polem, rostou na úkor jiných domén, což vede ke keramice s větší polarizací. Když je titaničnan barnatý ochlazen v el. poli, domény se „uzamknou“ a materiál je označen jako pólovaný. Pokud se systém ještě jednou zahřeje na teploty blížící se T_C, stačit tepelná energie k opětovné depolarizaci orientace domén, což je proces známý jako depólování.

Kromě tepelného depólování mohou být domény přeorientovány i aplikací vysokých tlakových sil. Při aplikaci ve směru polarizace to může vést k opětovné randomizaci doménových orientací [42]. V nedopovaném $BaTiO_3$ jsou doménové stěny poměrně tuhé, přičemž méně než 10% 90° domén je obecně přeorientováno působením tlaku, ve srovnání s až 50% těchto domén v jiných materiálech, jako je PZT [6]. To znamená, že $BaTiO_3$ a jeho dopované variace mohou být obzvláště užitečné v aplikacích, jako je vysoce výkonná akustika, kde nemůže vysoké tlakové napětí vést k depolarizaci.

Úhly, ve kterých se sousední domény navzájem tvoří, jsou závislé na trojrozměrné formě jednotkové buňky, a také se mění s polymorfní fází. V tetragonální $BaTiO_3$ se domény tvoří navzájem v úhlu 90° a 180° [42]. V ortorombické fázové doméně existují také při 60° a 120°, zatímco v romboedrické fázové doméně existují při ~ 70°, ~ 110° a 180°.

2.5.3 Dopovaný titaničitan barnatý

Jako perovskitový materiál je titaničitan barnatý schopen pojmout mnoho různých kationtových i aniontových dopantů, Většina dopovaných přípravků BaTiO3, včetně dopantů studovaných v mých pracích, je zaměřena na kationtovou substituci dopantů, a proto bude tato diskuse omezena na účinky kationtových dopantů.

Doping umožňuje přizpůsobení fyzikálních vlastností titaničitanu barnatého, včetně T_C a jeho relativní permitivity, širokému spektru použití. Dopanty lze využít k posunu T_C k nižším teplotám. Dopanty mohou také způsobit rozšíření vrcholu permitivity, což vedlo k plošším relativnímu profilu permitivity a nižší teplotě T_c [43, 46]. To lze použít pro zařízení kondenzátorového typu, která nevyžadují velké relativní permitivity, ale vyžadují stabilnější teplotní profil a často širší teplotní rozsah provozu.

Doping má obvykle jednu ze tří forem. Prvním z nich je isovalentní doping, který zahrnuje substituci dopantovými druhy stejného náboje jako druhy, které nahrazuje. Druhým je akceptorový doping, který zahrnuje částečnou substituci kationtových druhů kationty s nižším nábojem. Třetí typ je donorový doping, který zahrnuje částečnou substituci kationtů vysoce nabitými kationty. Druhý i třetí typ dopingu zahrnují částečnou substituci odlišně nabitým druhem než originál, a proto se o nich říká, že jsou aliovalentní.

Isovalenttní dopování

K tzv. izovalentní substituci dochází, pokud jsou kationty nahrazeny ionty se stejným nábojem (Sr^{2+}/Ba^{2+} za Pb^{2+}; Sn^{4+} za Ti^{4+}/Zr^{4+}). Dopanty tohoto typu mají za následek nárůst dielektrických a piezoelektrických vlastností výměnou za snížení Curieovy teploty. Byl studován vliv každého z dopantů, obr.2.12, přičemž z výsledků vyplynulo, že přidání $SrTiO_3$ způsobuje stálé snížení T_C o 3,7 °C na každé procento přidané dopující látky. Přidání $PbTiO_3$ způsobuje stálé zvýšení T_C o 3,7 °C na každé procento dopantů. Přidání $CaTiO_3$ zpočátku způsobuje mírné zvýšení T_C s úrovněmi dopantu až 8%, než způsobí pokles T_C s dalším přidáním dopantu [47,48].

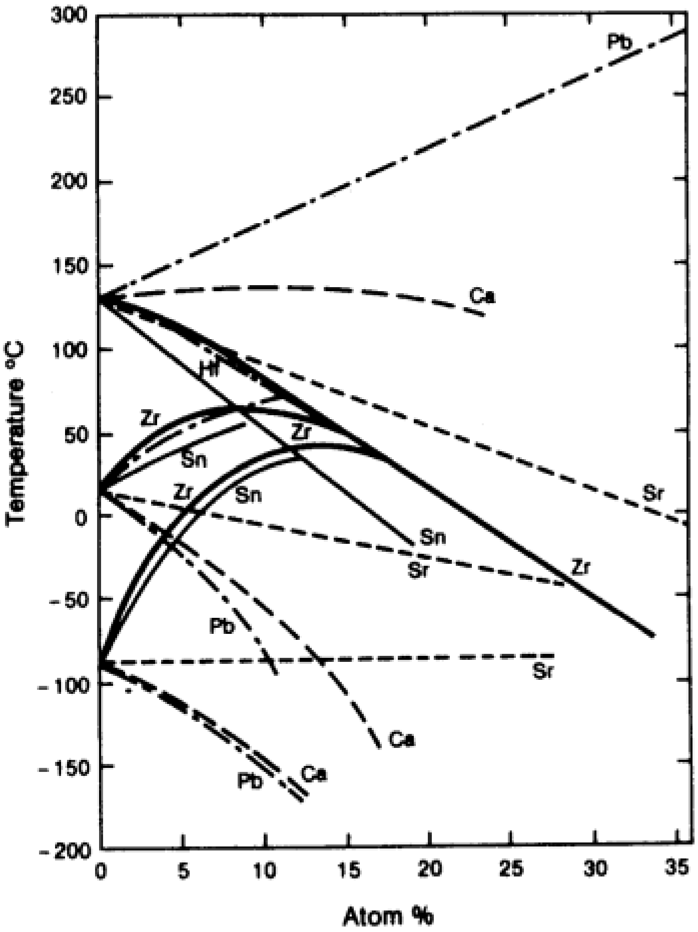

Obr. 2.12 Účinky dopingu jediným iontem isovalentními na teploty fázového přechodu různých polymorfů nedopovaného BaTiO3.[47]

Tabulka 2.2. Vliv isovalentní substituce na fázový přechod teploty nedopovaného BaTiO3

Dopant	ΔTc	Ortorombický / tetragonální přechod, TO / T (°C)	Rhombohedral / orthorhombic přechod. TR / O (°C)
PbTiO3	+3.7	-9,5	-6,0
SrTiO3	-3.7	-2	0
CaTiO3	Nelineární	6,7	-6,0
BaYrO3	-5.3	-7	+18
BaSno3	-8	+5	+16
BaHfO3	-5.0	+7	+16

Kromě posunu fázových hranic může přidání dopantů také způsobit změnu typu feroelektrického chování od chování typického feroelektrického k relaxačnímu feroelektrickému [48,51]. Relaxační materiály jsou komerčně důležité pro zařízení včetně senzorů, kondenzátorů s vysokou permitivitou, převodníků a elektromechanických akčních členů. Důležité jsou zejména kvůli přítomnosti velkého rozšířeného píku v relaxačním spektru materiálů, který umožňuje relativně velký teplotní rozsah, a také možnosti dosáhnout velmi vysoké permitivity. Toto je vlastnost, která je běžná v materiálech na bázi BaTiO3, které mají PPB v důsledku izovalentního nebo aliovalentního dopingu.

Současná isovalentní substituce jak A, tak B-místa je obecně považována za kumulativní účinek každého ze samostatných druhů dopantů. Nejvíce prostudovaným z nich je CaZrO3.[49,50,53]

2.5.4 BCZT keramika - (Ba, Ca) (Zr, Ti) O_3

Nejnověji do rodiny piezomateriálů přibyl systém bezolovnatého materiálu s přesným složením (1-x) Ba ($Ti_{0,8}Zr_{0,2}$) O_3 - x ($Ba_{0,7}Ca_{0,3}$) TiO_3 ve zkratce (1-x) BZT-xBCT nebo BZT-BCT, nebo jen zkráceně BCZT. Tento systém je intenzivně zkoumán jako náhrada za materiály na bázi olova. V současné době systém vykazuje velmi vysoké piezoelektrické vlastnosti, například d_{33} byl změřen ≈ 600 pC/N pro složení 0,50 BZT-0,50 BCT (50BCZT) a ≈ 350 pC/N pro složení 0,55 BZT-0,45 BCT (45BCZT) stejně jako pro 0,45 BZT-0,55 BCT (55BCZT) [12]. Důvodem tak vysokých piezoelektrické vlastnosti pro 50BCZT je morfotropní fázová hranice (MPB) [26], jak je uvedeno na obrázku 2.13, podobně jako u PZT. Jediným rozdílem v keramice BCZT od hranice morfotropní fáze PZT je křivka MPB. Takto zakřivená křivka MPB představuje také závislost na stechiometrii a teplotě, což vede k degradaci stability materiálu z hlediska teploty. Fázový diagram je charakterizován MPB oddělujícím feroelektrickou R (strana BZT) a T (strana BCT). Nejdůležitější vlastností systému BZT-BCT ve fázovém diagramu je existence kubikoromboedricko-tetragonálního (C-R-T) trojitého bodu [26]. Z obrázku 2.13 je také zřejmé, že pro 50BCZT, 30BCZT, 20BCZT leží hranice R-T blízkosti teploty okolí. V blízkost takových strukturálních nestabilit, feroelektrika často vykazuje velké, anizotropní zvýšení piezoelektrických, dielektrických a elastických vlastností [53]. Zahřátím materiálu z hranice R-T do T-C zůstává piezoelektrická odezva dostatečně velká, přestože fáze R a T jsou odděleny pouze asi o ~ 80 °C (obr. 2.16). Vylepšená odezva ve fázi T je tedy poháněna nestabilitami při přechodech R-T i T-C, přičemž každá nestabilita zvyšuje piezoelektrické koeficienty podél různých krystalografických směrů. Proto většina zrn ve vzorku vykazuje zvýšenou odezvu bez ohledu na jejich orientaci vzhledem k elektrickému poli.

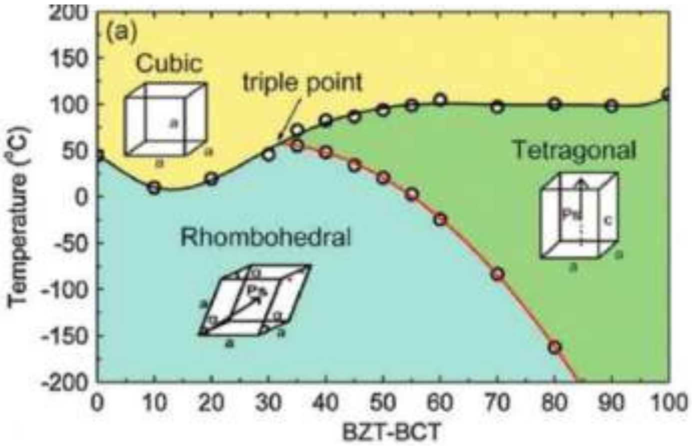

Obr. 2.13 Schematické fázové schéma pseudobinárního feroelektrického systému (1-x) Ba (Zr0,2Ti0,8) O3-x (Ba0,7Ca0,3) TiO3, zkráceně BZT-BCT

Aby bylo možné pochopit piezoelektrické jevy a neobvyklou povahu fázového přechodového řádu Rhombohedral-Tetragonal-Cubic (R-T-C), který dříve uváděli Lui a Ren, bylo provedeno opětovné zkoumání, které provedli Keeble a kol. o strukturní fázové transformaci keramiky BCZT [56], [12]. Bylo zjištěno, že oblast mezi romboedrickou a tetragonální fází překlenuje ortorombická fáze Amm2 (O-fáze), čímž bylo vytvořeno nové pořadí fází jako Rhombohedral-Tetragonal-Orthorhombic-Cubic (R-T-O-C), jak je znázorněno na obrázku 2.14 [56]. Klíčový bod, kde dochází k přechodu mezi R-fází na T-fázi přes mezilehlou O-fázi, se nazývá oblast fázové konvergence. V této oblasti leží potenciálně velmi vysoké piezoelektrické vlastnosti.

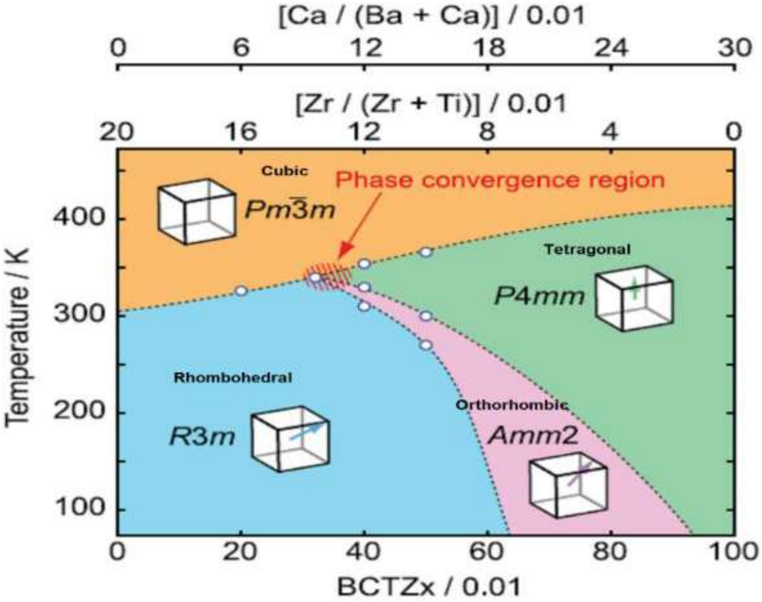

Obr. 2.14 Revidovaná fázová struktura keramiky BCZT

Jednou z největších nevýhod tohoto materiálu je nízká *Tc* ~ 93 °C, stejně jako vysoké teploty slinování (> 1450 °C) [12, 49], které jsou nutné k získání nejlepších vlastností. Další nevýhoda je velká rychlost růstu zrna. Tyto podmínky nejsou vhodné pro průmyslovou výrobu. Proto strategie zahrnující doping, úpravu složení a různé metody zpracování patří mezi aktuální témata současného materiálového výzkumu. Výsledky vedou ke snížení teploty syntézy a zpracování pro tvorbu keramiky o velikosti zrna pod 10 µm. Již byly provedeny výzkumy týkající se účinků velikosti zrna souvisejících s teplotou slinování na piezoelektrické vlastnosti keramiky BCZT [57 - 60].

Kromě toho mohou být vlastnosti keramiky BCZT ovlivněny různými parametry, například Bai a kol. popsal parametry a podmínky zpracování, které by mohly potenciálně přizpůsobit piezoelektrické vlastnosti jako d_{33} a *kp* v závislosti na různých velikostech zrn [58]. Závislost piezoelektrických vlastností BCT-BZT na pólovacích podmínkách, jako je elektrické pole a teplota, publikovali Wu et al. [61]. Nejčastěji se u strukturovaných materiálů perovskitového typu dosahuje vysokých funkčních vlastností v blízkosti MPB. Kromě vysokých funkčních vlastností v blízkosti fázové hranice je aliovalentní doping dalším způsobem přizpůsobení elektrických vlastností této keramiky, stejně jako pro doping PZT keramiky.

Doping může způsobit vnitřní bodové defekty, které mohou potenciálně ovlivnit stabilitu doménových stěn a struktury domény, což vede k různým modifikacím, jako jsou vylepšené dielektrické vlastnosti [58, 59], zvýšení tepelné stability [57], úprava *Tc* [50, 60] atd. Přesto je MPB keramiky BCZT více závislá na teplotě, což vede k překážce teplotní stability materiálového systému [57].

Ke snížení teploty slinování z 1550 °C na 1450 °C, byla použita slinovací pomůcka Li_2CO_3. U takto upravené BCZT keramiky byly pozorovány d_{33} = 512 pC/N, kp = 45% a relativně nízká T_C = 80 °C [60]. Při použití 1,5% hmotnostního CuO se teplota slinování snížila až na 1430 °C s velmi vysokým d_{33} = 670 pC/N, kp = 57% a T_C = 75 °C. [A9]

2.6 DIELEKTRICKÉ A KRYSTALOGRAFICKÉ PARAMETRY BCZT

V této kapitole tomto se zaměřím na dielektrickou a krystalografickou analýzu piezokeramických materiálů. Po 5 letech od obhájení disertační práce jsem opustil analýzu směsných vztahů a společně se skupinou oddělení keramiky CEITEC jsem začal spolupracovat na vývoji zejména bezolovnaté keramiky pro systémy „energy harvester“. Všechny uvedené výsledky jsem měřil nebo se z velké části podílel na jejich měření a prováděl jejich vyhodnocení.

2.6.1 BCZT - yCeO2 keramika slinovaná technikou TSS

Nejprve jsem se věnoval analýze “green body“ BCZT - yCeO_2 (y = 0, 0,02, 0,04, 0,07% hmot.) MPB byl nalezen v rozmezí složení yCeO_2 (y = 0 - 0,1%) a v tomto rozmezí byly pozorovány vysoké funkční vlastnosti. Na základě těchto poznatků konvenční technikou slinování byl zvolen rozsah obsahu CeO_2 (y = 0, 0,02, 0,04, 0,07% hmotn.). Poté byly realizovány piezokeramické vzorky technikou TSS. V prvním kroku byla pec naprogramována s teplotní spádem 10 °C/min na teplotu T_1 (1350, 1400, 1450 °C) s prodlevou 30 minut, aby byla zajištěna rovnoměrnost tepelné atmosféry uvnitř komory. Poté byla pec ochlazena s teplotním spádem 30 °C/min na nižší teplotu T_2. Tato teplota je fixována na 1275 °C, aby se zastavil růst zrn, a udržuje se zde po dobu 4 hodin. Nakonec se teplota snižuje na teplotu okolí rychlostí 10 °C/min.

U těchto vzorků byla nejprve provedena analýza objemové hmotnosti obr. 2.15 a na SEM analýza velikosti zrn 2.16 [A9, A12].

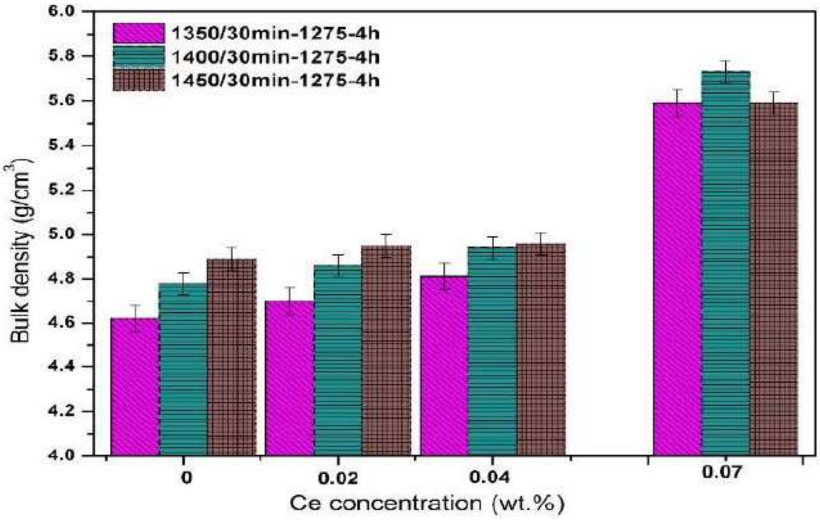

Obr. 2.15 Analýza objemové hmotnosti pro obsah CeO_2 (y = 0, 0,02, 0,04, 0,07% hmotn.) v BCZT [A9]

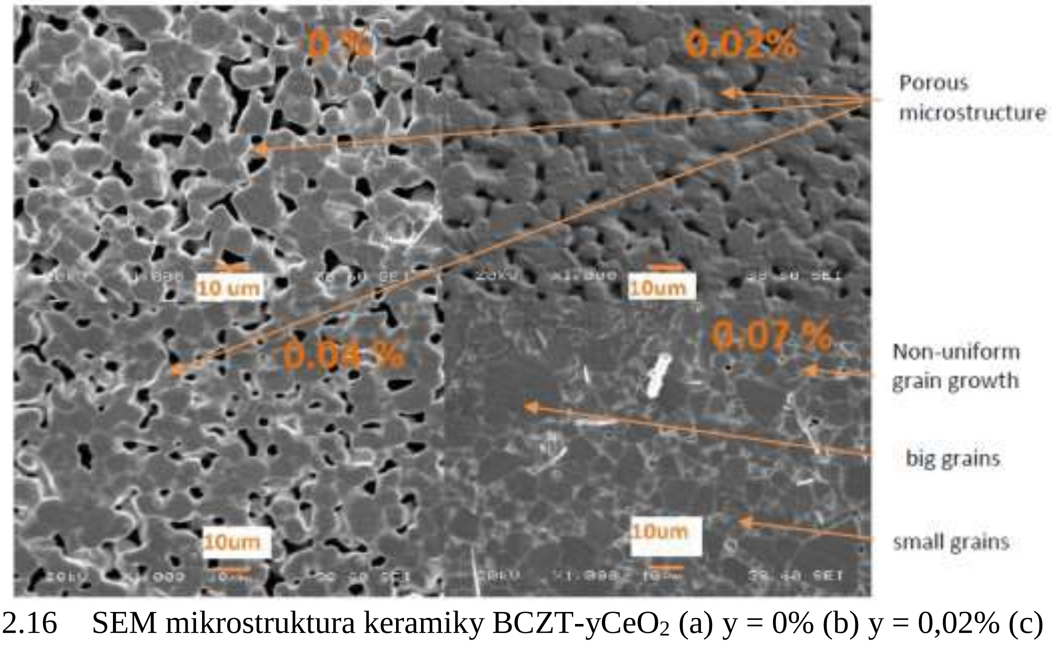

Obr. 2.16 SEM mikrostruktura keramiky BCZT-yCeO_2 (a) y = 0% (b) y = 0,02% (c) y = 0,04% (d) y = 0,07% při T_1 - 1350 °C/30 min & T_2 - 1275 °C/4h [A9,A10]

Piezoelektrické a dielektrické vlastnosti keramiky BCZT-CeO$_2$ při slinování, T$_1$ - 1400 °C/30 min a T$_2$ - 1275 °C/4 h

Obrázek 2.17 a obrázek 2.18 ukazují piezoelektrické a dielektrické vlastnosti keramiky BCZT-xCeO$_2$ při slinování při T$_1$ - 1400 °C/30 min a T$_2$ - 1275 °C/4 h. Bylo pozorováno, že planární vazební koeficient (k_p) a piezoelektrická konstanta d_{33} se zvyšovaly se zvyšujícím se obsahem Ce a současně se snižoval ztrátový činitel *tan δ*. Pro 0,07% hmotn. zastoupení CeO$_2$ bylo jasně pozorováno zvýšení hodnot d_{33} a k_p. Hodnota piezoelektrické konstanty d_{33} se zvýšila z hodnoty 295 ± 15 pC/N čistého BCZT na 353 ± 7 pC/N. Kromě toho byl k_p zvýšen z 23,2 ± 2% na 40 ± 1%, zatímco relativní permitivita se zvýšila z 1906 ± 80 na 3393 ± 100. Zlepšení hustoty d_{33}, k_p, ε_r a snížení *tan δ* je připisováno zhutnění keramiky. Tento jev je dobře znám, neboť CeO$_2$ se používá jako přísada do PZT a BNBT bezolovnatých materiálů a vykazuje podobný trend [61].

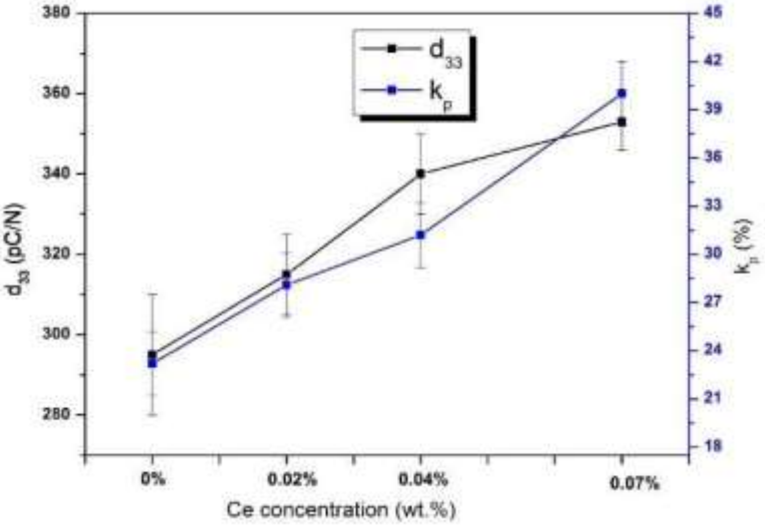

Obr. 2.17 d_{33} a k_p jako funkce koncentrace Ce za podmínek slinování, T$_1$ - 1400 °C/30 min a T$_2$ - 1275 °C/4 h.

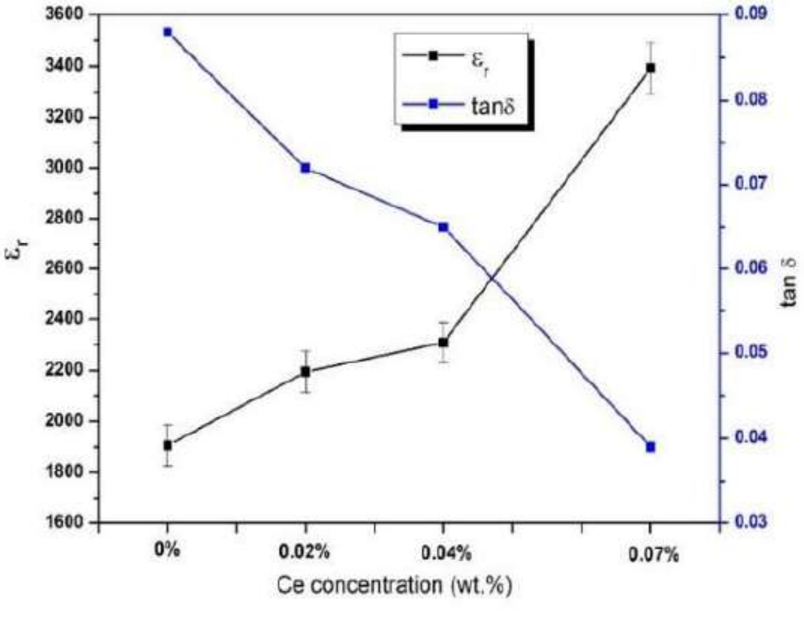

Obr. 2.18 Relativní permitivita a ztrátový činitel tan δ jako funkce koncentrace Ce za podmínek slinování, T$_1$ - 1400 °C/30 min a T$_2$ - 1275 °C/4 h. [A9,A11]

V tomto případě působí Ce^{3+} jako donorový dopant vedoucí na některá volná místa kationtů na místě A, která mohou usnadnit pohyb doménové stěny a zlepšit tak piezoelektrické vlastnosti keramiky BCZT. Naproti tomu Ce^{4+} má ve srovnání s Ce^{3+} menší iontové poloměry a pravděpodobně zaujímá B-místo buď Ti^{4+} nebo Zr^{4+}. Obsazení Ce^{4+} v místě B může změnit volný náboj k potlačení pohybu doménových stěn a je zachycen volnými místy kyslíku, což způsobuje snížení ztrátového činitele (tan δ). Hodnoty dielektrických a piezoelektrických vlastností jsou shrnuty v tabulce 2.3

Tabulka 2.3 - Piezoelektrické a dielektrické vlastnosti keramiky BCZT-yCeO_2 při slinování, T_1 - 1400 °C/30 min a T_2 - 1275 °C/4 h.

BCZT - yCeO2	*Velikost zrn (μm)*	d_{33} *(pC/N)*	k_p *(%)*	ε_r *(-)*	T_c *(°C)*
y = 0	8,0±0,75	295±15	23,2±2	1906±80	103,4
y = 0,02	6,9±0,29	315±10	28,1±1	2193±80	100,1
y = 0,04	7,24±0,44	240±10	28,9±2	2308±80	101,2
y = 0,07	7,96±0,71	253±7	40±1	3393±100	96,2

Graf 2.19 zobrazuje závislost permitivity na teplotě keramiky BCZT-yCeO_2 měřenou při 1 kHz. Všechny vzorky procházejí dvoufázovými přechody, tj. feroelektrickým rhombohedrálně-feroelektrickým tetragonálním fázovým přechodem (TR-T) poblíž teploty okolí a feroelektrickým tetragonálně-paraelektrickým kubickým fázovým přechodem kolem teploty $T_C \approx 100$ °C. Z výše uvedeného vyplívá, že malé množství dopingu CeO_2 nemění krystalovou strukturu, ale výrazně zvyšuje dielektrickou permitivitu ε_r. Maximální hodnota ε_r pro vzorek y = 0,07% hmotn. byla 15067 [-] ve srovnání s 6659 [-] zjištěnými pro čistý BCZT. Zvýšení dielektrické permitivity lze připsat rovnoměrné velikosti zrna a vyšší hustotě způsobené dopantem CeO_2.

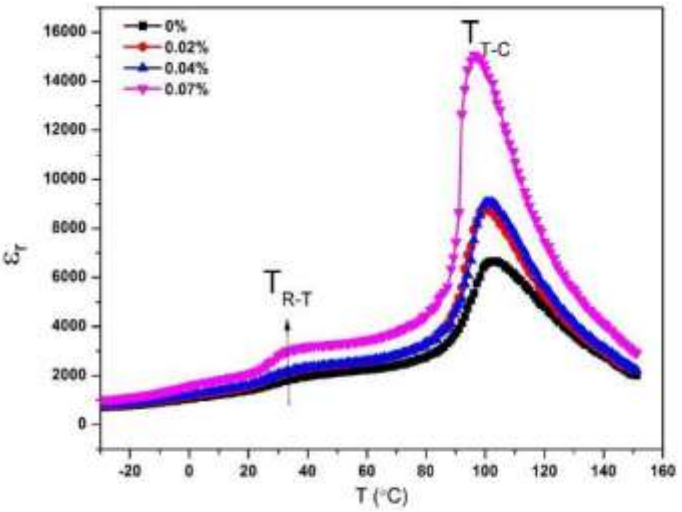

Obr. 2.19 Graf permitivity na teplotě BCZT-yCeO_2 (y = 0 - 0,07% hmot.) keramiky za podmínek slinování, T_1 - 1400 °C/30 min a T_2 - 1275 °C/4 h. [A11,A13]

Graf 2.20 (a) - (e) zobrazuje teplotní a frekvenční závislosti permitivity a ztrátového činitele BCZT keramiky s různými přísadami CeO_2 za různých slinovacích podmínek. Výsledky ukazují, že přidání CeO_2 způsobuje mírný posuny Curieovy teploty, což platí i při různých slinovacích podmínkách. Grafy naznačují stejných charakter chování dielektrických i piezoelektrických parametrů jako v případě slinovacích podmínek T_1 - 1400 °C/30 min a T_2 – 1275 °C/4 h.

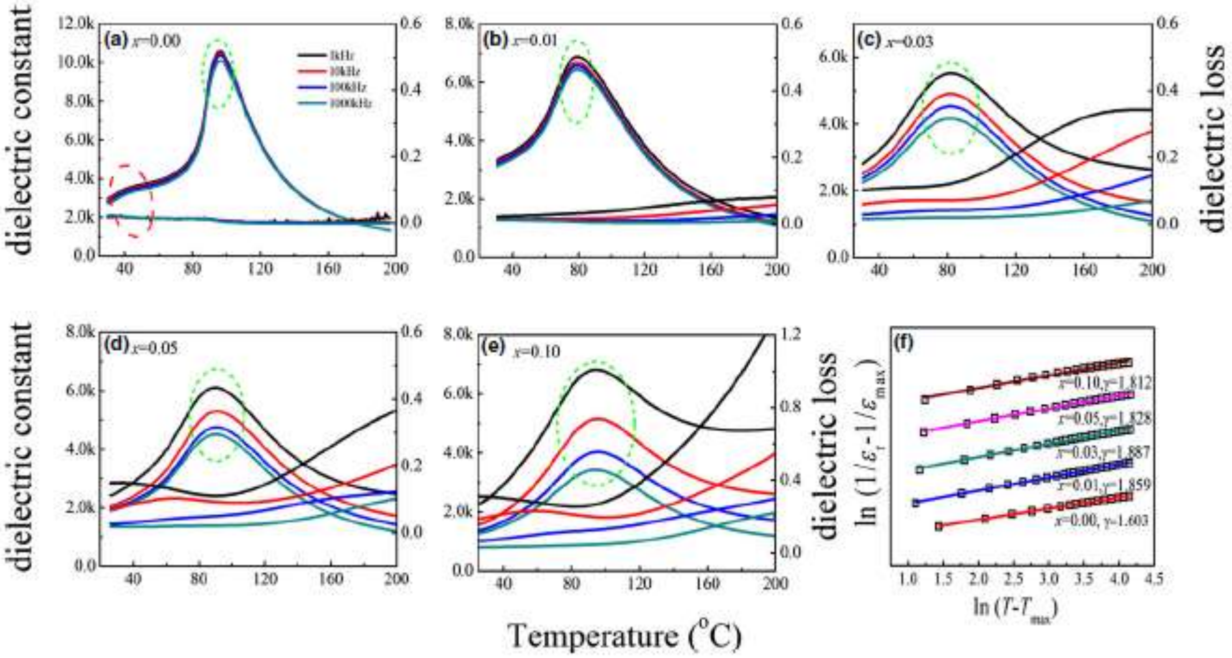

Obr. 2.20 Grafy Teplotní závislost ε_r a tan δ při 1, 10, 100, 1000 kHz keramiky BCZT - yCeO2 (y = 0 - 0,1% hmot.) keramiky za podmínek slinování, T_1 - 1300 °C/60 min a T_2 - 1275 °C/4 h.

Obrázek 2.20 (f) ukazuje grafy ln ($1/\varepsilon_r$ - $1/\varepsilon_{max}$) jako funkci ln (T-T_{max}) při 10 kHz pro vzorky BCZT s různým množstvím přísady CeO_2. Je vidět, že u všech vzorků je pozorován lineární vztah. S vrůstajícím hmotnostním zastoupením CeO_2 se směrnice přímky zvětšuje z hodnoty 1,603 na 1,887. Tato změna indikuje, že přidání CeO_2 zlepší chování dielektrického přechodu keramiky BCZT na rozhraní zrn.

2.7 CHARAKTERIZACE ($BA_{0.85}$ $CA_{0.15}$-Y CE_Y) ($ZR_{0.1}$ $TI_{0.9}$) O_3 KERAMIKY

Experimenty se zpracováním této keramiky jsou podrobně popsány v [A12]. CeO_2 byl použit jako substituce na Ca v místě A struktury BCZT podle stechiometrického vzorce ($Ba_{0,85}$ $Ca_{0,15}$-y Ce_y) ($Zr_{0,1}$ $Ti_{0,9}$) 0_3 a poté kalcinován. „Green body“ keramika byla slinována při různých teplotách od 1275 °C do 1450 °C po dobu 4 hodin.

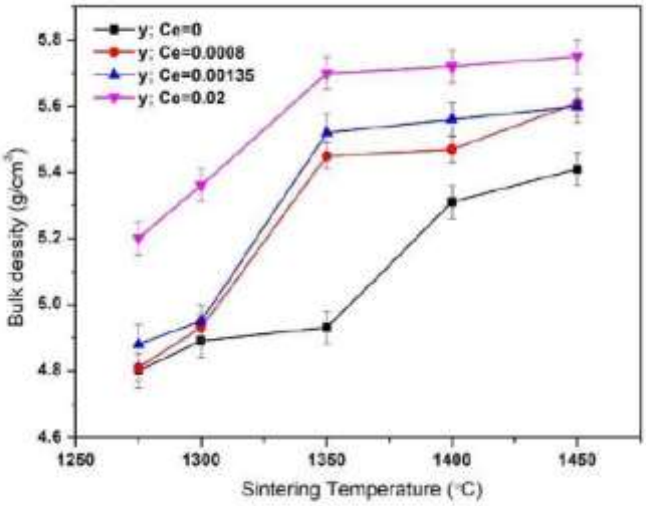

Obr. 2.21 Graf hustoty jako funkce teploty slinování ($Ba_{0,85}$ $Ca_{0,15}$-y Ce_y) ($Zr_{0,1}$ $Ti_{0,9}$) O_3 keramiky [A11,A12]

Na obr. 2.21 je znázorněna očekávaná závislost, že se vzrůstající sintrovací teplotou roste i objemová hustota keramiky u všech připravených kompozicí. Maximální hustoty 5,75 g/cm^3 bylo dosaženo pro y:C$_e$ = 0,02. Obrázek 2.22 ukazuje mikrostruktury této keramiky slinované při 1350 °C. U vzorků slinutých při 1350 °C nejsou mikrostruktury y = 0, 0,0008 a 0,00135 dostatečně husté ve srovnání se vzorkem y = 0,02. U vzorků slinutých při 1450 °C v rozmezí y = 0 - 0,00135 zrna rychle rostou, což zvyšuje hustotu vzorků.

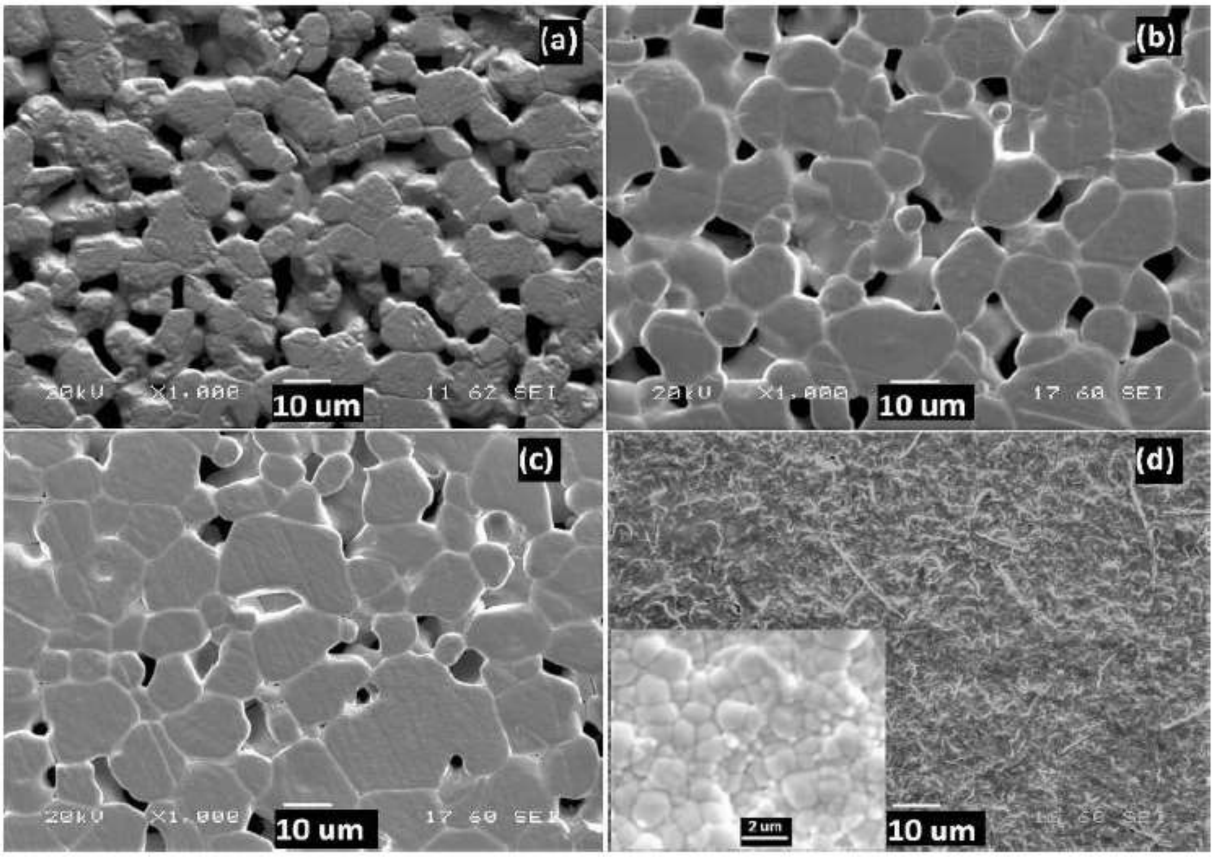

Obr. 2.22 SEM obrázky (Ba$_{0,85}$ Ca$_{0,15}$-y Ce$_y$) (Zr$_{0,1}$ Ti$_{0,9}$) O$_3$ keramiky pro hodnoty y:Ce (a) 0 (b) 0,0008 (c) 0,00135 (d) 0,02 a slinované při 1350 °C pro 4 h.

Piezoelektrické a dielektrické vlastnosti keramiky (Ba$_{0,85}$ Ca$_{0,15}$-y Ce$_y$) (Zr$_{0,1}$ Ti$_{0,9}$) O$_3$ při slinování 1350 °C po dobu 4 h

Obrázek 2.23 vlevo) a vpravo) ukazují piezoelektrický koeficient d_{33} a planární vazební faktor k_p pro různé teploty slinování. Jak teplota slinování stoupá, hodnoty koeficientu d_{33} se zvyšují až do maximální hodnoty pro y = 0,00135 (při 1350 °C) a poté výrazně klesají. U vzorků slinutých při 1350 °C má čistý BCZT (y = 0) hodnotu d_{33} ~ 290 pC/N s relativně nízkou velikostí zrna ~ 7,6 µm. Při zvýšení koncentrace Ce na 0,02 se d_{33} snižuje, což lze připsat velmi malé velikosti zrna ≃ 0,76 µm. Toto snížení je patrné pro všechny sintrovací teploty. Planární vazební faktor k_p sleduje stejný trend s velikostí zrna a byla pozorována maximální hodnota = 38,5% pro y = 0,00135 slinutá při 1350 °C/4 h.

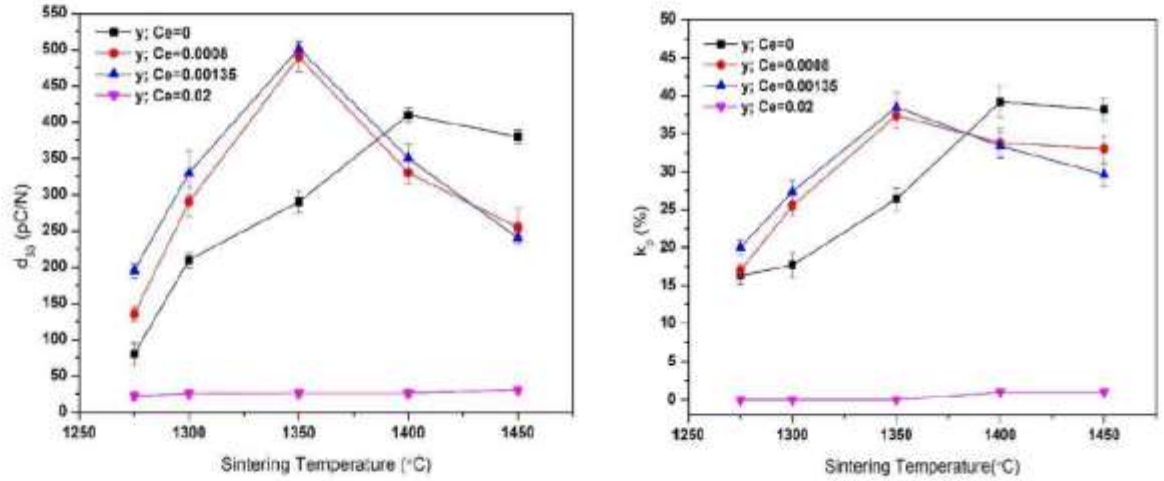

Obr. 2.23 Závislost d_{33} (vlevo) a k_p (vpravo) na teplotě slinování $(Ba_{0,85}\ Ca_{0,15}\text{-}y\ Ce_y)\ (Zr_{0,1}\ Ti_{0,9})\ O_3$ keramiky

Tabulka 2.3 - Piezoelektrické a dielektrické vlastnosti keramiky $(Ba_{0,85}\ Ca_{0,15}\text{-}y\ Ce_y)\ (Zr_{0,1}\ Ti_{0,9})\ O_3$ při slinování 1350 °C/4 h.

y=mol	*Velikost zrn (μm)*	d_{33} *(pC/N)*	k_p *(%)*	ε_r *(-)*	T_c *(°C)*
y = 0	7,6±2	290±15	26,4±1	1808±80	105,4
y = 0,0008	12,16±2,39	490±20	37,7±1,69	2154±80	103,2
y = 0,00135	11,26±1,97	501±10	38,5±1,92	2584±80	108,1
y = 0,02	0,76±0,08	60±5	8,5±1,35	1858±80	72,6

Obrázek 2.24 (vlevo), (vpravo) zobrazuje graf relativní permitivity ε_r a ztrátového činitele *tan δ* na teplotě při 1 kHz pro $(Ba_{0,85}\ Ca_{0,15}\text{-}y\ Ce_y)\ (Zr_{0,1}\ Ti_{0,9})\ O_3$ vzorky slinované při 1350 °C/4 h. Maximální relativní permitivita ε_r je při Curieově teplotě a zvyšuje se pro y = 0,0008 - 0,00135 na hodnotu cca. 11500, ve srovnání s čistou keramikou BCZT cca. 8 000. V případě nadměrné substituce u Ce y = 0,02) byl pozorován významný pokles ε_r, který lze připsat malé velikosti zrna a s tím spojené nehomogenity v materiálu. Dále pro y = 0,02 se vrchol dielektrické permitivity stává plošším, což vede k výraznější povaze difuzního fázového přechodu (DPT), která je podrobně popsána v [A9]. Tuto povahu lze připsat velikosti jemných zrn (~ 0,76 μm) v důsledku nadměrného obsahu Ce, který vede k posunu feroelektricko-paraelektrického fázového přechodu na nižší teplotu.

Na obrázku 2.24 (a) je zřejmé, že dielektrické vlastnosti jako T_C a ε_r značně závisí na velikosti zrn, což dříve potvrdili Martirenat a Burfoot [62]. Výsledky, také podporuje chování DPT pro y = 0,02, které ukazují široký vrchol poblíž feroelektricko-kubické fázové přeměny při 72,6 °C. Je evidentní, že $(Ba_{0,85}\ Ca_{0,15}\text{-}y\ Ce_y)\ (Zr_{0,1}\ Ti_{0,9})\ O_3$ keramika (y = 0; 0,0008; 0,00135) představuje tři přechody, a to RO, OT, TC, což je pozorováno třemi vrcholy reprezentovanými na obrázku 2.24 (vpravo).

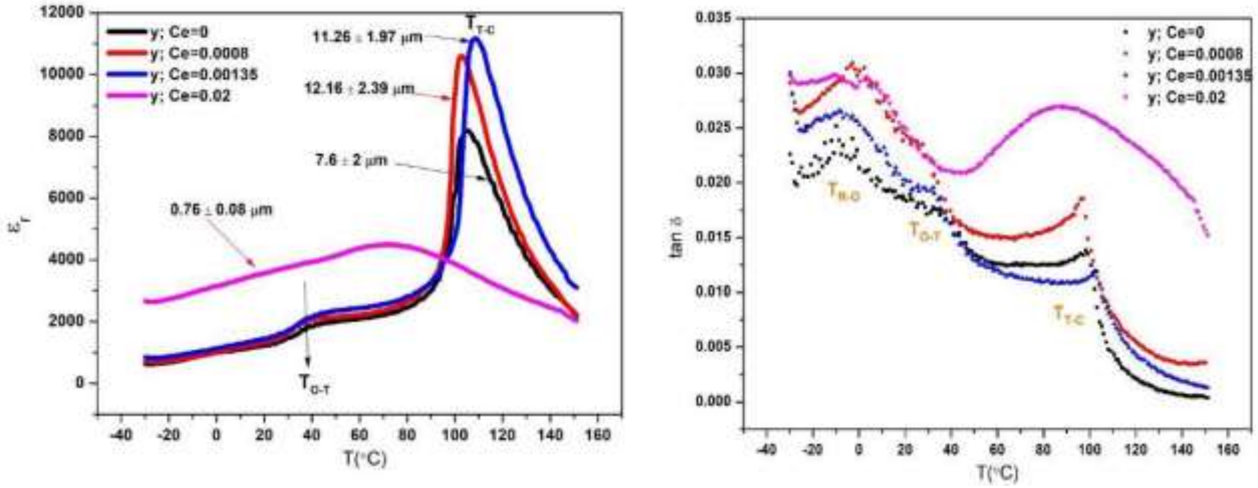

Obr. 2.24 (vlevo) Teplotní závislost relativní permitivity (vpravo) ztrátová činitele $Ba_{0,85}$ $Ca_{0,15}$-y Ce_y) ($Zr_{0,1}$ $Ti_{0,9}$) O_3 keramiky slinované při 1350 °C/4 h.

2.8 CHARAKTERIZACE PZT KERAMIKY

Jedná se výsledky měření, která jsem nikde nepublikoval, sloužily jako ověřovací výsledky výrobních technologií, měřicích metod a postupů při výrobě bezolovnaté keramiky a byly součástí hospodářské spolupráci s fy. Huawei 2015. Na této keramice nebyl prováděn žádný další výzkum, neboť do budoucna se díky přítomnosti olova nejeví jako perspektivní, ovšem z historického hlediska byla jedna z nejvíce prostudovaných. Dalším faktorem nepokračujícího výzkumu v této oblasti je obtížnější zpracování této keramiky z hlediska specializovaných pecí, které následně již není možné využit na bezolovnatou keramiku.

Jako vzorky nedopované PZT ($PbZr_{0.75}Ti_{0.25}O_3$) keramiky byly disky o průměru 12 mm a tloušťce 0,8 mm. Jejich chemické složení bylo ověřeno měřením energetické disperzní spektrometrie (EDS) pomocí rastrovací elektronové mikroskopie (SEM). Na každé straně disku byla nanesena metodou naprašování platinová elektroda. Elektrické vlastnosti byly stanoveny ve frekvenčním rozsahu 20–10^6 Hz s impedančními analyzátory HP4284A a HP4291A.

Dielektrická měření byla realizována pro teplotní rozsah 20-1000 K ve frekvenčním rozsahu 10 Hz až 1 MHz. Toto umožňuje zkoumání přechodu mezi rhobedrickým feroelektrickým stavem a kubickým paraelektrickým stavem. Na obrázku 2.25 vlevo je zobrazen frekvenční charakteristika ε a ztrátového činitele.

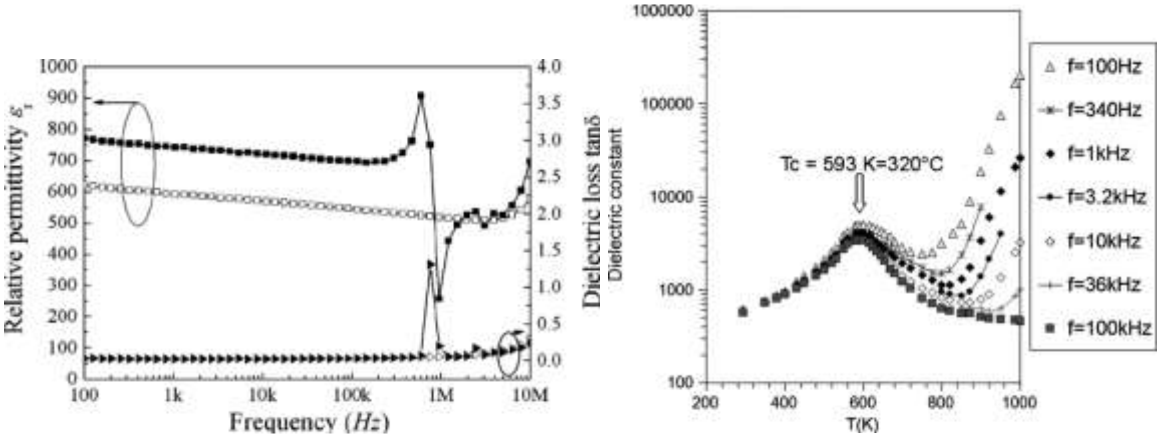

Obr. 2.25 (vlevo) frekvenční závislost permitivity a ztrátového činitele PZT keramiky (vpravo) teplotní závislost permitivity PZT keramiky

Na obr. 2.25 vpravo teplotní závislost permitivity a je zřetelně označena hodnota Curieovy teploty T_c, která je frekvenčně nezávislá. Tato teplota přesně odpovídá publikovaným výsledkům v odborné literatuře.

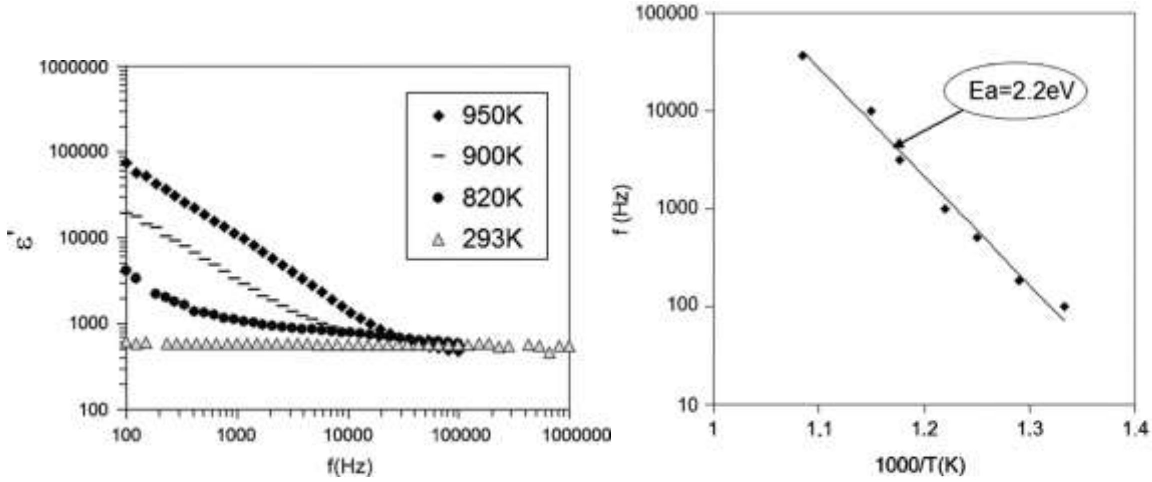

Obr. 2.26 (vlevo) frekvenční závislost permitivity a ztrátového činitele PZT keramiky pro teploty 293-980K
(vpravo) relaxační mapa PZT keramiky

Nárůst ε při vysokých teplotách, jak je uvedeno na obr. 2.26 vlevo, v paraelektrické oblasti a při frekvencích nižších než 100 kHz je způsoben migrací kyslíkových iontů [64]. Na obrázku 2.26 vpravo je uvedena relaxační mapa PZT keramiky s vypočítanou aktivační energii 2,2 eV. Všechny hodnoty jsou v korelaci s dřívějšími výsledky [64,65].

3 ZÁVĚR

Práce byla zaměřena na popis dosavadní vědecké činnosti, kdy v první fázi byla zaměřena na popis a analýzu dielektrických kompozitních systémů. V práci bylo ukázáno, že dielektrická relaxační spektroskopie je vhodný nástroj, který umožňuje charakterizovat dielektrické kompozitní systémy a je také využitelný pro charakterizaci a návrh nového směsného vztahu, který umožňuje predikovat výsledné vlastnosti kompozitního systémů s kovovými kulovými částicemi. Nevýhoda vztahu je samozřejmě dána jeho specifikací na kulové částice. Samozřejmě by bylo možné navázat na dosavadní výzkum a rozšířit jej na ostatní popsané typy částic, ovšem materiálový výzkum jde tak rychle dopředu a zaměřuje se čím dál více na nanočástice, že výzkum takového charakteru by byl enormně náročný a pravděpodobně byl stále pozadu proti materiálnímu, kdy je většinou mnohem jednodušší „něco namíchat a změřit“, než širokosáhle materiál analyzovat proč má takové či onaké vlastnosti.

V další části jsem se zaměřil zejména na analýzy dielektrických a piezoelektrických spekter u olovnaté a bezolovnaté keramiky a vliv různých dopantů na tyto struktury.

Při analýze bezolovnaté keramiky jsem se zaměřil zejména na analýzu dopantů, mající výrazný vliv na sintrovací teplotu a posun Curieovy teploty. Nedílnou součástí těchto analýz byla samozřejmě i charakterizace ε_r, $tan\ \delta$, k_p. Experimentální výsledky ukazují výrazný vliv ceria na BCZT keramiku s různými iontovými poloměry na strukturní, mikrostrukturní a funkční vlastnosti této keramiky. Ce byl použit jako aditivum i jako náhrada v místě A a B perovskitové struktury BCZT. V obou případech byly prozkoumány a porovnány dielektrické i pizezoelektrické vlastnosti.

Pokud je Ce použito jako přísada, vytvoří se čistá perovskitová struktura, ve které nebyla pozorována žádná sekundární nebo nečistá fáze. Teplota a velikost zrna hrají důležitou roli při dosahování vysokých funkčních vlastností, ale zároveň množství CeO_2 může také ovlivnit slinovatelnost a hustotu keramiky BCZT.

Všechny vzorky procházejí dvoufázovými přechody, tj. feroelektrickým rhombohedrálně-feroelektrickým tetragonálním fázovým přechodem (TR-T) poblíž teploty okolí a feroelektrickým tetragonálně-paraelektrickým kubickým fázovým přechodem T_C kolem teploty 100 °C. Z čehož vyplívá, že malé množství dopingu CeO_2 nemění krystalovou strukturu, ale drasticky zvyšuje dielektrickou permitivitu ε_r.

Poté byl Ce použit jako substituce perovskitové struktury BCZT v místě A a B a výsledky byly porovnány s výsledky získanými přidáním Ce k keramice BCZT. Bylo zjištěno, že přidání Ce ($y = 0{,}07\%$ hmotn.) A substituce Ce v místě A (0,00135 mol.) Mohou snížit teplotu slinování na 1350 °C s vysokými piezoelektrickými vlastnostmi ($d_{33} \sim 500$ pC/N). Byly naměřeny dielektrická spektra permitivity, ztrátového činitele i ztrátového čísla, pro všechny realizované vzorky.

V této práci byly prezentovány výsledky (PZT), které byly prvotně využity při řešení hospodářské smlouvy pro zahraničního partnera jako validační. Sloužili pro posouzení správnosti materiálových postupů výroby piezokeramiky. Z analýzy SEM byla určena primární velikost částic prášku v rozsahu 1µm - 500nm. Tepelné závislosti ukazují, že syntetizovaný PZT je tepelně stabilní do 360 °C.

SEZNAM POUŽITÉ LITERATURY

PUBLIKACE AUTORA PRÁCE

[A1] Holcman, V.; Liedermann, K.; Stráník, R. Změny dielektrického spektra polymeru při dlouhodobé expozici při nízkých teplotách. Jemná mechanika a optika, 2010, roč. 2010, č. 10, s. 279-281. ISSN: 0447- 6441.

[A2] Holcman, V.; Grmela, L.; Liedermann, K. New Mixing Rules for Composite Polymer Materials. IEEJ Transactions on Electrical and Electronic Engineering, 2010, roč. 5, č. 4, s. 381-385. ISSN:1931-4973.

[A3] Holcman, V. Dielectric characteristics of composite systems. In ISSE 2008 31st International Spring Seminar on Electronics Technology. 1. Budapest: 31st International Spring Seminar on Electronics Technology, 2008. s. 77-81. ISBN: 978-963-06-4915- 5.

[A4] Holcman, V.; Liedermann, K.; Grmela, L.; Raška, M. New mixed rules on coposiste materials. In Proceedings of 2008 International Symposium on Electrical Insulating Materials. IEEJ Transactions on Electrical and Electronic Engineering. 1. Japonsko, Yokkaichi: Proceedings of 2008 International Symposium on Electrical Insulating, 2008. s. 71-74. ISBN:978-4-88686-006-4.I SSN:1931-4973.

[A5] Liedermann, K.; Palai-Dany, T.; Holcman, V. Dielektrická charakterizace sodné soli karboxymetylcelulózy. In 18th International Conference DISEE 2010 Dielectric and Insulating Systems In Electricl Engineering - Proceedings, September 22 - 24, Demänovská Dolina, Slovensko. 2010. Bratislava, Slovensko: Nakladatel'stvo STU v Bratislave,2010. s.101-104. ISBN:978-80-227-3366-3.

[A6] Holcman, V.; STRÁNÍK, R. Dielectric relaxation in Glycerol at long-time exposure to low temperatures. In ISSE 2008 31st International Spring Seminar on Electronics Technology. 1. Budapest: 31st International Spring Seminar on Electronics Technology, 2008. s. 86-90. ISBN: 978-963-06-4915-5.

[A7] Liedermann, K.; Holcman, V.; Ee-Fakri, S. Dielectric Spectroscopy of Hyaluronic Acid and its Salts. In Proceedings of 2008 International Symposium on Electrical Insulating Materials. Yokkaichi, Japonsko: IEE Japan, 2008. s. 234-237. ISBN: 978-4-88686-006-4.

[A8] Liedermann, K.; Holcman, V.; Klampár, M. Dielectri relaxation of CCTO ceramics. In New Trends in Physics 2012, Nové trendy ve fyzice NTF 2012. první. Brno: Brno University of Technology, 2012. s. 61-64. ISBN: 9788021445949

[A9] Bijalwan, V.; Hughes, H.; Pooladvand, H.; Tofel, P.; B.; Holcman, V.; Bai, Y.; Button, T. The effect of sintering temperature on the microstructure and functional properties of BCZT-xCeO2 lead free ceramics. MATERIALS RESEARCH BULLETIN, 2019, roč. 114, č. 1, s. 121-129. ISSN: 0025-5408.

[A10] Sobola, D.; Kaspar, P.; Tofel, P.; Holcman, V. Scanning electron microscopy and energy-dispersive X-ray spectroscopy analysis of electrochemically etched graphite tips created from pencil lead. MICROSCOPY RESEARCH AND TECHNIQUE, 2020, č. 1, s. 196-201. ISSN: 1097-0029.

[A11] Tofel, P.; Machů, Z.; Chlup, Z.; Hadraba, H.; Drlík, D.; Ševeček, O.; Majer, Z.; Holcman, V.; Hadaš, Z. Novel layered architecture based on Al2O3/ZrO2/BaTiO3 for SMART piezoceramic electromechanical converters. European Physical Journal-Special Topics, 2019, roč. 228, č. 7, s. 1575-1588. ISSN: 1951-6355.

[A12] Bijalwan, V.; Tofel, P.; Holcman, V. Grain size dependence of the microstructures and functional properties of (Ba0.85 Ca0.15–x Cex) (Zr0.1 Ti0.9) O3 lead-free piezoelectric ceramics. Journal of Asian Ceramic Societies, 2018, roč. 6, č. 4, s. 384-393. ISSN: 2187-0764.

[A13] Kaspar, P.; Škarvada, P.; Holcman, V.; Grmela, L. Characterization of argon etched Ta2O5 thin films. Applied Physics A, 2019, roč. 125, č. 820, s. 1-7. ISSN: 0947-8396.

[A14] Kaspar, P.; Sobola, D.; Sedlák, P.; Holcman, V.; Grmela, L. Analysis of Color Shift on Butterfly Wings by Fourier Transform of Images from Atomic Force Microscopy. MICROSCOPY RESEARCH AND TECHNIQUE, 2019, č. 1, s. 1-7. ISSN: 1097-0029.

[A15] Sobola, D.; Papež, N.; Dallaev, R.; Ramazanov, S.; Hemza, D.; Holcman, V. Characterization of nanoblisters on HOPG surface. In Journal of ELECTRICAL ENGINEERING. Journal of Electrical Engineering. FEI STU Bratislava: De Gruyter OPEN, 2019. s. 132-136. ISSN: 1335-3632.

[A16] Knápek, A.; Sobola, D.; Tománek, P.; Pokorná, Z.; Urbánek, M.; Holcman, V. Field emission from the surface of highly ordered pyrolytic graphite. Applied Surface Science, 2016, roč. 2016, č. 12, s. 1-5. ISSN: 0169-4332.

[A17] Sedlák, P.; Šikula, J.; Vondra, M.; Sedláková, V.; Majzner, J.; Holcman, V. Fluctuation-enhanced gas sensing using polypyrrole-based QCM and its adsorption- desorption kinetics. In Proceedings MIDEM 2012. Ljubljana: MIDEM, 2012. s. 399-404. ISBN: 978-961-92933-2- 4.

PUBLIKACE OSTATNÍCH AUTORŮ

[1] Florin Ciuprina, Ilona Plesa, Petru V. Notingher, Tiberiu Tudorache, and Denis Panaitescu. Dielectric properties of nanodielectrics with inorganic fillers. In 2008 Annual Report Conference on Electrical Insulation and Dielectric Phenomena. Institute of Electrical & Electronics Engineers (IEEE), oct 2008. doi: 10.1109/ceidp.2008.4772905.

[2] Bryan H. : Engineering coposite materials, [PhD thesis]. The Institute of Materials, London, 1999.

[3] Kováčiková, S., Vicente, R., Hudec. I. Composite materials based on polymer matrix and magnetic filler. Electrical insulating and cable industries, 53, 2000, pages 43 - 46, ISSN 0322-7111.

[4] Bareš, A. Composite materials. State Publishing House of Technical Literature Prague 1988 p.105-135th

[5] Hudec, I., Alex, P., Kraus, Z., Chodák, I., Feranc, J.: New Fillers in Elastomers. Editor (s): Hans-Joachim Radusch, The 21st mannual meeting of the PPS, Leipzig D, page 213, 2005.

[6] Hassdentefel, J., Dubský, J., Raposo, M., Sander, J. Electrical materials. The state publishing technical literature Praha 2000 pp. 20-280.

[7] Yaya A., Agyei-Tuffour B., Dodoo-Arhin D., Nyankson E., Annan E., Konadu D.S., Sinayobye E., Baryeh E.A., Ewels C.P., G.J.E.D.T. 1(2) 32, (2012)]

[8] Riande, E. DIAZ-Calleja, R.: Electrical properties of polymers, USA Publishing 2004, ISBN: 0-8247-5346-1.

[9] Frohlich J., Niedermeier W., Luginsland H.D., Composites: Part A 36, 449 (2005).]

[10] Van Beek, LKH, Dielectric behavior of heterogenous systems, in Progress in Dielectrics, edited by JB Birks, pp. 69-114, CRC Press, Cleveland, Ohio, 1967.

[11] Schneider, U. Breitbandige dielektrische Studien der Dynamik struktureller Glasbildner. [PhD thesis]. University of Augsburg, 2000.

[12] M. Akay, G. R. Spratt, and B. Meenan. The efects of long-term exposure to high temperatures on the ilss and impact performance of carbon fibre reinforced bismaleimide. Comp. Sci. Technol., 63:1053{1059, 2003.

[13] Logakis, E.; Pandis, C.; Pissis, P.; Pionteck, J.; Pötschke, P. Highly conducting poly (methyl methacrylate)/carbon nanotubes composites: Investigation on their thermal, dynamic-mechanical, electrical and dielectric properties. Compos. Sci. Technol. 2011, 71, 854–862.

[14] Mentlík, V. Dielectric components and systems. Prague: Ben technical literature, 2006, ISBN 80-7300-189-6

[15] Sinclair, D.C. and A.R. West, Impedance and modulus spectroscopy of semiconducting BaTiO3 showing positive temperature coefficient of resistance. J. Appl. Phys., 1989. 66: p. 3850-3856.

[16] Irvine, T.S., D.C. Sinclair, and A.R. West, Electroceramics : Characterization by Impedance Spectroscopy. Advanced Materials, 1990. 2(3).

[17] Hirose, N. and A.R. West, Impedance spectroscopy of undoped BaTiO3 ceramics. J. Am. Ceram. Soc., 1996. 79(6): p. 1633-1641.

[18] Wu, T.B. and J.N. Lin, Transition of compensating defect mode in niobium-doped barium-titanate. J. Am. Ceram. Soc., 1994. 77(3): p. 759-764.

[19] Chan, N.H. and D.M. Smyth, Defect Chemistry of Donor-Doped BaTiO3. J. Am. Ceram. Soc., 1984. 67(4): p. 285-288.

[20] Friend, C., Smart Materials: The Emerging Technology, Materials World, 4 [1], pp. 16-18, 1996.

[21] Gahdhi. M.V. and Thompson, B.S., Smart Materials and Structures, Champman & Hall, London (1992).

[22] Curie, J., and Curie, P., Development par compression de l'electricite polaire dans les cristaux hemiedres a faces inclinees, Bulletin de la Societe Mineralogique de France, 3, pp. 90-93, 1880.

[23] Jaffe, B., Roth, R.S., and Marzullo, S., Piezoelectric Properties of Lead Zirconate-Titanate Solid-Solution Ceramics, J.Appl. Phys., 25 [6] 809-810 (1954).

[24] Ikeda, T., Fundamentals of piezoelectricity. Oxford University Press (1990). Uchino, K., Piezoelectric actuators and ultrasonic motors. Kluwer Academic Publishers. (1997).

[25] IEEE Standard 176-1978, Standard on Piezoelectricity.

[26] J Burfoot, D Van Nostrand. An introduction to the physical principles, Ferroelec., pp.1-12, pp.46-54, 1967.

[27] Fialka, J., Měření parametrů piezoelektrických aktivním prvků snímačů akustické emise, Brno VUT v Brmě, FEKT, Disertační práce 2015

[28] A Chandrasekaran. Experimental and first-principles study of point defects,domain walls, and point-defect / domain-wall interactions inferroelectric oxides. Ecole polytechnique fédérale de Lausanne, PhD Thesis, 2016.

[29] B. Jaffe. Piezoelectric Ceramics, Academic Press, New York, 1971

[30] Haertling. Ferroelectric ceramics: history and technology, Journal of American Ceramic Society, vol.82, pp.797-818, 1999

[31] A.J. Moulson, J.M. Herbert. Electroceramics - Materials, Properties, Applications. Chapman & Hall, London, 1990. [24] J Van Randeraat, RE Setterington, Piezoelectric ceramics. Mullard Limited, pp 4-13, 1974. [25] S Roundy, PK Wright, J Rabaey. A study of low level vibrations as a power source for wireless sensor nodes. Comp. Comm., vol.26, pp.1131–1144, 2003.

[32] GA Smolenskii, New ferroelectrics of complex composition. Soviet Physics-Solid State, vol. 2, pp.2651-2654, 1961.

[33] Y Li, W Chen, J Zhou, Q Xu, H Sun, R Xu. Dielectric and piezoelecrtic properties of lead-free (Na0.5Bi0.5)TiO3–NaNbO3 ceramics. Mat. Sci. Eng. B, Vol. 112, pp. 5-9, 2004.

[34] A Herabut, A Safari. Processing and Electromechanical Properties of (Bi0.5Na0.5)(1−1.5x)LaxTiO3 Ceramics. J. Am. Ceram. Soc., vol. 80, pp.2954–2958, 1997.

[35] Y Li, W Chen, Q Xu, J Zhou, X Gu, S Fang. Piezoelectric and ferroelectric properties of Na0.5Bi0.5TiO3–K0.5Bi0.5TiO3–BaTiO3 piezoelectric ceramics. Mat. Let., vol. 59, 1361–1364, 2005.

[36] BJ Chu, DR Chen, GR Li, QR Yin. Electrical properties of Na1/2Bi1/2TiO3–BaTiO3 ceramics. J. Eur. Ceram. Soc., vol. 22, pp.2115–2121, 2002.

[37] Unruan, M., et al., Changes in dielectric and ferroelectric properties of Fe3+/Nb5+ hybrid-doped barium titanate ceramics under compressive stress. J. Appl. Phys., 2008. 104(12).

[38] Goldschmidt, V.M., Die Gesetze der Krystallochemie. Die Naturwissenschaften, 1926. (1: p. 477-487.

[39] Cohen, R.E., Origin of ferroelectricity in perovskite oxides. Nature, 1992. 358(6382): p. 136-138.

[40] Lin, D.M. and K.W. Kwok, Dielectric and piezoelectric properties of (Bi1-xyNdxNa1-y)(0.5)BayTiO3 lead-free ceramics. Curr. Appl. Phys. 1)(2): p. 422-427.

[41] Ye, F., et al., Incommensurate magnetic structure in the orthorhombic perovskite ErMnO3. Phys. Rev. B, 2007. 76.

[42] Heywang, W., K. Lubitz, and W. Wersing, eds. Piezoelectricity : Evolution and Future of a Technology. Springer Series Mate. 2008, Springer.

[43] Lines, M.E. and A.M. Glass, Principles and Applications of Ferroelectrics and Related Materials. Oxford Classic Texts in the Physical Sciences. 2001: Oxford University Press Inc., New York.

[44] Yun, S. and X. Wang, Dielectric properties of (Ba1-2xSrxCax)TiO3 ferroelectric ceramics. J. Electroceram., 2008. (1(1-4): p. 585-588.

[45] Reddy, S.B., K.P. Rao, and M.S.R. Rao, Structural and dielectric characterization of Sr substituted Ba(Zr,Ti)O3 based functional materials. Appl. Phys. A-Mater., 2007. 89(4): p. 1011-1015.

[46] Dong, L., D.S. Stone, and R.S. Lakes, Enhanced dielectric and piezoelectric properties of xBaZrO3-(1-x)BaTiO3 ceramics. J. Appl. Phys., 2012. 111(8).

[47] Qi, J.Q., et al., Dielectric properties of barium zirconate titanate (BZT) ceramics tailored by different donors for high voltage applications. Solid State Sciences, 2012. 14(10): p. 1520-1524.

[48] Datta, K. and P.A. Thomas, Structural investigation of a novel perovskitebasedlead-free ceramics: xBiScO3-(1-x)BaTiO3. J. Appl. Phys., 2009. 1)7(4): p.1-5.

[49] Mitsui, T. and W.B. Westphal, Dielectric and X-ray studies of CaxBa1-xTiO3 and CaxSr1-xTiO3. Phys. Rev., 1961. 1(4(5): p. 1354.

[50] Wei, X. and X. Yao, Preparation, structure and dielectric property of barium stannate titanate ceramics. Mater. Sci. Eng. B, 2007. 137(1–3): p. 184-188.

[51] Chen, J., et al., Microstructures, dielectric and ferroelectric properties of BaHfxTi1−xO3 ceramics. J. Alloy. Comp., 2012. 544(0): p. 82-86.

[52] Shvartsman, V.V., W. Kleeman, and J. Dec, Diffuse phase transition in BaTi1- xSnxO3 ceramics: An intermediate state between ferroelectric and relaxor behavior. J. Appl. Phys., 2006. 99(124111).

[53] Jeong, J. and Y.H. Han, Electrical Properties of Acceptor Doped BaTiO3. J. Electroceram., 2004. 13: p. 549-553.

[54] Zhang, L., et al., Mn dopant on the “domain stabilization” effect of aged BaTiO3 and PbTiO3-based piezoelectrics. Appl. Phys. Lett., 2012. 1)1(242903).

[55] Morrison, F.D., D.C. Sinclair, and A.R. West, Electrical and structural characteristics of lanthanum-doped barium titanate ceramics. J. Appl. Phys., 1999. 86(11): p. 6355-6366.

[56] Maso, N., et al., Synthesis and electrical properties of Nb-doped BaTiO3. J. Mater. Chem., 2006. 16: p. 3114-3119.

[57] Villegas, M., et al., Factors affecting the electrical conductivity of donor-doped Bi4Ti3O12 piezoelectric ceramics. J. Am. Ceram. Soc., 1999. 8((9): p. 2411-2416.

[58] Jonker, G.H. and E.E. Havinga, The influence of foreign ions on the crystal lattice of barium titanate. Mater. Res. Bull., 1982. 17: p. 345-350.

[59] Gillot, C., et al., Microscopic origin of the PTC effect in niobium-doped barium titanate. J. Am. Ceram. Soc., 1997. 8)(4): p. 1043-1046.

[60] Gulwade, D. and P. Gopalan, Diffuse phase transition in La and Ga doped barium titanate. Solid State Communications, 2008. 146(7-8): p. 340-344.

[61] Feteira, A., D.C. Sinclair, and J. Kreisel, Average and Local Structure of (1- x)BaTiO3-xLaYO3 (0 <= x <= 0.50) Ceramics. J. Am. Ceram. Soc., 2010. 93(12): p. 4174-4181.

[62] X Wang, Helen Lai-Wa Chan, Chung-loong Choy, Piezoelectric and dielectric properties of CeO2-added (Bi0.5Na0.5)0.94Ba0.06TiO3 lead-free ceramics. Sol. State Comm., vol. 125, pp.395–399, 2003.

[63] JC Burfoot, H T Martirena. Grain-Size Effects on Properties of Some Ferroelectric Ceramics. J. Phys. C: Solid State Phys, vol. 7, pp.3182–3192, 1974.

[64] Pelaiz Barranco, A., Calderon Pinar, F., Perez Martinez, O., De Los SantosGuerra, J. and Gonzalez Carmenate, I., ac behaviour and conductive mech-anisms of 2.5 mol% La2O3doped PbZr0. 53Ti0. 47O3ferroelectric ceramics.J. Eur. Ceram. Soc., 1999,19, 2677–2683.

[65] Wang, B., Chan, H. L. W., Kwok, K. W., Ploss, B., Choy, C. L. and Tong,K. Y., Effect of fatigue on the pyroelectric and dielectric properties of PZTfilms.J. Eur. Ceram. Soc., 2001,21, 1589–1592.

IEEJ TRANSACTIONS ON ELECTRICAL AND ELECTRONIC ENGINEERING
IEEJ Trans 2010; **5**: 381–384

Paper

New Mixing Rules for Composite Polymer Materials

Vladimír Holcman[*a], Non-member
Lubomír Grmela[*], Non-member
Karel Liedermann[*], Non-member

This paper studies the dielectric properties of an elastomer filled with spherical Ni particles of different sizes the range 35–115 μm. The experimental analysis is followed by an examination of the permittivity/conductivity mixing rules. A new mixing formula for the composite system consisting of spherical metallic particles and the polymer matrix is presented. This formula includes both Ni particle content and Ni particle size as two independent variables. © 2010 Institute of Electrical Engineers of Japan. Published by John Wiley & Sons, Inc.

Keywords: dielectric, composites, polymers, mixing rules

Received 28 May 2009; Revised 29 October 2009

1. Introduction

Composite materials with metallic fillers represent a two-component or multicomponent system whose properties are affected by the properties of polymeric matrix [1] and of the metallic filler as well as by their mutual interaction at the filler–polymer interface. Composites are often a subject of the current materials research, yet only very little attention is paid to the impact of the particle size. This topic becomes increasingly important with the advance of nanocomposites.

This work was focused on the experimental studies and numerical analysis of the impact of Ni filler size on the dielectric properties of the whole composite, even as the total Ni content remains constant. Based on experimental findings, a formula for the permittivity (dielectric constant) of the composite, accounting for both concentration and size of metallic filler particles, is developed.

2. Experimental

The objective of the research was the observation and subsequent evaluation of the impact of Ni metallic filler, in different concentrations, for five different particle sizes within the range 35–115 μm on their dielectric properties.

The matrix material was an ethylene–vinyl acetate copolymer (PEVAc) with 45% (w/w) vinyl acetate. Nickel powder filler was used in different Ni particle sizes (referred to as ‘fractions’) and concentrations. The details of the fractions and the overall Ni contents studied are given in Table I [2].

2.1. Sample preparation

Samples were prepared at the Slovak University of Technology in Bratislava, in the form of foils. Nickel concentrations in the matrix were selected according to the anticipated and desired conductivity features. The composites with Ni powder fractions denoted as 1520, 1320, 1120, 1020, and 1010 contained 15–34% (v/v) Ni powder in the matrix. Fraction 1120 was studied more extensively, in a wider concentration range, including 42–75% (v/v) Ni powder in the matrix.

2.2. Measuring apparatus

Measurements were carried out using various impedance analyzers—HP 4284A Precision LCR Meter, Alpha-Analyzer by Novocontrol, and E4991A RF Impedance/Material Analyzer by Agilent (Fig. 1). The samples were of a circular shape ($d = 55$ mm) of 2.5 mm thickness. Besides that, rectangular samples with dimensions 15 × 15 × 1 mm were used in the measurements with the Alpha-Analyzer. Test samples were measured at frequencies 1 Hz–10 MHz; however, the focus of this paper is on the concentration and particle size dependence of electric properties. Therefore, only the results at 1 kHz are reported [3]. All measurements were carried out at the room temperature.

3. Measurement Results

Measurement of dielectric properties of all the available samples yielded results that clearly prove the impact of the size of added spherical Ni particles on the electric properties measured. Figure 2 shows the relative permittivity (dielectric constant) ε' and loss number ε'' as a function of the Ni particle size at the same Ni content (i.e. the number of larger particles is kept smaller in order to keep the concentration constant).

The distinction between the measured fractions can also be observed on the resistivity plot presented in Fig. 3. Full lines indicate best fits to the values measured, assuming a linear dependence. The figure shows a decrease of the resistivity with increasing Ni particle size. Also, the rate of this decrease (slope of the curve) increases with increasing Ni content in the matrix, and the magnitude of the resistivity generally decreases with increasing Ni content.

In the next part, an attempt is made to mathematically describe the relation between the resistance of the sample and the size of metallic particles. The objective is to find a suitable formula on the basis of established mixing rules as well as the numerical values of any would-be coefficients.

In the first part of the analysis, a number of classical mixing rules [4] were applied to the measurement results as shown in Table II.

None of tested formulas contained explicitly the particle size and, hence, none of them was found satisfactory (Fig. 4).

A major drawback of most mixing formulas was the fact that they were valid only up to 50% of the filler content. However, the

---

[a] Correspondence to: Vladimír Holcman. E-mail: holcman@feec.vutbr.cz

[*] Faculty of Electrical Engineering and Communication BUT Brno, Technická 8, 616 Brno, Czech Republic

Table I. Fraction parameters

Fraction	Range of sizes of 99.99% of all particles from the fraction (µm)	Average particle size (diameter) parameter *b*(µm)
1520	90–140	115
1320	45–125	85
1120	30–96	63
1020	20–71	45
1010	3–73	35

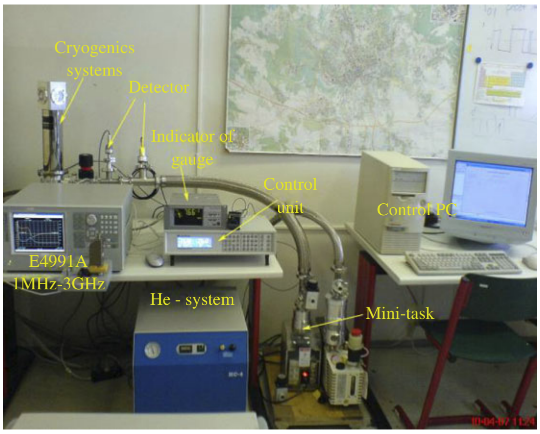

Fig. 1. Overview of the experimental setup

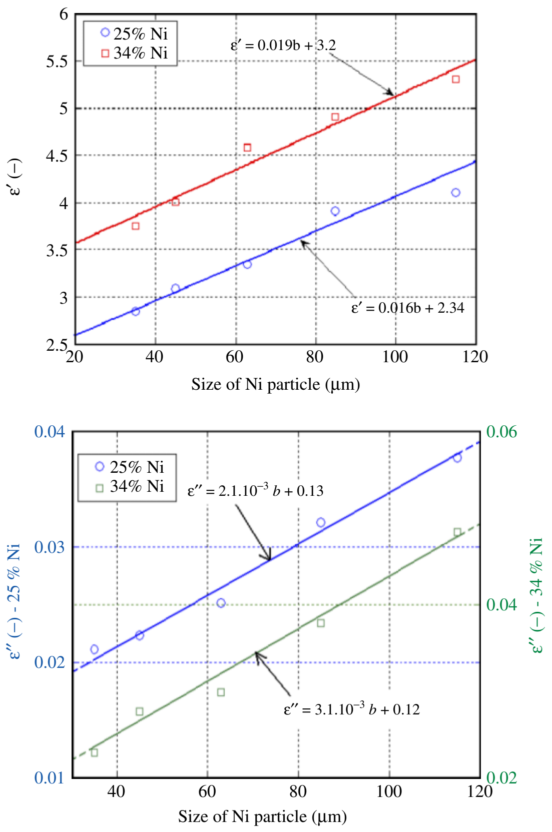

Fig. 2. Relative permittivity ε' and loss number ε'' as a function of Ni particle size

Lichtenecker power-law mixing rule [4] with exponent $k = 0.1$ seemed to fit best to the Ni–PEVAc composite, and therefore, the Lichtenecker power-law rule was used as a starting point for the deduction of the new formula, which would also account for the particle size.

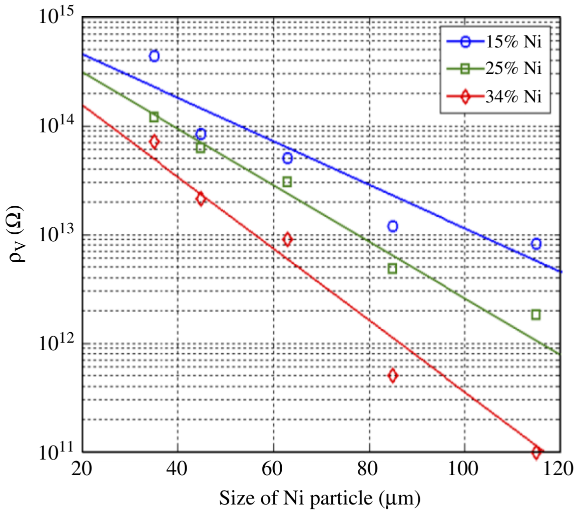

Fig. 3. Resistivity *versus* particle size for 15, 25, and 34% (volume) Ni content in the matrix

Table II. Root-mean-square error of fractions 1120 and 1520

Mixing rules	Root-mean-square error fraction 1120	Root-mean-square error fraction 1520
Newly proposed rule	1.8×10^{-1}	1.1×10^{-1}
Maxwell	1.3×10^{2}	5.3×10^{2}
Lichtenecker log.	5.8×10^{6}	8.1×10^{3}
Lichtenecker exp. $k = 0.1$	273.1	771.8
Botcher	3.5×10^{3}	4.1×10^{3}

The Lichtenecker power-law formula for the internal resistivity (for the sake of simplicity, the word 'internal' is henceforth omitted) of a multicomponent composite system is as follows:

$$\rho_{VS}^{k} = \sum_{i=1}^{n} v_i \cdot \rho_{Vi}^{k} \tag{1}$$

where k is an empirical parameter, which depends primarily on the shape and the orientation of particles, ρ_{Vi} are the resistivities and v_i are the volume fractions of the individual components. The parameter k lies in the interval $(-1, +1)$ [4].

In our case, the volume concentration of Ni particles in the matrix ranges from 15 to 75%. In order to establish a new mixing

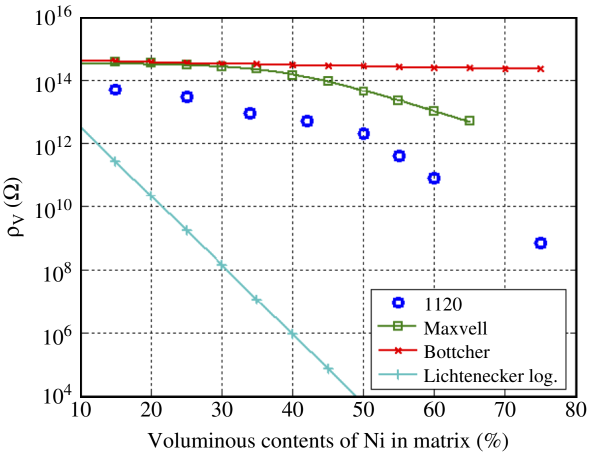

Fig. 4. Sample application of known mixed equation [17]

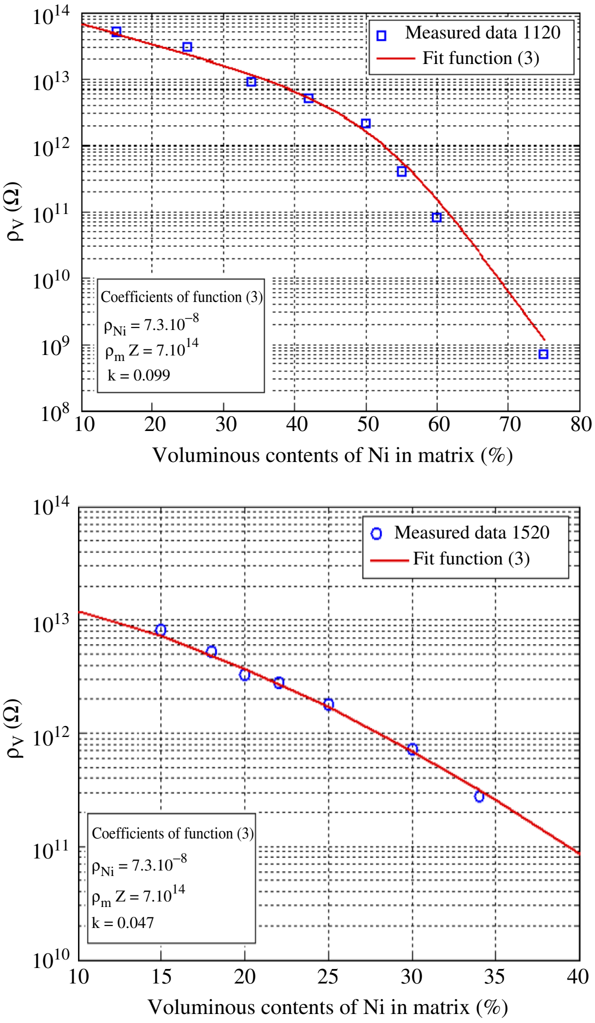

Fig. 5. Application of the new mixing rule for fractions 1120 and 1520

rule, it is necessary to find a function that would characterize the decrease of the resistivity curves with increasing particle size toward lower resistivity values. The analysis of the measured curves leads to the conclusion that the contribution of the matrix must be scaled with respect to the particle size, using an exponential dependence of the form:

$$\rho_{\mathrm{m}} = \rho_{\mathrm{mm}} \cdot \exp(-0.035.b) \tag{2}$$

where ρ_{mm} denotes the experimentally established value of the resistivity of the matrix, b is the Ni particle diameter in micrometers, and ρ_{m} denotes the particle-size-scaled resistivity of the matrix, which would enter (1).

The resistivity curves not only tend to lower values with the increasing particle size, but their slope also change depending on the Ni content, as can be seen from Fig. 3. Therefore, it was necessary to include the change of slope in the new mixing rule. The best way to include the change of the slope was to make the coefficient k particle-size-dependent. The dependence was analyzed and found to satisfy the function $k = -9.8 \times 10^{-4}b + 0.16$.

As all features related to the change of the Ni particle size in the composite system have thus been found, the newly modified Lichtenecker formula can be proposed as follows:

$$\rho_{\mathrm{vs}}^{k} = \frac{v_1 \cdot \rho_{\mathrm{Ni}}^{k} + v_2 \cdot (\rho_{\mathrm{mm}} \cdot \exp[-0.035.b])^{k}}{v_1} \tag{3}$$

where b denotes the diameter of Ni spherical particles dispersed (μm). After some rearrangement, the above equation can be written as:

$$\rho_{\mathrm{vs}} = \exp\left[\frac{\log(v_1^2 \rho_{\mathrm{Ni}}^{k} + v_2(\rho_{\mathrm{mm}} \cdot (-0.035.b))^{k})}{v_1 . k}\right] \tag{4}$$

This new mixing rule satisfies very well the full analyzed range of Ni contents and Ni particle sizes. A graphical interpretation of the presented formula for the Ni–PEVAc system is presented in Fig. 5.

4. Conclusion

The addition of the Ni filler (spherical particles) with different particle sizes but with the same Ni concentration to the polymer matrix results in composites with different dielectric properties. The newly proposed mixing rule describes very nicely the behavior of the Ni–polymer system in the full range of Ni concentrations available, i.e. in the interval 0–75% of the Ni content; and moreover, it includes a coefficient characterizing the particle size, too. The new formula was established and experimentally verified for the Ni–PEVAc system only. It seems probable that a mixing rule of the same type will apply for other systems containing spherical particles in the polymer matrix. This, however, has not yet been experimentally proved.

Acknowledgements

This research was supported by the Czech Ministry of Education in the frame of MSM 0021630503 Research Intention MIKROSYN New Trends in Microelectronic System and Nanotechnologies and GA research project 120/07/0113 Schottky cold emission diodes.

References

(1) Holcman V, Liedermann K. New mixing rule of polymer composite systems. *WSEAS Transactions on Electronics* 2007; **4(9)**:181–185.
(2) Holcman V. Dielectric relaxation spectroscopy of composite systems. Dissertation Thesis, Brno University of Technology, Brno, 2007.
(3) HP 4284A Precision LCR meter—Operation manual. Hewlett—Packard Ltd Yokogawa, 1989.
(4) Kováčiková S, Vicen R, Hudec I. Composite materials based on a polymer matrix and a magnetic filler (in Slovak), *Elektroizolačná a káblová technika (Electrical Insulation and Cable Technology),* 2000; **53**:43.

Vladimír Holcman (Non-member) was born in 1979 in Brno, Czechoslovakia. He received the BE and ME degrees in 2001 and 2004, respectively, from the Brno University of Technology (BUT), Brno, Czech Republic. From 2004 to 2007, he pursued the PhD degree in the Microelectronics and Technologies program at the Department of Physics, Faculty of Electrical Engineering and Communications (FEEC), BUT, Brno. His work focused mainly on composites and fluctuation processes in solids. In 2005, he joined as a teaching staff at the Department of Physics at the FEEC, BUT, Brno. In the same year, he also joined the research group dealing with fluctuation processes in solids. He has authored or co-authored 25 papers, presented mostly at international conferences.

Lubomír Grmela (Non-member) was born in 1958 in Prostějov, Czechoslovakia. He graduated from the Faculty of Electrical Engineering, Brno University of Technology (BUT), in 1982. From 1984 to 1988, he was pursuing the PhD degree. In 1985, he was appointed as a Lecturer at the Department of Physics, Faculty of Electrical Engineering and Communications (FEEC), Brno University of Technology. From 1989 to 1991, he was associated with the Czech Academy of Science, Institute of Scientific Instruments, Brno. In 2002, he was appointed as a Professor and currently he is the Head of the Department of Physics, FEEC, BUT. He is involved in the research of stochastic processes and nanometric measurements as a base for the study of nondestructive diagnostic methods in semiconductor devices.

Karel Liedermann (Non-member) was born in 1959 in Brno, Czechoslovakia. He obtained the ME and PhD degrees from the Brno University of Technology (BUT), Brno, Czech Republic, in 1983 and 1988, respectively. He joined as a teaching staff at the Department of Physics, Faculty of Electrical Engineering of the same university in 1983. He spent the year 1989–1990 in the Research Institute of Electrical Machines in Brno, where he was involved in the development of nondestructive diagnostic methods for testing insulation systems of electrical machines. In 1991–1992, he carried out research at Institute of Physics, Johannes-Gutenberg University, Mainz, Germany. In 1997, he was appointed as an associate professor in Mathematical and Physical Engineering at BUT. His main research interest is dielectric relaxation spectroscopy, in particular, studies of microscopic mechanisms of relaxation in polymers, development of mathematical methods for their separation, and studies of the correlation between polymer degradation and the corresponding changes of the dielectric spectrum.

Key Engineering Materials Vols. 592-593 (2014) pp 529-532
Online available since 2013/Nov/15 at www.scientific.net

doi:10.4028/www.scientific.net/KEM.592-593.529

Experimental Studies of Excess Noise Sources in Concrete Based Materials as a Limiting Factor for Electromagnetic Emission Measurement

Robert Macku[1*], Pavel Koktavy[1], Tomas Trcka[1] and Vladimir Holcman[1]

[1]Department of Physic, Brno University of Technology,
Faculty of Electrical Engineering and Communication,
Technicka 10, Brno 616 00, Czech Republic
[*]macku@feec.vutbr.cz

Keywords: Johnson-Nyquist noise, 1/*f* noise, dielectric, concrete, noise spectral density.

Abstract. This paper deals with excess noise sources in dielectric materials. We focus especially on the concrete samples that are frequently tested to ensure information about the reliability and level of degradation. Nevertheless, the testing methods are limited mainly by the proper contact creation, signal detection and noise defined sensitivity. Our efforts are directed to the noise properties assessment. It turns out that the Johnson-Nyquist noise and the 1/*f* (flicker) noise are generated in the different regions with the different response to the internal or external electric field. In addition the noise analysis is affected by the internal polarization phenomena and the material residual humidity. This issue in connection with the sample geometrical properties and the dielectric noise measurement methodology take part in this paper.

Introduction and theoretical background

We provide research on electromagnetic emission (EME) as a result of mechanical loading and micro-scale crack creation in composite materials (not presented here in details, see [1]). The EME signal carry lot of interesting information about the material. Nevertheless, signal analysis and material fundamental research are limited by excess noise presence reducing the ability to detect or to recognize low-energy random EME pulses. That is why, our final aim is to maximize signal to noise ratio by means of the sample geometry optimization, electrical contacts improvement and/or by correlation analysis of noise spectral densities under different measurement conditions.

Stochastic fluctuation of the voltage or current is under observation mainly in case of semi or conductive materials [2]. The dielectric materials require special efforts to establish experimental set-up and the sample parameters stabilization to avoid humidity and leakage current effects. In addition, the dielectrics exhibit specific features connected with the random dielectric or magnetic polarization. Charge carriers and the electric dipoles fluctuate in position due to the thermal energy and the macroscopic stochastic electric field is generated. The physical properties are defined on the basis of the fluctuation-deviation theorem and the Johnson-Nyquist (thermal) noise is produced. The physical variable under consideration is the power spectral density of voltage fluctuation S_U given by well-known formula $S_U = 4kTR$ [3]. Here k is the Boltzmann constant, T temperature and R is static resistance. Other significant noise contributions are in the 1/*f* form. This process results from the sample resistance fluctuation. That is why an external bias voltage is required and electric current starts to flow. The power spectral density (for homogeneous layers) is given by

$$S_R / R^2 = S_u / U^2 = S_i / I^2 = \alpha_H / fN. \qquad (1)$$

Here S_R is the power spectral density of resistance fluctuation, R is static resistance of the sample, S_I is power spectral density of current fluctuation, I is bias current flowing thought sample, α_H is dimension less Hooge's constant, f is frequency and N is number of free carriers participating in fluctuation process [3]. The 1/*f* noise is usually supposed to be result of bulk imperfections. Nevertheless, point metallic contacts and grainy layers produce 1/*f* noise, too [3].

Another electric noise is associated with the random fluctuation of the macroscopic electric or magnetic dipole moment in the dielectric materials. The magnetic dipole variation produces mainly Barkhausen noise [4]; nevertheless, it may be neglected. On the other hand, the electric field assisted polarization noise is non-stationary process and it could play role here [5]. The theoretical noise analysis (not presented here) proves that noise level is below detection limit of the contemporary technology and the polarization noise is unlikely to observe.

Experimental details and samples under investigation

The noise-based measurement has been done by means of the Agilent 35670A two-channel FFT dynamic spectral analyzer, see Fig. 1c. The analyzer is equipped by the custom-made two-channel ultra-low noise preamplifier (LNA). The noise background of LNA is about 3.1 nV/√Hz at 100 Hz. The 3 dB bandwidth is 50 µHz ÷ 10 kHz with voltage amplification 100. For sensitive measurement are analyzer and LNA used in two-channel cross-spectral density mode. Characteristics of the spectral densities as a function of the bias current has been done by means of the Keithley 6220 precision current source and the resistance temporal analysis was realized by the Keithley 6517B electrometer. Prepared samples of concrete with common composition of aggregates (aggregates size range (0 ÷ 4) mm, (4 ÷ 8) mm), Portland cement (EN197-1, 32.5 MPa) and water were used (mean compressive strength 37 MPa). Available thicknesses are l = (10; 20; 30; 40; 50) mm and available cross-section dimensions are A = (20 x 20; 30 x 30; 40 x 40; 50 x 50) mm. Metallic contacts are prepared as a full cross-section carbon layers with sheet resistance about 90 Ω/sq.

Measurement results and discussion

Johnson – Nyquist noise analysis. The measured typical voltage spectral densities S_u of the samples with different geometry are shown in Fig. 1a. There are only three groups of the samples with the same geometry to keep figure readable. The first group of the samples B7, B8 has thickness t = 10 mm and cross section (40 x 40) mm, the second group B9, B10, B11 has t = 10 mm and cross section (50 x 50) mm and finally the group B12, B13 has t = 20 mm and cross section (30 x 30) mm. Each measurement has been done without electrical excitation and noise contributions are supposed to be Johnson – Nyquist type but apparently affected by the measurement circuit.

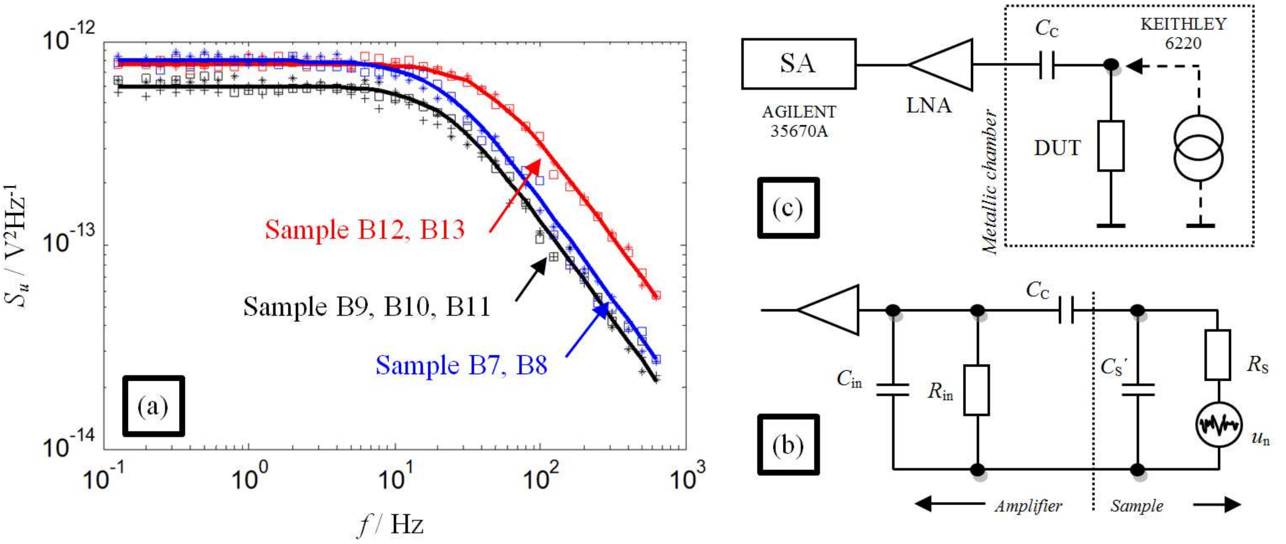

Fig. 1. (a) Selected results of the voltage spectral density measurement of the samples with different geometry. Ambient temperature 300 K. (b) The equivalent model of the input circuits including sample, LNA and noise source under investigation. (c) Scheme of the experiment.

The fundamental equivalent model of input circuits including sample is illustrated in Fig. 1b. Here u_n is internal voltage noise of the sample; C_S is sample capacitance; R_S sample resistance; C_C

coupling capacitance and R_{in}, C_{in} are input resistance and input capacitance of LNA (here 82 MΩ; 17 pF).The input components form modified first order low pass filter, see Fig. 1a. The cut-off frequency is shifted slightly higher and the insertion loss is introduced because of input resistance R_{in}. Technically, the high input resistance and the sample capacitance along with the capacitance of the cables and feed thought connectors (C_S') ale limiting factors for the dielectric noise measurement. Nevertheless, the equivalent circuit frequency dependent transmission function $|S_{21}|$ was calculated (not presented here). We consider that the Johnson-Nyquist noise is primary produced and the spectral density of voltage fluctuation follows from the fluctuation-deviation theorem as mentioned before [3]. Nonlinear regression based on $|S_{21}|$ has been done by means of the MathWorks Matlab. Obtained results for the individual samples group are depicted in Fig. 1a as a solid line and fits experimental data very well. The regression output parameters are $C_S' = 154$ pF, $R_S = 118$ MΩ (group B7, B8), $C_S' = 194$ pF, $R_S = 66$ MΩ (group B9, B10, B11), $C_S' = 76$ pF, $R_S = 110$ MΩ (group B12, B13).

Another interesting phenomenon is the determination of the sample static DC resistance. For the measurement must be strictly used high resistivity meter or combination of the electrometer and the constant voltage source (e.g. Keithley 6517B). It turns out very early that the volume resistivity ρ of the individual samples is different even if the same material was used. The reasons are probably to small dimensions to ensure the long-range order organization considering aggregates. With a view to the Johnson – Nyquist noise modeling the correct approach is to measure the static resistance of the individual samples. Nevertheless, to ensure sufficient measurement accuracy the voltage in the range (10 ÷ 40) V must be applied. Relatively high electric field introduces significant dielectric polarization and the relaxation process take place in the material [5]. In any case, the material is in the different state compared with noise measurement from Fig. 1a. The long-term monitoring of the sample resistance development was done for the each sample under investigation. It turns out that the sample resistance increase monotonically just like the relaxation processes disappears. Characteristics appear to be saturated after 6-hour measurement interval. Let us point out results related to groups mentioned before. We get the mean value of resistance $R_{S,m} = 116.0$ MΩ for the samples B7, B8; $R_{S,m} = 67.1$ MΩ for the samples B9, B10, B11 and $R_{S,m} = 108.3$ MΩ for the samples B12, B13. It corresponds to the extracted data form the noise measurement as presented before.

The flicker noise analysis. Other interesting results are associated with the electrical bias application. We expect $1/f$ current noise because of samples resistance fluctuation as mentioned above (see Eq. 1). The noise level and the Hooge's constant, respectively, correlate with the sample quality and the region of the material where noise is generated. For the research was selected sample B18 because of the low self-capacitance and resistance. The measurement results are illustrated in the Fig. 2a. In this case, the sample was biased by the constant current source Keithely 6220. The $1/f$ fluctuation is evidently superposed on the thermal noise. The background noise is defined as a state when the current source is set to the zero Amps but it is still connected to the circuit. Experimental data (see Fig. 2a) pointed out $1/f$ noise development with the bias current according to the Eq. 1 as is expected.

The voltage spectral density is proportional to f^b where b belongs to the interval (1.2 ÷ 1.5) in case of the all samples under inspection. The slope variation is supposed to be a result of the measurement uncertainty rather than natural evolution. Following research is related to the region where the $1/f$ noise is generated. We provide an experiment where the voltage spectral density is monitored for the different thickness of the samples with the same cross-section (not presented here). With increasing volume we naturally expect decreasing $1/f$ noise level because of increasing number of free particles N. Instead of this, we observe invariant behavior with the marginal reduction of the measurement uncertainty. On the other hand, if we analyze the samples with the uniform thickness and different cross-sections the voltage spectral density is inversely proportional. Let us see curve in Fig. 2b. Here independent variable is the relative-cross section of the sample. Now we should conclude that the region of interest is carbon – concrete interface.

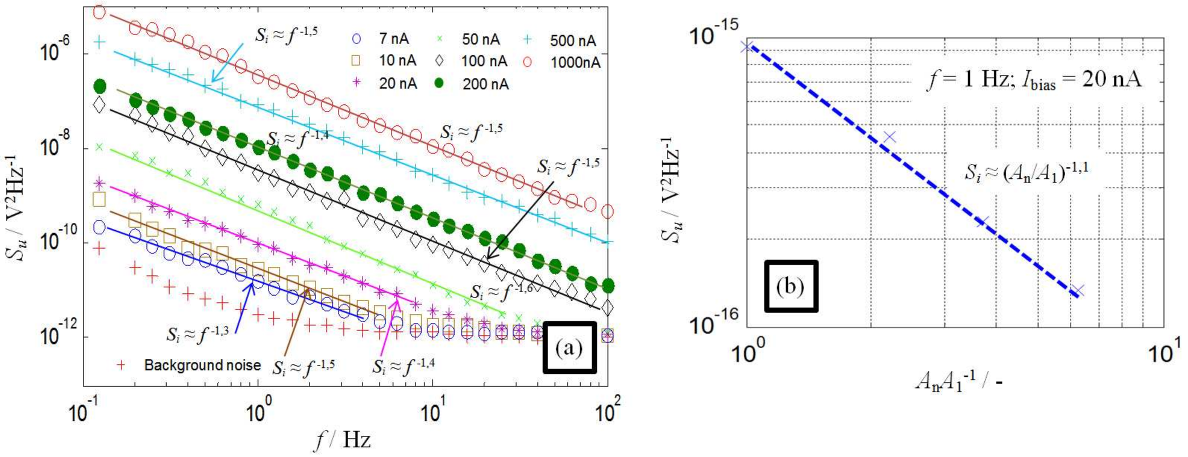

Fig. 2. (a) The voltage spectral density measurement for different bias current. Sample B18, ambient temperature $T = 300$ K and six hours settling time. (b) The voltage spectral density vs. relative sample cross-section. Inspection frequency $f = 1$ Hz, temperature $T = 300$ K and six hours settling time. Symbol A_1 denotes the minimal cross-section and n is a sample index.

Conclusions

We have studied samples made of concrete in order to understand the excess noise sources taking place inside the material. It turns out, that the thermal noise is apparent according to the Johnson – Nyquist theory. Nevertheless, the experimental data must be corrected because of the high samples resistance, self-capacitance and the finite amplifier input resistance. The input resistance increase is limited by stray currents and predisposing to the electromagnetic interference. Further the static resistance of the samples was measured. It is necessary to establish few hours settling time to avoid the dielectric relaxation phenomena. The obtained static resistance matches very well the Johnson – Nyquist noise as predicted before. Another recognized noise is in the 1/*f* form. It develops with bias current according to the square law. On the other hand, the noise is invariant to the sample thickens change and it is inversely proportional to the sample cross-section. It indicates that the region responsible for the noise generation is the carbon – concrete interface.

Acknowledges

This work was supported by Czech Science Foundation Agency within the framework of the project GAP 104/11/0734 by Ministry of Industry and Trade FR-TI1/305 and by European Union in the project CZ.1.07/2.3.00/30.0039 (Excellent young researchers at Brno University of Technology), SIX research center CZ.1.05/2.1.00/03.0072, CZ.1.07/2.2.00/15.0147 and CZ.1.05/1.1.00/02.0068 project.

References

[1] P. Koktavy: *Experimental study of electromagnetic emission signals generated by crack generation in composite materials*. Measurement Science and Tech., Vol. 10, pp. 0-7. (2008)

[2] R. Macku, P. Koktavy: *Analysis of fluctuation processes in forward-biased solar cells using noise spectroscopy*, Physica status solidi(a), Vol. 207, pp. 2387-2394. (2010)

[3] A. Van Der Ziel: *Noise in solid state devices and circuits*, 1st ed., John Wiley & Sons. (1986)

[4] H. Bittel: *Noise in magnetic and dielectric materials*, Physica B, Vol. 83, Issue 1. (1967)

[5] V. Daniel: *Dielectrics relaxation*, Academic press, London. (1970)

Materials Structure & Micromechanics of Fracture VII
10.4028/www.scientific.net/KEM.592-593

Experimental Studies of Excess Noise Sources in Concrete Based Materials as a Limiting Factor for Electromagnetic Emission Measurement
10.4028/www.scientific.net/KEM.592-593.529

New mixing rule of polymer composite systems

Article *in* WSEAS Transactions on Electronics · September 2007

2 authors:

Holcman Vladimír
Brno University of Technology
5 PUBLICATIONS **9** CITATIONS
SEE PROFILE

Karel Liedermann
Brno University of Technology
27 PUBLICATIONS **101** CITATIONS
SEE PROFILE

New mixing rule of polymer composite systems

HOLCMAN VLADIMÍR, LIEDERMANN KAREL
Department of Physics
Brno University of Technology, Faculty of Electrical Engineering and Communication
Technicka 8, 616 00 Brno,
CZECH REPUBLIC
holcman@feec.vutbr.cz

Abstract: - The paper studies dielectric properties of elastomer filled with Ni spherical particles of different sizes within the range 35 – 115 µm. The experimental analysis is followed by the examination permittivity/conductivity mixing rules. A new mixing formula for the composite system consisting of spherical metallic particles and polymer matrix is presented. This formula includes both Ni particle content and Ni particle size as two independent variables

Key-Words: - composites, polymer, permittivity, mixing rule, rules of mixture, measurement

1 Introduction

Composite materials with metallic fillers represent a two-component or multi-component system, whose properties are affected by the properties of polymeric matrix [1], properties of metallic filler and by their mutual interaction at the filler-polymer interface. Composites are often a subject of the current material research, yet only a little attention is paid to the impact of the particle size. This topic becomes increasingly important with the advance of nanocomposites.

This work was focused toward experimental studies and numerical analysis of the impact of Ni filler size on the dielectric properties of the whole composite, even if the total Ni content remains constant. Based on experimental findings, a formula for the permittivity (dielectric constant) of a composite, accounting for both concentration and size of metallic filler particles, is developed.

2 Problem Formulation

The objective of the research was the observation and subsequent evaluation of the impact of Ni metallic filler, in different concentrations, for 5 different particle sizes within the range 35 – 115 µm on their dielectric properties. Matrix material was ethylene – vinyl acetate copolymer (PEVAc) with 45 % (w/w) share of vinyl acetate. Nickel powder filler was used in different Ni particle sizes (referred to as „fractions“) and concentrations. The overview of fractions and overall Ni contents studied is given in the following table:

Table 1. Size of Ni particles

Fraction	Range of sizes of 99.99 % of all particles from the fraction	Average particle size (diameter) parameter-*b*
1520	90-140 µm	115 µm
1320	45-125 µm	85 µm
1120	30-96 µm	63 µm
1020	20-71 µm	45 µm
1010	3-73 µm	35 µm

2.1 Sample preparation

Samples were prepared at the Department of Plastics and Rubber, Faculty of Chemical and Food Technology, Slovak University of Technology in Bratislava, Slovakia, in the form of foils. Nickel concentrations in the matrix were selected according to anticipated and desired conductivity features. The composites with Ni powder fractions denoted as 1520, 1320, 1120, 1020 and 1010 contained 15, 18, 21, 25, 30 and 34 % (v/v) Ni powder share in the matrix. Fraction 1120 was studied more extensively, in a wider concentration range, including 42, 50, 55, 60 and 75 % (v/v) Ni powder share in the matrix.

2.2 Measuring apparatus

Measurements were carried out using various impedance analyzers – HP 4284A, Alpha-Analyzer and E4991A by Agilent. Samples were of a circular shape (d = 55 mm) and 2,5 mm thick. Besides that, rectangular samples with dimensions 15x15x1 mm were used in the measurements with the Alpha-Analyzer. Test samples were measured at frequencies 1 Hz – 10 MHz; however, the focus of this paper is on the concentration and particle size dependence of electric properties. Therefore, only the results at 1 kHz are reported [3].

3 Measurement results

Results of relative permittivity and loss number fraction 1120 are shown in Figs. 1 – 2.

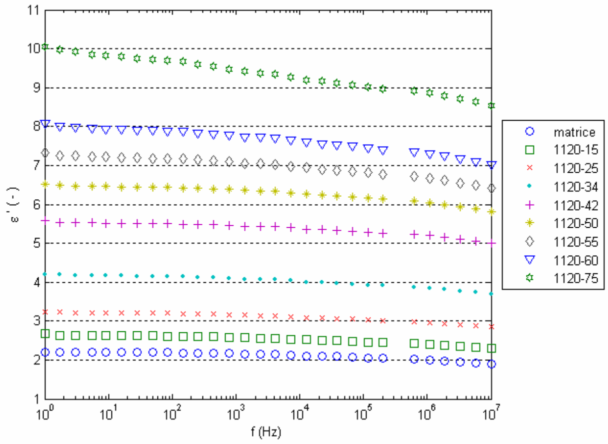

Figure 1. Relative permittivity ε' vs. frequency for metal filler type 1120

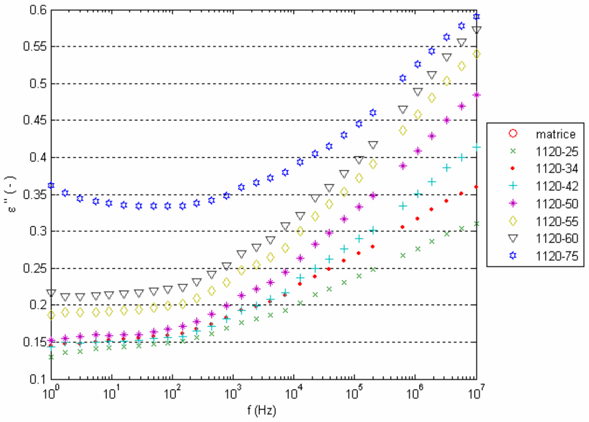

Figure 2. Loss number ε'' vs. frequency for metal filler type 1120

Measurement at all available samples yielded results, which clearly prove the impact of the size of added Ni spherical particles on the electric properties measured. Figure 3 shows the relative permittivity (dielectric constant) ε' and loss number ε'' as a function of Ni particle size at the same Ni content (i.e., the number of larger particles is smaller in order to keep the Ni content constant).

The distinction between the measured fractions can also be observed on the resistivity plot presented in Fig. 4. Full lines indicate best fits to the values measured, assuming linear dependence.

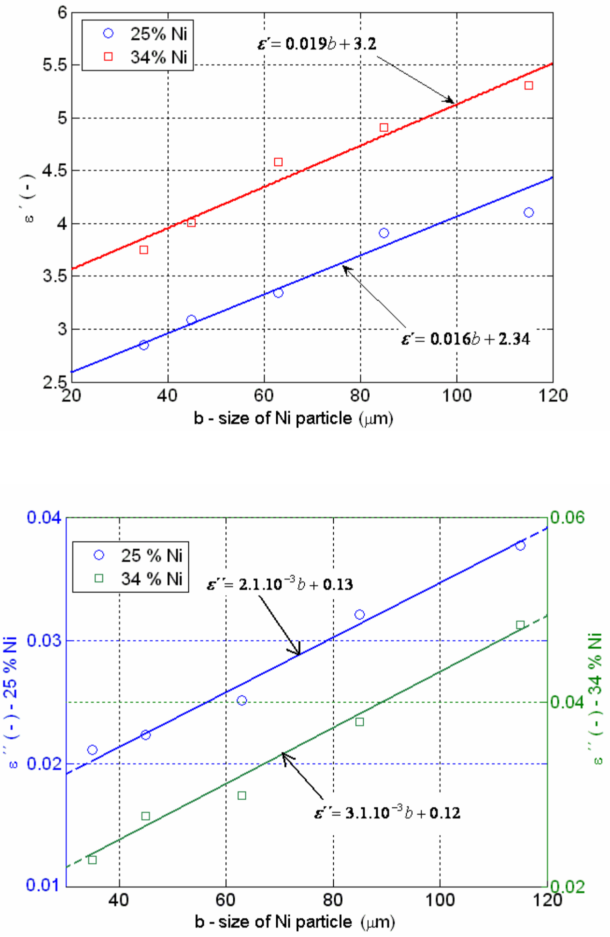

Figure 3. Relative permittivity ε' and loss number ε'' as a function of Ni particle size for 25 % and 34% volume Ni content in the matrix

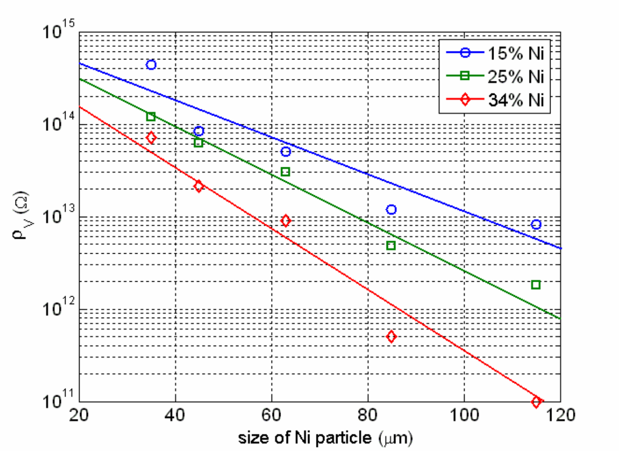

Figure 4. Resistivity *vs.* particle size for 15 %, 25 % and 34 % (volume) Ni content in the matrix

The distinction between the measured fractions can also be observed on the resistivity plot presented in Fig. 2. Full lines indicate best fits to the values measured, assuming linear dependence. The figure shows the decrease of the resistivity with the increasing Ni particle size as well as the fact that the rate of this decrease (slope of the curve) increases with increasing Ni content in the matrix. Also, the magnitude of the resistivity generally decreases with increasing Ni content.

In the next part, an attempt is made to mathematically describe the relation between the resistance of the sample and the size of metallic particles. The objective is to find a suitable formula on the basis of established mixing rules as well as the numerical values of any would-be coefficients. In the first part of the analysis, a number of classical mixing rules [4] were applied to the measurement results Fig. 5 and table 2.

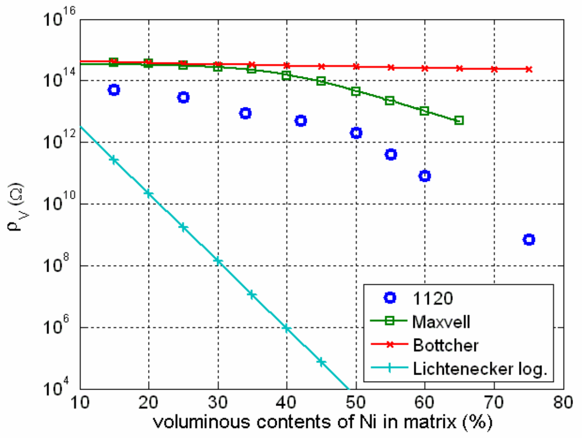

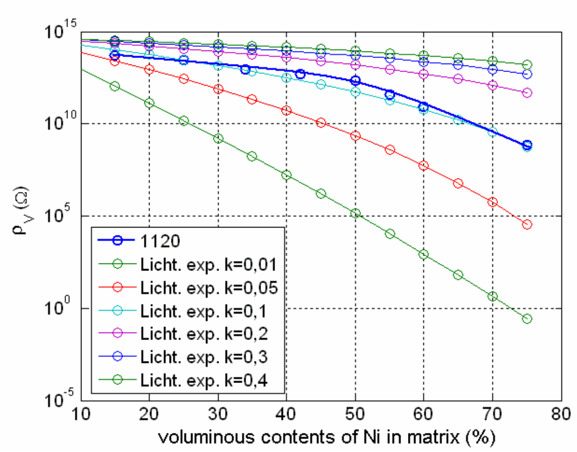

Figure 5. Application of mixing rules [4]

Table 2. Root-mean-square error of fraction 1120 and 1520

Mixing rules	root-mean-square error Fraction 1120	root-mean-square error Fraction 1520
my new rule	$1,8.10^{-1}$	$1,1.10^{-1}$
Maxwell	$1,3.10^{2}$	$5,3.10^{2}$
Lichtenecker log.	$5,8.10^{6}$	$8,1.10^{3}$
Lichtenecker exp. k=0.1	273,1	771,8
Botcher	$3,5.10^{3}$	$4,1.10^{3}$

None of tested formulas contained explicitly the particle size and, hence, none of them was found satisfactory. A major drawback of most mixing formulas was the fact, that they were valid only up to 50 % of the filler content. However, the Lichtenecker power-law mixing rule [4] with exponent $k = 0,1$ seemed to fit best to the Ni-PEVAc composite, and therefore, the Lichtenecker power-law rule was used as a starting point for the derivation of the new formula, which would also account for the particle size.

The Lichtenecker power-law formula for the internal resistivity [for the sake of simplicity, the word „internal" is henceforward omitted] of a multi-component composite system is as follows:

$$\rho_{VS}^{k} = \sum_{i=1}^{n} v_i.\rho_{Vi}^{k} \qquad (1)$$

where k is an empirical parameter, which depends primarily on the shape and the orientation of particles, ρ_{Vi} are resistivities and ν_i are volume shares of individual components. Parameter *k* lies in the interval (-1, +1) [4].

In our case, the volume concentration of Ni particles in the matrix ranges from 15 % to 75 %. In order to establish a new mixing rule, it is necessary to find a function which would characterize the decrease of the resistivity curves with increasing particle size toward lower resistivity values. The analysis of measured curves yielded lead to the conclusion that the contribution of the matrix must be scaled with respect to the particle size, using an exponential dependence of the form:

$$\rho_m = \rho_{mm}.\exp(-0{,}035.b) \qquad (2)$$

where ρ_{mm} denotes the experimentally established value of the resistivity of the matrix, *b* is the Ni particle diameter in μm and ρ_m denotes the particle-size-scaled resistivity of the matrix that would enter Eq. [1].

Resistivity curves not only decrease to lower resistivity values with the increasing particle size, but their slope also change depending on the Ni content, as can be seen from Fig. 4. Therefore, it was necessary to include the change of the slope in the new mixing rule. The best way how to include the change of the slope was to make the coefficient k particle-size-dependent. The dependence was analyzed and found to satisfy the function k=-9.8.10^{-4}.b+0.16.

As all features related to the change of the Ni particle size in the composite system have thus been found, the newly modified Lichtenecker formula can be proposed as follows:

$$\rho_{vs}^{k} = \frac{v_1.\rho_{Ni}^{k} + v_2.\left(\rho_{mm}.\exp[-0{,}035.b]\right)^{k}}{v_1} \qquad (3)$$

where $k = -9{,}8.10^{-4}.b + 0{,}16$ and b denotes the diameter of Ni spherical particles dispersed [μm]. After some rearrangement, the above equation can be written as:

$$\rho_{vs} = \exp\left[\frac{\log(v_1^2\rho_{Ni}^{k} + v_2\left(\rho_{mm} * (-0{,}035 * b)\right)^{k})}{v_1.k}\right] \qquad (4)$$

This new mixing rule suits very well the full analyzed range of Ni contents and Ni particle sizes. Graphical interpretation of the presented formula for the Ni-PEVAc system is presented in Fig. 6.

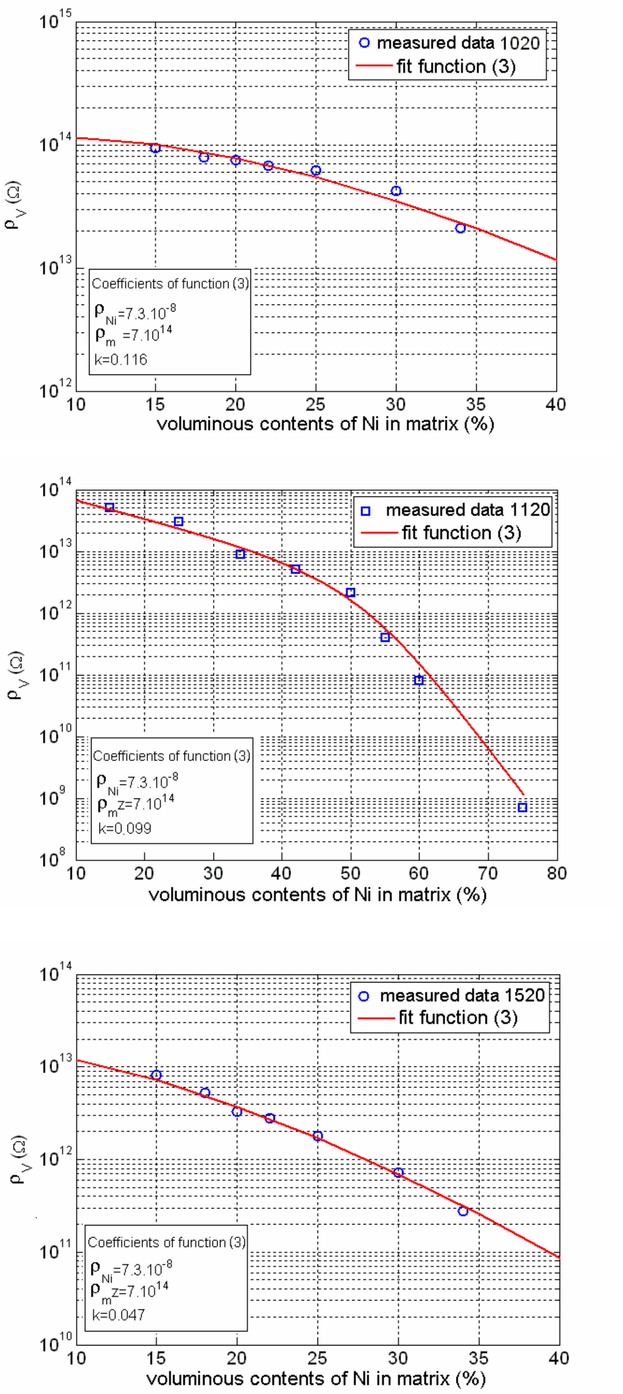

Figure 6. Application of the new mixture rule for fractions 1020, 1120 and 1520

4 Conclusion

Levapren 450 and his conducting composites can be considered polar materials. The results of the measurements yield the following facts:

- By increasing the specific contents of nickel in matrix the relative permittivity, loss factor and loss number increase, as was expected.

- The increase of the specific contents of nickel brings about a decrease of internal resistivity.
- Indicates a relaxation peak somewhere around 30 MHz.Apparently, the position of the relaxation peak does not change with varying Ni contents. It is only the magnitude of the relaxation peak that changes.
- Increasing particle size in the Ni powder results in the increase of the loss factor and loss number.

The addition of the Ni filler (spherical particles), with different sizes but with the same Ni concentration, to the polymer matrix results in composites with different dielectric properties. The newly proposed mixing rule describes very nicely the behaviour of the Ni-polymer system in the full range of Ni concentrations available, i.e., in the interval 0 % -75 % of the Ni content, and moreover, it includes a coefficient characterizing the particle size, too. The new formula was established and experimentally verified for the Ni-PEVAc system only. It seems probable, that a mixing rule of the same type will apply for other system containing spherical particles in the polymer matrix; this, however, has not been yet experimentally proved.

Acknowledgement:

This research has been supported by the Czech Ministry of Education in the frame of MSM 0021630503 Research Intention MIKROSYN New Trends in Microelectronic System and Nanotechnologies and GA 102/07/0113 – Diagnostics of Schottky and cold emission cathodes with electronic noise.

References:

[1] I. Kováčiková, S. Vicen, R. Hudec, Elektroizolačná a káblová technika, 53 (2000) 43 – 46.
[2] U. Schneider, Breitbandige dielek-trische Studien der Dynamik struktu-reller Glasbildner, University of Augsburg, Augsburg, 2000.
[3] V. Holcman, Dielectric relaxation spectroscopy of composite systems, Brno University of Technology, Faculty of Electrical Eng. and Communication, Brno, 2007.
[4] L. K. H. van Beek, in: J. B. Birks (Ed.), Progress in Dielectrics, CRC Press, Cleveland, Ohio, 1967, pp. 69 – 114.
[5] P. Lunkenheimer, Dielectric spectro-scopy of glassy dynamics, Shaker Verlag, Aachen, 1999.
[6] E. Riande, R. Díaz-Calleja: Electrical properties of polymers, Marcel Dekker, New York, 2004.
[7] Wehn, R: Dielektrische Spektroskopie zur Untersuchung der Glasdynamik im Nichtgleichgewicht. Augsburg 2005,
[8] Hassdentefel, J., Dubský, J., Rapoš, M., Šandera, J. Elektrotechnické materiály. Státní nakladatelství technické literatury Praha 1978 str. 20-280 .
[9] TARJUS, G., KIVELSON, D., KIVELSON, S.: Supercooled Liquids, Advances and Novel Applications, ACS Symposium Series, vol. 676, American Chemical Society, Washington, DC, 1997, p. 67.
[10] LEON, C., NGAI, K. L.: The excess wing in the relaxation of a glass formers: a Coupling Model perspective, GMFC Univ. Complutence, Madrid Spain, 2001.
[11] LUNKENHEIMER, P., PIMENOV, A., SCHIENER, B., BÖHNER, R., LOIDL, A.: Europhys. Lett. 33 (1996) 611.
[12] TARJUS, G., KIVELSON, D., KIVELSON, S.: Supercooled Liquids, Advances and Novel Applications, ACS Symposium Series, vol. 676, American Chemical Society, Washington, DC, 1997, p. 67.
[13] JOHARI, G.P.: The Glass Transition and the Nature of the Glassy State, Annals of the New York Academy of Sciences, vol. 279, 1976, p. 117.
[14] LUNKENHEIMER, P., PIMENOV, A., DRESSEL, M., GORSHUNOV, B., SCHNEIDER, U., SCHIENER, B., LOIDL, A.: Advances and Novel Applications, ACS Publications, Washington, DC, 1997, p. 168.

Acta Polytechnica **53**(2):98–102, 2013

MULTIGROUP APPROXIMATION OF RADIATION TRANSFER IN SF_6 ARC PLASMAS

Milada Bartlova*, Vladimir Aubrecht, Nadezhda Bogatyreva, Vladimir Holcman

Faculty of Electrical Engineering and Communication, Brno University of Technology, Technicka 10, 616 00 Brno, Czech Republic

* corresponding author: `bartlova@feec.vutbr.cz`

Abstract. The first order of the method of spherical harmonics (P1-approximation) has been used to evaluate the radiation properties of arc plasmas of various mixtures of SF_6 and PTFE ($(C_2F_4)n$, polytetrafluoroethylene) in the temperature range $(1000 \div 35\,000)$ K and pressures from 0.5 to 5 MPa. Calculations have been performed for isothermal cylindrical plasma of various radii $(0.01 \div 10)$ cm. The frequency dependence of the absorption coefficients has been handled using the Planck and Rosseland averaging methods for several frequency intervals. Results obtained using various means calculated for different choices of frequency intervals are discussed.

Keywords: SF_6 and PTFE plasmas, radiation transfer, mean absorption coefficients, P1-approximation.

1. Introduction

An electric (switching) arc between separated contacts is an integral part of a switching process. For all kinds of high power circuit breakers, the basic mechanism is to extinguish the switching arc at the natural current zero by gas convection.

The switching arc is responsible for proper disconnection of a circuit. In the mid and high voltage region, SF_6 self-blast circuit breakers are widely used. Radiation transfer is the dominant energy exchange mechanism during the high current period of the switching operation. Due to the extreme conditions, experimental work only gives global information instead of local information, which may be important for determining the optimum operating conditions; theoretical modelling is then of great importance. Several approximate methods for radiation transfer in arc plasma have been developed (isothermal net emission coefficient method [7, 1, 8], partial characteristics method [2, 11], P1-approximation [9], discrete ordinates method [9], etc.). In this paper, the P1-approximation has been used to predict radiation processes in various mixtures of SF_6 and PTFE plasmas.

2. P1-approximation

If diffusion of light is neglected and local thermodynamic equilibrium is assumed, the radiation transfer equation can be written as

$$\mathbf{\Omega} \cdot \nabla I_\nu(\mathbf{r}, \mathbf{\Omega}) = \kappa_\nu (B_\nu - I_\nu), \tag{1}$$

where I_ν is the spectral intensity of radiation, $\mathbf{\Omega}$ is a unit direction vector, κ_ν is the spectral absorption coefficient, and B_ν is the Planck function – the spectral density of equilibrium radiation. In P1-approximation, the angular dependence of the specific intensity is assumed to be represented by the first two terms in a spherical harmonics expansion

$$I_\nu(\mathbf{r}, \mathbf{\Omega}) = \frac{c}{4\pi} U_\nu(\mathbf{r}) + \frac{3}{4\pi} \mathbf{F}_\nu(\mathbf{r}) \cdot \mathbf{\Omega}\,, \tag{2}$$

where U_ν denotes the radiation field density, $\mathbf{F}_\nu$ is the radiation flux, and c is the speed of light. Combining this expression with Eq. 1, one finds for radiation flux

$$\mathbf{F}_\nu(\mathbf{r}) = -\frac{c}{3\kappa_\nu} \nabla U_\nu(\mathbf{r}) \tag{3}$$

and a simple elliptic partial differential equation for the density of radiation U_ν

$$\nabla \cdot \left[\frac{-c}{3\kappa_\nu(T)} \nabla U_\nu(\mathbf{r}) \right] + \kappa_\nu(T) c U_\nu(\mathbf{r}) = \kappa_\nu(T) 4\pi B_\nu(T)\,. \tag{4}$$

Integrating over frequency, the total density of the radiation and the total radiation flux are obtained

$$U(\mathbf{r}) = \int_0^\infty U_\nu(\mathbf{r})\,\mathrm{d}\nu,$$
$$\mathbf{F}(\mathbf{r}) = \int_0^\infty \mathbf{F}_\nu(\mathbf{r})\,\mathrm{d}\nu. \tag{5}$$

3. Absorption coefficients

Prediction of both radiation emission and absorption properties requires knowledge of the spectral coefficients κ_ν of absorption as a function of radiation frequency. These coefficients are proportional to the concentration of the chemical species occurring in the plasma, and depend on the cross sections of various radiation processes.

In the mixture of SF_6 and PTFE (C_2F_4) we assume the following species: SF_6 molecules, S, F, C atoms,

S^+, S^{+2}, S^{+3}, F^+, F^{+2}, C^+, C^{+2}, C^{+3} ions and electrons. The equilibrium concentrations of each species in various SF_6 + PTFE mixtures were taken from [3].

Spectral coefficients of absorption were calculated using semi-empirical formulas to represent both continuum and line radiation. The continuum spectrum is formed by bound-free transitions (photo-recombination, photo-ionization) and free-free transitions (bremsstrahlung). The photo-ionization cross sections for neutral atoms were calculated by the quantum defect method of Seaton [12], the cross sections of the photo-ionization of ions and free-free transitions were treated using Coulomb approximation for hydrogen-like species [6]. In the discrete radiation calculations, spectral lines broadening and their complex shapes have to be carefully considered. The lines are broadened due to numerous phenomena. The most important are Doppler broadening, Stark broadening, and resonance broadening. For each line, we have calculated the values of half-widths and spectral shifts. The line shape is given by convolution of the Doppler and Lorentz profiles, resulting in a simplified Voigt profile. The lines that overlap have also been taken into account. Due to lack of data, from molecular species we have only considered SF_6 molecules with their experimentally measured absorption cross sections [5].

4. Absorption means

One of the procedures for handling the frequency variable in the radiation transfer equation is the multigroup method [10, 4]. It is based on a simplified spectral description with only some spectral groups assuming grey body conditions within each group with a certain average absorption coefficient value, i.e. for the k-th spectral group

$$\kappa_\nu(\mathbf{r},\nu,T) = \overline{\kappa}_k(\mathbf{r},T); \quad \nu_k \le \nu \le \nu_{k+1}. \tag{6}$$

The mean absorption coefficient values are generally taken as either the Rosseland mean or the Planck mean.

The Planck mean is appropriate in the case of an optically thin system. The Planck mean absorption coefficient is given by

$$\overline{\kappa}_P = \frac{\int_{\nu_k}^{\nu_{k+1}} \kappa_\nu B_\nu \,\mathrm{d}\nu}{B_k}\,, \tag{7}$$

where

$$B_k = \int_{\nu_k}^{\nu_{k+1}} B_\nu \,\mathrm{d}\nu.$$

The Rosseland mean is appropriate when the system approaches equilibrium (almost all radiation is reabsorbed). The Rosseland mean is given by

$$\overline{\kappa}_R^{-1} = \frac{\int_{\nu_k}^{\nu_{k+1}} \kappa_\nu^{-1} \frac{\mathrm{d}B_\nu}{\mathrm{d}T}\,\mathrm{d}\nu}{\int_{\nu_k}^{\nu_{k+1}} \frac{\mathrm{d}B_\nu}{\mathrm{d}T}\,\mathrm{d}\nu}. \tag{8}$$

The total radiation density value is then given by

$$U(\mathbf{r}) = \sum_k U_k(\mathbf{r}), \tag{9}$$

where U_k are solutions of Eq. 4 with frequency independent $\overline{\kappa}_k(T)$ and $B_k(T)$.

5. Net emission coefficients

Assuming local thermodynamic equilibrium, coefficient of absorption κ_ν is related to the coefficient of emission ε_ν by Kirchhoff's law

$$\varepsilon_\nu = B_\nu \kappa_\nu. \tag{10}$$

Strong self-absorption of radiation in the plasma volume occurs, and this must be taken into account in the calculations. The net emission coefficient of radiation, $\varepsilon_{N\nu}$ is defined by Lowke [7] as

$$\varepsilon_{\mathrm{N}\nu} = \varepsilon_\nu - J_\nu \kappa_\nu\,, \tag{11}$$

where J_ν is an average radiation intensity, which is a function of temperature. For an isothermal plasma sphere at radius R (the results are approximately the same as for the isothermal cylinder), it is defined as

$$J_\nu = B_\nu[1 - \exp(-\kappa_\nu R)]. \tag{12}$$

A combination of Eqs. 10–12 gives the expression for the net emission coefficient

$$\varepsilon_{\mathrm{N}} = \int_0^\infty B_\nu \kappa_\nu \exp(-\kappa_\nu R)\,\mathrm{d}\nu. \tag{13}$$

The isothermal net emission coefficient corresponds to the fraction of the total power per unit volume and unit solid angle irradiated into a volume surrounding the axis of the arc plasma and escaping from the arc column after crossing thickness R of the isothermal plasma. It is often used for predicting the energy balance, since the net emission of radiation (the divergence of the radiation flux) can be written as

$$\nabla \cdot \mathbf{F}_R = 4\pi \varepsilon_{\mathrm{N}}. \tag{14}$$

In multigroup P1-approximation, the net emission coefficient can be determined from Eq. 4. In the case of cylindrically symmetrical isothermal plasma, Eq. 4 has constant coefficients $\overline{\kappa}_k$ and B_k, and depends only on one variable – radial distance r. It represents the modified Bessel equation, and can be solved analytically. Taking into account the boundary condition (no radiation enters into the plasma cylinder from outside)

$$\mathbf{n} \cdot \mathbf{F}_k(R) = -\frac{c\,U_k(R)}{2} \tag{15}$$

the net emission over the volume of the arc for the k-th frequency group is

$$(w_{\mathrm{avg}})_k = \frac{2\pi}{\pi R^2} \int_0^R r\,\nabla \cdot \mathbf{F}_k(r)\,\mathrm{d}r = \\ = \frac{2}{R}\,\frac{4\pi B_k}{2I_1(\sqrt{3}\,\overline{\kappa}_k R) + \sqrt{3}\,I_0(\sqrt{3}\,\overline{\kappa}_k R)}\,I_1(\sqrt{3}\,\overline{\kappa}_k R) \tag{16}$$

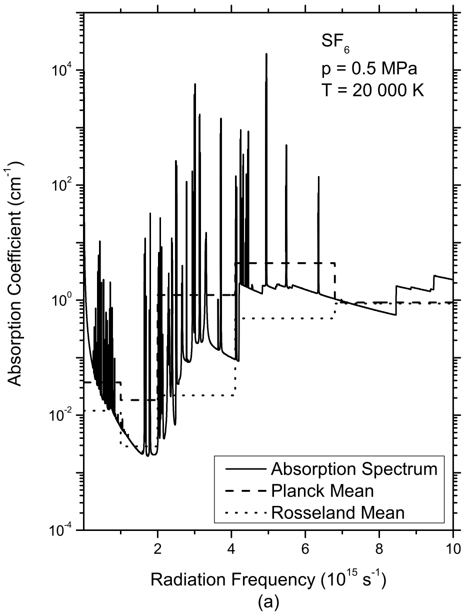

FIGURE 1. The real absorption spectrum of SF$_6$ plasma at $p = 0.5\,\mathrm{MPa}$ and $T = 20\,000\,\mathrm{K}$ compared with the Planck and Rosseland means.

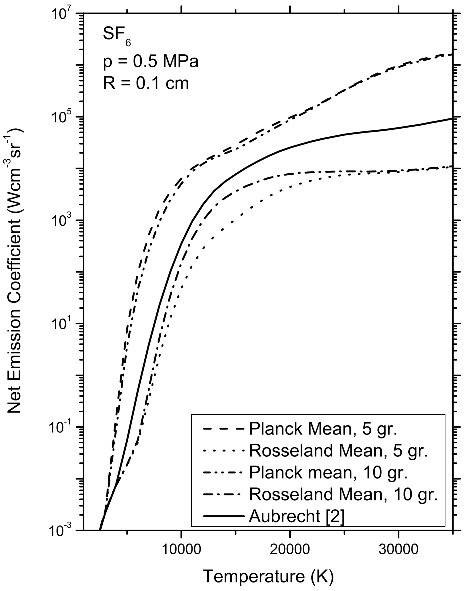

FIGURE 2. Net emission coefficients of SF$_6$ plasma with radius 0.1 cm as a function of temperature for two different cuttings of the frequency interval and various absorption means; comparison with results of Aubrecht [1].

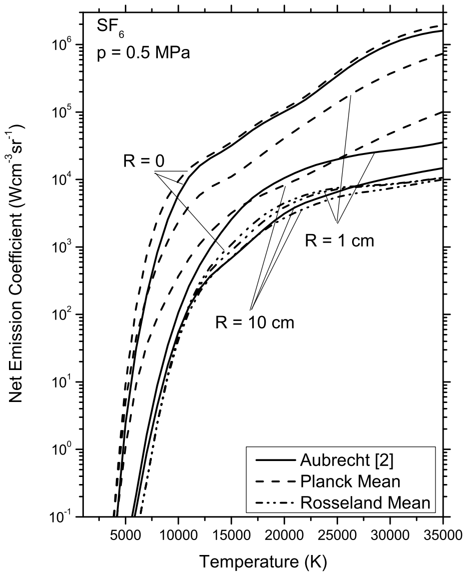

FIGURE 3. Net emission coefficients of SF$_6$ plasma as a function of temperature for various thicknesses of the plasma and various absorption means.

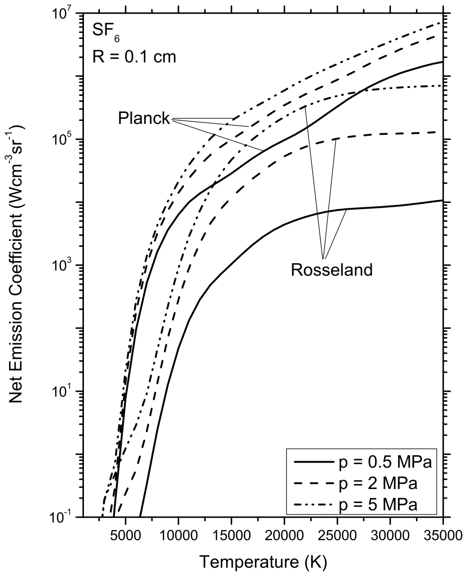

FIGURE 4. Net emission coefficients of SF$_6$ plasma with radius 0.1 cm as a function of temperature for various pressures.

where $I_0(x)$ and $I_1(x)$ are modified Bessel functions. Summing over all frequency groups gives the net emission of radiation

$$\nabla \cdot \mathbf{F}_R = \sum_k (w_{\mathrm{avg}})_k = 4\pi\varepsilon_{\mathrm{N}}. \qquad (17)$$

6. RESULTS

The mean absorption coefficient values depend on the choice of the frequency interval cutting. The cutting frequencies are mainly defined by the steep jumps of the evolution of the continuum absorption coefficients that correspond to individual absorption edges. However, the number of groups should be minimized to decrease the computation time. In this work, the frequency interval $(10^{12} - 10^{16})\,\mathrm{s}^{-1}$ was cut into

(a) five frequency groups with cutting frequencies

$$(0.001, 1, 2, 4.1, 6.8, 10) \times 10^{15}\,\mathrm{s}^{-1}\,, \qquad (18)$$

(b) ten frequency groups with cutting frequencies

$$\begin{gathered}(0.001, 1, 1.4, 1.77, 2, 2.2, 2.5, 3,\\ 4.1, 6.8, 10) \times 10^{15}\,\mathrm{s}^{-1}\,.\end{gathered} \qquad (19)$$

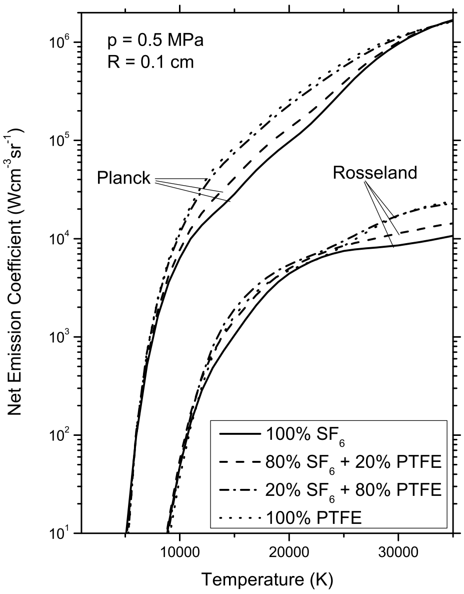

Figure 5. Net emission coefficients of different mixtures of SF_6 and PTFE plasmas as a function of temperature at pressure 0.5 MPa for various absorption means.

The two cuttings differ in the frequency interval $(1 \div 4.1) \times 10^{15}\,\mathrm{s}^{-1}$, which is split into two groups in case (a), and in greater detail into seven groups in case (b). The absorption spectrum evaluated at 20 000 K compared with various averaged versions for five groups cutting is shown in Fig. 1.

The net emission coefficients were calculated by combining Eqs. 16 and 17. Results for an isothermal plasma cylinder of radius $R = 0.1\,\mathrm{cm}$ for two different cuttings Eqs. 18, 19 of the frequency interval are given in Fig. 2. In the case of the Planck averaging method, cutting the spectrum into more frequency groups influences the resulting net emission coefficients only slightly. A comparison is also provided with the values of Aubrecht [1], which were obtained by direct integration from Eq. 13. It can be seen that the Planck mean leads to an overestimation of the emitted radiation, while the Rosseland approach underestimates it.

An example of the calculated temperature dependence of the net emission coefficients for various thicknesses of pure SF_6 plasma at a pressure of 0.5 MPa is presented in Fig. 3. The strong effect of plasma thickness can be seen both for direct frequency integration Eq. 13 and for Planck means; Rosseland averages are influenced only slightly. As can be expected from the definition of the Planck and Rosseland means, by omitting self-absorption ($R = 0$) the Planck means give good agreement with the results of direct integration, while for thick plasma ($R = 10\,\mathrm{cm}$) the Rosseland mean is a good approach.

The influence of the plasma pressure on the net emission coefficient values is shown in Fig. 4. Net emission coefficients increase with increasing pressure, mainly for Rosseland means.

The influence of an admixture of PTFE on the values of the net emission coefficients of SF_6 plasma is given in the Fig. 5 for plasma thickness 0.1 cm. The differences between net emission coefficients are very small. This can be explained by the approximately equivalent role of sulphur and carbon species. Sulphur and carbon atoms and ions have similar radiation emission behavior.

7. Conclusions

Net emission coefficients for various mixtures of SF_6 and PTFE plasmas have been calculated using P1-approximation for an isothermal plasma cylinder. Multigroup approximation for handling the frequency variable has been used. Both Planck and Rosseland averaging methods have been applied to obtain mean values of absorption coefficient values. A comparison with the net emission coefficients calculated by direct frequency integration has been provided. It has been shown that Planck means generally overestimate the emission of radiation, while Rosseland means underestimate it. Planck means give good results only for a very small plasma radius (omitting self-absorption). The Rosseland mean is a suitable approach for thick plasma (absorption dominated system). In reality, neither mean is correct in general. The simplest procedure for improving the accuracy is to use the Planck mean for frequency groups with low absorption coefficient values and the Rosseland mean for groups with high absorption coefficient values.

Another approach was suggested in [9], where each group based on original frequency splitting was further divided according to the absorption coefficient values, and Planck averaging for these new groups was calculated. This procedure partially solves the problem of overestimation of the role of lines in the Planck averaging method. Another correction of the influence of lines on Planck means was presented in [4], where the escape factor was introduced.

Acknowledgements

This work has been supported by the Czech Science Foundation under project No. GD102/09/H074 and by the European Regional Development Fund under projects Nos. CZ.1.05/2.1.00/01.0014 and CZ.1.07/2.3.00/09.0214.

References

[1] V. Aubrecht, M. Bartlova. Net emission coefficients of radiation in air and SF_6 thermal plasmas. *Plasma Chem Plasma Process* **29**(2):131–147, 2009.

[2] V. Aubrecht, J. J. Lowke. Calculations of radiation transfer in SF_6 plasmas using the method of partial characteristics. *J Phys D: Appl Phys* **27**(10):2066–2074, 1994.

[3] O. Coufal, P. Sezemsky, O. Zivny. Database system of thermodynamic properties of individual substances at high temperatures. *J Phys D: Appl Phys* **38**(8):1265–1274, 2005.

[4] Y. Cressault, A. Gleizes. Mean absorption coefficients for CO_2 thermal plasmas. *High Temp Mat Process* **10**(1):47–54, 2006.

[5] A. R. Hochstim, G. A. Massel. *Kinetic Processes in Gases and Plasmas.* Academic Press, New York, 1969.

[6] R. W. Liebermann, J. J. Lowke. Radiation emission coefficients for sulfur hexafluoride arc plasmas. *J Quant Spectrosc Radiat Transfer* **16**(3):253–264, 1976.

[7] J. J. Lowke. Prediction of arc temperature profiles using approximate emission coefficients for radiation losses. *J Quant Spectrosc Radiat Transfer* **14**(2):111–122, 1974.

[8] Y. Naghizadeh-Kashani, Y. Cressault, A. Gleizes. Net emission coefficients of air thermal plasmas. *J Phys D: Appl Phys* **35**(22):2925–2934, 2002.

[9] H. Nordborg, A. A. Iordanidis. Self-consistent radiation based modeling of electric arcs: I. Efficient radiation approximations. *J Phys D: Appl Phys* **41**(13):135205, 2008.

[10] G. C. Pomraning. *The Equations of Radiation Hydrodynamics.* Dover Publications, New York, 2005.

[11] G. Raynal, A. Gleizes. Radiative transfer calculations in SF_6 arc plasmas using partial characteristics. *Plasma Sources Sci Technol* **4**(1):152–160, 1995.

[12] M. Seaton. Quantum defect method. *Monthly Not Royal Astronom Society* **118**(5):504–518, 1958.

JINST

PUBLISHED BY IOP PUBLISHING FOR SISSA MEDIALAB

RECEIVED: *October 1, 2012*
REVISED: *March 7, 2013*
ACCEPTED: *May 5, 2013*
PUBLISHED: *June 7, 2013*

14th INTERNATIONAL WORKSHOP ON RADIATION IMAGING DETECTORS,
1–5 JULY 2012,
FIGUEIRA DA FOZ, PORTUGAL

Study of electric field distribution and low frequency noise of CdZnTe radiation detectors

O. Sik,[a,1] **L. Grmela,**[a] **H. Elhadidy,**[a,b,c] **V. Dedic,**[b] **J. Sikula,**[a] **P. Grmela ,**[a] **J. Franc,**[b] **P. Skarvada**[a,d] **and V. Holcman**[a]

[a]*Department of Physics, Faculty of Electrical Engineering and Communication,*
Brno University of Technology, Technicka 3058/10, 61600 Brno, Czech Republic
[b]*Institute of Physics, Faculty of Mathematics and Physics, Charles University,*
Ke Karlovu 5, 121 16 Prague 2, Czech Republic
[c]*Faculty of Science, Department of Physics, Mansoura University,*
Mansoura 35516, Egypt
[d]*Central European Institute of Technology,*
Technicka 3058/10, 61600 Brno, Czech Republic

E-mail: `xsikon00@stud.feec.vutbr.cz`

ABSTRACT: Polarization phenomena in a metal-semiconductor-metal (M-S-M) structure of metallic Schottky contacts deposited on CdZnTe radiation detectors were studied. We evaluate the distribution of the electric field along the biased M-S-M structure by Pockels measurements. The results show that almost all the electric field is developed across the depletion layer of the reverse-biased contact. The noise measurements of the CdZnTe detectors studied show that the dominant noise is $1/f^m$ noise. The $1/f^m$ noise, with the parameter m close to one, is present at frequencies below 100 Hz and its bandwidth decreases in the course of the polarization process. At higher frequencies, we observed an increase of the m parameter to 2, which indicates a strengthened effect of the generation-recombination processes. In the frequency band of dominating $1/f^{m=1}$ noise, the increase of magnitude of the noise spectral density was proportional to the power of 6, in relation to the current through the detector. This high value is explained as a result of a screening effect of the space charge buildup during the polarization.

KEYWORDS: Charge transport and multiplication in solid media; Detector modelling and simulations II (electric fields, charge transport, multiplication and induction, pulse formation, electron emission, etc); Gamma detectors (scintillators, CZT, HPG, HgI etc)

---

[1] Corresponding author.

doi:10.1088/1748-0221/8/06/C06005

2013 JINST 8 C06005

Contents

1 Introduction

Cadmium-Telluride (CdTe) is currently a very promising material for semiconductor radiation detectors for nuclear imaging and detection, which is also able to operate at room temperature. This is due to its 1.5 eV wide direct band gap and a high attenuation coefficient. The progress in detectors, with the widely used process of manufacturing a detector with Schottky contacts [1], showed significant advances in the semi-insulating substrate manufacturing process. Nowadays, the most advanced crystal growth technologies, such as High Pressure Bridgman and Travelling Heater Method, produce crystals with specific resistivity reaching up to 10^{11} Ωcm [2]. Substrate with added zinc (CdZnTe) shows higher uniformity of grown crystals and a wider band gap; CdZnTe has comparable spectroscopic performance as CdTe detectors [3]. Nevertheless, both CdTe and CdZnTe suffer from the presence of uncompensated traps (characterized by their capture cross sections and energy levels [4]) that lead to a limited charge collection. Numerous studies [5–7] showed that those disturbances cause electric field formation in the detector bulk after biasing, i.e., the polarization effect. The polarization effect is observable for both irradiated and unirradiated detectors. Beside the polarization effect, imperfections cause an increase of undesired leakage current, which limits the application of a high electric field to assure good charge collection of the detector [8]. The presence of the DC component of the leakage current is not the only problem. In addition, fundamental charge transport mechanisms, such as generation-recombination processes, diffusion, etc., result in the presence of noise in the detector system. Most published studies concern the maximization of the detector signal, whilst studies about noise origin and experiments about reducing detector noise are rarely published [9, 10].

In this study, we investigate the dynamics of the polarization effect and its influence on the electric field distribution in the detector system using an optoelectrical method — the Pockels measurements [11]. The macroscopic nature of the polarization is analyzed by the characterization of the current-time dependence and, so far unpublished, the evolution of the noise spectral density during polarization of the detector.

2013 JINST 8 C06005

2 Experimental result and analysis

Analytical results were received on an Au/CdZnTe/Au planar detector with dimensions $5\times5\times2.5$ mm^3. The crystal was grown by the Vertical Gradient Freeze Method at the Institute of Physics, Charles University in Prague [12]. Symmetric Au Schottky contacts were deposited from aqueous solution of AuCl$_3$. The specific resistivity of (111) oriented CdZnTe (Zn = 10%) n type crystal is 7×10^7 Ωcm. Even though the crystal does not meet the requirements to obtain a high quality x-ray detector (a crystal with a high specific resistivity $> 10^8$ Ωcm), this sample was chosen because of its significant polarization. All measurements were performed at 300 K.

Pockels effect measurements were used to monitor the spatial distribution of the electric field through the studied detector. CdZnTe is a zinc-blend crystal exhibiting a linear electro-optic (Pockels) effect. It acts as an optically isotropic material in the absence of an applied voltage. When a voltage is applied, CdZnTe becomes a double-axis anisotropic material and its refractive indices are dependent on the electric field E. Using this effect, the distribution of the electric field through the sample can be estimated by a crossed-polarizer technique, where the local electric field strength in the direction perpendicular to light propagation is given by:

$$E(x,y) = \arcsin\frac{\sqrt{I(x,y)/I_0(x,y)}}{\gamma}, \quad \gamma = \frac{\sqrt{3}\pi n_0^3 r_{41} d}{2\lambda}.$$

With respect to the direction of the applied electric field and crystal orientation, where $I(x,y)$ is the transmitted light intensity; $I_0(x,y)$ transmitted light intensity with parallel polarizers and no bias; $\lambda = 980$ nm is the wavelength of the used light; $n_0 = 2.8$ is the field-free refractive index of CdZnTe at 980 nm; $r_{41} = 6.5\times10^{-12}$ m/V the linear electro-optic coefficient and $d = 5$ mm is the optical path length.

The detector signal was sampled by a nano-voltmeter on the load resistor. The noise voltage was transformed into the corresponding noise spectral density using the FFT. The setup allows us to measure the sample current and the noise voltage simultaneously without any effect on the noise. The measured values were recorded and analyzed in a PC.

2.1 Long time sample current measurements

Figure 1 shows the measured current evolution after the start of the detector biasing. The applied bias voltage was 100 V. The sample current showed a transient of the detector leakage current. The leakage current increased from initial 60 nA to 160 nA in the course of 10 hours after starting the detector biasing.

2.2 Electric field distribution through the sample after biasing

The electric field distribution in the sample is a result of the Pockels measurements, plotted in figure 2 (left). This figure represents the one hour time decay of the internal electric field profiles in the studied sample when the bias is 100 V. Figure 2 (right) suggests that most of the bias is developed across the reverse-biased contact of the structure. In our case the decrease of the electric field is observed at the cathode (n type semiconductor).

Because of the existence of the barrier, which is given by the difference between the CdTe and Au work functions, reverse biasing creates the electric field that blocks major carriers. This field is

2013 JINST 8 C06005

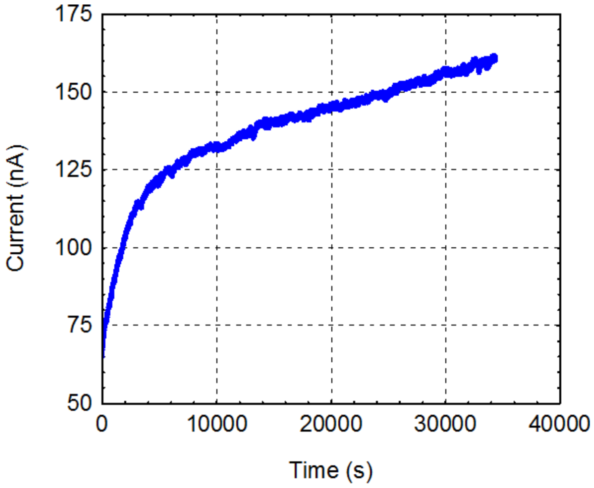

Figure 1. Detector leakage current evolution in time. Applied voltage was 100 V.

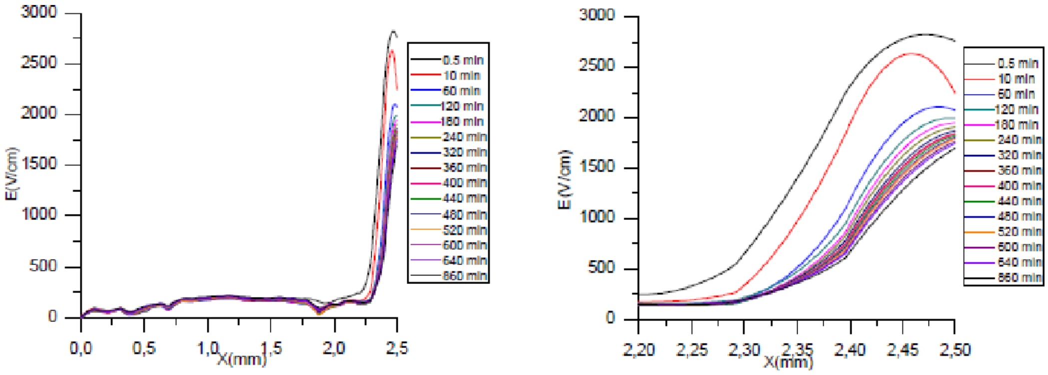

Figure 2. Time evolution of electric field distribution through the detector (left) and at the cathode area (right).

theoretically sustained by a positive space charge. Our measurements showed decreases from the cathode side (figure 2 right). The decrease of electric field is due to the ionization of deep levels in time, followed with space charge formation when the detector is biased.

2.3 Long time detector noise evolution

Figure 3 shows the evolution of the low frequency noise spectrum of the analyzed detector in time. We have observed a $1/f^m$ noise as the dominant noise type, which has the highest impact on the signal to noise ratio of the detector. At frequencies below 100 Hz, the slope m of the $1/f^m$ noise was very close to 1. The corner frequency of the $1/f^m$ noise with $m = 1$ gets lower during the polarization. This trend is followed by the $1/f^m$ noise with $m > 1$. The increase of the m parameter is caused by an increasing ratio of the generation-recombination processes in the total noise spectrum.

The signal spectrum sampled in time of biasing shows a dominant $1/f$ noise with a corner frequency of 200 Hz. At higher frequencies, the detector noise signal spectrum showed a shot noise shape, for which the slope m is typically 0. The noise spectrum acquired 10 minutes after biasing, exhibits a $1/f^m$ noise corner at units of kHz. Later noise spectra, sampled 20, 30, 40 and 50 minutes after detector biasing, exhibit a decrease of shot noise spectral density level, which

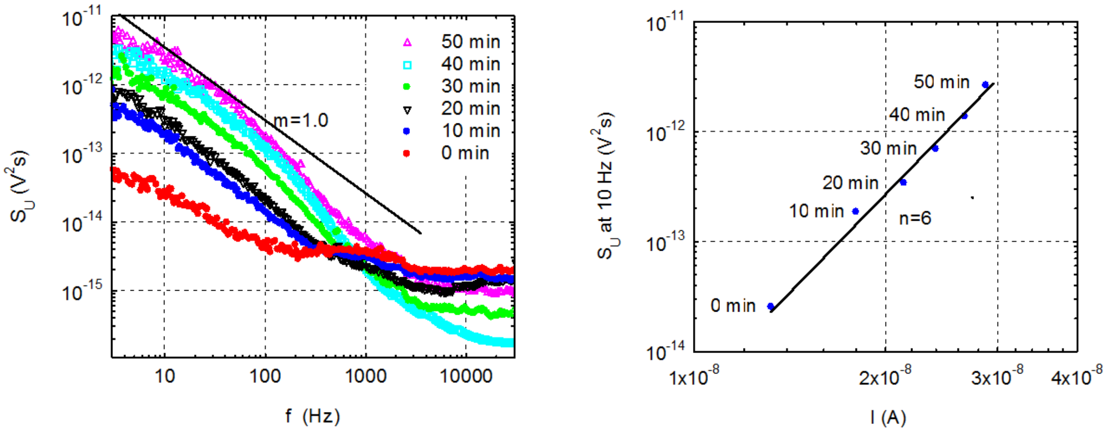

Figure 3. Noise spectral density evolution during polarization of the analyzed detector (left) and an increase of the noise spectral density with current. Applied voltage was 100 V.

indicates a lowering effect of the shot noise during the polarization. For certain frequencies, e.g. at 100 Hz ($t = 30\,\mathrm{min}$) and at 70 Hz ($t = 50\,\mathrm{min}$), we observed an increase of the slope of the $1/f^m$ spectra from $m = 1.4$ ($t = 20\,\mathrm{min}$) to $m = 2$ ($t = 50\,\mathrm{min}$). As in case of the $1/f^m = 1$ noise, the reason for this increase is a strengthened effect of the generation-recombination noise, which is typical for the trapping-detrapping process of carriers from energy states located in the band gap [13]. The nature of fluctuations is based on temporary excess of carriers during the generation process and its reduction during the recombination process. The resulting sum of the generation and recombination processes produces the Lorentzian shape of the spectrum with its typical slope of $m = 2$ [14].

Figure 3 (right) shows the dependence of the power spectral density on the leakage current during the polarization process. The increase is proportional to the power of $n = 6$ of the current. This finding is in contrast with theory, proposed by Hooge [14], which presumes an increase of the power spectral density with the square of the detector current. This disproportion can be described as follows: Hooge assumes a constant number of charge carriers in the system. This idea can be accepted in case of devices, where polarization is absent (MOSFETs devices etc). In our case, after biasing the detector, charge carriers are detrapped from deep energy levels also in the space charge region forming a screen to the applied electric field. Carriers situated “in the shadow” of space charge become inactive for the overall electric charge transport of the detector. This mechanism causes an increase of the noise spectral density not only due to the current increase, but also due to the change of total carrier number in the detector system. Of course, this idea is in contraction with the measured increase of the detector current in time, but the increase is primarily a result of the potential barrier height lowering during the polarization [15].

3 Conclusion

The analyzed sample suffers from significant current instability in time. In the observed time interval of 45 000 seconds, the detector current transient has not ended. During the investigated time interval, the electric field showed a drop of the strength at the cathode area. As a result of the space charge build-up, the noise spectral density shows a higher increase during the detector polarization than proposed by the Hooge theory.

Acknowledgments

Research described in the paper was financially supported by the European Centres of Excellence CEITEC CZ.1.05/1.1.00/02.0068, by the project Sensor, Information and Communication Systems CZ.1.05/2.1.00/03.0072, the project Nanoscience for electrical engineers CZ.1.07/2.2.00/15.0147 and with a financial contribution of SoMoPro (South Moravian Program, Czech Republic) fellowship of the European Union, within the 7th framework program (FP/2007-2013, grant agreement No. 229603). These supports are gratefully acknowledged.

References

[1] C. Szeles, *CdZnTe and CdTe materials for X-ray and γ ray radiation detector applications*, *Phys. Stat. Sol.* **241** (2004) 783.

[2] J. Franc et al., *CdTe and CdZnTe crystals for room temperature γ-ray detectors*, *Nucl. Instrum. Meth.* **A 434** (1999) 146.

[3] Y. Eisen and A. Shor, *CdTe and CdZnTe materials for room-temperature X-ray and γ ray detectors*, *J. Cryst. Growth* **184-185** (1998) 1302.

[4] J. Fink et al., *Characterization of charge collection in CdTe and CZT using the transient current technique*, *Nucl. Instrum. Meth.* **A 560** (2006) 435.

[5] H. Elhadidy et al., *Deep Level defects in CdTe materials studied by thermoelectric effect spectroscopy and photo-induced current transient spectroscopy*, *Semicond. Sci. Tech.* **22** (2007) 537.

[6] R. Grill et al., *Polarization study of defect structure of CdTe radiation detectors*, *IEEE Trans. Nucl. Sci.* **58** (2011) 3172.

[7] A. Mohammadi, M. Baba and H. Hirayama, *Simulation of the carrier trapping effect in a Schottky CdTe detector by considering non-uniform electric field*, *J. Nucl. Sci. Technol.* **46** (2009) 1032.

[8] M. Niraula et al., *Stability issues of high-energy resolution diode type CdTe nuclear radiation detector in a long-term operation*, *Nucl. Instrum. Meth.* **A 491** (2002) 168.

[9] A. Andreev et al., *Investigation of excess $1/f$ noise in CdTe single crystals*, *Semicond. Sci. Technol.* **20** (2010).

[10] K.H. Kim et al., *Passivation of semi-insulating polycrystalline CdZnTe films*, *J. Korean Phys. Soc.* **53** (2008) 317.

[11] I. Farella et al., *Study on instability phenomena in CdTe diode like detectors*, *IEEE Trans. Nucl. Sci.* **58** (2009) 1736.

[12] J. Franc et al., *Development of inclusion-free CdZnTe substrates from crystals grown by the vertical-gradient freeze method*, *J. Electron. Mater.* **32** (2003) 761.

[13] F.N. Hooge, *On the additivity of generation — recombination spectra. Part 1: conduction band with two centers*, *Physica* **B 311** (2002) 238.

[14] F.N. Hooge, *$1/f$ noise sources*, *IEEE Trans. Electron. Dev.* **41** (1994) 1926.

[15] H. Tozama et al., *Quantitative analysis of polarization in CdTe radiation detectors*, *Jpn. J. Appl. Phys.* **46** (2006) 8842.

Eur. Phys. J. Special Topics **228**, 1575–1588 (2019)

https://doi.org/10.1140/epjst/e2019-800153-0

THE EUROPEAN
PHYSICAL JOURNAL
SPECIAL TOPICS

Regular Article

Novel layered architecture based on $Al_2O_3/ZrO_2/BaTiO_3$ for SMART piezoceramic electromechanical converters

P. Tofel[1,a], Z. Machu[2], Z. Chlup[3], H. Hadraba[3], D. Drdlik[2,4], O. Sevecek[2], Z. Majer[2], V. Holcman[1], and Z. Hadas[2]

[1] Faculty of Electrical Engineering and Communication, Brno University of Technology, Technická 3058/10, 616 00 Brno, Czech Republic
[2] Faculty of Mechanical Engineering, Brno University of Technology, Technická 2896/2, 616 69 Brno, Czech Republic
[3] CEITEC IPM, Institute of Physics of Materials of the Academy of Sciences of the Czech Republic, Zizkova 513/22, 61662 Brno, Czech Republic
[4] CEITEC BUT, Brno University of Technology, Purkynova 123, 612 00 Brno, Czech Republic

Received 27 September 2018 / Received in final form 19 December 2018

Abstract. The paper is focused on a very hot topic of SMART materials and their architectures for energy conversion systems designed for conversion of mechanical to electrical energy using the piezoelectric effect. The aim of the study is to increase both the reliability and efficiency of electromechanical conversion compared to standard concepts. Our new design of piezoelectric cantilever is made with multi-layer ceramic composite, where piezoelectric layer $BaTiO_3$ is covered by protective ceramics layers of different residual stresses, where Al_2O_3 and ZrO_2 is used. Utilization of controlled residual stresses into new multi-layer architecture is the key idea and it is crucial for optimal design of the individual layers of the proposed concept. The multi-layer ceramic composite is fabricated by electrophoretic deposition, where the composite is assembled from different ceramic materials during processing and after sintering we get inseparable ceramic laminate consisting of piezoelectric and protective layers of ceramics. This approach of processing multi-layer ceramic material including lead free piezoelectric layers is innovative and has never been published before.

1 Introduction

A piezoelectric energy harvester device can be fabricated depending on the desired operational frequency and applied amplitude of displacement with a design such as unimorph [1], bimorph [2], multilayer [3], macro fibre composite layers [4], piezoelectric actuator stack [5], etc. All mentioned structures consist of piezoelectric layers and electrodes serving for poling of the piezo ceramics and physical path of the electrical output. These harvesters could provide enough energy for powering of ultralow-power

---

[a] e-mail: `tofel@feec.vutbr.cz`

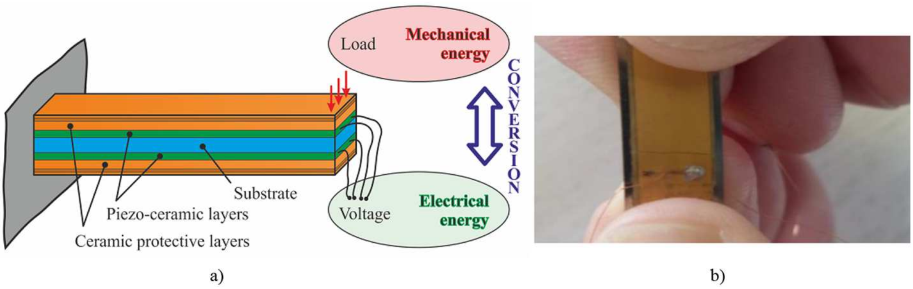

Fig. 1. (a) New concept of energy harvester with protective layers bringing pre-straining to the piezo-ceramics. (b) Observed cracking of the standard 3 layer piezo-harvester (2 piezo-layers outwards the metallic substrate).

electronics [6]. In most cases, the piezoelectric cantilevers are used as a device for energy harvesting [2,7,8]. Nevertheless, such energy harvesters have also certain limitations, such as low efficiency of the energy conversion or short lifetime because piezoelectric ceramics are brittle, constraining their mass use [9]. From mechanical protection point of view, in general, an additional protective layer is added on a piezoelectric material with effort to protect the piezoelectric material and its electrodes against mechanical impacts and scratches. A company Mide Technology has patented process for packaging piezoelectric ceramics, where an FR-4 epoxy is used as a protective layer. However, the lamination occurs after fabrication of piezoelectric ceramics, when all layers are assembled together and fixed by epoxy. Our proposed laminate is inseparable multi-layer ceramic material, which includes $BaTiO_3$, Al_2O_3 and ZrO_2.

The idea of this design follows from the enhancement of reliability and fracture resistance of inherently brittle materials, together with the possibility to precisely manufacture complicated layered ceramic composites [10–13]. The outer layer prepared from the mechanically durable material, enhanced via internal compressive stresses, can protect the inherently brittle piezo ceramics and the additional presence of internal stresses in the piezo ceramic layers can further enhance the electromechanical characteristics. By this approach the reliability of electromechanical converters based on lead-free piezo ceramic materials can be enhanced via employment of controlled and properly designed internal stresses through material selection and layer thickness management. The proposed concept is based on tailoring of the layered structure according to the obtained results from numerical simulations, where particular layers serve as both the protective and functional components of the multi-layer cantilever. However, there are many questions, such as what will be done during poling, when the piezoelectric material changes its dimension, or how to put the electrodes as close to the piezoelectric layer as possible. These issues are still being studied. The electrodes should be manufactured from a conductive material with high melting point, such us titanium. After poling of the piezoelectric layer, the piezoelectric layer is mechanically fixed in between protective layers. This pre-straining for the poled piezoelectric layer can bring higher efficiency of electromechanical conversion. This paper describes preliminary results of the proposed ceramic composite with numerical analysis of individual ceramic layers and fabrication of the ceramic composite. Our concept is illustratively shown in Figure 1a, where the outer protective layers are applied on the piezoelectric layer. These protective layers provide higher reliability of the piezo-ceramics and they also change the electromechanical properties of the functional piezo-ceramic structure. These introduce residual stresses (positive or negative) in the whole multilayer system [14,15], and is described in detail in Section 3.1. Such architecture brings new reliable SMART components for wider applications in ultralow power electronics or other future SMART applications. Ordinary concept of three-layered piezoelectric harvester device without protective layers is shown in Figure 1b. These standard concepts are very fragile and tend to be easily damaged, as is shown in Figure 1b, where a crack can be observed. The crack was made by displacement more than 2 mm applied into the free end of this cantilever.

In an effort to replace conventional lead-based piezoelectric ceramics, the barium titanate was used as a piezoelectric ceramic layer. Functional properties of lead-free piezoelectric ceramics are very sensitive to processing conditions as is already reported for BCZT [16–19], KNN [20] and BT [21–24]. From this point of view it is very important to control a grain size and density of the piezoelectric layer during processing of the composite. The protective layers consist of zirconia and alumina. Fabrication of ceramic materials $BaTiO_3$, ZrO_2 and Al_2O_3 is discussed below at Section 3.1. The laminate structure was prepared by electrophoretic deposition (EPD), which is suitable for precise preparation of laminate structures with strong interface bonding [25–27].

2 Experimental

Commercial alumina (∼470 nm, Malakoff, USA), zirconia (∼140 nm, Tosoh, Japan) and barium titanate (∼500 nm, ABCR, Germany) ceramic powders were selected as starting materials in this study. The electrophoretic deposition (EPD) was used for the preparation of standards from each ceramic as well as the layered structure. The suspensions contained 15 wt.% of powder, 12.75 wt.% of stabilizer – monochloroacetic acid (Merck, Germany) and 72.25 wt.% of 2-propanol. Alumina or zirconia suspensions were stirred in an ultrasonic bath for 30 min. Temperature of the bath was 23 °C. Barium titanate suspension was milled in a planetary mill with zirconia balls for 60 min. The balls to powder weight milling ratio was 10:1. The mean particle size of starting powders and powders dispersed in the suspensions after preparation was measured via laser diffraction using the LA950 analyzer (Horiba, Japan).

During the EPD, the stainless steel electrodes with polished surfaces were placed 26 mm apart in a vertical position and a current density of $0.27\,\mathrm{mA/cm^2}$ was carried out. The depositions of all standards lasted for 60 min. Each deposition was stopped in 5 min intervals for the mechanical stirring of the suspension to eliminate particle sedimentation. The laminate structure was fabricated by moving of a deposition electrode from one suspension to another one. The deposition times of layers varied and they depended on the kinetic study of individual materials [28]. The prepared ceramics were dried for at least 24 h in a desiccator. After that, they were removed from electrodes and annealed at 800 °C for 1 h in air to burn out the organic additives. The standards were sintered at 1300 °C for 0, 30 and 60 min in air. The ceramic laminate was sintered at 1300 °C without a dwell in the air. The sintering behaviour of the materials was determined using a contact high-temperature dilatometer (Linseis, Germany). The samples were heated at a heating rate of 5 °C/min to 1500 °C with 2 h dwell time. The density of the ceramic bodies was measured using the Archimedes method (EN 623-2). The density was measured 3 times on each sample. The microstructure was observed using the scanning electron microscope (SEM) (Lyra 3 XMU, Tescan, Czech Republic). The mean grain size was determined using linear intercept method on at least 3 images for each sample with following multiplication by a shape correction factor of 1.56. Piezoelectric properties were evaluated using the aixPES (aixACCT Systems, Germany). The piezoelectric coefficient was measured by the indirect method, where a voltage is applied on a piezoelectric sample and the thickness dimension change of the sample is measured. The d_{33}^* was evaluated in the area of zero bias voltage from the piezoelectric loop for all piezoelectric samples. The average values and standard deviations of d_{33}^* were established from measurements made on 3 samples.

3 Computational model of the energy harvester

Candidates for optimal architecture design have to contain suitably distributed internal residual stresses in particular layers (at least one compressive layer outside the piezo layer) and must not exhibit excessive deformations after the processing. In addition, the whole system should provide higher resistance to the mechanical failure than standardly used concepts. The stress and strain distribution is calculated both analytically and numerically for various material combinations, layer stacking and layer thicknesses of the multilayer composite. Analytical calculations are employed for fast optimization of the design parameters. Numerical, piezoelectric model solved by a finite element method (FE), prepared in the ANSYS environment [29,30], was done for optimization of the dynamic response of the selected architecture, for estimation of the effects of pre-strained layers on the natural frequencies and for simulations of the electromechanical behaviour of the studied structure. It is necessary to note that energy harvesting devices and semi-active damping systems are complex multi-domain systems requiring advanced methodologies to maximise their performance [31].

3.1 Structure of the proposed model

The considered structure of a composite laminate beam can be seen in Figure 2. The proposed model contains seven ceramic layers in total. The system is designed as symmetric to avoid any distortions during fabrication as well as harmonic oscillation of the harvester. There are two piezoelectric layers on each side of the base material and outside these layers, two protective layers follow. On both sides of the piezoelectric layers, the conductive electrodes are present and are used both for poling of the piezoceramics and for the subsequent collection of the electric charge.

The proposed laminate beam with dimensions $60 \times 10 \times 1.5\,\mathrm{mm}$ is clamped on one side and is kinematically excited by a harmonic displacement amplitude. At the free end of the cantilever beam an extra tip mass is added (usually in order to lower eigen-frequency of the energy harvester and to increase vibrational amplitudes of the free end) – as shown in Figure 3, where a typical piezoelectric bimorph cantilever is shown, which was fabricated for wearable applications [2].

In order to find an optimal design of the cantilever energy harvester, its analytical model, enabling fast exploration of a large number of potential material, geometric and composite configurations have to be developed. The analytical model is able to calculate a natural frequency of the system as well as the generated electric power upon the steady-state or transient vibrations in the vicinity of the natural frequency. The developed model is used for an optimization of the multilayer energy harvester from both the electrical and the fracture-mechanics point of view where the influence of various levels of residual stresses in particular layers on the resistance to surface crack propagation are analyzed.

3.2 Analytical model

3.2.1 Calculation of residual stresses

Due to the manufacturing process of the ceramic laminate, significant residual stresses are originated inside particular layers and have to be taken into account in the harvester design. The in-plane residual stresses within ideal boundless symmetric laminate (containing elastic materials) can be calculated using explicit formulae from the classical laminate theory published e.g. in [13]. Distribution of stresses in individual

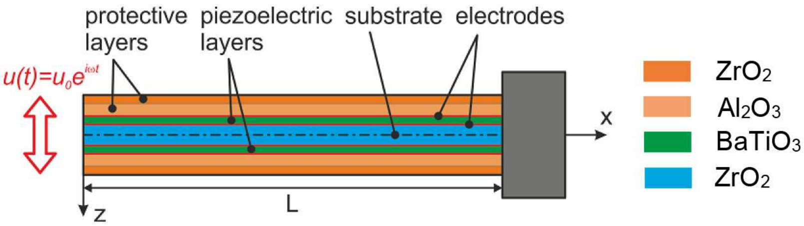

Fig. 2. Considered model of the multilayer vibrational energy harvester with a tip mass containing 2 piezo layers, totally 5 Al_2O_3/ZrO_2 layers and 4 electrodes.

Fig. 3. Example of the real energy harvester with a tip mass.

layers (due to the various coefficients of thermal expansion – CTE) can be determined analytically. Inside each layer (far enough from free edges), a homogeneous and biaxial residual stress state exists. The stress magnitude $\sigma_{res,i}$ can be calculated as follows:

$$\sigma_{res,i} = \frac{E_i}{1-\nu_i}\left(\bar{\alpha}-\alpha_i\right)\Delta T = \frac{E_i}{1-\nu_i}\Delta\varepsilon_i, \quad \text{where} \quad \bar{\alpha} = \sum_{i=1}^{N}\frac{E_i\cdot\alpha_i\cdot t_i}{1-\nu_i}\Bigg/\sum_{i=1}^{N}\frac{E_i\cdot t_i}{1-\nu_i}. \tag{1}$$

In (1) E_i, ν_i and α_i are the Young's modulus, Poisson ratio and CTE of the ith layer respectively $(\bar{\alpha}-\alpha_i)\,\Delta T$, resp. $\Delta\varepsilon_i$ is the mismatch strain of the ith layer. ΔT is the temperature difference and can be calculated as $T_0 - T_{ref}$. T_0 represents the room temperature and T_{ref} refers to a temperature at which the laminate is considered to be stress-free (reference temperature). The coefficient $\bar{\alpha}$ represents an averaged expansion coefficient of the whole laminate, t_i is the thickness of the ith layer and N is the number of layers.

3.2.2 Fracture resistance of the laminated structure

Vibrations and the associated deformation of piezo-ceramics often cause an initiation of unstable crack propagation through the piezo layer (see e.g. Fig. 1b) and practically immediately result in a malfunction of the system. Fracture resistance of particular ceramic components in the proposed ceramic based energy harvester is relatively low, nevertheless, by their combination in a multilayer structure (containing tensile/compressive residual stresses), a significant increase of the apparent fracture toughness can be achieved – see e.g. [13]. The aim is thus to find an optimal design (number and thickness of individual, ceramic-based, protective and active piezoelectric layers) of the energy harvester with respect to highest possible resistance to propagation of surface cracks through the rest of the structure and simultaneously induce the lowest possible tensile stresses within the piezo-layer.

The apparent fracture toughness K_{eff} can be determined analytically, assuming a basic rule that the crack can propagate if the stress intensity factor at the crack tip K_{tip} is equal to or greater than the intrinsic fracture toughness K_0

$$K_{tip} = K_{appl} + K_{res} \geq K_0. \tag{2}$$

By expressing applied stress intensity K_{appl}, we then obtain an effective (apparent) fracture toughness value K_{eff}:

$$K_{appl} \geq K_0 - K_{res} = K_{eff}. \tag{3}$$

For the calculation of the apparent fracture toughness K_{eff}, it is necessary to determine the term K_{res}. It can be computed e.g. by means of the weight function approach [32] or numerically using FEA. The weight function procedure developed in [33] simplifies the determination of the stress intensity factor K. This method is also applicable for the calculation of residual stresses in multilayer composites [34]. Adopting this concept, K_{res} can be determined as follows:

$$K_{res} = \int\limits_0^a h(x,a)\,\sigma_{res}(x)\,dx, \tag{4}$$

where $h(x,a)$ is the appropriate weight function, a is the crack length and x is the distance from the surface. For non-homogeneous material, the functionality of this approach was verified by Fett [35].

3.2.3 Dynamical and electrical analysis of the energy harvester

To optimize the energy harvester also from the electro-mechanical point of view, an analytical model of the vibrating multilayer beam with a tip mass containing piezo layers was developed and is briefly described in this section. Following assumptions were made to derive the governing equations of the analytical model:

- Euler-Bernoulli beam theory is used.
- Used layer combination is symmetric.
- No axial loads are present.
- Linear energy conversion is assumed (the frequency of the generated electrical current is proportional to the kinematic excitation forcing frequency ω).
- Electric field intensity can change linearly with z-coordinate in each layer and electric field intensity together with electric flux density has only its z-component, other components are being zero.
- Each piezoelectric layer has its own connected resistor of value R.
- All piezoelectric layers have the same poling direction.

Using Hamilton's principle and by consideration of the stiffness part of Rayleigh's damping we obtain a differential equation of motion (5) with its essential and natural boundary conditions:

$$J_y^* \frac{\partial^4 w}{\partial x^4} + \frac{2b_r}{\Omega_0} J_y^* \frac{\partial^5 w}{\partial x^4 \partial t} + m^* \frac{\partial^2 w}{\partial t^2} = 0, \tag{5}$$

where Ω_0 represents the first undamped natural frequency and br is a damping ratio. The general solution of equation (5) is:

$$w(x) = C_1 \cosh(\beta x) + C_2 \sinh(\beta x) + C_3 \cos(\beta x) + C_4 \sin(\beta x),$$
$$\text{where} \quad \beta = f(\omega) = \sqrt[4]{\frac{m^* \omega^2}{J_y^* \left(1 + i \frac{2br}{\Omega_0} \omega\right)}}. \tag{6}$$

3.3 FE numerical model

To verify the outputs of the analytical model, a numerical (FE) analysis of the laminate composite was simultaneously performed (using the commercial FE system ANSYS). The created FE model contains around 1000 3D quadratic brick elements of three types. SOLID186 is used for all composite layers except piezo layers, which are meshed using the SOLID226 elements. CIRCU94 elements are used to simulate a resistor connected to piezo layers. The boundary conditions (BCs) in the case of modal analysis were prescribed at the fixed end of the beam (as zero displacements in all directions) and in the case of harmonic analysis, the displacement BC at the fixed end in the z-direction was prescribed as an amplitude of time-harmonic displacement (see also Fig. 2 in Sect. 3.1).

3.3.1 Fracture mechanics optimization of the cantilever energy harvester

First, the magnitudes of residual stresses in individual layers of the multilayer structure are calculated using equation (1). Subsequently, the apparent fracture toughness for such configuration was calculated by means of the weight function method – equations (2)–(4). The representative result for selected "optimal" configuration is plotted in Figure 4a. One can see relatively high compressive residual stresses in the second and sixth layer which are used to arrest the potentially originated crack at the free surface and will not allow its further propagation into the piezo layer. This fact can also be demonstrated by Figure 4b where a significant increase of the apparent fracture toughness in the second outer layer is observed.

In Figure 4b, it is necessary to draw attention to a discrepancy between analytical and numerical calculations, especially in the second and third layer. These are caused mainly by the fact that the weight functions do not consider different Young's moduli of adjacent layers and are primarily intended for materials with similar stiffness (in our case Al_2O_3 layer has Young's modulus of 280 GPa and $BaTiO_3$ layer 70 GPa, measured by the indentation technique on prepared samples with given density). Nevertheless, for the qualitative assessment of different laminate designs, the weight function method is also useful since it is fast and a large number of material designs can be assessed in a short time. The FE solution is then used just to refine the results of selected configurations. Based upon the obtained results one can briefly conclude that for the high apparent fracture toughness of the second layer high magnitudes of compressive stresses are essential.

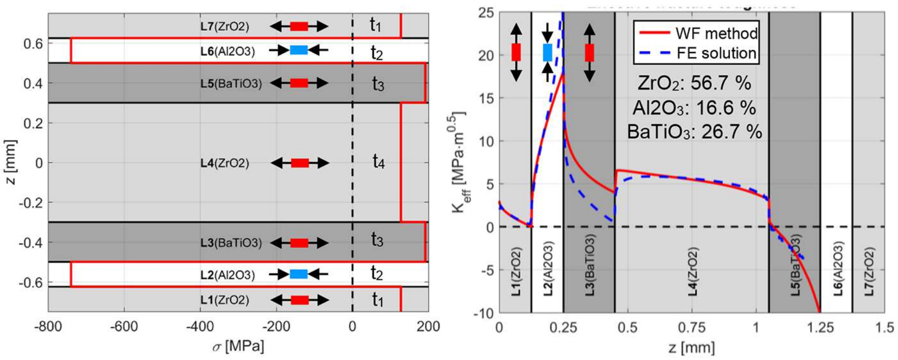

a) b)

Fig. 4. (a) Residual stresses in particular laminate layers calculated for (optimized layer setup with the highest fracture resistance). (b) Effective fracture toughness of the designed laminate for various crack lengths (from left side) – solid curve denotes the results calculated using the weight function method, dotted curve denotes the FE solution of K_{eff}.

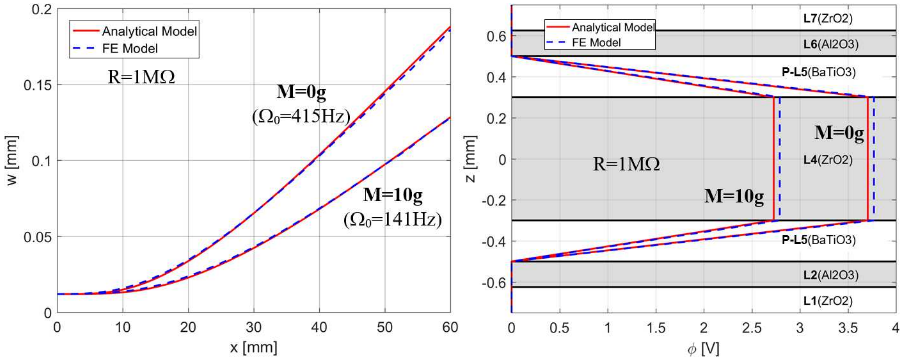

a) b)

Fig. 5. (a) Displacement calculated at eigenfrequency Ω_0 along the beam's centerline for various tip mass. (b) Electric potential values of the designed laminate for various tip mass. Both plots were obtained for the resistance of the electrical load R = 1MΩ.

3.3.2 Electro-mechanical response of the harvester

The transverse displacement amplitude w of the beam's centerline along the beam length for different tip mass is determined using the differential equation (6) and is depicted in Figure 5a. The smaller deflections in case of the added mass at the free beam end are caused by a lower acceleration amplitude of the clamped end which is given by the 1st natural frequency of the corresponding configuration. By adding the tip mass, the 1st natural frequency of the system decreases. The acceleration amplitude is then governed by relation $a = u_0\omega^2$ (note that the value of u_0 remains the same for all studied configurations and $\omega = \Omega_0$ in our case).

The voltage output for the same configuration as in Figure 5a and previous Figure 4 is shown in Figure 5b. The voltage output tends to increase with resistive load, which agrees with the basic principles of the electrical theory. Due to the same poling direction of both piezoelectric layers and the same distance from the beam centerline, the voltage generated in both piezoelectric layers has the same value but an opposite sign. The lower values of generated voltage in case of the beam with an added mass are caused by a smaller deflection of the beam's free end. The smaller deflection is caused by the lower natural frequency and thus lower applied acceleration in the z-direction on the beam's fixed end during the simulation.

Based upon the theory presented in Section 3.1, an optimal design of the cantilever piezoelectric energy harvester can be found – from both the mechanical and electrical point of view. Such (or very similar) configurations will be subsequently fabricated and subjected to experimental testing.

4 Results and discussions

4.1 Fabrication and characterization of the individual ceramic components

The systematic study of the selected materials had to be done before their integration into a layered structure. It is well-known fact that the particle size must be selected carefully to achieve an appropriate density of the green body after EPD [36]. The particle size distribution of the starting powders is given in Figure 6a. From Figure 6a there is an obvious discrepancy between mean particle sizes provided by producers and measured values. All powders were strongly agglomerated. Alumina powder had a trimodal particle size distribution with maxima at 0.3, 1.0 and 24.3 μm. Zirconia powder had a bimodal particle size distribution with maxima at 0.8 and 23.8 μm. Barium titanate powder has unimodal distribution with maxim at 12.0 μm. Therefore the powders had to be consequently processed using ultrasound or milling for disruption of aggregates because such particle size is inappropriate for successful EPD [36]. Moreover, the deposition of smaller particles minimizes cracking of deposit [37]. The particle size distribution after additional powder processing is shown in Figure 6b. Alumina and barium titanate powders had unimodal particle size distribution with maxima at 0.32 and 0.9 μm, respectively. The bimodal particle size distribution preserved in zirconia powder but with lower maxims at 0.08 and 2.2 μm.

The preparation of EPD standards of all materials allowed to construct kinetics curves of electrophoretic deposition which are necessary for deposition time prediction for individual layers of the laminated structure. It was found that the highest deposition yields during were obtained from the suspension containing alumina powder contrary to nearly identical yields provided by both zirconia and barium titanate suspensions. This result is consistent with particle distribution measurement in Figure 6b. Alumina suspension had a high volume of small particles, i.e. particles with the high surface area. Alumina green body had a relative density of 59.7% whereas zirconia and barium titanate green bodies had a relative density of 47.4 and 47.5%, respectively.

The good understanding of sintering behaviour of individual materials is a key factor for the successful fabrication of a ceramic laminate. The sintering shrinkage curves for all materials are shown in Figure 7. It can be seen that sintering shrinkage of alumina ceramics (18.4%) is smaller than that of the zirconia (23.0%) and barium titanate (20.2%). The reason can be the aforementioned higher green density of the alumina. It should be also noted that the barium titanate starts to shrink at a lower temperature than alumina and zirconia. This difference could be a critical issue for fabrication of such structured laminate because a delamination of layers may occur during heating on the sintering temperature. On the other hand, this situation can be favourable for internal stresses evolution which takes place during cooling [38]. The cooling stage of the sintering process provides the CTE values further implemented into the modelling of the layered system. The resulting internal stresses occurring in the individual layers of the laminated structure are affected also by co-sintering effects.

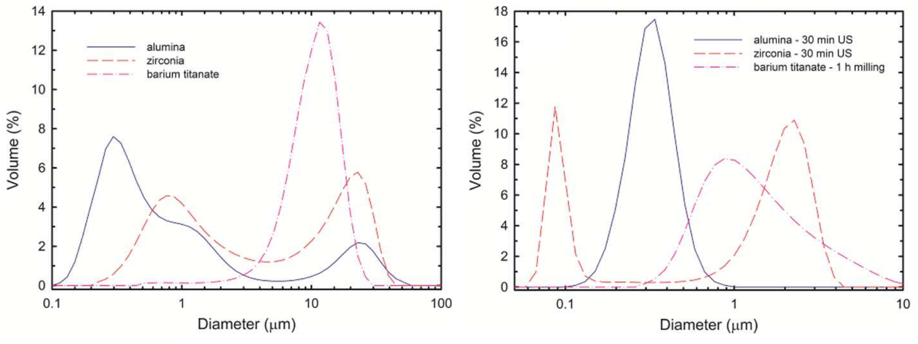

a) b)

Fig. 6. Particle size distribution (a) as received and (b) processed ceramic powders.

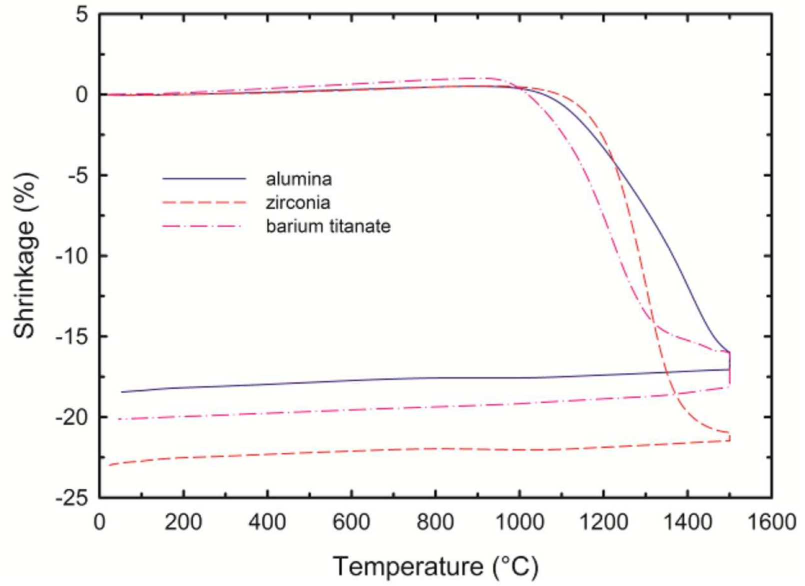

Fig. 7. Sintering shrinkage of alumina, zirconia and barium titanate ceramics prepared by EPD.

The deep study of alumina/zirconia laminates, as well as determination of their basic properties, were published before [10,28,39]. From this point of view, we investigated the barium titanate only as a main part of the laminate. The summary of relative densities and d_{33}* of barium titanate ceramics sintered at various conditions are listed in Table 1. From the presented values it is evident that the relative density increased with the dwell time on the sintering temperature and nearly full dense barium titanate ceramics was prepared at a dwell of 60 minutes. It is very well known that the piezoelectric properties of barium titanate are strongly affected by their mean grain size and density [23,40]. The mean grain size measurement showed significant increase with sintering dwell time as a consequence of grain growth [41]. The lowest mean grain size of 1.8 µm was measured for sample without dwell time on the sintering temperature. This value was close to the most published grain size (1 µm) which is consider as favourable for obtaining of the highest d_{33} values [22–24].

Table 1. Summary of relative density, mean grain size and d_{33}* of differently the sintered barium titanate.

Material	Sintering/dwell time (°C/min)	Relative density (%)	Mean grain size (μm)	d_{33}* (pC/N)
$BaTiO_3$	1300/0	78.5 ± 0.2	1.8 ± 0.2	364 ± 21
	1300/30	90.0 ± 0.1	11.1 ± 5.2	218 ± 10
	1300/60	94.6 ± 0.1	27.6 ± 11.4	200 ± 8

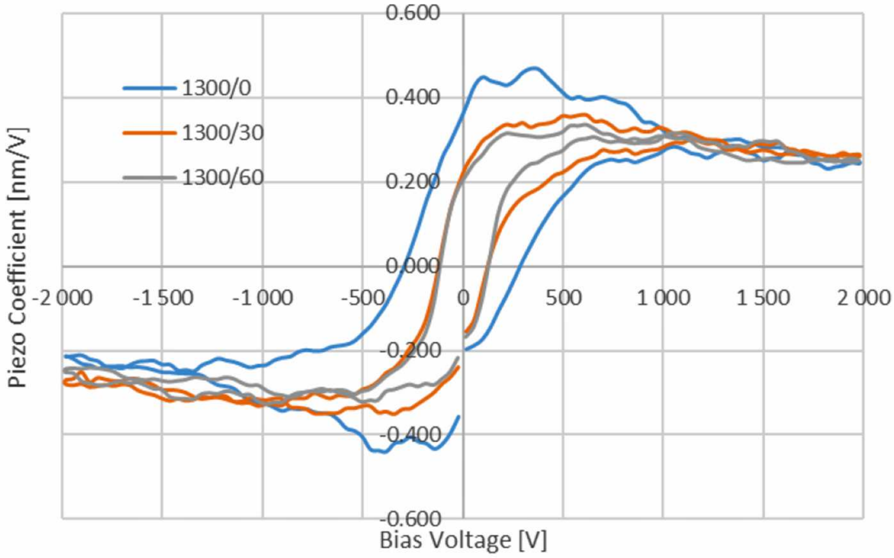

Fig. 8. Piezoelectric loops generated for samples $BaTiO_3$.

The more dense samples had substantially bigger grains and abnormal grain growth was observed.

In regard to the previous results the piezoelectric coefficient d_{33}* evaluated for all samples decreased with the dwell time on the sintering temperature. The highest value of 364 pm/V reached the sample sintered without the dwell time. The value of d_{33}* was measured on unpoled samples with bias voltage up to 2 kV, together with small signal amplitude of 50 V and frequency 1 kHz. Then a piezoelectric loop is generated as is shown in Figure 8, where the d_{33}* was evaluated in the area of zero bias voltage. From that point of view, it should be noted, that this value of d_{33}* is comparable with value of d_{33} measured by direct method. Based on this result, the laminate was sintered under the same conditions.

4.2 Fabrication of the laminate and proof of the concept

The electrophoretic deposition technique has demonstrated the ability to prepare layered architecture according to the theoretically designed model. An example of manufactured seven layers symmetrical non-periodic ceramic laminate containing alumina, barium titanate and zirconia layers is shown in Figure 9. The strong and sharp interface formation between barium titanate and zirconia was observed. On the other hand, the interface between alumina and barium titanate exhibits development of some form of the transitional reaction zone. The size of this transition zone

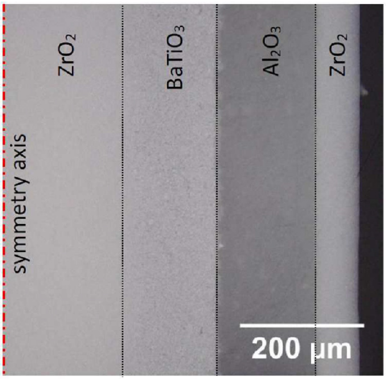

Fig. 9. An example of alumina, zirconia and barium titanate symmetric seven layers ceramic laminate prepared by EPD.

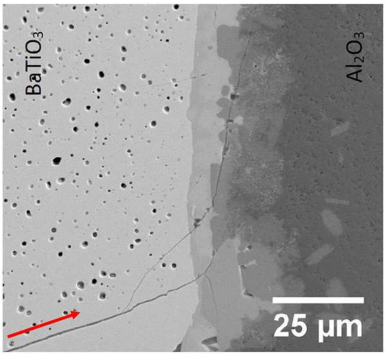

Fig. 10. SEM detailed view of barium titanate – alumina interface in the backscattered electrons signal (red arrow shows the crack propagation direction from the corner of the Vickers indent).

is strongly dependent on the sintering conditions. The formation of this zone is not fully understood yet and will be subject to further detailed investigation. The crack behaviour observed at the alumina – barium titanate interface (an example shown in Fig. 10) suggest that the formation of the described transitional zone has no strong effect on the quality of the interface from the development of residual stresses point of view. The crack is shown in Figure 10 propagates from the barium titanate layer to the alumina layer where tends to bifurcate and/or deflect the crack path to the layer interface. Finally, the crack is stopped as a consequence of the presence of compressive stresses in the alumina layer. This is exactly the crack behaviour predicted by numerical simulations (see for example Fig. 5b) used for the design of layered architecture.

5 Conclusions

A novel layered architecture based on $Al_2O_3/ZrO_2/BaTiO_3$ for SMART piezoceramic electromechanical converters was introduced in this study. For the optimization purposes an analytical model of the vibrating multilayer piezoelectric energy harvester containing significant residual stresses in particular layers has been developed. Using this model, natural frequencies of the system as well as the generated electric voltage upon steady state or transient vibrations and corresponding mechanical stresses within particular layers can be calculated. To optimize fracture mechanics resistance of the harvester a model based on the weight functions technique and calculating apparent fracture toughness of the laminate was also prepared. Functionality of both models has been verified in parallel using numerical FE solutions. A design exhibiting high resistance to origination and extension of surface cracks (thanks to high compressive residual stresses in the outer layers) has been found and subjected to an electromechanical analysis upon vibrations at natural frequency considering various added masses at the end of the cantilever. Ceramic laminate proposed based upon outputs of the mentioned models is composed of seven layers symmetrically distributed over the laminate height and having various thicknesses (related to the predetermined internal stresses for each layer). The fabrication process of individual components of the ceramic laminate was described and the ability of the electrophoretic deposition technique serves as a robust processing method was proven. The determination of basic physical and electrical properties was conducted and both shows promising results even though further enhancement is needed. Based on the results of the analytical and numerical models, the first version of the SMART piezoceramic electromechanical converter was prepared as a proof of concept. Creation of this architecture is aimed at a new perspective and reliable SMART materials for wider applications in ultralow power electronics or other future SMART applications, where the reliable lead-free piezoelectric devices are required. Our new concept of the multilayer piezoelectric laminate system increases the durability of the piezoelectric layer and thereby the reliability of such a piezoelectric device is enhanced.

This work has been supported through a grant number 17-08153S of the Czech Science Foundation. The research has also been financially supported by the Ministry of Education, Youth and Sports of the Czech Republic under the project CEITEC 2020 (LQ1601).

References

1. J.W. Yi, W.Y. Shih, W.-H. Shih, J. Appl. Phys. **91**, 1680 (2002)
2. Y. Bai, P. Tofel, Z. Hadas et al., Mech. Syst. Signal Process. **106**, 303 (2018)
3. H.-C. Song, H.-C. Kim, C.-Y. Kang et al., J. Electroceram. **23**, 301 (2009)
4. K. Tungpimolrut, N. Hatti, J. Phontip et al., in *2011 International Symposium on Applications of Ferroelectrics (ISAF/PFM) and 2011 International Symposium on Piezoresponse Force Microscopy and Nanoscale Phenomena in Polar Materials* (IEEE, 2011), p. 1
5. Y. Wang, W. Chen, P. Guzman, J. Intell. Mater. Syst. Struct. **27**, 2324 (2016)
6. M. Zielinski, F. Mieyeville, D. Navarro, O. Bareille, in *Federated Conference on Computer Science and Information Systems, 2014*, (IEEE, 2014), p. 1065
7. Y. Bai, Z. Havránek, P. Tofel et al., Eur. Phys. J. Special Topics **224**, 2675 (2015)
8. O. Rubes, M. Brablc, Z. Hadas, Mech. Syst. Signal Process. **125**, 170 (2019)
9. T.-Y. Zhang, M. Zhao, P. Tong, Adv. Appl. Mech. **38**, 147 (2002)
10. H. Hadraba, D. Drdlik, Z. Chlup et al., J. Eur. Ceram. Soc. **32**, 2053 (2012)
11. H. Hadraba, Z. Chlup, D. Drdlik, J. Cihlar, J. Eur. Ceram. Soc. **36**, 365 (2016)
12. Z. Chlup, H. Hadraba, L. Slabáková et al., J. Eur. Ceram. Soc. **32**, 2057 (2012)
13. L. Sestakova, R. Bermejo, Z. Chlup, R. Danzer, Int. J. Mater. Res. **102**, 613 (2011)
14. P. Parente, Y. Ortega, B. Savoini et al., Acta. Mater. **58**, 3014 (2010)
15. M. Mehrali, H. Wakily, I.H.S.C. Metselaar, Adv. Appl. Ceram. **110**, 35 (2011)
16. K. Castkova, K. Maca, J. Cihlar et al., J. Am. Ceram. Soc. **98**, 2373 (2015)
17. Y. Jiang, T. Thongchai, Y. Bai et al., in *IEEE International Ultrasonics Symposium, IUS* (2014)

18. Y. Bai, A. Matousek, P. Tofel et al., J. Eur. Ceram. Soc. **35**, 3445 (2015)
19. V. Bijalwan, P. Tofel, V. Holcman, J. Asian. Ceram. Soc. **6**, 384 (2018)
20. Y. Bai, P. Tofel, J. Palosaari et al., Adv. Mater. **29**, 1700767 (2017)
21. Y. Huan, X. Wang, J. Fang, L. Li, J. Am. Ceram. Soc. **96**, 3369 (2013)
22. Y. Huan, X. Wang, J. Fang, L. Li, J. Eur. Ceram. Soc. **34**, 1445 (2014)
23. J.C. Wang, P. Zheng, R.Q. Yin et al., Ceram. Int. **41**, 14165 (2015)
24. Y. Wu, J. Zhang, Y. Tan, P. Zheng, Ceram. Int. **42**, 9815 (2016)
25. L. Cheng, M. Sun, F. Ye et al., Int. J. Light. Mater. Manuf. **1**, 126 (2018)
26. K. Maca, H. Hadraba, J. Cihlar, Ceram. Int. **30**, 843 (2004)
27. H. Hadraba, K. Maca, J. Cihlar, Ceram. Int. **30**, 853 (2004)
28. H. Hadraba, D. Drdlik, Z. Chlup et al., J. Eur. Ceram. Soc. **33**, 2305 (2013)
29. D. Benasciutti, L. Moro, S. Zelenika, E. Brusa, Microsyst. Technol. **16**, 657 (2010)
30. Z. Hadas, L. Janak, J. Smilek, Mech. Syst. Signal. Process. **110**, 152 (2018)
31. C.R. Bowen, H.A. Kim, P.M. Weaver, S. Dunn, Energy Environ. Sci. **7**, 25 (2014)
32. T. Fett, D. Munz, *Stress intensity factors and weight functions* (Computational Mechanics Publications, Southampton, UK, Boston, MA, USA, 1997)
33. H.F. Bueckner, *Novel Principle for the Computation of Stress Intensity Factors* (Akademie-Verlag GmbH, Berlin, 1970)
34. M. Lugovy, V. Slyunyayev, N. Orlovskaya et al., Acta. Mater. **53**, 289 (2005)
35. T. Fett, D. Munz, Y.Y. Yang, Eng. Fract. Mech. **65**, 393 (2000)
36. L. Besra, M. Liu, Prog. Mater. Sci. **52**, 1 (2007)
37. N. Sato, M. Kawachi, K. Noto et al., Physica C **357**, 1019 (2001)
38. P.Z. Cai, D.J. Green, G.L. Messing, J. Am. Ceram. Soc. **80**, 1929 (2005)
39. K. Maca, V. Pouchly, D. Drdlik et al., J. Eur. Ceram. Soc. **37**, 4287 (2017)
40. L.-F. Zhu, B.-P. Zhang, J.-Q. Duan et al., J. Eur. Ceram. Soc. **38**, 3463 (2018)
41. S.J.L. Kang, *Sintering: Densification, Grain Growth and Microstructure* (Elsevier Science, 2004)

JOURNAL OF ASIAN CERAMIC SOCIETIES
2018, VOL. 6, NO. 4, 384–393
https://doi.org/10.1080/21870764.2018.1539211

FULL LENGTH ARTICLE

OPEN ACCESS

Grain size dependence of the microstructures and functional properties of $(Ba_{0.85}\ Ca_{0.15-x}\ Ce_x)\ (Zr_{0.1}\ Ti_{0.9})\ O_3$ lead-free piezoelectric ceramics

Vijay Bijalwan [a], Pavel Tofel [a,b] and Vladimir Holcman [b]

[a]Advanced Materials, CEITEC—Central European Institute of Technology, Brno, Czech Republic; [b]Department of Physics, Brno University of Technology, Brno, Czech Republic

ABSTRACT

By the solid-state reaction route, $(Ba_{0.85}Ca_{0.15-x}\ Ce_x)\ (Zr_{0.1}Ti_{0.9})\ O_3$ (BCCeZT) lead-free piezoelectric ceramics were prepared. The powder was processed at 1250 °C for 2 h, and compacted green bodies were then sintered at various sintering temperatures. X-ray diffraction analysis and Raman spectra confirmed the rhombohedral-tetragonal phase coexistence of $x = 0–0.00131$. Addition of CeO_2 facilitated development of grain sizes greater than 10 µm at low sintering temperatures. The effects of grain size on the ferroelectric and piezoelectric properties were studied systematically and it was found that a ~ (10–12) µm grain size is critical for the processing of high-performance lead-free BCCeZT ceramics. CeO_2 substitution at the A site may bring down the sintering temperature by about 200 °C without significant loss of properties. The best properties were obtained for $x = 0.00131$ at a low sintering temperature of 1350°C for 4 h exhibiting $d_{33} = 501 \pm 10$ pC/N, $k_p = 38.5 \pm 1.92$ %, $P_r = 12.19$ µC/cm^2, $T_C = 108.1$°C, and a large strain of 0.14%. These results show that BCCeZT ceramics could be promising candidates for the fabrication of lead-free devices.

ARTICLE HISTORY
Received 13 July 2018
Accepted 7 October 2018

KEYWORDS
Lead-free ceramics; sintering; grain size; piezoelectric properties; micro- structure

1. Introduction

For many years, lead-derived piezoelectric materials such as lead zirconate titanate (PZT) have been used for various applications including sensors, fuel injectors, actuators, and transducers due to their excellent piezoelectric properties [1]. Lead-based piezo ceramics contains as much as 60% lead in their composition, which is a major concern due to the toxicity of lead in the environment. The demand for the replacement of these ceramics has emerged as a result, and now research is focused on the development of new lead-free efficient ceramic systems whose properties are comparable to PZT [2–7]. In 2009, Lui and Ren reported a new lead-free ceramic system $(Ba_{0.2}\ Zr_{0.8})\ TiO_3–x(Ba_{0.7}\ Ca_{0.3})TiO_3$ (BZT)–x(BCT), are commonly referred to as BCZT that represents excellent piezoelectric properties at $x = 0.5$ [8] that are mainly comparable to those of their lead-based counterparts. This ceramic system has similar morphotropic phase boundaries (MPB) to PZT except for its strong dependence on temperature and stoichiometry. Since its development has been conducted to study its structure and its effect on the functional properties [5,9,10] of lead-free ceramics (including BCZT). The piezoelectric and dielectric properties mainly depend on the grain sizes, and it is commonly believed that their functional properties could be enhanced with proper grain sizes [11–16]. A significant research is being done on lead-free ceramics in which dependence on grain size of their physical and functional properties has been reported. For instance, the grain size effect on the ferroelectric properties and electrostrictive coefficients of Fe^{3+} doped 0.5BCT–0.5BZT ceramics was studied [17]. Long and Yi recently showed that if the grain size is between 8 and 15 µm, higher d_{33} (= 560 pC/N) could be achieved for $(Ba_{0.85}Ca_{0.15})\ (Zr_{0.1}T_{i0.9})O_3$ ceramics [18]. For potassium sodium niobate (K,Na)NbO3-based materials, the particle size effect on their functional properties has been studied recently [19]. So far, a superior d_{33} (~ 570 pC/N) value has been reported recently for a KNN-based material, which they ascribed to the nanoscale domains and high density of ferroelectric domain boundaries [20].

CeO_2 is a dopant/additive commonly used in the past for lead-based compositions to enhance the piezoelectric and dielectric properties [21–23]. Recently, CeO_2 has been used as an additive in lead-free compositions such as $BaTiO_3–CeO_2$ [24], KNN–CeO_2 [25], BNBT–CeO_2 [26], BNKT–CeO_2 [27], and BNKLT–CeO_2 [28] to obtain better piezoelectric properties and densities. Cui et al. [29] used CeO_2 as an additive with BCZT lead-free systems mainly to reduce the sintering temperature while maintaining a very high piezoelectric constant of $d_{33} = 600$ pC/N. There are no reports available regarding temperature and grain size dependence on its functional properties when CeO_2 is used as an A-site substituent in the ABO_3 structure of BCZT perovskite materials.

CONTACT Vijay Bijalwan vijay.bijalwan@ceitec.vutbr.cz CEITEC—Central European Institute of Technology, Purkyňova 123, 61200 Brno, Czech Republic

Therefore, we used CeO_2 (in × mol.) in the A site in the composition $(Ba_{0.85}Ca_{0.15-x}\ Ce_x)\ (Zr_{0.1}T_{i0.9})\ O_3$ in order to study its crystal structure, its microstructure and the effect on its functional properties, including its ferroelectric properties which were lacking in the previous report [29]. A comprehensive study has been done on temperature and grain size dependence of the piezoelectric and ferroelectric properties. It was discovered that CeO_2 addition may reduce the sintering temperature of BCZT ceramics while maintaining significantly high piezoelectric properties.

2. Experimental

$(Ba_{0.85}Ca_{0.15-x}\ Ce_x)\ (Zr_{0.1}T_{i0.9})\ O_3$ where x(moles) = 0, 0.0008, 0.00131, 0.02 were fabricated according to the stoichiometric formula by the solid-state reaction method. The initial powder for each batch was prepared as 200 g. $BaCO_3$ (Dakram, UK, 99.9%), $CaCO_3$ (Lachner, CZ, 99.9%), ZrO_2 (Dakram, UK, 99.9%), TiO_2 (Dakram, UK, 99.9%) and CeO_2 (Sigma Aldrich, UK, 99.9%) were used as raw materials. Before milling, the powders were first dried at 220 °C/1h in the laboratory oven (Lenton MMD/0229, UK) and then weighed stoichiometrically. Mixing of the powder was performed in a horizontal ball mill with deionized water for 24 h. The ratio of powder to zirconia milling media to water was 2:1:1. The resulting slurry was dried in an oven at 90°C for 15 h and sieved (300 microns, VWR, UK), after which it was calcined at 1250 °C for 2 h in a zirconia crucible using a muffle furnace (Lenton, 5696, UK). After calcination, the calcined powders were re-milled for 24 h to reduce the particle size and avoid agglomeration. During the last hour of milling, ~ 5 wt.% of each binder, Duramax B1000 (Product No. 74,821, Chesham Chemicals Ltd., UK), and B1007 (Product No. 74,823, Chesham Chemicals Ltd., UK), were added. The resulting powders were then sieved and pressed (Instron, 5507, UK) in a steel die (P. T. No. 3000, Specac, UK) of 13 mm diameter and 1 mm thickness at pressure of 155MPa. Finally, the circular discs were sintered in the muffle furnace at different temperatures. The X-ray diffraction (Equinox 3000, INEL, France) with Cu-Kα radiation (λ = 1.54178 Å) was conducted to determine and understand the phase structure of the sintered samples. Raman spectra (Renishaw inVia, UK) were used to confirm the phase transformation. The bulk densities were calculated by the Archimedes method using distilled water as a medium. In the present study, the bulk density of the samples was calculated by the following formula: $d_{bulk} = d_w\ (w_{dry}/(w_{soak-}w_{sus}))$, where d_w is the density of water and w_{dry}, w_{soak}, and w_{sus} are the dry, soaked, and suspended weights of sintered samples. Chromium (Cr)–gold (Au) electrodes were applied to the sintered discs using a sputter coater (K575X, Emitech, UK) and then poled in silicon oil at 3 kV/mm for 10 min at room temperature. The dielectric properties were measured by an impedance analyzer (4294, Agilent, USA) at a frequency of 1 kHz, and the piezoelectric constant (d_{33}) was measured with a Berlincourt d_{33} m (YE2730A, Sinocera, China) at room temperature. The ferroelectric properties were investigated with the help of AixACCT systems, GmBH (Germany). The sintered samples were polished and thermally etched at 100 °C below their sintering temperatures with ramp up and ramp down temperatures of 20 °C/min. Scanning electron microscopy (JEOL 6060LV, Japan) was used for the investigation of surface morphologies, and the grain size was calculated by the linear intercept method.

3. Results and discussions

3.1 Crystal structure

3.1.1 XRD analysis

Figure 1 represents the XRD patterns of pressed samples of $(Ba_{0.85}\ Ca_{0.15-x}\ Ce_x)\ (Zr_{0.1}\ Ti_{0.9})\ O_3$ measured at room temperature. All peaks were indexed to tetragonal cells and no secondary phase was observed. Figure 1(b) and 1(c) presents expanded views of the 2θ angles between 45°–47° and 65°–68°, respectively. Splitting of the peaks (002)/(200) and (220)/(202) was investigated for the samples $x = 0$–0.00131, with the results suggesting the existence of a tetragonal–rhombohedral (T–R) phase transition [8]. At higher Ce concentrations ($x = 0.02$) the splitting merges to form a single peak, suggesting that the ceramics may have a tendency to transform into another phase, i.e. the pseudo-cubic phase.

Taking tolerance factors into consideration, the small ions $[r(R^{3+})] < 0.087$ nm will occupy the B site, relatively large ions $[r(R^{4+})] > 0.094$ nm will occupy the A-sites and moderate ions are believed to occupy both sites [30]. It is well known in the case of another perovskite, $BaTiO_3$, that Ce^{3+} substitutes the A-site while Ce^{4+} substitutes the B-site but that self-compensation occurs when Ba/Ca = 1 [24]. Ce exists in both valence states as Ce^{3+} (0.134 nm) and Ce^{4+} (0.087 nm) [31]; therefore, according to crystal chemistry and the radius matching rule, Ce^{3+} ions may occupy the A-site of either Ca^{2+} (0.134 nm) or Ba^{2+} (0.161 nm) due to the similar ionic radii. Also, Ce^{4+} ions have ionic radii greater than those of the B-site elements, Ti^{4+} (0.060 nm) and Zr^{4+} (0.072 nm). Thus, it is least possible for Ce^{4+} ions to occupy the B-site. Interestingly, when $x > 0$, the intensity peaks are shifted slightly toward higher angles, indicating cell contraction. Since the ionic radii of Ce^{4+} are less than those of Ca^{2+}, Ce^{4+} ions might go into the Ca^{2+} positions of the A- site and cause lattice distortion and decreased lattice size.

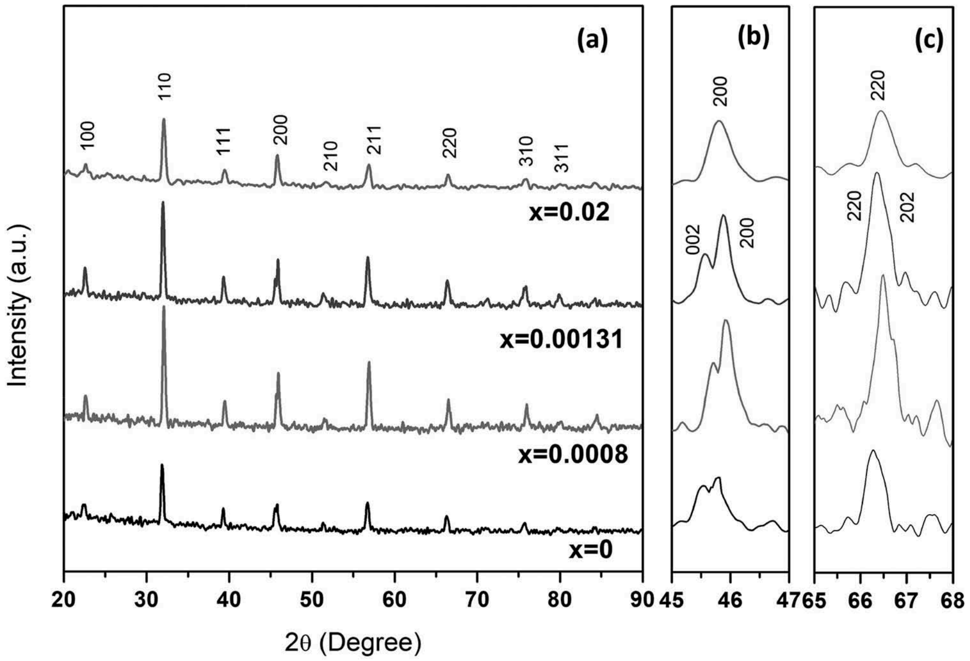

Figure 1. (a) Room temperature XRD patterns of ($Ba_{0.85}$ $Ca_{0.15-x}$ Ce_x) ($Zr_{0.1}$ $Ti_{0.9}$) O_3 samples, (b) magnification of Figure 1(a) in the range of 45°–47° and (c) magnification of Figure 1(a) in the range of 65°–68° sintered at 1350 °C for 4 h.

3.1.2 Raman spectra

Raman spectroscopy was performed on ($Ba_{0.85}$ $Ca_{0.15-x}$ Ce_x) ($Zr_{0.1}$ $Ti_{0.9}$) O_3 ceramics to further clarify the effect of Ce content on the phase evolution of the BCZT system and corroborate the XRD results shown earlier. Figure 2 shows room temperature Raman spectra in the range of 50–800 cm^{-1}. Here the R and T phases coexisted for the samples $x = 0$, 0.0008, 0.00131, in which modes at 93, 151, 201, 248, 294, 524,726 cm^{-1} are related to the R phase, especially at 151 and 190 cm^{-1}, while the modes at 248, 294, 524, 726 cm^{-1} are related to the T phase [32]. No mode at 490 cm^{-1} was observed which is believed to be a signature of the O phase. This suggests that the 490 cm^{-1} peak merges with the 524 cm^{-1} peaks. Therefore, we can assume that the R and T phases coexisted for the samples $x = 0$, 0.0008, 0.00131, which agrees with the XRD results. Further, for $x = 0.02$, the intensity of the modes becomes weak at 93 cm^{-1} and

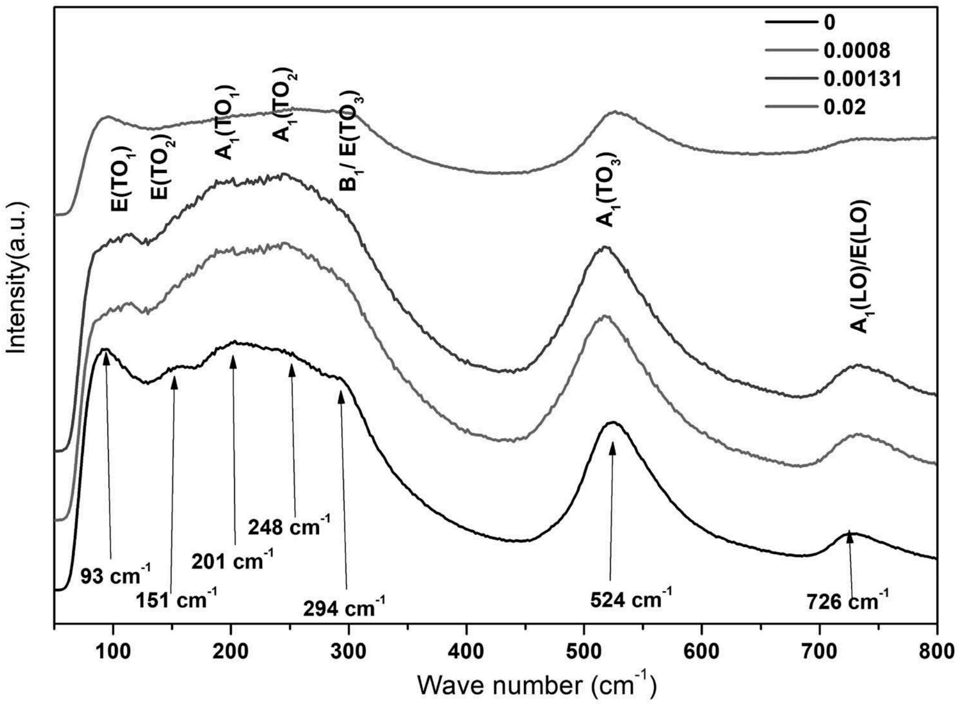

Figure 2. Room temperature Raman spectra of ($Ba_{0.85}$ $Ca_{0.15-x}$ Ce_x) ($Zr_{0.1}$ $Ti_{0.9}$) O_3 ceramics sintered at 1350 °C/4 h.

294 cm^{-1} and other peaks between them vanish, while the modes at 524, 726 cm^{-1} peaks remain. In addition, broad modes of 294 cm^{-1} and 726 cm^{-1} are features of the pseudo-cubic phase. Similar results were reported in previous studies [33–35].

3.2 Bulk density, microstructures and grain sizes

It is evident from Figure 3 that as the sintering temperature increases the bulk density increases obviously. Much higher bulk densities (5.40 g/cm^3) were observed for the samples $x > 0$ as compared to pure BCZT ($x = 0$) at the sintering temperature of 1350°C/4h. This shows that a small amount of CeO_2 was useful for improving the densification of the samples. Maximum density was observed for $x = 0.02$ as 5.75 g/cm^3. It is also noted that the bulk density remains more or less constant for the samples $x > 0$ at above 1350°C/4h. Thus, a small amount of CeO_2 is useful to improve the densities of BCZT ceramics.

Figures 4 and 5 show microstructures of these ceramics heated at 1350 °C and 1450 °C for 4 h. At 1350 °C, the microstructures of $x = 0$, 0.0008 and 0.00131 are not dense enough as compared to $x = 0.02$. It is important to notice that the grain sizes are very small for $x = 0.02$ and that the microstructure becomes much denser compared to other compositions at different sintering temperatures. At 1450 °C, the grains grow steadily, which brings a moderate increase in the densities of the samples when $x = 0–0.00131$. Sample $x = 0.02$ remains sufficiently dense, while no improvement in grain growth was observed. It seems that addition of CeO_2 (less than or equal to 0.00131) enhances grain growth. Grain growth remains steady with CeO_2 addition of $x = 0.02$. Hence, the amount of CeO_2 in the BCZT composition concerns a change in the grain growth.

In general, grains grow with increase in sintering temperatures and a condition that is valid for $x = 0–0.00131$. Sample $x = 0.02$ limits grain growth, irrespective of increase in sintering temperature, which clearly shows that large amounts of CeO_2 are effective in suppressing the melting and grain growth of BCZT ceramics during sintering, which might be due to the accumulation of Ce ions at the grain boundaries. From the above results, it is concluded that CeO_2 has a solubility up to $x = 0.00131$ in a BCZT system.

Proper grain size is an important for obtaining high piezoelectric properties for BCZT ceramics; the best properties can be obtained with a grain size > 10 μm [5] and can deteriorate at a grain size smaller than 10 μm [36], which result was found to be valid for the sample $x = 0.02$, which has a < 1 μm grain size, as shown in Figure 6. At 1350 °C, the average grain size was calculated as about 6 μm for pure BCZT ($x = 0$), while when Ce contents of 0.0008 and 0.00131 were slowly introduced, the grain sizes were increased in the range of 10–12 μm. A high Ce concentration ($x = 0.02$) limits grain growth, which might affect the properties of these ceramics. This should be attributable to the donor-type nature of Ce ions.

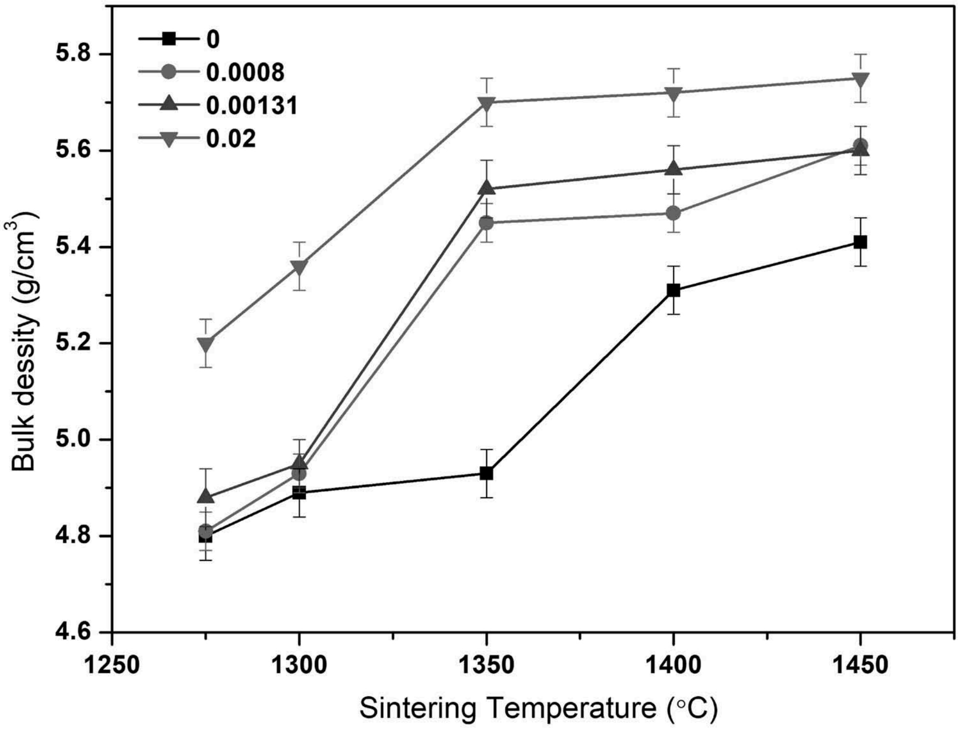

Figure 3. Bulk density of $(Ba_{0.85}Ca_{0.15-x}Ce_x)(Zr_{0.1}T_{i0.9})O_3$ ceramics as a function of sintering temperature (4h).

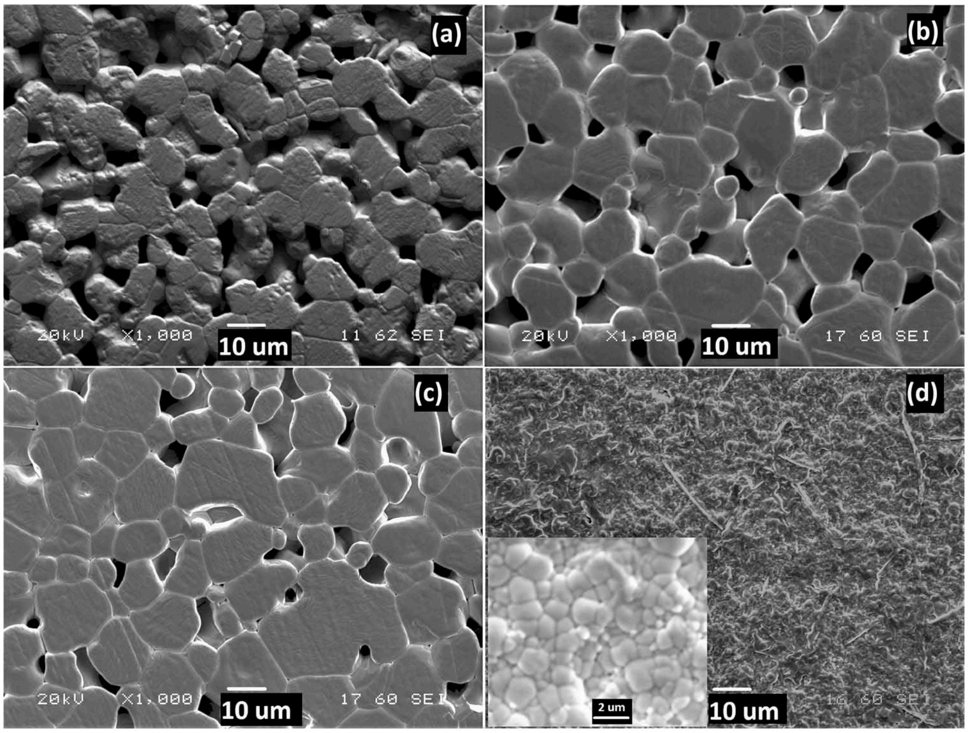

Figure 4. SEM images of $(Ba_{0.85}Ca_{0.15-x}\ Ce_x)\ (Zr_{0.1}Ti_{0.9})\ O_3$ ceramics (a) 0, (b) 0.0008, (c) 0.00131, and (d) 0.02 at 1350 °C for 4 h.

For PZT-based ceramics, donor dopants generally limit grain growth [25,37]. The sintering kinetics can be explained by the lattice diffusion of vacancies from pores to grain boundaries, and donor doping reduces the diffusion coefficient: the vacancies (e.g. A-site vacancies in this case) created by doping are supposed to be bound to the impurity ion (e.g. Ce^{3+} in the present study). When, Ce content is low (up to $x = 0.00131$) the diffusion coefficient may increase, making mass transport strong. As a result, the grains grow, and the structure becomes dense. When Ce content is high ($x = 0.02$), meanwhile, the diffusion coefficient weakens due to an excess of A-site vacancies, and mass transportation can be supposed to be lowered and grain growth was limited as a result.

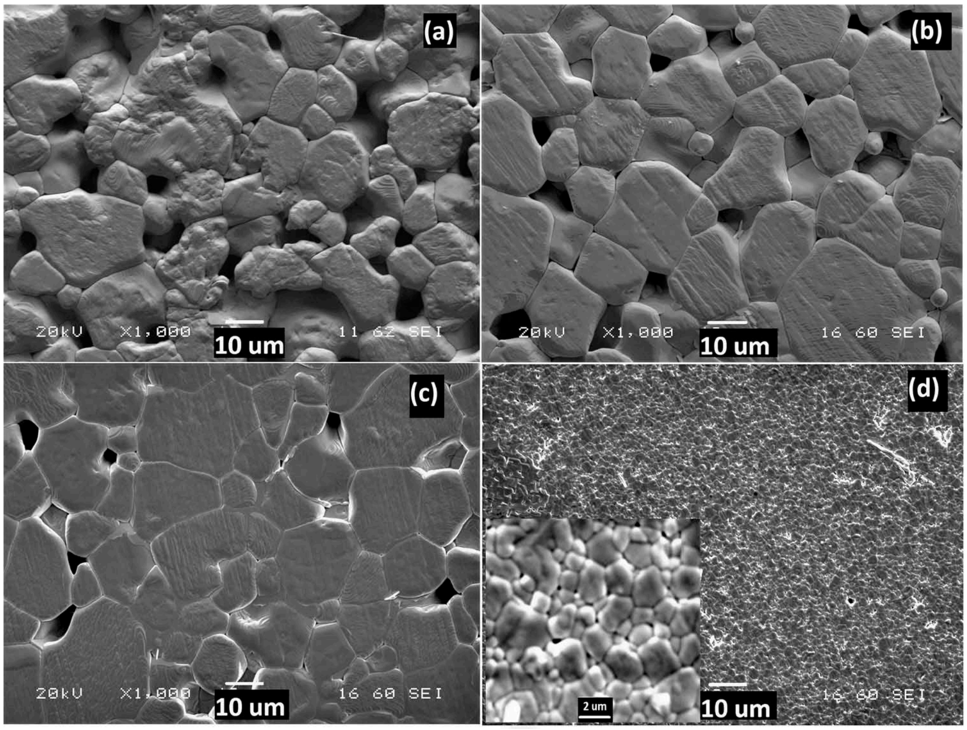

Figure 5. SEM images of $(Ba_{0.85}Ca_{0.15-x}\ Ce_x)\ (Zr_{0.1}Ti_{0.9})\ O_3$ ceramics (a) 0, (b) 0.0008, (c) 0.00131, and (d) 0.02 at 1450 °C for 4 h.

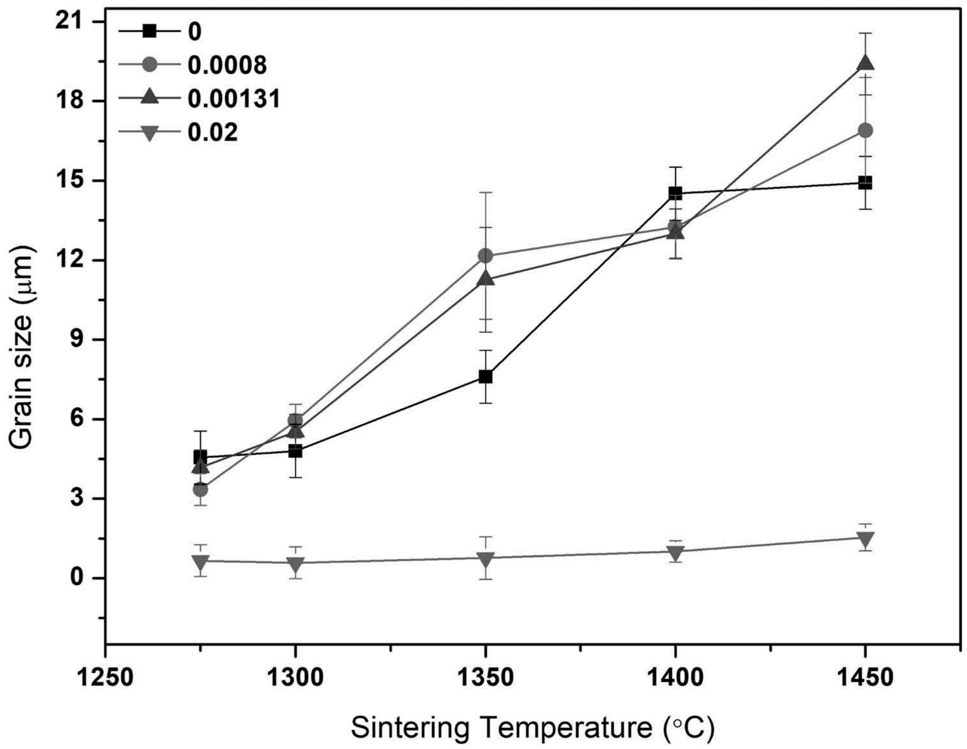

Figure 6. Average grain size of (Ba$_{0.85}$Ca$_{0.15-x}$ Ce$_x$) (Zr$_{0.1}$T$_{i0.9}$) O$_3$ ceramics as a function of sintering temperature (4h).

3.3 Piezoelectric and ferroelectric properties

Figure 7(a) and 7(b) shows the piezoelectric coefficient (d_{33}) and planar coupling factor (k_p), respectively, of BCCeZT ceramics at different sintering temperatures. As the sintering temperature increases, the d_{33} values sharply increase for $x = 0.0008$ and 0.00131 at 1350 °C and then decrease drastically with further increases in the sintering temperature. At 1350 °C, pure BCZT ($x = 0$) has a d_{33} value of around 290 ± 15 pC/N, while when the Ce concentration is slightly increased ($x = 0.00131$), a peak value of d_{33} ~ 501 ± 10 pC/N is revealed. Further increases in the Ce concentration ($x = 0.02$), ions of Ce caused drastic deterioration of $d_{33,}$ which can be attributed to the fine grain size. The planar coupling factor (k_p) follows the same trend: the maximum value of k_p was found to be 38.5 ± 1.92% for the sample $x = 0.00131$ but decreased remarkably for the sample $x = 0.02$ sintered at 1350 °C/4h, as shown in Figure 7(b). The piezoelectric properties are summarized in Table 1 at a sintering temperature of 1350 °C/4h.

The d_{33} and k_p of these ceramics decrease remarkably when the CeO_2 concentration increases ($x = 0.02$), replacing Ca^{2+} ions and making the lattice distortion ever larger. When Ce^{3+} and Ce^{4+} ions occupy Ca^{2+} positions, vacancies are formed in the lattice and grain growth slows (Also see Figures 4(d) and 5(d)) while the grain size of the BCZT ceramics is

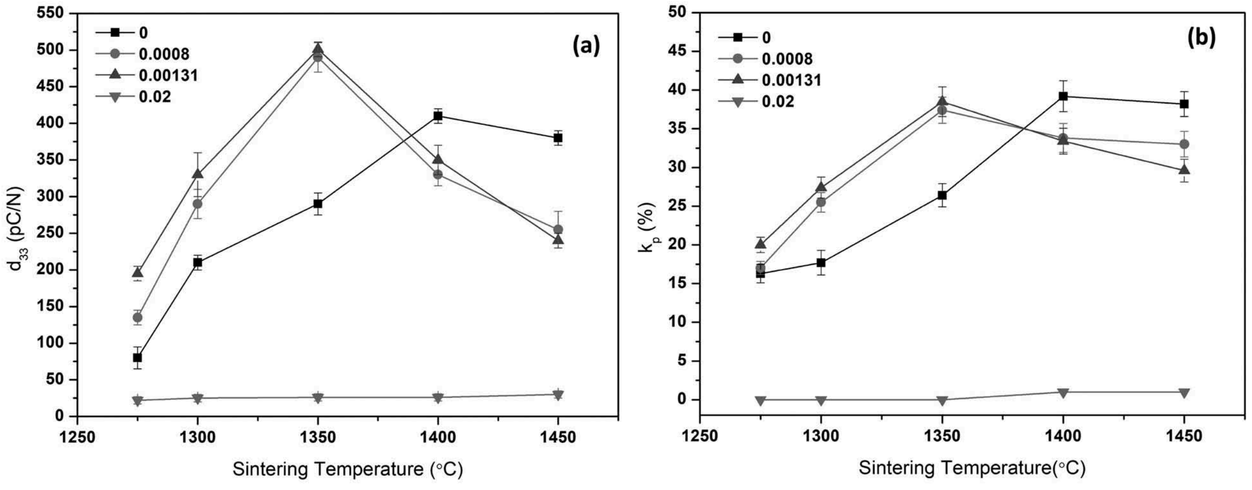

Figure 7. **(a)** Piezoelectric constant, d_{33}, and **(b)** planer coupling coefficient, k_p, of (Ba$_{0.85}$Ca$_{0.15-x}$ Ce$_x$) (Zr$_{0.1}$T$_{i0.9}$) O$_3$ ceramics as a function of sintering temperature.

Table 1. Summary of grain sizes, piezoelectric properties and Curie temperatures of $(Ba_{0.85}Ca_{0.15-x}\ Ce_x)\ (Zr_{0.1}Ti_{0.9})\ O_3$ ceramics at 1350 °C/4 h.

x = mol.	Grain size (μm)	d_{33} (pC/N)	k_p (%)	T_C (°C)
0	7.6 ± 2	290 ± 15	26.4 ± 1	105.4
0.0008	12.16 ± 2.39	490 ± 20	37.8 ± 1.69	103.2
0.00131	11.26 ± 1.97	501 ± 10	38.5 ± 1.92	108.1
0.02	0.76 ± 0.08	–	–	72.6

lowered as well [38]. In the process of replacing Ca^{2+} by Ce^{3+} and Ce^{4+}, moreover, when the CeO_2 concentration is low (up to $x = 0.00131$), Ca^{2+} vacancies are dominantly produced, which results in increased d_{33}. When the CeO_2 amount of $x = 0.02$ increase on the other hand, the lattice distortion effect dominates to drastically reduce the piezoelectric properties. Similar results were found previously [38–40].

The relationship between piezoelectric and ferroelectric data can be described logically by [41]:

$$d_{ij} = P_r.\varepsilon_r.\varepsilon_0.2Q_{ij,} \tag{1}$$

where d_{ij} is the piezoelectric constant, P_r is the remnant polarization), ε_r is the relative permittivity or dielectric constant), ε_0 is the permittivity in free space) and Q_{ij} is the electrostriction coefficient). As is clear from Equation (1), d_{33} is directly proportional to remnant polarization (P_r), suggesting that if the P_r increases, d_{33} also increases. In our research, P_r is dependent on grain size (see Figure 8(a)), i.e. when the grain size is large, the P_r parameter has a high value; therefore, based on Equation (1), d_{33} has a higher value. If the grain sizes are fine, then contribution by clusters of grains to polarization will be reduced because of domain wall pinning, which lowers the d_{33} value [42]. As is well documented in the previous literature, a 60–70% contribution to the increase in d_{33} is due to the displacement of domain walls [43]. Thus, it is believed that larger numbers of domain variants as well as displacement of domain walls are much easier to achieve with bigger grain sizes which can actuate a large strain and push enhancement of the piezoelectric constant (here, d_{33} = 501 ± 10 pC/N for $x = 0.00131$).

P–E hysteresis loops for $(Ba_{0.85}Ca_{0.15-x}\ Ce_x)\ (Zr_{0.1}T_{i0.9})\ O_3$ are shown in Figure 8(a) sintered at a temperature of 1350 °C for 4h. All samples represent typical ferroelectric loops under a switching frequency of 1Hz. Here we observed that the remnant polarization (P_r) is significantly dependent on the grain size. For pure BCZT ($x = 0$), a P_r value of 7.86 $\mu C/cm^2$ was observed. When the cerium content was increased to 0.00131, The P_r value also increased to 12.19 $\mu C/cm^2$. Further increases in the cerium content ($x = 0.02$) show a significant decrease in the P_r value (3.68 $\mu C/cm^2$), which was ascribed to the fine grain sizes of the samples.

A study of P–E responses to the grain sizes of ceramics has been proposed by Ohihara [43] in which fractions (f) of grains give rise to polarization reversal or domain switching and which is expressed as follows:

$$f = f_0\ [1 - \exp(-G_a d^3/kT)], \tag{2}$$

where f_o is the initial polarization or domain of ferroelectric materials, G_a is a constant that represents grain anisotropy energy density, and d is the grain size of the ceramics. Based on these conclusions, f has importance only to the grain size d. Therefore, if the grain size increases, the fraction of grains contributing to the polarization reversal also increases, which brings an improvement in the ferroelectric (P–E) characteristics (see Figure 8(a)).

Figure 8(b) represents the strain-electric field (S–E) loop with a typical butterfly nature. Pure BCZT ($x = 0$) shows strain on the order of 0.11% with a grain size of 7.6 ± 2 μm. As the Ce concentration increased slightly up to 0.00131, the grain size started to improve (11.26 ± 1.97 μm), which results in better strain characteristics (S = 0.14%). A further increase in the Ce

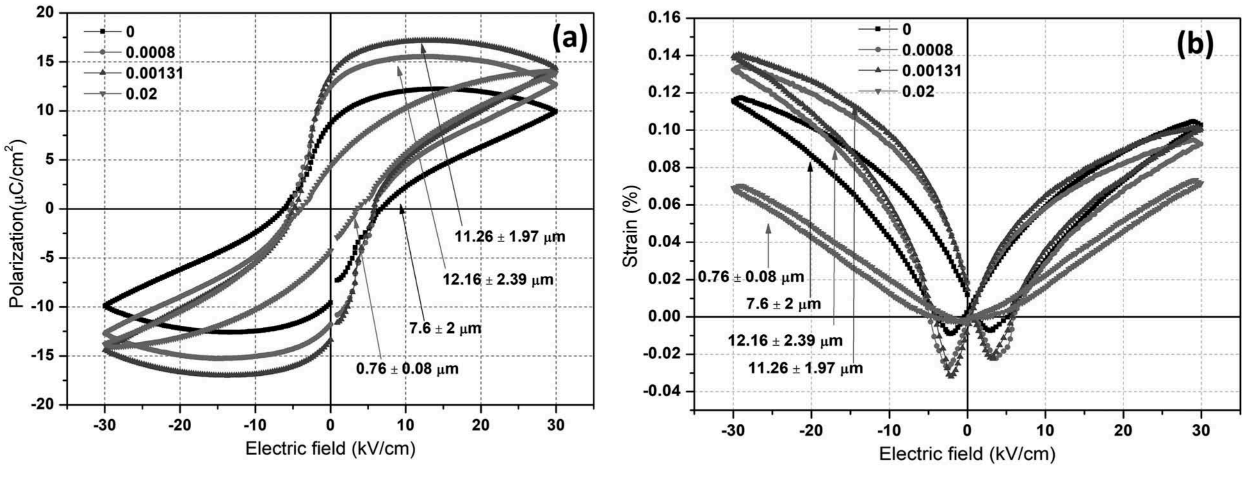

Figure 8. (a) P-E hysteresis loops and (b) strain hysteresis loops for $(Ba_{0.85}Ca_{0.15-x}\ Ce_x)\ (Zr_{0.1}Ti_{0.9})\ O_3$ ceramics sintered at 1350 °C/4 h.

concentration (x = 0.02) gave rise to inferior strain of S = 0.07%. This may be due to the very small grain size of 0.76 ± 0.02 µm.

The variations in grain size influence the domain size, and form the balance of depolarization energy as well as of domain wall energy [44]. The correlation between the domain size (d) and the grain size (t) can be denoted as $d = [(\sigma/\varepsilon_r \ . \ P_0\ ^2)] \ . \ t]^{1/2}$, where σ, ε_r, and P_0 are the energy density of the domain wall, the dielectric constant and spontaneous polarization, respectively. It can therefore be concluded that there is a strong dependence of domain size on grain size in perovskite type ferroelectrics, as was confirmed in the previous report [36]. Moreover, another important fact for the grain size effect on the piezoelectric properties of perovskite-type ferroelectrics is influence of the 90° domain walls [45,46].

Our present results correspond well with to the change in domain size of BCZT ceramics [36] as a function of grain size, showing d_{33} and k_p values around 480 pC/N and ~ 40% for ~ 10–12 µm grain sizes and d_{33} and k_p values around 50 pC/N and ~ 15% for ~ 0.4–1.5 µm grain sizes [36]. Based on the above findings, increased domain size should be the reason for the enhancement of piezoelectric properties with larger grain size, which is in line with our results. In addition, in sample x = 0.02 (cubic crystal structure from XRD) with grain size < 1 um, no piezoelectric properties were observed. This could result from the strong coupling between the grain boundaries and the domain walls which make domain reorientation extremely difficult and severely constraint the domain wall motion. The ferroelectric properties of these ceramics are summarized in Table 2.

Table 2. Summary of ferroelectric properties of $(Ba_{0.85}Ca_{0.15-x}\ Ce_x)\ (Zr_{0.1}T_{i0.9})\ O_3$ ceramics at 1350 °C/4 h.

x = mol.	P_r (µC/cm^2)	S_{max} (%)	E_C (kV/cm)
0	7.86	0.11	5.49
0.0008	11.29	0.13	5.16
0.00131	12.19	0.14	4.57
0.02	-	0.07	-

3.4 Dielectric properties

Figure 9 represents relative permittivity (ε_r) as a function of sintering temperature for $(Ba_{0.85}Ca_{0.15-x}\ Ce_x)\ (Zr_{0.1}T_{i0.9})\ O_3$ samples measured at 1 kHz. High relative permittivity (ε_r ~ 10,000–12,000) was measured for x = 0.0008, 0.00131 samples as compared to pure BCZT (ε_r ~ 8000). When the Ce content become excessive (x = 0.02), a significant drop in ε_r was observed (ε_r < 5000). The relative permittivity peak became broader for x = 0.02, which leads to a more conspicuous diffuse phase transition (DPT) character. This character may be ascribed to structural change due to the excess Ce content and consequently small grain size (0.76 ± 0.08 µm), which results in low relative permittivity and to a shifting of the ferroelectric-paraelectric phase transition to lower temperatures. This may be due to the pseudo-cubic character, in which tetragonal and cubic phases are believed to be very close to each other with a resulting T_C shift towards lower temperatures (see Figure 9).

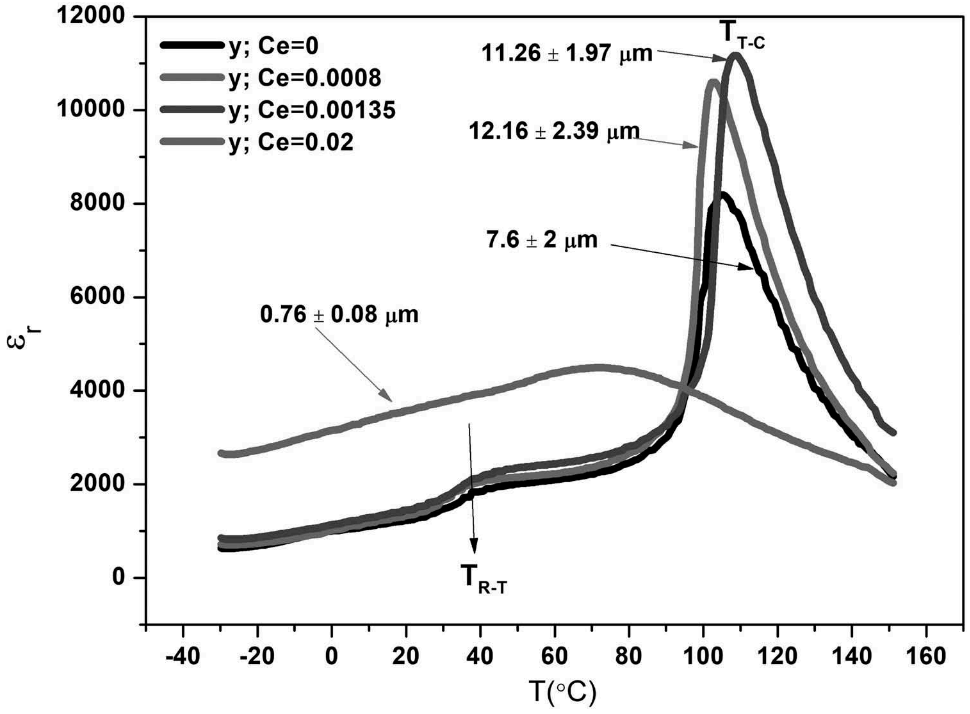

Figure 9. Temperature-dependent relative permittivity of $(Ba_{0.85}Ca_{0.15-x}\ Ce_x)\ (Zr_{0.1}T_{i0.9})\ O_3$ ceramics sintered at 1350 °C/4 h.

4. Conclusions

$(Ba_{0.85}Ca_{0.15-x}Ce_x)(Zr_{0.1}Ti_{0.9})O_3$ ceramics have been successfully synthesized via a solid-state reaction method. The ferroelectric, piezoelectric, and dielectric properties were systematically studied. It was found that high functional properties can be achieved when the grain sizes are between 10 and 12 µm. XRD and Raman analysis are in close agreement in confirming rhombohedral-tetragonal phase coexistence for $x = 0$–0.00131. The excellent properties were obtained for $x = 0.00131$ when sintered at 1350 °C for 4h, resulting in $d_{33} = 501 \pm 10$ pC/N, $k_p = 38.5 \pm 1.92$, $P_r = 12.19$ µC/cm^2, $S = 0.14\%$, $T_C = 108.1$ °C. The above-mentioned high performances of BCCeZT ceramics suggest that the lead-free piezoelectric ceramics could potentially be useful for the fabrication of various electronic devices.

Acknowledgments

The authors acknowledge the Grant Agency of the Czech Republic, National Sustainability Program for supporting this work under grant LO1401 and LQ1601. This work was also supported by the Grant Agency of the Czech Republic under grant no. 18-20498S. We also thank the School of Metallurgy and Materials, University of Birmingham, UK, and CEITEC, Brno University of Technology, Czech Republic, for the use of laboratory facilities.

Disclosure statement

The authors reported no potential conflict of interest.

Funding

The authors acknowledge the Grant Agency of the Czech Republic, National Sustainability Program for supporting this work under grant LO1401 and LQ1601. This work was also supported by the Grant Agency of the Czech Republic under grant number 18-20498S.

ORCID

Vijay Bijalwan http://orcid.org/0000-0003-2858-5736

References

[1] Damjanovic D, Klein N, Li J, et al. What can be expected from lead-free piezoelectric materials? Func Mat Lett. 2010;3:5–13.

[2] Saito Y, Takao H, Tani T, et al. Lead-free piezoceramics. Nature. 2004;432;84–87.

[3] Shrout TR, Zhang SJ. Lead-free piezoelectric ceramics: alternatives for PZT?. Electroceram. 2007;19:113–126.

[4] Yoon MS, Khansur NH, Choi BK, et al. Effect of nano-sized BNBT on microstructure and dielectric/piezoelectric properties. Ceram Int. 2009;35:3027–3036.

[5] Wang P, Li Y, Lu Y. Enhanced piezoelectric properties of $(Ba_{0.85}Ca_{0.15})(Ti_{0.9}Zr_{0.1})O_3$ lead-free ceramics by optimizing calcination and sintering temperature. J Eur Ceram Soc. 2011;31:2005–2012.

[6] Chen T, Zhang T, Zhou J, et al. Ferroelectric and piezoelectric properties of $[(Ba_{1-3x}/2Bi_x)_{0.85}Ca_{0.15}](Ti_{0.90}Zr_{0.10})O_3$ lead-free piezoelectric ceramics. Mat Res Bull. 2012;47:1104–1106.

[7] Panda PK. Review: environmental friendly lead-free piezoelectric materials. J Mater Sci. 2012;19:5049–5062.

[8] Liu W, Ren X. Large Piezoelectric effect in Pb-free ceramics. Phy Rev Lett. 2009;103:257602.

[9] Li W, Xu ZJ, Chu RQ, et al. Piezoelectric and dielectric properties of $(Ba_{1-x}Ca_x)(Ti_{0.95}Zr_{0.05})O_3$ lead-free ceramics. J Am Ceram Soc. 2010;93:2942–2944.

[10] Su S, Zuo RZ, Lu SB, et al. Poling dependence and stability of piezoelectric properties of $Ba(Zr_{0.2}Ti_{0.8})O_3$-$(Ba_{0.7}Ca_{0.3})TiO_3$ ceramics with huge piezoelectric coefficients. Curr Appl Phys. 2011;11:120–123.

[11] Frey MH, Payne DA. Grain-size effect on structure and phase transformations for barium titanate. Phy Rev B. 1996;54:3158–3167.

[12] Hiruma Y, Nagata H, Takenaka T. Grain-size effect on electrical properties of $(Bi_{1/2}K_{1/2})TiO_3$ ceramics. Jpn J Appl Phys. 2007;46:1081–1084.

[13] Tang XG, Chan HLW. Effect of grain size on the electrical properties of relaxor ferroelectric ceramics. J Appl Phys. 2005;97:034109.

[14] Martirenat HT, Burfoot JC. Grain-size effects on properties of some ferroelectric ceramics. J Phys C: Solid State Phys. 1974;7:3182–3192.

[15] Bai Y, Matousek A, Tofel P, et al. (Ba, Ca)(Zr, Ti) O_3 lead-free piezoelectric ceramics—the critical role of processing on properties. Jr Eur Ceram Soc. 2015;35:3445–3456.

[16] Castkova K, Maca K, Cihlar J, et al. Chemical synthesis, sintering and piezoelectric properties of $(Ba_{0.85}Ca_{0.15})(Ti_{0.9}Zr_{0.1})O_3$ lead-free ceramics. J Am Ceram Soc. 2015;98:2373–2380.

[17] Jin L, Huo R, Guo R, et al. Diffuse phase transitions and giant electrostrictive coefficients in lead-free Fe^{3+} doped $0.5Ba(Zr_{0.2}Ti_{0.8})O_3$-$0.5(Ba_{0.7}Ca_{0.3})TiO_3$ ferroelectric ceramics. ACS Appl Mater Inter. 2016;8(45):31109–31119.

[18] Long P, Yi Z. Fabrication and properties of $(Ba_{0.85}Ca_{0.15})(Ti_{0.9}Zr_{0.1})O_3$ ceramics and their multilayer piezoelectric actuators. Int J Appl Ceram Tech. 2017;14:16–21.

[19] Wang C, Chen J, Shen L, et al. Particle size effect on the electrical properties of spark-plasma sintered relaxor potassium sodium niobate ceramic. Jr Ceram Sci Tech. 2017;8(2):255–258.

[20] Xu K, Li J, Lv X, et al. Superior piezoelectric properties in potassium–sodium niobate lead-free ceramics. Adv Mater. 2016;28:8519–8523.

[21] Sahoo B, Panda PK. Effect of CeO_2 on dielectric, ferroelectric and piezoelectric properties of PMN–PT (67/33) compositions. J Mater Sci. 2007;42:4745–4752.

[22] Jin D, Hing P, Sun CQ. Growth dynamics and electric properties of $PbTi_{0.1}Zr_{0.9}O_3$ ceramics doped with cerium oxide. J Phys D: Appl Phys. 2000;33:744–752.

[23] Srimaungsong P, Udomkan N, Pdungsap L, et al. Effect of CeO_2 on sintering temperature and piezoelectric properties PZT (Zr: ti= 52:48) ceramics. Int J Mod Phys. 2005;19:1757–1769.

[24] Makovec D, Samardzija Z, Kolar D. Solid solubility of cerium in $BaTiO_3$. J Sol Stat Chem. 1996;123:30–38.

[25] Gao D, Kwok KW, Lin D, et al. Microstructure, electrical properties of CeO_2-doped $(K_{0.5}Na_{0.5})NbO_3$ lead-free piezoelectric ceramics. J Mater Sci. 2009;44:2466–2470.

[26] Shia J, Yanga W. Piezoelectric and dielectric properties of CeO_2-doped $(Bi_{0.5}Na_{0.5})_{0.94}Ba_{0.06}TiO_3$ lead-free ceramics. J All Comp. 2009;472:267–270.

[27] Li Y, Chen W, Xu Q, et al. Piezoelectric and dielectric properties of CeO_2-doped $Bi_{0.5}Na_{0.44}K_{0.06}TiO_3$ lead-free ceramics. Ceram Int. 2007;33:95–99.

[28] Liao Y, Xiao D, Lin D, et al. The effects of CeO_2-doping on piezoelectric and dielectric properties of $Bi_{0.5}(Na_{1-x-y}K_xLi_y)_{0.5}TiO_3$ piezoelectric ceramics. Mat Sci Engg B. 2006;13:72–176.

[29] Cui Y, Liu X, Jiang M, et al. Lead-free $(Ba_{0.85}Ca_{0.15})(Ti_{0.9}Zr_{0.1})O_3$ - CeO_2 ceramics with high piezoelectric coefficient obtained by low-temperature sintering. Ceram Int. 2012;38:4761–4764.

[30] Tsur Y, Dunbar TD, Randall CA. Crystal and defect chemistry of rare earth cations in BaTiO3. J Electroceram. 2001;7:25–35.

[31] Shannon RD. Revised effective ionic radii and systematic studies of interatomic distances in halides and chalcogenides. A Crys. 1976;32:751–767.

[32] Bondarenko EI, Yu V, Topolov AV, et al. The role of 90° domain wall displacements in forming physical properties of perovskite ferroelectric ceramics. Ferro Lett. 1991;13:13–19.

[33] Zhao L, Zhang BP, Zhou PF, et al. Effect of Li_2O addition on sintering and piezoelectric properties of (Ba, Ca)(Ti, Sn) O3 lead-free piezoceramics. J Eur Ceram Soc. 2015;35:533–540.

[34] Dobal PS, Katiyar RS. Studies on ferroelectric perovskites and Bi-layered compounds using micro-Raman spectroscopy. J Ram Spec. 2002;3:405–423.

[35] Farhi R, El Marssi M, Simon A, et al. A Raman and dielectric study of ferroelectric ceramics. Eur Phys J B. 1999;9(4):599–604.

[36] Hao J, Bai W, Li W, et al. Correlation between the microstructure and electrical properties in high performance $(Ba_{0.85}Ca_{0.15})(Ti_{0.9}Zr_{0.1})O_3$ lead-free piezoelectric ceramics. J Am Ceram Soc. 2012;95:1998–2006.

[37] Lee BW, Lee EJ. Effects of complex doping on microstructural and electrical properties of PZT ceramics. J Electroceram. 2006;17:597–602.

[38] Huang X, Xing R, Gao C, et al. Influence of CeO_2 doping amount on property of BCTZ lead-free piezoelectric ceramics sintered at low temperature Jr. Rar Eart. 2014;32:733–737.

[39] Huang XY, Wei MX, Chen ZG, et al. The influence of CeO_2 doping on NBT-KBT-BT lead-free piezoelectric ceramics' performance. Jr Synt Cryst. 2008;33:1489–1495.

[40] Chen M, Xu O, Kim BH, et al. Effect of CeO_2 addition on structure and electrical properties of $(Na_{0.5}Bi_{0.5})_{0.93}Ba_{0.07}TiO_3$ ceramics prepared by citric method. Mater Res Bull. 2008;43: 1420–1430.

[41] Park SE, Shrout TR. Characteristics of relaxor-based piezoelectric single crystals for ultrasonic transducers. IEEE trans Uttras ferro freq cont. 1997;44:1140–1147.

[42] Bharathi KBR, Varma P. Grain and the concomitant ferroelectric domain size dependent physical properties of $Ba_{0.85}Ca_{0.15}Zr_{0.1}Ti_{0.9}O_3$ ceramics fabricated using powders derived from oxalate precursor route. J Appl Phys. 2014;116:64107.

[43] Orihara H, Hashimoto S, Ishibashi Y. A theory of DE hysteresis loop based on the Avrami model. J Phys Soc Jap. 1994;63:1031–1035.

[44] Randall C, Kim N, Kucera JP, et al. Intrinsic and extrinsic size effects in fine grained morphotropic phase boundary lead zirconate titanate ceramics. J Am Ceram Soc. 1998;81:677–688.

[45] Shao SF, Zhang JL, Zhang Z, et al. High piezoelectric properties and domain configuration in $BaTiO_3$ ceramics obtained through solid state reaction route. J Phys D: Appl Phys. 2008;41: 125408.

[46] Demartin M, Damjanovic D. Dependence of the direct piezoelectric effect in coarse and fine grain barium titanate ceramics on dynamic and static pressure. Appl Phys Lett. 1996;68:3046.

Journal of ELECTRICAL ENGINEERING, VOL 70 (2019), NO-7S, 132–136

COMMUNICATIONS

Characterization of nanoblisters on HOPG surface

Dinara Sobola*, Nikola Papež*, Rashid Dallaev*,
Shikhgasan Ramazanov, Dušan Hemzal*** , Vladimír Holcman***

We report on influence of the surface functionalization on the properties of highly oriented pyrolytic graphite. The samples were processed in nitric acid and characterized by XPS, Raman and EDX spectroscopies, AFM, SEM and optical microscopy. It is shown that interaction of nitric acid with the surface of HOPG leads to two types of reactions: oxidation of the graphite and intercalation of the nitrate ions at the blistered areas.

Keywords: graphite, nitric acid, surface, delamination, topography

1 Introduction

Under normal conditions, graphite is the most stable allotropic form of carbon. Variation of its physical and chemical properties define the application range of graphite from pencil leads to cutting-edge calibration etalons in scientific applications. Thermal characteristics of graphite make it interesting for aerospace applications [1]. Intercalation of compounds can further spread properties of graphite and increase is application potential.

Both HOPG (highly oriented pyrolytic graphite) and HAPG (highly annealed pyrolytic graphite) exhibit pronounced layered structure. HOPG consists of hexagonal carbon planes situated in ABAB positions. Due to Van der Waals bonding between the planes this material is utilized for study and preparation of graphene structures. The interplanar distance between layers can be changed by intercalation of metals.

Graphene nanoblisters and nanobubbles are partially delaminated areas of one or several graphite layers. Both can be prepared on graphite itself or on interfaces of graphite with substrates from other materials. The nanobubbles are of interest because they can trap molecules from gases [2]. There are several methods of graphite nanobubbles formation on HOPG surface: pure chemical, electrochemical, plasma processing, *etc* [3]. Formation of blisters consists of penetration of the reagent through defects into near-surface layers and oxidation of graphite. In result, formation and dissociation of carbonic acid leads to blistering.

Braking of interplanar bonds at HOPG near-surface area and appearance of round-shaped blisters were reported before [4]–[6]. Our study contributes to this field by confirmation of the theoretical work of Tang and Cao [7] about stronger adsobtion of NO_3 in comparison to other nitrogen oxides. The NO_3 anion could be detected by Raman spectrsocopy at the blistered areas. We also demonstrate by XPS and Raman spectroscopies presence of NH_2 group whish is important for surface functionalization for biomedical application [8].

Appearance of blisters, delamination and "bubbles" could also occur during films deposition using carbon materials as substrates. Since control of the surface condition of the substrate is important part of deposition technologies [4, 5], modified carbon surfaces are thus of interest also for growth control during deposition of thin films [11].

2 Experiment

HOPG samples of ZYB quality (purchased from TipsNano OÜ) were exfoliated by tape and exposed to 65% nitric acid (HNO_3) under ambient conditions for 8 minutes. After the exposition, the samples were washed using demineralized water. Optical imaging of the samples before treatment and after treatment is shown in Fig. 1. The position of AFM probe is shown in Fig. 1(a).

The obtained surfaces were studied using atomic force microscopy (AFM) in semi-contact mode in order to not damage the surface features [7, 8]. The blistered areas tend to form "bubbles" on the surface with height up to 1 μm (see Fig. 2). It was suggested by Burgess at al. [14] that the blistering occurs due to functionalization of the surface defects by oxygen-containing bonds [15].

The blistered areas were also observed by SEM (scanning electron microscopy): maximum diameter of the nanobubbles was up to 3 μm (see Fig, 3).

---

*Department of Physics, Faculty of Electrical Engineering and Communication, Brno University of Technology, Technick 2848/8, 616 00 Brno, Czech Republic, nikola.papez@vutbr.cz, **Faculty of Physics, Dagestan State University, 367015 Makhachkala, st. M. Gadjieva 43-a, Dagestan Republic, Russia, ***Department of Condensed Matter Physics, Faculty of Science, Masaryk University, Kotlářská 267/2, 611 37 Brno, Czech Republic

DOI: 10.2478/jee-2019–0055, Print (till 2015) ISSN 1335-3632, On-line ISSN 1339-309X

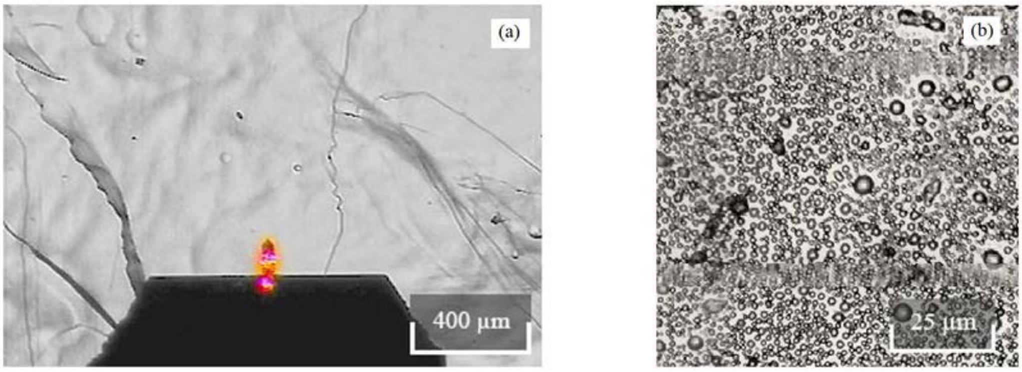

Fig. 1. Optical images: HOPG (ZYB) surface: (a) – before and, (b) – after 8 minutes of processing by HNO_3

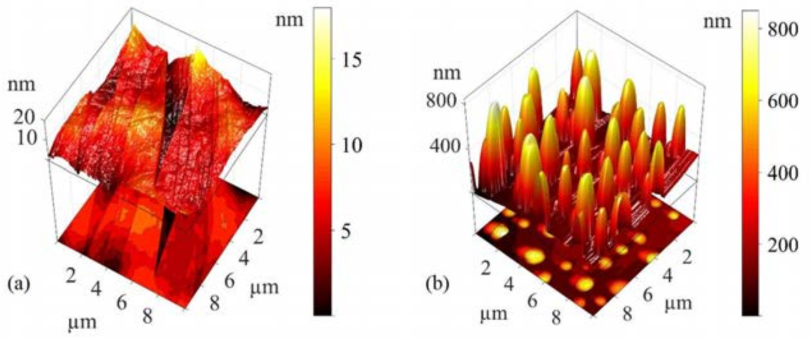

Fig. 2. AFM images: HOPG (ZYB) surface: (a) – before, and (b) – after 8 minutes processing in HNO_3 .

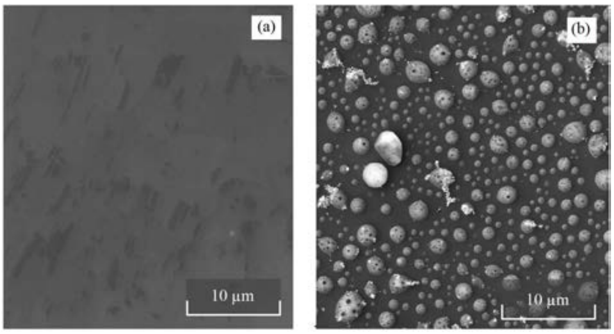

Fig. 3. SEM images: HOPG (ZYB) surface: (a) – before, and (b) – after 8 minutes of processing by HNO_3

Concerning chemical analysis, XPS showed presence of several peaks after treatment of HOPG surface with nitric acid (see Fig. 4). The N1s nitrogen peak occurring at ∼400 eV is usually assigned to $C-NH_2$ bond and its appearance corresponds with theory [14]. However, only 2 minutes of etching by 5 keV argon ions is sufficient to almost completely remove N1s peak, Fig. 4(b). It happens because of preferential etching of nitrogen which occurs by Ar irradiation. The other peak that emerged after HNO_3 treatment is the oxygen peak O1s at 532.4 eV corresponding to the C-O bond. To remove the O1s peak entirely, much longer Ar exposition would be required: even after 20 minutes of etching remnants of this peak persist, Fig. 4(c). Ion beam etching was performed in situ in the XPS chamber. The samples were not exposed to air in order to avoid influence of atmospheric oxygen to the surface condition.

Additionally, EDS (Energy Dispersive X-Ray Spectroscopy) was used for determination of oxygen abundance in the near-surface area. Although EDS did not prove the presence of nitrogen (which was observed by XPS due to its higher sensitivity to surface condition), oxygen content in the measured samples increased from 0.59 up to 1.02 atomic % after treatment.

The amount of oxygen increased twice after treatment, which confirms redox reaction between HOPG and HNO_3. First, surfactant elements from the acid create chemical bonds with graphite surface during reactions:

$$C + 4HNO_3 \longrightarrow H_2CO_3 + 4NO_2 .$$

Subsequently, the carbonic acid instantly decomposes into carbon dioxide and water:

$$C + 4HNO_3 \longrightarrow CO_2 + 2H_2O + 4NO_2 .$$

The produced stress occurs between the reacted near-surface area and the rest of the sample. The delamination of the layers and formation of blisters occurs where Van der Waals bonds are broken. Finally, Raman spectroscopy is widely used for characterization of carbon materials. We used Renishaw InVia spectrometer with laser power of 1 mW and wavelength 532 nm [16]. The observed Raman peaks (see Fig. 5) correspond to graphite intercalation

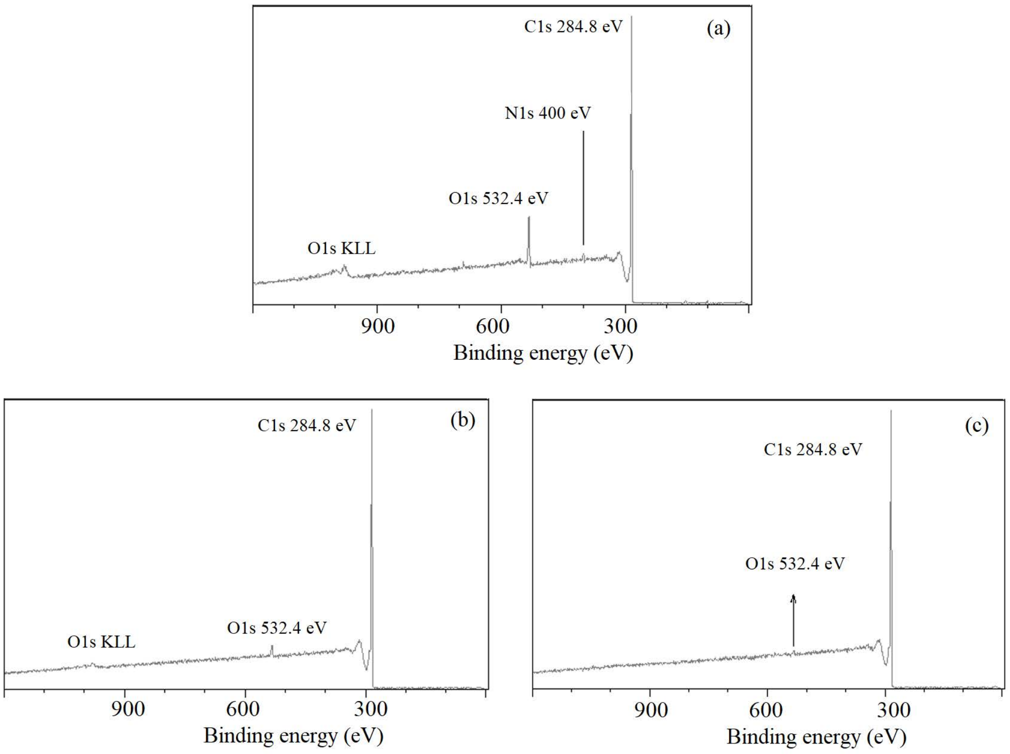

Fig. 4. Wide XPS spectra of HOPG treated with HNO_3 during 8 minutes: (a) – before Ar etching, (b) – 2 min Ar etching, and (c) – 20 min Ar etching

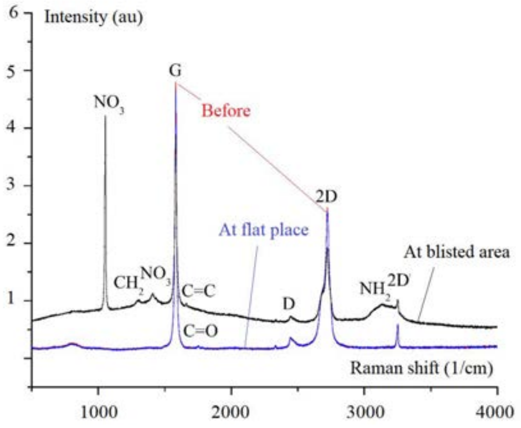

Fig. 5. Raman spectra: HOPG (ZYB) surface before and after 8 minutes of processing by HNO_3

compounds. According to Dunaev and Shapoev [17] the intercalation process could be presented as:

$$2HNO_{3\ adsorbed} \longrightarrow H_2O + NO_3^- + NO_{2\ adsorbed}^+$$

$$NO_{2\ adsorbed}^+ + C \longrightarrow NO_{2\ adsorbed} + C^+$$

$$NO_{2\ adsorbed} \longrightarrow NO_{2\ gas}$$

$$nC^+ + NO_3^- + xHNO_3 \longrightarrow C_n^+NO_3^-xHNO_3$$

The main differences in comparison to pristine HOPG are in spectra from the blister areas. The common areas are observed at 1582 cm^{-1} and 2721 cm^{-1} which are positions of G and 2D peaks of HOPG [18]. Doublet of 2450 cm^{-1} and 3248 cm^{-1} is assigned to D and 2D modes of HOPG, correspondingly [19]. The blister areas show, however, additional features:

- peak at 1053 cm^{-1} refers to macro-cation NO_3 trapped between the graphite layers and the rest of non-dissociated HNO_3 [20],
- peak at 1300 cm^{-1} is connected with transverse vibrations of CH_2 group [21],
- appearance of the 1409 cm^{-1} peak can be attributed to incorporated nitrate anion [22],
- features of C=C and C=O stretching modes are noted by 1660 cm^{-1} and 1748 cm^{-1} peaks, correspondingly [23],
- peak at 3130 cm^{-1} occurs due to NH_2 groups [24].

Thus, the Raman measurement confirms presence of bonds which result from intercalation and oxidation reactions [25]. In order to check the inner structure of the surface features which occurs after the acid treatment the depth-scan Raman measurement was done. The largest blister on the surface was funded by optical microscope for this aim, Fig. 6(a). Contrasted images for NO_3 peak and G-peak at the surface, in middle(and at the bottom are investigated (Fig. 6(b)-(d). The results indicate presence of NO_3^- ions and intensive G-peak on the surface. G-peak decreases during scanning inside the blisters and growths with approaching to the HOPG bulk. The content of nitrogen oxide is higher in the middle of the blister. Peak ratio demonstrates presence of several carbon layers on the surface of the delaminated area and higher amount of the nitrogen compounds (NO_3 and NH_2) below them.

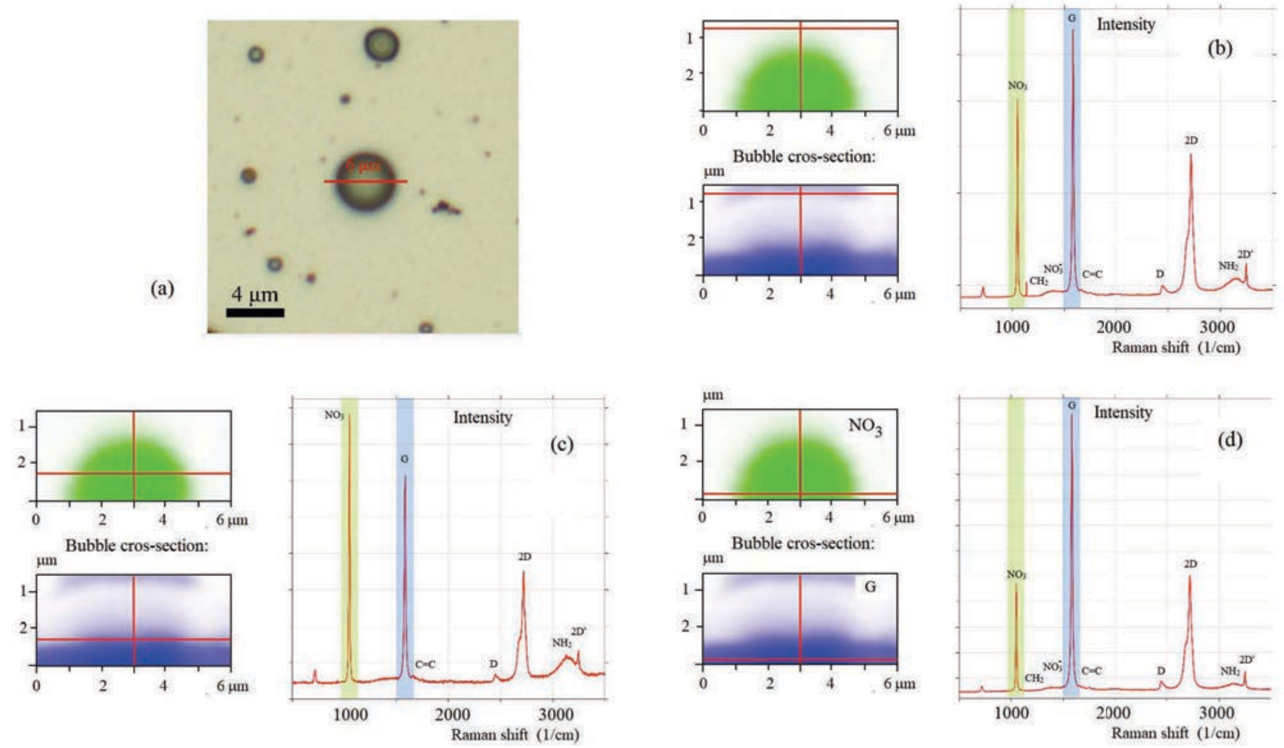

Fig. 6. Raman spectra of the blistered area in depth: (a) – optical top view of the blister for Raman depth-scan, (b) – blister cross-section, top view, (c) – bBlister cross-section, middle view, and (d) – blister cross-section, bottom view

3 Conclusion

Treatment of the surface by HNO_3 created blistered areas. AFM, SEM and optical images demonstrate formation of nanoblisters with different size but similar shape. According to EDS, there are changes in oxygen abundance in the near-surface area after processing by HNO_3.

In summary, nitric acid attacks graphite as oxidant by taking forth an electron (three electrons participate in plain covalent bonding). It is expected that CO_2, NO_2 and water occur in result of reaction between HNO_3 and graphite. Intercalated elements consist of products of redox reactions between graphite and HNO_3. We observed the presence of electron acceptor NO_3^- at the blistered areas. XPS and Raman data confirmed surface functionalization by NH_2 group.

All these defects influence physical and chemical properties of the surface and also affect the performance of the material in its potential applications. In particular, formation of blisters should be considered when HOPG is used as a substrate for epitaxy and heterostructures preparation.

Acknowledgements

Research described in the paper was financially supported by the Ministry of Education, Youth and Sports of the Czech Republic under the project CEITEC 2020 (LQ1601), by the National Sustainability Program under grant LO1401, and by Internal Grant Agency of Brno University of Technology, Grant No. FEKT-S-17-4626. For the research, infrastructure of the SIX Center was used. Part of the work was carried out with the support of CEITEC Nano Research Infrastructure (MEYS CR, 2016-2019).

REFERENCES

[1] E. Ancona and R. Y. Kezerashvili, “Temperature restrictions for materials used in aerospace industry for the near-Sun orbits”, *Acta Astronaut.*, 2017.

[2] E. Khestanova, F. Guinea, L. Fumagalli, A. K. Geim, and I. V. Grigorieva, “Universal shape and pressure inside bubbles appearing in van der Waals heterostructures”, *Nat. Commun.*, 2016.

[3] L. Liu, M. Qing, Y. Wang, and S. Chen, “Defects in Graphene: Generation, Healing, and Their Effects on the Properties of Graphene: A Review”, *J. Mater. Sci. Technol.*, 2015.

[4] S. Yang, P. Tsai, E. S. Kooij, A. Prosperetti, H. J. W. Zandvliet, and D. Lohse, “Electrolytically generated nanobubbles on highly orientated pyrolytic graphite surfaces”, *Langmuir*, 2009.

[5] E. Bouleghlimat, P. R. Davies, R. J. Davies, R. Howarth, J. Kulhavy, and D. J. Morgan, “The effect of acid treatment on the surface chemistry and topography of graphite”, *Carbon N. Y.*, 2013.

[6] O. V. Sinitsyna, G. B. Meshkov, A. V. Grigorieva, A. A. Antonov, I. G. Grigorieva, and I. V. Yaminsky, “Blister formation during graphite surface oxidation by Hummers method”, *Beilstein J. Nanotechnol.*, 2018.

[7] S. Tang and Z. Cao, “Adsorption of nitrogen oxides on graphene and graphene oxides: Insights from density functional calculations”, *J. Chem. Phys.*, 2011.

[8] H. J. Kim et al., “Synthesis and characteristics of NH 2-functionalized polymer films to align and immobilize DNA molecules”, *Nanoscale Res. Lett.*, 2012.

[9] M. M. Koc, M. J. McNally, K. von Haeften, and M. J. Watkins, “AFM induced self-assembling and self-healing mechanism of silicon oxide nanoparticle linear array domains templated on Moir superlattice patterns on HOPG”, *Surf. Sci.*, 2019.

[10] M. Kettner, C. Stumm, M. Schwarz, C. Schuschke, and J. Libuda, “Pd model catalysts on clean and modified HOPG: Growth, adsorption properties, and stability”, *Surf. Sci.*, 2019.

[11] R. Shikhgasan, T. Stefan, S. Dinara, S. Sebastian, and R. Guseyn, “Epitaxy of silicon carbide on silicon: Micromorphological analysis of growth surface evolution”, *Superlattices Microstruct.*, vol. 86, pp. 395–402, 2015.

[12] D. Sobola, S. Talu, S. Solaymani, and L. Grmela, “Influence of scanning rate on quality of AFM image: Study of surface statistical metrics”, *Microsc. Res. Tech.*, vol. 80, no. 12, 2017.

[13] S. Talu, D. Sobola, and N. Papež, “Analysis and Recommendations for Education Process of Experts in the Field of Scanning Probe Microscopy”, *DEStech Trans. Soc. Sci. Educ. Hum. Sci.*, vol. 0, no. aetms, 2017.

[14] R. Burgess et al., “The functionalisation of graphite surfaces with nitric acid: Identification of functional groups and their effects on gold deposition”, *J. Catal.*, 2015.

[15] S. Talu, D. Sobola, S. Solaymani, R. Dallaev, and J. Brüstlová, “Scale-depended Choice of Scanning Rate for AFM Measurements”, *DEStech Trans. Comput. Sci. Eng.*, no. cnai, 2018.

[16] N. Papež et al., “Degradation analysis of GaAs solar cells at thermal stress”, *Appl. Surf. Sci.*, 2018.

[17] A. S. A. Dunaev, “Prolific Family of Carbon Materials”, Online: http://www.nanometer.ru.

[18] P. H. Tan, Y. M. Deng, Q. Zhao, and W. C. Cheng, “The intrinsic temperature effect of the Raman spectra of graphite”, *Appl. Phys. Lett.*, 1999.

[19] P. H. Tan, Y. M. Deng, and Q. Zhao, “Temperature-dependent Raman spectra and anomalous Raman phenomenon of highly oriented pyrolytic graphite”, *Phys. Rev. B - Condens. Matter Mater. Phys.*, 1998.

[20] R. L. F. J. Theo Kloprogge, D. Wharton, L. Hickel, “Infrared and Raman study of interlayer anions CO3 2- , NO3 - , SO4 2- and ClO4 - in Mg/Al- hydrotalcite”, *Am. Mineral.*, 2002.

[21] R. W. C. G. Wood, “Raman Spectra of a Series of Normal Alcohols and Other Compounds”, vol. 42, no. 1, pp. 386–393, 1932.

[22] V. Rives, “Layered Double Hydroxides: Present and Future”, 2011.

[23] P. Meksiarun, N. Spegazzini, H. Matsui, K. Nakajima, Y. Matsuda, and H. Satoa, “In vivo study of lipid accumulation in the microalgae marine diatom Thalassiosira pseudonana using Raman spectroscopy”, *Appl. Spectrosc.*, 2015.

[24] A. L. M. B. De Carvalho, S. M. Fiuza, J. Tomkinson, L. A. E. B. De Carvalho, and M. P. M. Marques, “Pt(II) complexes with linear diamines-Part I: Vibrational study of Pt-diaminopropane”, *Spectrosc. (New York)*, 2012.

[25] N. Papež et al., “Surface morphology after reactive ion etching of silicon and gallium arsenide based solar cells”, *J. Phys. Conf. Ser.*, vol. 1124, pp. 041015, 2018.

Received 19 March 2019

Materials Research Bulletin 114 (2019) 121–129

Contents lists available at ScienceDirect

Materials Research Bulletin

journal homepage: www.elsevier.com/locate/matresbu

The effect of sintering temperature on the microstructure and functional properties of BCZT-xCeO_2 lead free ceramics

Vijay Bijalwan[a,*], Hana Hughes[a,b], Hojat Pooladvand[b], Pavel Tofel[a,c], Bo Nan[a], Vladimir Holcman[c], Yang Bai[a,b], Tim W. Button[a,b]

[a] *CEITEC—Central European Institute of Technology, Purkyňova 123, 612 00, Brno, Czech Republic*
[b] *School of Metallurgy and Materials, University of Birmingham, Birmingham, B15 2TT, United Kingdom*
[c] *Brno university of Technology Dept. of Physics, Technicka 10, 61600, Brno, Czech Republic*

ARTICLE INFO

Keywords:
Lead free ceramics
Sintering temperature
Grain size
XRD

ABSTRACT

We report $(Ba_{0.85}Ca_{0.15})(Zr_{0.1}Ti_{0.9})O_3$ + x wt.% CeO_2 lead free piezoelectric ceramics fabricated by conventional solid-state reaction routes. The phase structure, microstructure and functional properties have been systematically investigated. The morphotropic phase boundary was investigated in the range of x = 0 - 0.1%. A comparative study of their functional properties as a function of sintering temperature is presented. The study shows the important role of sintering temperature and grain size on the functional properties of these ceramics. Enhanced properties are observed for x = 0.07% at a sintering temperature 200 °C lower than for pure BCZT, in which, $d_{33} = 507 \pm 20$ pC/N, $k_p = 51.8\%$, $\varepsilon_r = 4091 \pm 100$, tan $\delta = 0.02$, $P_r = 16.32\ \mu m/cm^2$, $E_C = 2.13$ kV/cm and $T_C = 104.6$ °C indicating that these ceramics are promising lead-free substitutes for the widely used lead-based ceramics.

1. Introduction

Piezoelectric ceramic materials are important for many technological applications and are commonly used as sensors, actuators and electronic components. Such applications are currently dominated by the use of lead zirconate titanate (PZT) materials due to their outstanding piezoelectric and ferroelectric properties ascribed to the co-existence of rhombohedral and tetragonal phases at the morphotropic phase boundary (MPB) [1]. However, PZT contains more than 60% lead in its basic composition which, due to the toxicity of lead, is a major environmental concern. As a result, legislative activity by the European Commission has been prepared in order to eradicate such toxic substances from industrial and household equipment and thus minimise their impact on the environment [2–4]. Much research has therefore been initiated worldwide in the quest for new lead free piezoelectric ceramics suitable to replace PZT [5–8]. One particular landmark in the field of lead free piezoelectric materials was reported by Lui and Ren concerning the solid solution of $(1-x)Ba(Zr_{0.2}Ti_{0.8})O_3-x(Ba_{0.7}Ca_{0.3})TiO_3$ (1-xBCT-xBZT, also referred to as BCZT) with a very high value of $d_{33} \sim 620$ pC/N for x = 0.5 [9], which is much higher than other lead free piezoelectric compositions such as $Bi_{1/2}Na_{1/2}TiO_3$ - $BaTiO_3$ (BNT-BT) and $K_{1-x}Na_xNaO_3$ (KNN) [8,10]. The BCT-BZT phase diagram shows an MPB that has a strong curvature implying that the properties of materials in the region of the MPB depend on both stoichiometry and temperature. Previous reports suggest that grain size, sintering temperature and poling conditions can all play important roles in determining the dielectric and piezoelectric behaviour of BCZT ceramics [11–17].

The grain size dependence of the dielectric, piezoelectric and domain wall motion properties of lead free piezoelectric ceramics, particularly materials based on barium titanate (BT), have been widely reported [18–21]. For example, Martirena and Burfoot reported that the average value of dielectric constant (ε_r) at room temperature increases when grain size decreases (1500 for 5 μm and 6000 for 1 μm) [18]. Also, with decreasing grain size T_C decreases and the peak in dielectric constant broadens. An increase in piezoelectric constants d_{31} and d_{33} was also seen with increasing grain size [18]. Domain wall motion is one of the main effects that can be influenced by the grain size and which is known to contribute to ferroelectric, dielectric and piezoelectric properties. It is well known that domains exist inside a grain when the domain wall thickness is smaller than the grain size, such that the walls will be able to move by the application of an electric field, thus affecting some properties [18]. Therefore, it could be expected that domain walls will be more mobile in larger grains and could be

---

[*] Corresponding author.
E-mail address: vijay.bijalwan@ceitec.vutbr.cz (V. Bijalwan).

https://doi.org/10.1016/j.materresbull.2019.02.031
Received 8 September 2018; Received in revised form 11 January 2019; Accepted 26 February 2019

inhibited when grain size reduces, such that their contribution on properties may also decrease. It has been shown that $BaTiO_3$ ceramics with grain sizes of 10–20 µm have well developed domain structures. Similar trends have been reported for 0.5BCT-0.5BZT ceramics, as grain size increases, d_{33} increases [22–24].

However, although densification of BCZT ceramics may occur around 1300 °C when smaller particle size powder (1 µm) is used, the functional properties are not maximized until larger grains are developed. One of the main drawbacks of BCZT ceramics is the very high sintering temperatures (> 1475 °C) required to obtain optimized properties and where the formation of very large grains (> 30 µm) [12] may be an addition issue. Both these factors could reduce the industrial use of such materials for particular applications. Therefore, the control of grain growth, and hence grain size, and the lowering of sintering temperatures in high density BCZT ceramics are desirable for BCZT to be useful in real device applications. Investigations concerning the reduction of grain size by different sintering methods such as spark plasma sintering and two-step sintering techniques on BCZT ceramics have been reported [24] but materials with sub-10 µm grain size are not suiatble for achieving high piezoelectric properties. Therefore, the use of metal oxide dopants such as ZnO, CeO_2, CuO and Y_2O_3 have been explored to reduce sintering temperature as well as to obtain better grain size in order to give enhanced piezoelectric properties [25–29]. In particular, 0.04 wt.% CeO_2 addition has been shown to accelerate the grain growth and reduce sintering temperature drastically to 1350 °C, with excellent piezoelectric properties (d_{33} ~ 600 pC/N, k_p ~ 52%) being reported [26]. However, this study was concerned only with the dielectric and piezoelectric properties sintered at 1350 °C. Thus, there is a scope for a detailed study of the structural and microstructure evolution as well as on ferroelectric properties over a wider range of CeO_2 addition.

In this paper, we report a significant extension to previous work with a comprehensive investigation of the effect of increased ranges of both CeO_2 doping (0–3 wt.%) and sintering temperatures (1275–1450 °C). The novelties of this research are, (a) a detailed and systematic study of structure and microstructures, (b) a detailed and systematic study of the ferroelectric properties, (c) the determination of optimized processing parameters e.g. sintering temperature and grain size (d) the reporting of enhanced piezoelectric constant (d_{33}), Planer coupling coefficient (k_p), and remnant polarization (P_r) of BCZT-CeO_2 ceramics.

2. Experimental

$(Ba_{0.85}Ca_{0.15})(Zr_{0.1}Ti_{0.9})O_3$ + x wt.% CeO_2 (x = 0, 0.02, 0.04, 0.07, 0.1, 0.5, 3) materials were processed by conventional solid state reaction routes. Raw materials of $BaCO_3$ (Dakram, Great Britain, 99.9%) $CaCO_3$ (Lachner, Czech Republic, 99.9%), ZrO_2 (Dakram, Great Britain, 99.9%), TiO_2 (Dakram, Great Britain, 99.9%) and CeO_2 (Sigma Aldrich, Great Britain, 99.9%) were dried in an oven (Lenton MMD/0229, England) at 220 °C/1 h before being weighed according to their stoichiometric ratios. The raw powders were then mixed in a horizontal ball mill with zirconia milling media in deionized water for 24 h. The weight ratio of powder to zirconia milling media was 2:1. The resulting slurry was dried in the oven at 90 °C for 15 h and then calcined in a muffle furnace (Lenton, 5696, England) at 1250 °C for 2 h. The different amounts of CeO_2 were added to 30 gm batches of the calcined BCZT powders and re-milled in deionized water for 24 h. Approximately 5 wt.% each of two binders, Duramax B1000 (Product No. 74821, Chesham Chemicals Ltd., UK) and B1007 (Product No. 74823, Chesham Chemicals Ltd., UK), were added during the last hour of milling. The particle sizes of the milled powders were measured using a particle size analyzer (Gracell, SympaTec, Germany) and the average particle size of all batches were found to be ~ 2 µm. After drying, the resulting powders were sieved (300 microns, VWR, England) and then uniaxially pressed at 155 MPa pressure (Instron, 5507, England) into the green bodies using a 13 mm diameter cylindrical steel die (P.T. No. 3000, Specac, UK). The green bodies were sintered in a muffle furnace (Lenton, 5696, England) at different temperatures between 1275–1450 °C for 4 h.

The phase structure of sintered discs was examined by X ray diffraction (SmartLab, Rigaku, Japan). Raman spectra were recorded using a Raman spectrometer (Renishaw InVia, UK) in a back scattered mode; the excitation laser was irradiated from an Ar^+ laser with an output power of 50 mW. Bulk density was calculated from the measured dry mass and dimensions as the samples were in the form of regular cylinders. Chromium (Cr) – Gold (Au) electrodes were sputtered on the circular faces of the sintered samples using a sputter coater (K575X, Emitech, UK), following which samples were poled in silicone oil with an electric field of 3 kV/mm applied for 10 min at room temperature. The dielectric properties and k_p were measured at room temperature using an impedance analyzer (4294, Agilent, USA). The piezoelectric constant d_{33} was measured using a Berlincourt d_{33} meter (YE2730 A, Sinocera, China). The average values and standard deviations of bulk densities, piezoelectric properties (d_{33} & k_p), and dielectric properties (ε_r & tan δ) were established from measurements made on 5 samples. The surface microstructure was observed by scanning electron microscopy (JEOL 6060 L V, Japan) on samples which had been firstly polished and thereafter thermally etched for 10 min. at a temperature 100 °C below the sintering temperature. The grain size was calculated by the linear intercept method. The average values and standard deviation of the grain size were established from 15 measurements on 3 samples. Ferroelectric properties were measured using a piezoelectric evaluation system (aixPES, aixACCT systems GmbH, Germany) at 1 Hz frequency.

3. Results and discussion

3.1. Effects of sintering temperature on density, grain size, piezoelectric and dielectric properties

The bulk densities of BCZT ceramics with different Ce concentrations and sintered at various temperatures for 4 h are depicted in Fig. 1. Bulk density increases with increasing sintering temperature, however, samples with x = 0.04% and x = 0.07% exhibit maximum density when sintered at 1350 °C, with values of 5.57 g/cm^3 and 5.64 g/cm^3 respectively, corresponding to respective values of nearly 95% and 97% of the theoretical density of 5.81 g/cm^3 of 50/50 BCZT ceramics previously reported [13]. At higher sintering temperatures, the density of samples with x = 0.04, 0.07, 0.1 and 3% CeO_2 either remain

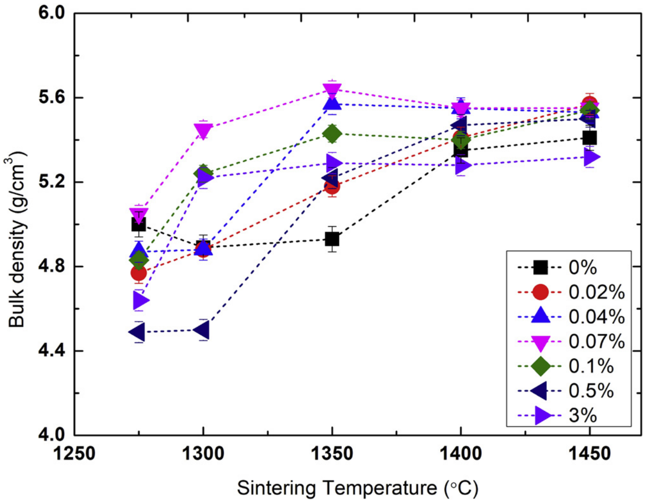

Fig. 1. (a) Dependence of bulk density on sintering temperatures for BCZT-xCeO_2 ceramics.

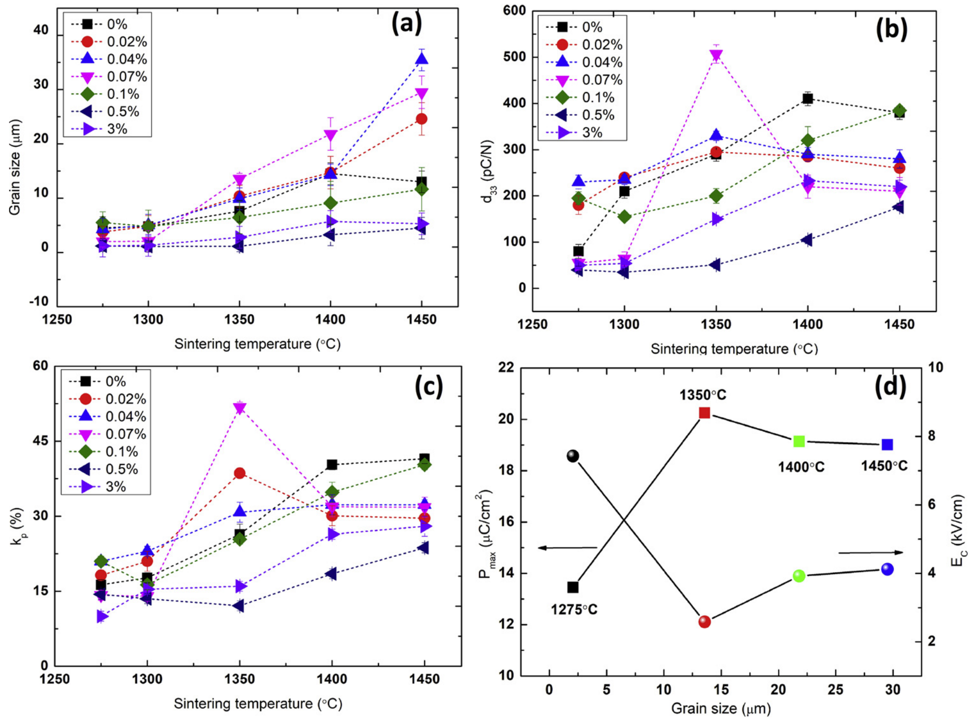

Fig. 2. Dependence of (a) Grain size (b) Piezoelectric coefficient (c) Planar coupling factor on sintering temperatures for BCZT-xCeO_2 ceramics and (d) Maximum polarization P_{max}, and coercive field E_C, as a function of grain size for the sample x = 0.07%.

approximately constant or show a slight decrease, whereas for all other compositions the density continues to rise with increasing sintering temperature.

Fig. 2(a) shows the dependence of grain size dependence on sintering temperature and CeO_2. It is well known that grain size is controlled by grain boundary mobility which increases with increasing in sintering temperature [12,30]. Here in our study, at 1450 °C the grains grow rapidly to ≥ 20 μm for compositions in the range x = 0.02 - 0.07%. In addition, grain size is continuously increased (≤ 15 μm) for the sample x = 0% as the sintering temperature is increased up to 1450 °C. On the other hand, small grain sizes (≤ 10 μm) were observed for samples with compositions of x = 0.1, 0.5, 3% during the entire sintering regime, indicating that higher amounts of CeO_2 could limit grain growth.

The effect of sintering temperature on the piezoelectric charge constant d_{33} and planar coupling coefficient (k_p) for sintered BCZT samples with different amounts of CeO_2 are shown in Fig. 2(b) and (c) respectively. It can be seen that both properties generally increase with increased sintering temperature up to 1350 °C. For samples with composition x = 0.02 - 0.07%, the values of d_{33} and k_p peak at this temperature, before decreasing with further increase in sintering temperature. For samples with compositions x = 0, 0.1, 0.5, and 3% CeO_2 the values of d_{33} and k_p increase further as the sintering temperature is increased beyond 1350 °C, with values levelling off for some compositions at 1400 °C. The maximum values of d_{33} and k_p were observed as 507 ± 20 pC/N and 51.8% respectively for the x = 0.07% composition, sintered at 1350 °C. These very high piezoelectric properties may be ascribed to the larger grain size (> 10 μm) of BCZT ceramics facilitated by the CeO_2 addition at this sintering temperature. Also, samples with compositions x > 0.07% sintered at 1350 °C, exhibited inferior piezoelectric properties, which may be attributed to the smaller grain sizes < 5 μm (see Fig. 1a). Other reports confirm the appropriate grain size ~ 10–20 μm for obtaining high piezoelectric properties (d_{33} > 450pC/N) in BCZT [12,24,30]. Compared to pure BCZT (x = 0%, grain size 7.6 ± 2 μm) sintered at 1350 °C the grain size has increased (10–15 μm) due to small amount of Ce content (x = 0.02 - 0.07%) which causes relatively high piezoelectric activity. There is also an indication from the data presented here that grain sizes larger than approximately 20 μm may be deleterious to the piezoelectric properties. Grain sizes that are too large (here defined as > 20 μm), often reduce piezoelectric and dielectric properties due to excessive back switching [31,32]. Also, higher sintering temperatures or longer dwell times could be the possible cause of point defects which tend to migrate to the domain boundaries/grain boundaries. Therefore, these point defects pin the domain walls, which is the main factor for the decrease in piezoelectric properties [33]. For instance, in the 0.07% sample, domain wall pinning effects seem to increase at higher sintering temperature (> 1350 °C) i.e. large grain size, as plotted in Fig. 2(d). Firstly, the values of P_{max} is increased and E_C decreased with increase in sintering temperature (grain size ~ 2–13 μm) up to 1350 °C. Further increase in sintering temperature (grain size > 20 μm), leads to a decrease in P_{max} and increase in E_C.

The variation with sintering temperature and CeO_2 content of relative permittivity ε_r and loss tangent tan δ, measured at 1 kHz for poled samples, are shown in Fig. 3(a) and (b). For sintering temperatures ≤1350 °C, the dielectric properties of the ceramics show a similar pattern to the bulk density (Fig. 1) with relative permittivity rising with increasing sintering temperature and achieving a maximum value of 4091 ± 100 for the x = 0.07% composition, sintered at 1350 °C/4 h. This is in line with the reduction in porosity. This relative permittivity value is much higher than the value (ε_r = 3060) reported by Liu and Ren for 50/50 BCT-BZT [9] and significantly higher than other lead-free piezoelectric materials (ε_r ~ 290–1740) [7–9] and is comparable to soft PZT (ε_r ~ 1700–3500) [1,9]. As the sintering temperature was increased beyond 1350 °C for the x = 0.04 - 0.07% compositions, the relative permittivity started to decrease possibly due to the increased porosity. For compositions with x = 0 - 0.02% and x > 0.07 wt.%, relative permittivity values were < 2500 for samples sintered at 1350 °C/4 h, correlating with the microstructural observations of small grains discussed below. For these compositions, the relative permittivity continued to increase with increased sintering temperatures. The dielectric loss of all compositions of these ceramics is improved with

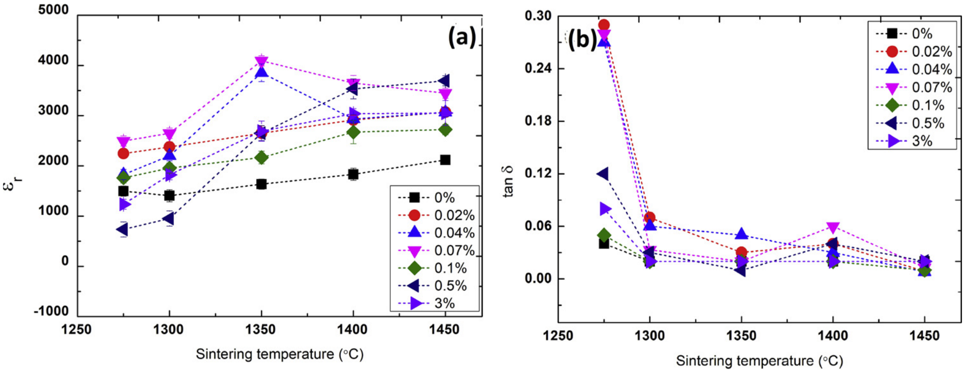

Fig. 3. (a) Relative permittivity, ε_r and (b) loss tangent, tan δ for BCZT-xCeO_2 ceramics sintered at different temperatures.

increasing sintering temperature and reach values between ∼ 0.02 – 0.06 (i.e. 2–6%) for samples sintered at 1350 °C/4 h with the range narrowing to ∼ 0.02 – 0.04 (i.e. 2–4%) for samples sintered at 1450 °C. Therefore, it can be concluded that a proper amount of CeO_2 addition can improve the dielectric properties of BCZT ceramics. Supplementary Table S1 summarizes physical and functional properties of these ceramics sintered at 1350 °C/4 h.

As high piezoelectric and room temperature dielectric properties and high densification is observed at 1350 °C/4 h for the x = 0.07% composition, from here on, we show and discuss other properties including temperature dependent dielectric properties, structural analysis and ferroelectric properties for samples sintered at this temperature only.

3.2. *Properties of BCZT-CeO_2 ceramics sintered at 1350 °C for 4 h*

3.2.1. *Effects of CeO_2 content on microstructure*

It is observed that the density of these samples is strongly dependent both upon their sintering temperature and composition. As an example, the micrographs of BCZT - xCeO_2 ceramics sintered at 1350° C for 4 h are shown in Fig. 4(a–g). The grain size increases for compositions in the range x = 0 - 0.07% and the addition of CeO_2 has caused a significant change in the grain morphology and densification. For compositions in excess of x = 0.1%, there seems almost no change in the morphology and density, indicating a saturation of the effect of the CeO_2 additive. Pure BCZT sintered at 1350 °C (x = 0%, Fig. 4a) has an obvious porous microstructure. However, it is important to note that when x = 0.02% (Fig. 4b) the microstructure has already started to become less porous. Samples with further incorporation of CeO_2 up to x = 0.04% (Fig. 4c) exhibit dense microstructures with a number of large angular grains with small grains trapped between them. This abnormal grain growth implies a coarsening mechanism where a few large grains grow rapidly in a matrix of very small grains which have a much slower growth rate. In that sense, the microstructure can be considered to have a bimodal grain size distribution [34]. This may be due to the initial particle size distribution map (bimodal) for the sample x = 0.04%, and is in line with our findings as shown in Fig. 4(h).

For samples in which the CeO_2 content was increased to x = 0.07% (Fig. 4d) a much more homogeneous grain structure is observed comprising primarily of large angular grains, with just a few finer grains and porosity at their junctions. For 50/50 BCZT, high density (> 95%) has been reported for ceramics sintered at temperatures > 1500 °C [9] with grain sizes greater than 30 μm [12]. In the present work, we show that the addition of a small concentration of CeO_2 in the range x = 0.04 - 0.07% results in high densification for samples sintered at 1350 °C. However, it can be seen in Fig. 4 (e–g) that CeO_2 contents x = 0.1, 0.5 and 3% result in porous microstructures, the x = 0.1% sample being a particular contrast to x = 0.07%. Here at low temperature, small CeO_2 content (x = 0.02 - 0.07%) facilitates the grain growth of BCZT ceramics in contrast to reports for other lead free compositions [35,36]. It is evident that small amounts of CeO_2 addition (x = 0.02 - 0.07%) caused large increases in grain size and densification. Also, it enhances mobility of the grain boundaries, modifies the microstructure and enables a reduction in sintering temperature. It is shown in our previous research, that the small powder particle size promotes grain growth [12]. The average grain size of sintered materials made from 1 μm, 3 μm and 5 μm powders were about 55 μm, 35 μm and 20 μm, respectively for 50BCT-50BZT ceramics sintered at 1450 °C [12]. Here in our study, with ˜ 2 - 3 μm powder particle size, a pronounced grain growth (10–13 μm) is observed for x = 0.07% at lower sintering temperature 1350 °C, while higher grain growth ˜ 25–35 μm (Fig. 2a) is observed at 1450 °C which is in line with our previous findings.

3.2.2. *Temperature dependent dielectric properties*

The temperature dependence of the relative permittivity (ε_r) of BCZT-xCeO_2 ceramics sintered at 1350 °C/4 h and measured at 1 kHz is shown in Fig. 5(a). Two peaks were observed for compositions in the range x = 0 - 0.1% that could be ascribed to the orthorhombic-tetragonal (O–T) and tetragonal-cubic (T - C) phase transitions [37]. To confirm the (O – T) phase transition near room temperature, loss tangent vs. temperature is plotted in Fig. 5(b). Clearly, there are three peaks observed in the range x = 0 - 0.1%. An additional peak near 0 °C, is ascribed to rhombohedral-orthorhombic (R – O) phase transition. As the Ce concentration is increased from x = 0% to x = 0.07% the dielectric peaks appear sharper and the value of maximum relative permittivity (at the Curie Temperature) is increased from 7000 to nearly 14,000. This also corresponds with an increase in grain size at this sintering temperature. For higher Ce concentrations (x > 0.1%) the maximum relative permittivity is drastically reduced (∼ 4000) which may be due to the smaller grain size of these samples. Fine grains have also been reported to shift T_C towards lower temperatures due to internal stress in the materials which are relieved by twinning mechanisms in larger grained samples [18,19].

As the CeO_2 content is further increased to x = 0.5% the T_C decreased gradually to an indicative value of ∼ 97.5 °C. Furthermore, the decrement of T_C may be related to the fine-grained specimens as previously reported with BCZT-Bi_2O_3 ceramics [38] and in agreement with the stress model [39], or to the cell volume effect evolved by grain sizes [40], and will form the basis of future studies. It can also be seen that the dielectric peaks for samples with composition x = 0.5, and 3% become diffuse around T_C (see Fig. 5a), in line with their smaller grain size. The dielectric peak in small grain sized specimens is correlated to a diffuse phase transition (DPT) that can be increased by minimizing the grain size [18,24]. The DPT occurs due to an existence of small micro regions in the ceramic, switching statistically from the paraelectric to ferroelectric state but which do not have any interactions with neighbouring regions what so ever [18], and which might indicate each region having an independent transition temperature.

A modified Curie Weiss law proposed by Uchino and Nomura, to describe the diffuseness of ferroelectric phase transition is expressed as:

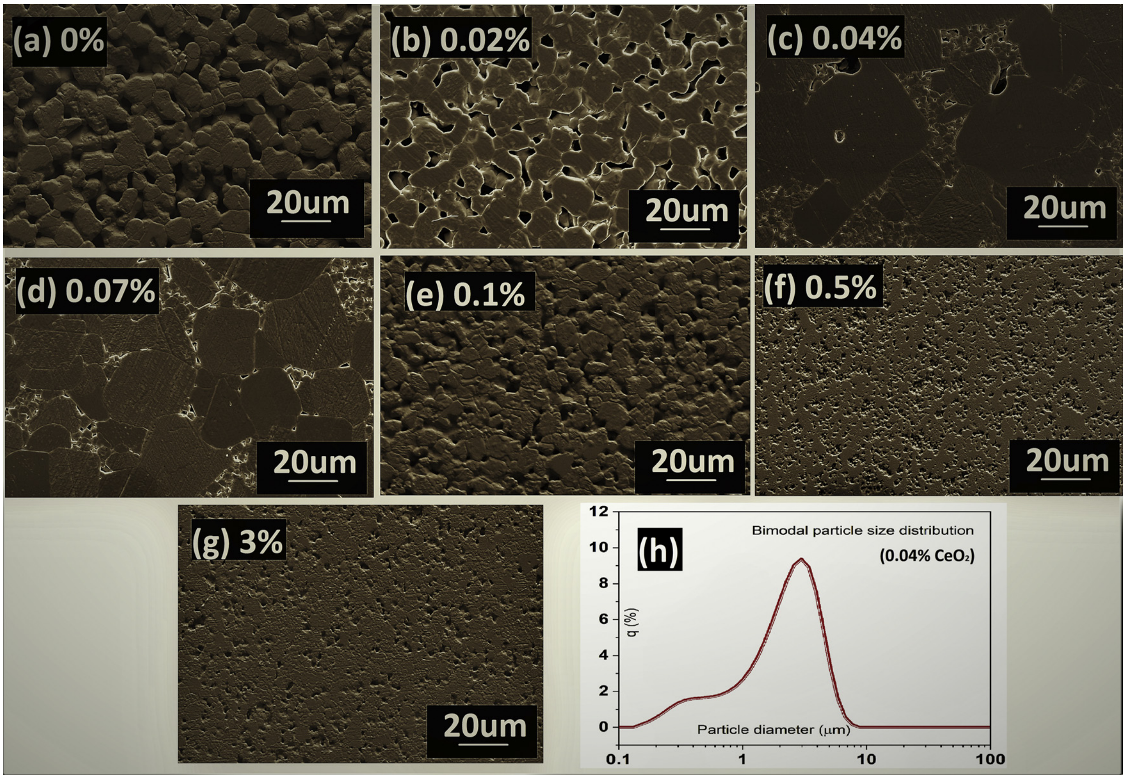

Fig. 4. SEM microstructures of BCZT - xCeO_2 samples for (a) x = 0% (b) x = 0.02% (c) x = 0.04% (d) x = 0.07% (e) x = 0.1% (f) 0.5% (g) x = 3% sintered at 1350 °C for 4 h, and (h) Particle size distribution map for the sample x = 0.04%.

$$1/\ \varepsilon_r - 1/\ \varepsilon_{r(max)} = (T - T_{max})^{\gamma} / C$$

where, T_{max} is the temperature at which the dielectric constant (ε_r) is maximum, γ is the diffusivity coefficient and C is the Curie Weiss constant. The limiting values of γ = 1 and γ = 2 follow the Curie Weiss equation for normal ferroelectric and ideal relaxor ferroelectric

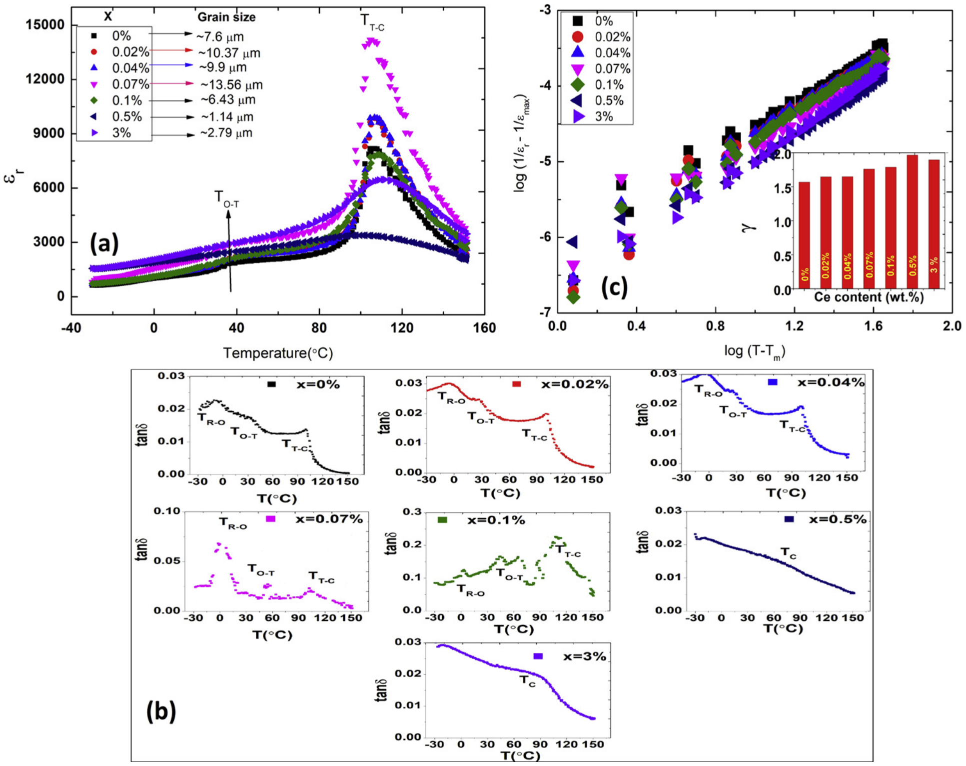

Fig. 5. (a) Temperature dependence of relative permittivity, and (b) Loss tangent (c) Plot between log ($1/\varepsilon_r$ - 1/ $\varepsilon_{r\ (max)}$) vs. log (T - T_{max}) of CeO_2-doped BCZT ceramics sintered at 1350 °C/4 h.

Table 1
The Curie–Weiss Temperature (T_o), the Curie–Weiss Constant (C) and the Diffuseness Coefficient (γ) for BCZT-xCeO_2 Ceramics sintered at 1350 °C/4 h and measured at 1 kHz and RT.

Ce Content (wt.%)	*0%*	*0.02%*	*0.04%*	*0.07%*	*0.10%*	*0.50%*	*3%*
Grain size (μm)	7.6 ± 2	10.37 ± 2	9.9 ± 2	13.56 ± 2	6.43 ± 3	1.14 ± 1	2.79 ± 2
T_0 [K]	373	374	375	380	364	320	358
C [10^5 K]	1.11	1.26	1.25	1.48	1.73	2.21	2.25
γ	1.56	1.64	1.64	1.75	1.78	1.96	1.89

transitions respectively. Fig. 5c shows a plot of log ($1/\varepsilon_r$ - $1/\ \varepsilon_{r\ (max)}$) versus log ($T$ - T_{max}) of BCZT-xCeO_2 ceramics sintered at 1350 °C/4 h. A linear relationship is obtained from the logarithmic plots for all samples. Finally, the slope of the fitting curves was used to determine the γ values which are shown in the inset of Fig. 5c. It can be noted that as the Ce content is increased, γ also increased and reaches a maximum of 1.96 indicating an occurrence of relaxor ferroelectric behaviour which could be partially caused by domain refinement and higher inner stress due to the small grain size [24,40]. In previous research, the γ values for the small grain size samples (0.4 and 1.5 μm) were observed as 1.96 and 1.76 respectively, while a γ value of 1.65 was calculated for larger grain size (10.8 μm) materials [24]. This agrees with our work. With increasing grain size, the γ value was reduced gradually from 1.96 (grain size, 1.14 ± 1 μm) to 1.64 (grain size, 13.56 ± 2 μm). The values of C, T_0 and γ with grain size are summarized in Table 1.

3.2.3. *X ray diffraction analysis*

X ray diffraction analyses carried out at room temperature are shown in Fig. 6(a). A pure perovskite phase is observed with no trace of secondary phase suggesting the Ce ions may diffuse into the BCZT solid solution, although any secondary phase may be below the detection limit. To analyze the influence of cerium on BCZT ceramics further analyses of the data has been carried out in the range of 2θ, 44° - 47° and 82° - 85° as shown in Fig. 6(b) and (c) respectively. The splitting of the 200 peak into (002)/(200) at around 45° along with the splitting of the (222) peak into (222)/(-222) peaks at around 83° suggests a mixture of tetragonal and rhombohedral phases for the samples with compositions x = 0 - 0.1%. However, single (200) and (222)/(-222) peaks split for samples with composition x = 0.5 & 3% indicate a single rhombohedral phase due to the small distortions which is discussed further below and is consistent with previous reports [41–43].

The occupancy of the two cation sites in the perovskite structure is often analyzed in terms of tolerance factors, with smaller ions [r (R^{4+})] < 0.087 nm occupying the B site and larger ions [r (R^{2+})] > 0.094 nm occupying the A site. It is possible for ions with intermediate sizes to occupy either or both sites [44,45]. Since Ce can exist in two valance states as Ce^{3+} (ionic radii, 0.134 nm) and Ce^{4+} (0.087 nm) [46], it is believed that Ce^{3+} ions may occupy the A site of either Ca^{2+} (0.134 nm) or Ba^{2+} (0.161 nm) and Ce^{4+} ions can occupy the B site of either Ti^{4+} (0.060 nm) and Zr^{4+} (0.072 nm). It is well known for $BaTiO_3$ that Ce^{3+} substitutes on the A site while Ce^{4+} substitutes on the B site, however self-compensation occurs when Ba/Ca = 1 [47].

According to the radius matching rule, it is inferred that neither Ce^{3+} or Ce^{4+} enters into the B-site of BCZT structure due to the small ionic radii of Ti^{4+}. If it replaces A-site (Ba/Ca) of the BCZT structure, the Ce acts as a donor dopant and cation vacancies are generated, in order to compensate the resulting positive charge and achieve equilibrium [48]. As a result, domain wall movement is facilitated so as to enhance piezoelectric properties. [48]. When the CeO_2 content is higher (> 0.1%), the concentration of Ce may not be homogeneous, with some segregation to the grain boundaries, which may pin the domains and, consequently, a decline in the piezoelectric properties were observed. However, we have no direct evidence of this, and is left for the future studies. The lattice parameters and phase structure of samples x = 0 - 0.1% are presented in Supplementary Table S2. Samples x > 0.1% were

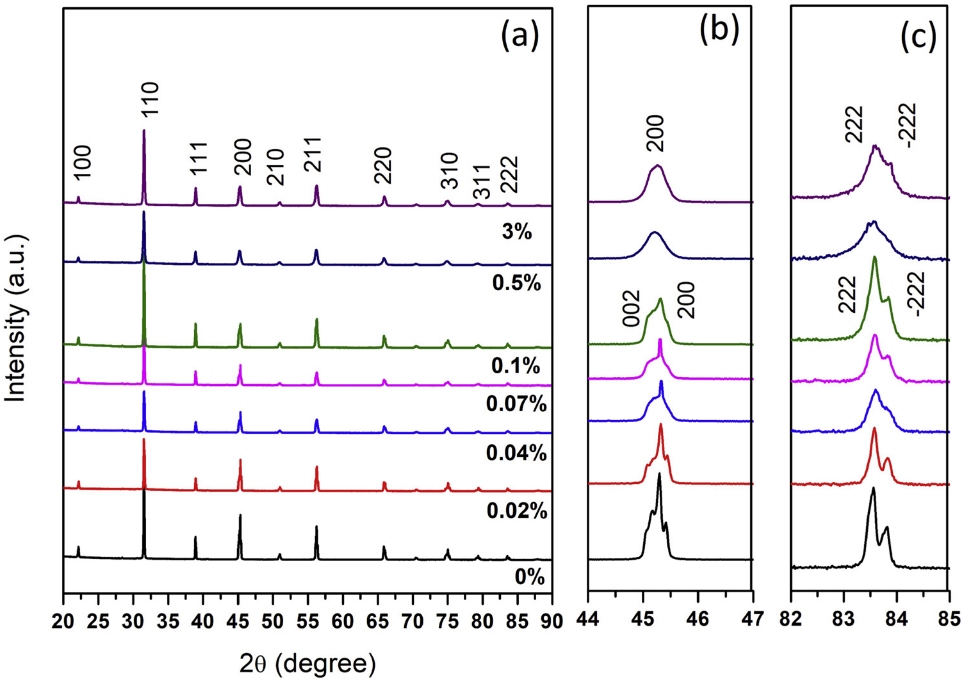

Fig. 6. Room temperature XRD patterns of BCZT-xCeO_2 ceramics (a) In the 2θ range of 20° - 90° (b) Enlarged view of 2 θ in the range 44° - 47° (c) Enlarged view of 2θ range of 82° - 85° sintered at 1350 °C/4 h.

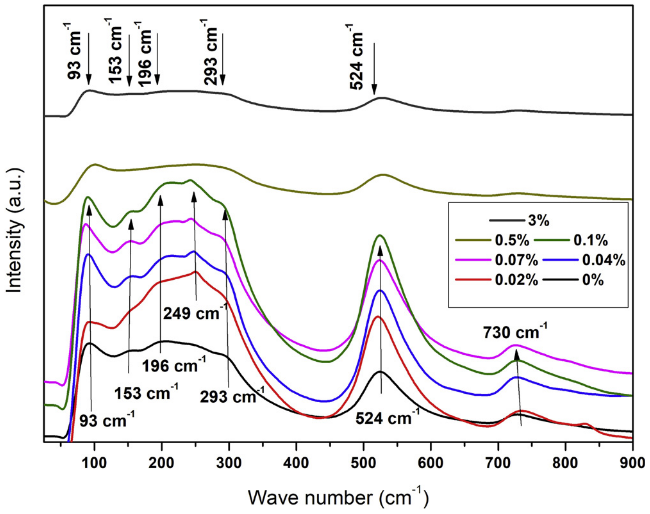

Fig. 7. Room temperature Raman spectra of BCZT-xCeO_2 ceramics sintered at 1350 °C/4 h.

identified to have either pseudo cubic or rhombohedral structures so are not included. It can be seen that the c/a ratio was in the range of 1.0035–1.0042 with coexistence of rhombohedral and tetragonal phase reflections indicating an existence of an MPB. As part of a study of undoped BCZT ceramics, we have previously reported a tetragonal phase with c/a ratio ˜ 1.0043 adjacent to an orthorhombic phase region [12] indicating nearly similar value for the sample x = 0.07% as presented in Supplementary Table S2. The data presented here are thus consistent with the formation of a bridging orthorhombic phase between the rhombohedral and tetragonal phase regions, although the orthorhombic phase was not separately identified, and could be a basis for the existence of the MPB previously published [49,50].

3.2.4. *Raman spectra*

The evolution of the Raman spectra of the BCZT-xCeO_2 ceramics sintered at 1350 °C/4 h and measured at room temperature are shown in Fig. 7. Modes at 93, 153,196, 249, 293, 524, 730 cm^{-1} are observed for samples with concentrations x = 0 - 0.1%. These modes are related to both the rhombohedral R phase, especially those at about 153 and 196 cm^{-1}, and the tetragonal T phases (including modes 249, 293, 524, 730 cm^{-1}) which agrees well with previous reports [51–54]. It has also been suggested that the presence of a mode at 490 cm^{-1} is important to confirm the orthorhombic O phase [53], but this has not been observed in the data reported here for the samples x = 0 - 0.1%. Therefore, it is believed that the R and T phases coexisted for the samples x = 0 - 0.1% at room temperature. Meanwhile, as the Ce concentration in increased to 0.5–3%, the intensity of the peaks gets weaker and low intensity modes at 293, 524 and 730 cm^{-1} indicate that the T phase has reduced although not vanished completely [55]. Furthermore, for the samples with composition x = 0.5, 3%, the overall intensity of all the peaks is very low, but those at 153 and 193 cm^{-1} can still be seen, although those at 249 cm^{-1} and 490 cm^{-1} have disappeared, indicating the presence of a single R phase. These results are in close agreement with the XRD analysis discussed earlier.

3.2.5. *Ferroelectric properties*

(P-E, I-E and S-E hysteresis loops)

The polarization vs electric field (P-E) and current vs electric field (I-E) loops for BCZT-xCeO_2 ceramics sintered at 1350 °C/4 h, and measured at 3 kV/mm are produced in Fig. 8. The bipolar strain values obtained from butterfly loops are also presented in Supplementary table S3 for the same conditions. The shape of the P-E loops varies with composition and the related current peaks are small and broad. P_r values increased with increasing CeO_2 content for the samples with compositions x = 0.02 - 0.07%. Simultaneously, a single sharp current peak was observed with an additional peak for the sample at the x = 0.04% composition, which may be ascribed to domain switching observed at $E = E_C$. This is typical for normal ferroelectric materials corresponding to a disturbance in the long-range ferroelectric ordering [56]. For the samples with compositions x = 0, 0.1 and 3% P-E hysteresis loops were observed with low P_r values and no sharp current peaks were seen, which may be ascribed to the lack of a switching processes. A broad P-E hysteresis loop and flat I-E platform with no obvious current peak was observed for the specimens of compositions x = 0.5 and 3%. This broad unsaturated hysteresis loop is indicative of a high leakage current which may guide the synthesis process of these ceramics.

P-E hysteresis loops with low P_r, values and also broad flat current peaks (as in the case of the x = 0.5, and 3% compositions) might be related to the emergence of a diffuse phase transition around T_C (see also Fig. 5a). With an introduction of CeO_2 concentrations (x > 0.1%), where domains in these compositions are frozen due to the finer grain size, inferior ferroelectric properties are observed. P_r, S and E_C values are summarized in Supplementary Table S3 for all samples. A maximum P_r value was observed for x = 0.07% as 16.32 μC/cm^2 with a corresponding E_C value as low as 2.58 kV/cm. High P_r, low E_C, low hysteresis loss, and well saturated hysteresis curves may be, at least partially, ascribed to the more homogeneous microstructure and grain sizes. The low E_C suggests a piezoelectrically "soft" material [9,57] which might be evidence for the Ce^{3+} acting as a donor dopant on the A site in the perovskite structure.

The unipolar strain plots of unpoled BCZT ceramics with different concentrations of CeO_2 and measured at room temperature and 1 kV/mm are produced in Fig. 9. In a practical sense, most piezoelectric actuators are operated mainly under unipolar electric field conditions as this mode of operation facilitates the use of proportional control systems [58]. The normalized strain (S_{max}/E_{max}) is calculated as the ratio of maximum electric field induced unipolar strain to the maximum electric field and is summarized in Supplementary Table S3. In the case of pure BCZT (x = 0%) the S_{max}/E_{max} was calculated to be about 481 pm/V whereas a much higher value of about 840 pm/V (comparable to the high-end values of soft PZT [8]) was observed for the x = 0.07% composition. This might indicate that the contribution of domain wall motion for this composition was a lot higher than that of pure BCZT (x = 0%). The large ferroelectric hysteresis response represents a large level of strain and can be aligned with the resultant piezoelectric response, which is primarily derived from extrinsic effects.

4. Conclusions

BCZT-xCeO_2 ceramics have been successfully fabricated by a conventional solid-state reaction route and a thorough systematic study has been reported. A detailed microstructural and structural characterisation has been presented along with corresponding functional properties including dielectric, ferroelectric and piezoelectric behaviour. With addition of CeO_2, significant effects have been observed with improved piezoelectric coefficients and higher planar coupling coefficients at reduced sintering temperatures. The influence of CeO_2 on the sintered grain size has also been elucidated. The properties were found to be optimised for the x = 0.07 wt.% composition sintered at 1350 °C, with values of d_{33} = 507 ± 20 pC/N, k_p = 51.8%, ε_r = 4091 ± 100, $\tan\delta = 0.02$, T_C = 104.6 °C, P_r = 13.58 μC/cm^2, E_C = 2.13 kV/cm, S_{max}/E_{max} = 840 pm/V and average grain size ∼ 13 μm being measured. Such property improvements at a low sintering temperature of 1350 °C/4 h may potentially be useful for the device fabrication.

Acknowledgements

The research described in this paper was financed by SoMoPro II as well as the Erasmus plus program. The Authors also wish to

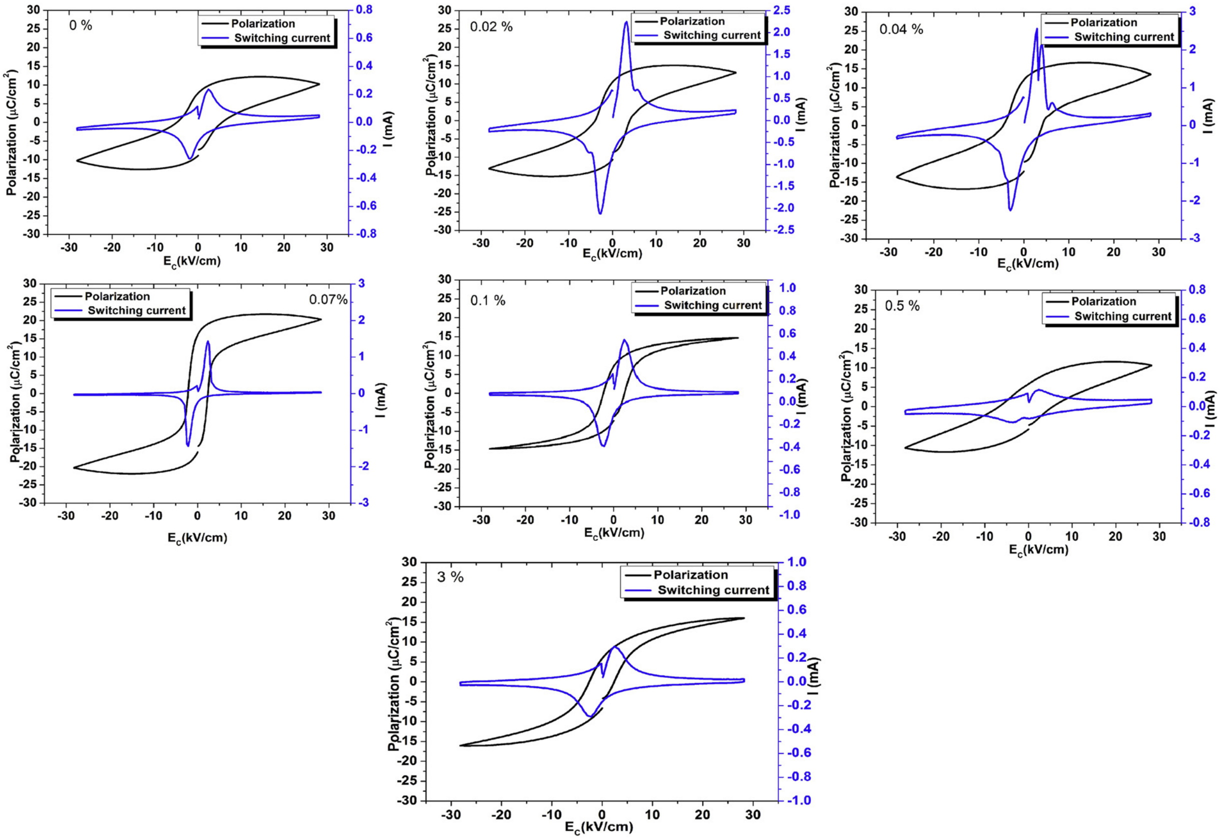

Fig. 8. Polarization and current vs electric field plots for BCZT-xCeO$_2$ ceramics sintered at 1350 °C/4 h and measured at room temperature.

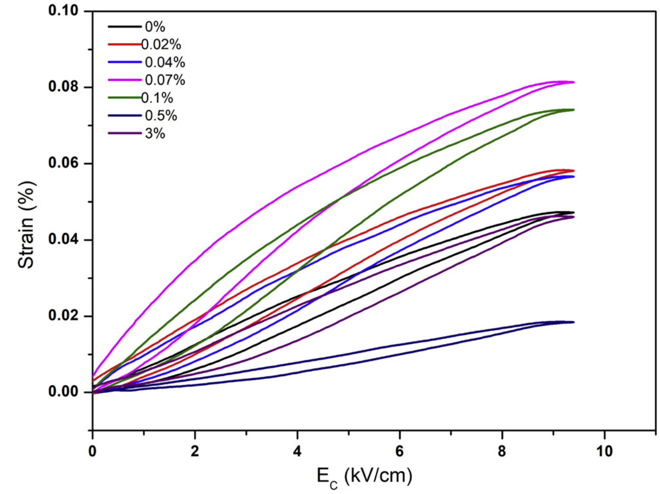

Fig. 9. Unipolar strain response of BCZT-xCeO$_2$ ceramics sintered at 1350 °C/4 h and measured at room temperature.

acknowledge financial support from Czech Ministry of Education in the frame of National Sustainability Program under grant LO1401 and Grant agency of Czech Republic under grant No. 18- 20498S. The Authors further acknowledge School of Metallurgy and Materials, University of Birmingham, UK and Department of Advanced Materials, CEITEC, Brno University of Technology, Czech Republic for the use of laboratory facilities.

Appendix A. Supplementary data

Supplementary data associated with this article can be found, in the online version, at https://doi.org/10.1016/j.materresbull.2019.02.031.

References

[1] Y. Saito, T. Tani, T. Nonoyama, K. Takatori, T. Homma, T. Nagaya, M. Nakamura, Lead-free piezoceramics, Nature 432 (2004) 84–87.
[2] EU-Commision Directive 2013/28/EU, Off. J. Eur. Union L135 (2013) 14–18.
[3] EU-Council Directive 89/677/EEC, Off. J. Eur. Commun L398 (1989) 19–23.
[4] EU-Commission Directive 2000/71/EC, Off. J. Eur. Commun. L287 (2000) 46–50.
[5] J. Wu, D. Xiao, J. Zhu, Potassium sodium niobate lead-free piezoelectric materials: past, present and future of phase boundaries, Chem. Rev. 115 (2015) 2559–2595.
[6] W. Jo, R. Dittmer, M. Acosta, J. Zang, C. Groh, E. Sapper, K. Wang, J. Rödel, Giant electric-field-induced strains in lead-free ceramics for actuator applications-status and perspective, J. Electroceram. 29 (2012) 71–93.
[7] M.D. Maeder, D. Damjanovic, N. Setter, Lead free piezoelectric materials, J. Electroceram. 13 (2004) 385–392.
[8] T.R. Shrout, S.J. Zhang, Lead free piezoelectric ceramics, J. Electroceram. 19 (2007) 113–126.
[9] W. Liu, X. Ren, Large piezoelectric effect in Pb-Free ceramics, Phys. Rev. Lett. 103 (2009) 257602.
[10] J. Rödel, W. Jo, K.T.P. Seifert, E.M. Anton, T. Granzow, D. Damjanovic, Perspective on the development of lead-free piezoceramics, J. Am. Ceram. Soc. 92 (2009) 1153–1177.
[11] J. Wu, D. Xiao, W. Wu, Q. Chen, J. Zhu, Z. Yang, J. Wang, Composition and Poling condition-induced electrical behavior of $(Ba_{0.85}Ca_{0.15})(Ti_{1-x}Zr_x)O_3$ lead-free piezoelectric ceramics, J. Eur. Ceram. Soc. 32 (2012) 891–898.
[12] Y. Bai, A. Matousek, P. Tofel, V. Bijalwan, B. Nan, H. Hughes, T.W. Button, (Ba,Ca)(Zr,Ti)O$_3$ Lead-Free Piezoelectric Ceramics-The Critical Role of Processing on Properties, Jr. Eur. Ceram. Soc. 35 (2015) 3445–3456.
[13] K. Castkova, K. Maca, J. Cihlar, H. Hughes, A. Matousek, P. Tofel, Y. Bai, T.W. Button, Chemical synthesis, sintering and piezoelectric properties of $Ba_{0.85}Ca_{0.15}Zr_{0.1T}i_{0.9}O_3$ lead-free ceramics, J. Am. Ceram. Soc. 98 (2015) 2373–2380.
[14] M.E.V. Castrejón, E. Morán, A.R. Montero, R.V. Ocampo, J.A.P. Jiménez, S.O.R. López, L. Pardo, Towards lead-free piezoceramics: facing a synthesis challenge, Materials 9 (2016) 21.
[15] J. Gao, D. Xue, W. Liu, C. Zhou, X. Ren, Recent progress on BaTiO$_3$-based piezoelectric ceramics for actuator applications, Actuators 6 (2017) 24.
[16] M. Acosta, N. Novak, V. Rojas, S. Patel, R. Vaish, J. Koruza, G.A. Rossetti Jr., J. Rodel, BaTiO3-based piezoelectrics: fundamentals, current status, and perspectives, App. Phys. Rev. 4 (2017) 041305.
[17] A.R. Montero, F.R. Marcos, L. Pardo, A.D. Campo, R.L. Juarez, M.E.V. Castrejon, Electric field effect on the microstructure and properties of $Ba_{0.9}Ca_{0.1}Ti_{0.9}Zr_{0.1}O_3$ (BCTZ) lead-free ceramics, J. Mater. Chem. A 6 (2018) 5419–5429.

[18] H.T. Martirena, J.C. Burfoot, Grain-size effects on properties of some ferroelectric ceramics, J. Phys. C: Sol. St. Phys. 7 (1974) 3182–3192.

[19] M.H. Frey, D.A. Payne, Grain-size effect on structure and phase transformations for barium titanate, Phys. Rev. B 54 (1996) 3158–3167.

[20] D. Berlincourt, O.E. Mattiat (Ed.), Ultrasonic transducer materials: piezoelectric crystals and ceramics, Plenum, London, 1971, pp. 63–124 Ch.2.

[21] T. Kanata, T. Yoshikawa, K. Kubota, Grain-size effects on dielectric phase transition of $BaTiO_3$ ceramics, Sol. St. Com. 62 (1987) 765–767.

[22] X.G. Tang, H.L.W. Chan, Effect of grain size on the electrical properties of (Ba,Ca)(Zr,Ti) O_3 relaxor ferroelectric ceramics, J. Appl. Phys. 97 (2005) 034109.

[23] J.P. Praveen, T. Karthik, A.R. James, E. Chandrakala, S. Asthana, D. Das, Effect of poling process on piezoelectric properties of sol-gel derived BZT–BCT ceramics, J. Eur. Ceram. Soc. 35 (2015) 1785–1798.

[24] J. Hao, W. Bai, W. Li, J. Zhai, Correlation between the microstructure and electrical properties in high-erformance $(Ba_{0.85}Ca_{0.15})$ $(Zr_{0.1}Ti_{0.9})$ O_3 lead-free piezoelectric ceramics, J. Am. Ceram. Soc. 95 (2012) 1998–2006.

[25] J. Wu, D. Xiao, W. Wu, Q. Chen, J. Zhu, Z. Yang, J. Wang, Role of room-temperature phase transition in the electrical properties of (Ba, Ca)(Ti, Zr)O3 ceramics, Scrp. Mat. 65 (2011) 771–774.

[26] Y. Cui, X. Liu, M. Jiang, X. Zhao, X. Shan, W. Li, C. Yuan, C. Zhou, Lead-free $Ba_{0.85}Ca_{0.15}Ti_{0.9}Zr_{0.1}O_3$-$CeO_2$ ceramics with high piezoelectric coefficient obtained by low-temperature sintering, Ceram. Int. 38 (2012) 4761–4764.

[27] E. Chandrakala, J.P. Praveen, D. Das, Effect of poling process on piezoelectric properties of BCZT – 0.08 wt.% CeO_2 lead-cree ceramics, AIP Conf. Proc. 1728 (2016) 020502, , https://doi.org/10.1063/1.4946553.

[28] T. Chen, T. Zhang, G. Wang, J. Zhou, J. Zhang, Y. Liu, Effect of CuO on the Microstructure and Electrical Properties of $(Ba_{0.85}Ca_{0.}15)(Ti0_{.90}Zr_{0.1})O_3$ piezo ceramics, J. Mater. Sci. 47 (2012) 4612–4619.

[29] Y. Cui, C. Yuan, X. Liu, X. Zhao, X. Shan, Lead-free $(Ba_{0.85}Ca_{0.15})(Ti_{0.9}Zr_{0.1})O_3$-$Y_2O_3$ ceramics with large piezoelectric coefficient obtained by low-temperature sintering, J. Mater. Sci. 24 (2013) 654–657.

[30] H.L. Sun, Q.J. Zhen, Y. Wan, Y. Chen, X. Wu, K.W. Kwok, H.L.W. Chan, D.M. Lin, Correlation of grain size, phase transition and piezoelectric properties in $Ba_{0.85}Ca_{0.15}Ti_{0.90}Zr_{0.10}O_3$ ceramics, J. Mater. Sci. Mater. Electr. 26 (2015) 5270–5278.

[31] V. Bijalwan, P. Tofel, J. Erhart, K. Maca, The complex evaluation of functional properties of nearly dense BCZT ceramics and their dependence on the grain size, Ceram. Int. 45 (2019) 317–326.

[32] Y. Tan, J. Zhang, C. Wang, G. Viola, H. Yan, Enhancement of electric field-induced strain in BaTiO3 ceramics through grain size optimization, Phys. Status Solidi A 212 (2015) 433–438.

[33] Y. Tan, J. Zhang, Y. Wu, C. Wang, V. Koval, B. Shi, H. Ye, R. McKinnon, G. Viola, H. Yan, Unfolding grain size effects in barium titanate ferroelectric ceramics, Sci. Rep. 5 (2015) 9953.

[34] S.J.L. Kang, Sintering, Densification, Grain Growth and Microstructure, Elsevier Butterworth-Heinemann publication, 2005, pp. 89–135 Chapter 9.

[35] Y. Li, W. Chen, Q. Xu, J. Zhou, Y. Wang, H. Sun, Piezoelectric and dielectric properties of CeO_2-Doped $Bi_{0.5}Na_{0.44}K_{0.06}TiO_3$ lead-free ceramics, Ceram. Internat 33 (2007) 95–99.

[36] D. Gao, K.W. Kwok, D. Lin, H.L.W. Chan, Microstructure, Electrical Properties of CeO_2-Doped $(K_{0.5}Na_{0.5})$ NbO_3 Lead-Free Piezoelectric Ceramics, J. Mater. Sci. 44 (2009) 2466–2470.

[37] L. Zhang, M. Zhang, L. Wang, C. Zhou, Z. Zhang, Y. Yao, L. Zhang, D. Xue, X. Lou, X. Ren, Phase transitions and the piezoelectricity around morphotropic phase boundary in $Ba(Zr_{0.2}Ti_{0.8})O_3$-$x(Ba_{0.7}Ca_{0.3})TiO_3$ lead-free solid solution, Appl. Phys. Lett. 105 (2014) 162908.

[38] R. Hayati, M.A. Bahrevar, T. Ebadzadeh, V.R.N. Novak, J. Koruza, Effects of Bi_2O_3 additive on sintering process and dielectric, ferroelectric, and piezoelectric properties of (Ba0.85Ca0.15)(Zr0.1Ti0.9)O3 lead free piezoelectric ceramics, J. Eur. Ceram. Soc. 36 (2016) 3391–3400.

[39] W.R. Buessem, L.E. Cross, A.K. Goswami, Phenomenological theory of high permittivity in fine-grained barium titanate, J. Am. Ceram. Soc. 49 (1966) 33–36.

[40] L. Zhang, W.L. Zhong, Y.G. Wang, P.L. Zhang, The cell volume effect in barium strontium titanate, Sol. State Commun. 104 (1997) 263–266.

[41] M.C. Ehmke, S.N. Ehrlich, J.E. Blendell, K.J. Bowman, Phase coexistence and ferroelastic texture in high strain $(1\text{-}x)Ba(Zr_{0.2}Ti_{0.8})O_3$– $(Ba_{0.7}Ca_{0.3})TiO_3$ piezoceramics, J. Appl. Phys. 111 (2) (2012) 124110.

[42] A.B. Haugen, J.S. Forrester, D. Damjanovic, B. Li, K.J. Bowman, J.L. Jones, Structure and Phase Transitions in $0.5(Ba_{0.7}Ca_{0.3}TiO_3)$-$0.5(BaZr_{0.2}$- $Ti_{0.8}O_3)$ from -100°C to 150°C, J. Appl. Phys. 113 (1) (2013) 014103.

[43] R. sasaki, R. Suzuki, S. Uraki, H. Kakimoto, T. Tsurumi, Low temperature sintering of alkaline niobate based piezoelectric ceramics using sintering aids, J. Ceram. Soc. Jpn. 116 (2008) 1182–1186.

[44] Y. Tsur, T.D. Dunbar, C.A. Randall, Crystal and Defect Chemistry of Rare Earth Cations in $BaTiO_3$, J. Electroceram. 7 (2001) 25–35.

[45] W. Li, Z. Xu, R. Chu, P. Fu, G. Zang, Temperature stability in Dy-Doped $(Ba_{0.99}Ca_{0.01})$ $(Ti_{0.98}Zr_{0.02})$ O_3 lead-free ceramics with high piezoelectric coefficient, J. Am. Ceram. Soc. 94 (2011) 3181–3183.

[46] R.D. Shannon, Revised effective ionic radii and systematic studies of interatomic distances in Halides and chalcogenides, Acta Cryst. 751-767 (1976) A32.

[47] D. Makovec, Z. Samardzija, D. Kolar, Solid Solubility of Cerium in $BaTiO_3$, J. sol. St. chem. 123 (1996) 30–38.

[48] M. Chena, Q. Xub, B.H. Kima, B.K. Ahna, Wen Chen, Effect of CeO_2 addition on structure and electrical properties of $(Na_{0.5}Bi_{0.5})_{0.93}Ba_{0.07}TiO_3$ ceramics prepared by citric method, Mater. Res. Bull. 43 (2008) 1420–1430.

[49] M. Acosta, N. Novak, W. Jo, J. Rodel, Relationship between electromechanical properties and phase diagram in the $Ba(Zr_{0.2}Ti_{0.8})O_3$–$x(Ba_{0.7}Ca_{0.3})TiO_3$ lead-free piezocermic, Acta Mater. 80 (2014) 48–55.

[50] D.S. Keeble, F. Benabdallah, P.A. Thomas, M. Maglione, J. Kreisel, Revised structural phase diagram of $(Ba_{0.7}Ca_{0.3}TiO_3)$-$(BaZr_{0.2}Ti_{0.8}O_3)$, Appl. Phys. Lett. 102 (2013) 092903.

[51] S. Miao, J. Pokorny, U.M. Pasha, O.P. Thakur, D.C. Sinclair, I.M. Reaney, Polar order and diffuse scatter in $Ba(Ti_{1-x}Zr_x)O_3$ ceramics, J. Appl. Phys. 106 (11) (2009) 114111.

[52] M. Deluca, L. Stoleriu, L.P. Curecheriu, N. Horchidan, A.C. Ianculescu, C. Galassi, High-field dielectric properties and Raman spectroscopic investigation of the ferroelectric to relaxor crossover in $BaSn_xTi_{1-x}O_3$ ceramics, J. Appl. Phys. 111 (8) (2012) 08410217.

[53] L. Zhao, B.P. Zhang, P.F. Zhou, L.F. Zhu, J.F. Li, Effect of Li_2O addition on sintering and piezoelectric properties of $(Ba,Ca)(Ti,Sn)O_3$ lead-free piezoceramics, J. Eur. Ceram. Soc. 35 (2015) 533–540.

[54] P.S. Dobal, R.S. Katiyar, Studies on ferroelectric perovskites and Bi-layered compounds using micro-raman spectroscopy, J. Raman Spectrosc. 33 (6) (2002) 405–423.

[55] R. Farhi, M. ElMarssi, A. Simon, J. Ravez, A Raman and Dielectric Study of Ferroelectric $Ba(Ti_{1-x}Zr_x)O_3$ Ceramicss, Eur. Phys. J. B 9 (4) (1999) 599–604.

[56] W. Zhao, R. Zuo, D. Zheng, L. Longtu, Dielectric relaxor evolution and frequency insensitive giant strains in $(Bi_{0.5}Na_{0.5})TiO_3$-Modified $Bi(Mg_{0.5}Ti_{0.5})O_3$–$PbTiO_3$ ferroelectric ceramics, J. Am. Ceram. Soc. 97 (2014) 1855–1860.

[57] A.R. Montero, L. Pardo, R.L. Juárez, A.M. González, S.O. Rea- López, M.P. Cruz, M.E.V. Castrejón, Sub-10μm grain size, $Ba_{1-x}Ca_xTi_{0.9}Zr_{0.1}O_3$ ($x = 0.10$ and $x = 0.15$) Piezoceramics Processed using a reduced Thermal Treatment, Sm. Mater. Struct 24 (2015) 065033.

[58] K.T. Lee, J.S. Park, J.H. Cho, Y.H. Jeong, J.H. Paik, J.S. Yun, The study on the phase transition and piezoelectric properties of $Bi_{0.5}(Na_{0.78}K_{0.22})_{0.5}TiO_3$-$LaMnO_3$ lead-free piezoelectric ceramics, J. Kor. Ceram. Soc. 52 (2015) 237–242.

Received: 29 August 2019 | Revised: 8 October 2019 | Accepted: 22 October 2019
DOI: 10.1002/jemt.23402

MICROSCOPY RESEARCH & TECHNIQUE WILEY

RESEARCH ARTICLE

Scanning electron microscopy and energy-dispersive X-ray spectroscopy analysis of electrochemically etched graphite tips created from pencil lead

Dinara Sobola | **Pavel Kaspar** | **Pavel Tofel** | **Vladimír Holcman**

Department of Physics, Faculty of Electrical Engineering and Communication, Brno University of Technology, Brno, Czech Republic

Correspondence
Dinara Sobola, Department of Physics, Faculty of Electrical Engineering and Communication, Brno University of Technology, Technicka 2848/8, Brno, 61600, Czech Republic.
Email: sobola@feec.vutbr.cz

Funding information
National Sustainability Program, SIX, Grant/Award Number: LO1401

Review Editor: Paul Verkade

Abstract

Modern day pencil lead is a material of many possibilities. Manufacture process is fast, easy, and well established, yet the full potential of its use still remains to be uncovered. Graphite content ratio to binding clays determines basic properties of the lead like its toughness and color, but more interesting qualities like conductivity and reactivity as well. Properly employed electrochemical etching with a bubble membrane creates sharp and smooth graphite tips, which can be, given enough graphite content, used as probes in several measurement techniques. Observing and adjusting the tip creation process and the results for use in further research are the objectives of this paper.

KEYWORDS

EDX, graphite, pencil lead, SEM

1 | INTRODUCTION

Interest in graphite structures has grown continuously ever since its first applications. This caused intensive research in the field, ranging from more theoretical and mathematical approach to carbon (Cataldo, Graovac, & Ori, 2011) through nanoscale applications (Popov, 2004) to purely practical use in everyday life. One of the more unusual areas of research focuses on pencil leads, an object known in its current form since its development in 1794 by Nicolas-Jacques Conté. He created a method of pencil lead manufacture, where graphite powder is mixed with clays and then baked (Cain, Cantu, Brunelle, & Lyter, 1978; Voice, 1949). The ratio of graphite powder to clay determines its blackness and toughness. From the point of view of today's science pencil leads, an object so easily manufactured and in such high numbers, have interesting properties that beg to be exploited. From the structural point of view, commonly used graphite of higher quality in nanoscale applications like Highly oriented pyrolytic graphite and highly annealed pyrolytic graphite are ordered in layers (Ţălu, 2015) in contrast to the polymer-glued carbon flakes of the pencil lead (Marchand et al., 1984). Because of the nature of its structure there are also conductive graphite laminar crystallites distributed through the pencil lead (Khairnar, Dharmadhikari, & Joag, 1989). The material also carries hydrophobic properties on pencil-drawn surfaces due to the presence of polymer clay and nano-texture created by lead material deposition. Research has already been done on pencil-on-paper approach for sensor design (Kurra & Kulkarni, 2013) and electrodes for strain gauges and chemiresistors (Lin, Zhao, Kim, & Huang, 2014). Some studies have also used either lightly altered or unaltered pencil lead as components in batteries, resistors, transistors (Kurra & Kulkarni, 2013), or even sources for field emission (Knapek, Sobola, Tomanek, Pokorna, & Urbanek, 2017). In other example, break of a pencil lead is a source for a test signal in acoustic emission systems for sensor calibration and tuning (Quang-Khang, Minh-Dung, Matsumoto, & Shimoyama, 2015).

This study focuses on the unexplored application of electrochemical etching on pencil lead in order to create a functional, cheap, and easy to produce probes for local electrical measurements at nanoscale. To achieve this, the composition of the pencil lead is studied and the optimal parameters and conditions for the etching process are developed.

2 | MATERIALS AND METHODS

The etching process on the electrodes was done in electrochemical etching apparatus (Figure 1). One electrode holds the pencil lead, while the other in the form of a circular aperture contains a bubble-like membrane of the NaOH (PENTA production) solution. Electrochemical etching takes place at the contact of the membrane and a middle of a pencil lead with the assistance of gravity (surrounding temperature was 23°C and humidity 60%). The etching process was performed at a voltage of 12 V of direct current for all the samples. Resulting etched samples were evaluated by scanning electron microscopy (SEM) for topography and energy-dispersive X-ray spectroscopy (EDX) for chemical composition, using Tescan LYRA3 SEM with EDX detector Oxford Instruments X-Max 50. Parameters of the SEM scanning were set at voltage of 10 kV and Secondary electron detection mode, parameters of EDX electron beam were set at voltage of 10 kV and spot size of 13 nm.

Samples used in the measurement were pencil leads of the KOH-I-NOOR brand with hard and black hardness on the graphite grading scale, which corresponds with composition of 68% graphite, 26% clay, and 5% wax (Navrátil et al., 2016). Two sets of pencil lead for mechanical pencil were tested, divided by diameter, specifically 0.3 and 0.7 mm. The samples were divided into three groups by the NaOH concentration. Group 1 was etched in a solution of 0.6 g NaOH in 10 ml of demi water, Group 2 in 1 g of NaOH in 10 ml of demi water, and Group 3 in 1.5 g of NaOH in 10 ml of demi water. All three groups contained both 0.3 and 0.7 mm thick pencil leads. Groups 1 to 3 were exposed to the electrochemical etching process for as long as was required for the pencil lead to erode in the middle and for the bottom part to drop off, thus forming the tip. Use of this type of bubble membrane provides very sharp and smooth tips in an apparatus that is easy and inexpensive to set up.

Second type of measurement was performed only on 0.3 mm thick pencil leads in 1 g NaOH in 10 ml demi water over 2, 3, and 7 min of exposure, to observe the effect of etching time on the material.

3 | RESULTS AND DISCUSSION

The etching process in different concentrations of NaOH solution resulted in different shapes of the tips. The highest concentration of NaOH caused the tip of the 0.7 mm thick pencil lead to appear deformed and rough (Figure 2), while the lowest concentration provided the smoothest overall shape. In this case the shape and topography of sample from Group 3 (etched by highest concentration of NaOH) is unsuitable for use as a probe of any kind, because a certain level of smoothness and shape regularity is required. Results from the thinner pencil lead samples however showed the reverse trend in shapes. Etching in higher concentration yielded tips with smoother surface (Figure 3), than in lower concentration of NaOH. This is in fact in a direct dependence on the thickness of the pencil lead. In the process of etching the material is dissolved into the etching membrane. Higher thickness of pencil lead means that there is more to dissolve before the bottom part of the lead drops off and a tip is formed. This extra dissolved material will irregularly deposit itself back onto the pencil lead, forming the topographical anomalies on an otherwise sharp tip, as seen in Figure 2 on the right. Smaller thickness of pencil lead means a higher chance that the etching membrane will not get saturated by dissolved material and that the back-deposition process will not occur.

Figure 4 shows progress of etching of a 0.3 mm thick pencil lead in a 1 g NaOH in 10 ml demi water solution over time. The thinning process does not follow a linear progression but slows down over the course of etching. To achieve a full drop-off of the bottom part of the lead, around 15 min was required. The timing is not exactly the same every attempt based on many variables, including small inaccuracies in solution concentration, current fluctuations, and others. Deviation of time required to achieve a full drop-off/tip forming is approximately 1 min.

Because the goal was to create a sharp and smooth tip, the apex of the tip needed to be examined on its own. Figures 5–7 show the tips of samples 1 to 3 of the 0.3 mm thick pencil lead. Result of the first sample (Figure 5) is very rough and uneven and the apex is not solitary, making the tip unviable for use. The occurrence of two apices is not guaranteed to happen at every attempt but given the roughness of the tip and the overall progress of etching by small concentration of NaOH the resulting tips are unlikely to be reliably suitable for use. Two higher concentrations of etchant, samples 2 and 3, produce smoother tips (Figures 6 and 7), both of which have a clear and sharp apex and appear suitable for use. Choosing a specific concentration

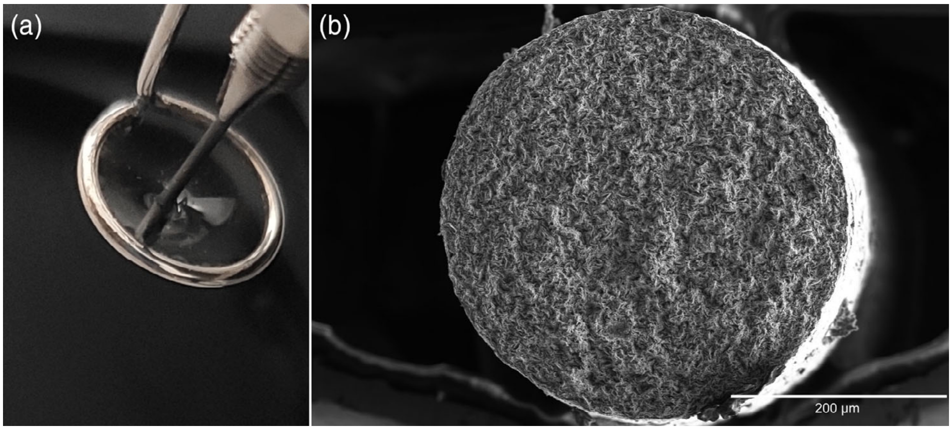

FIGURE 1 Detail of the electrochemical etching device membrane-lead contact (left) and graphite pencil lead cross section (right) [Color figure can be viewed at wileyonlinelibrary.com]

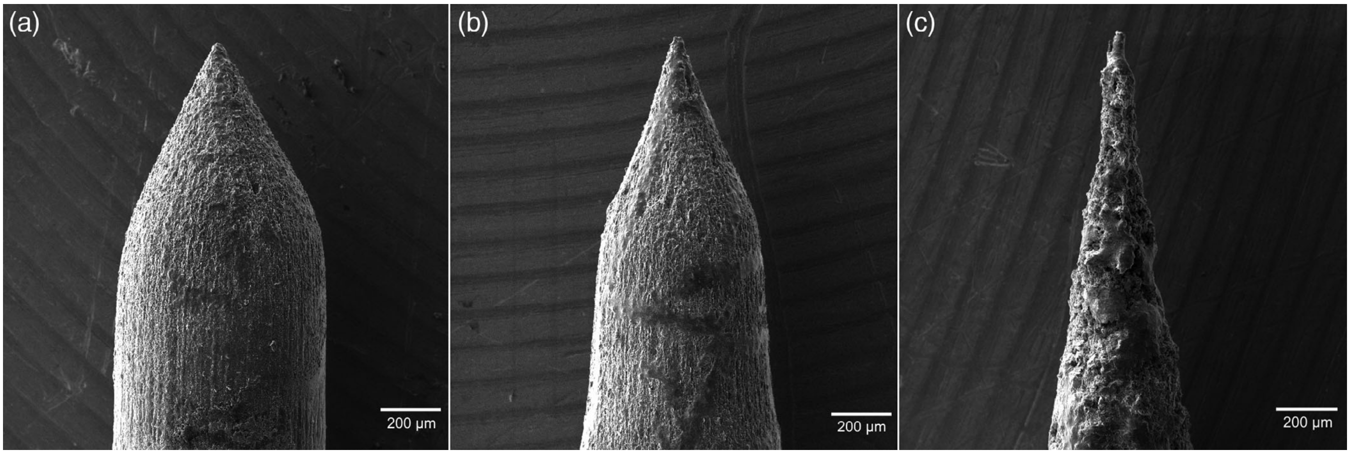

FIGURE 2 Etched tip of the 0.7 mm thick pencil lead, sample groups 1–3 from left to right, captured at working distance of 8.6 mm

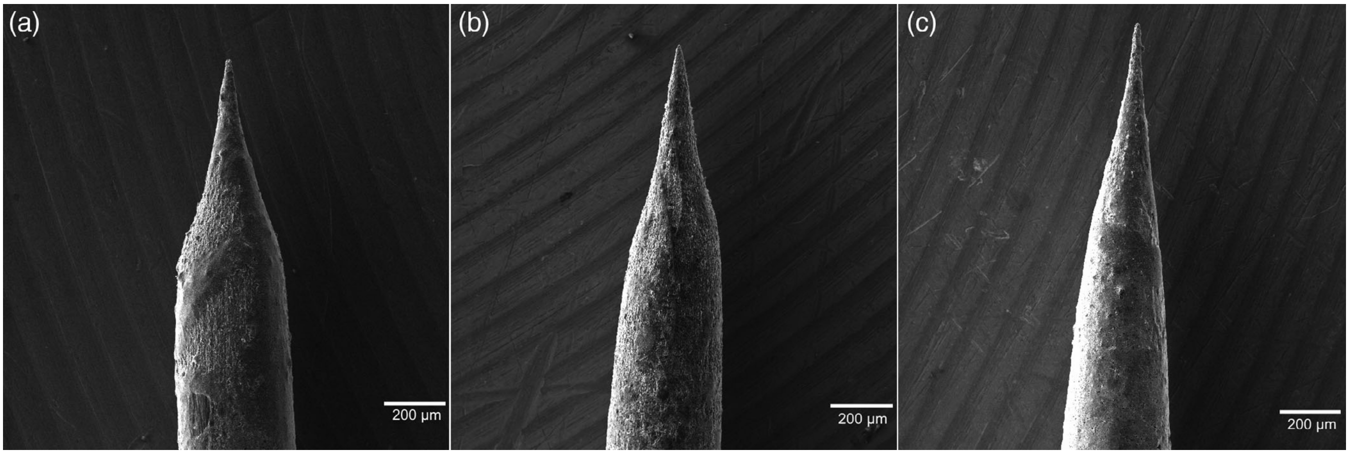

FIGURE 3 Etched tip of the 0.3 mm thick pencil lead, sample groups 1–3 from left to right, captured at working distance of 9 mm

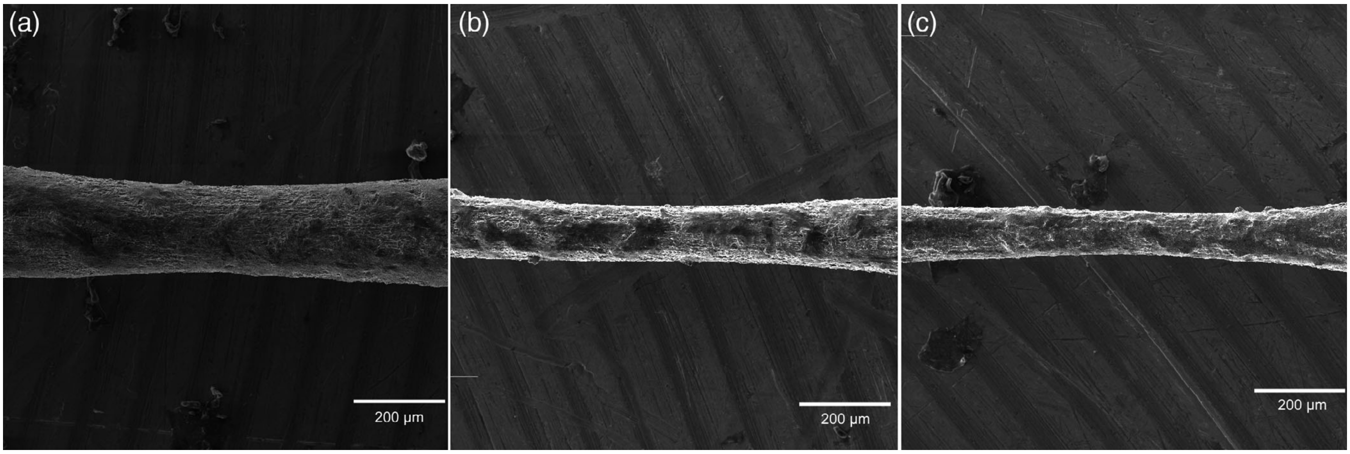

FIGURE 4 Etching progress over time, 2 min (left), 3 min (middle), and 7 min (right), captured at working distance of 11 mm

FIGURE 5 Closeup of the 0.3 mm thick pencil lead tip etched in 0.6 g NaOH in 10 ml demi water in microscale (left) and nanoscale (right), captured at working distance of 9 mm

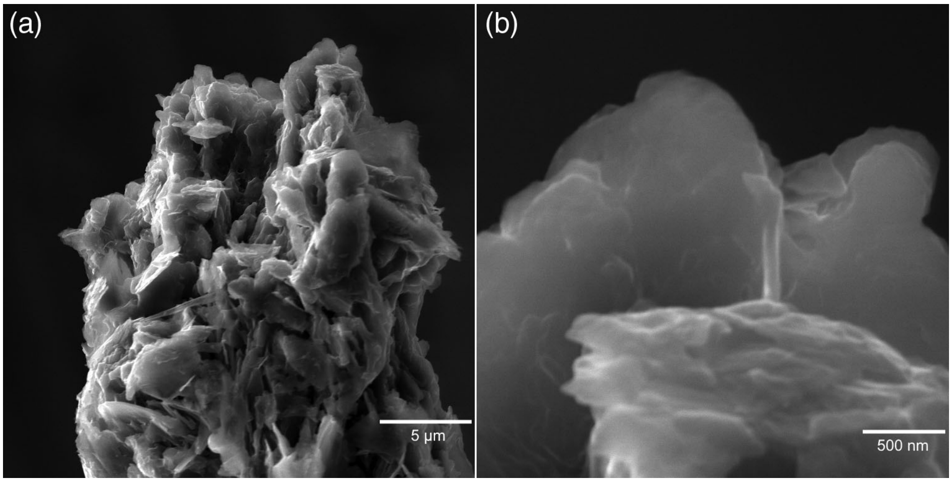

FIGURE 6 Closeup of the 0.3 mm thick pencil lead tip etched in 1 g NaOH in 10 ml demi water in microscale (left) and nanoscale (right), captured at working distance of 9 mm

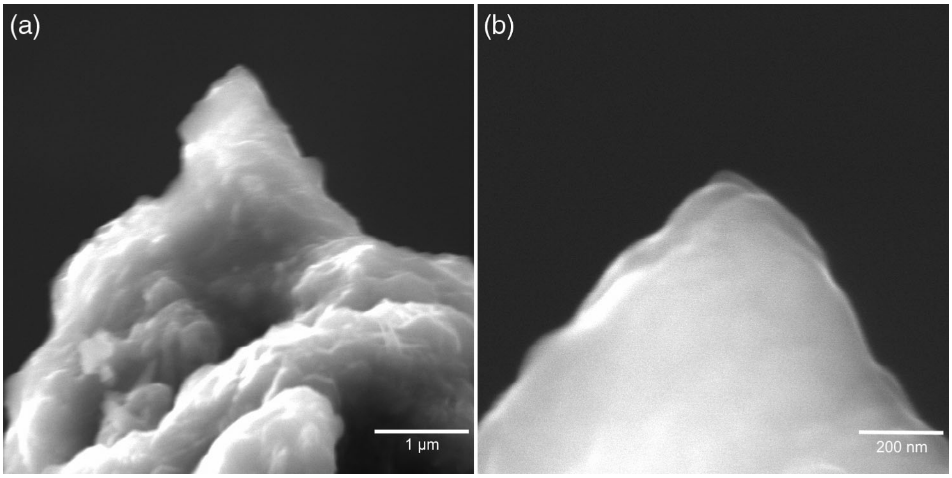

FIGURE 7 Closeup of the 0.3 mm thick pencil lead tip etched in 1.5 g NaOH in 10 ml demi water in microscale (left) and nanoscale (right), captured at working distance of 9 mm

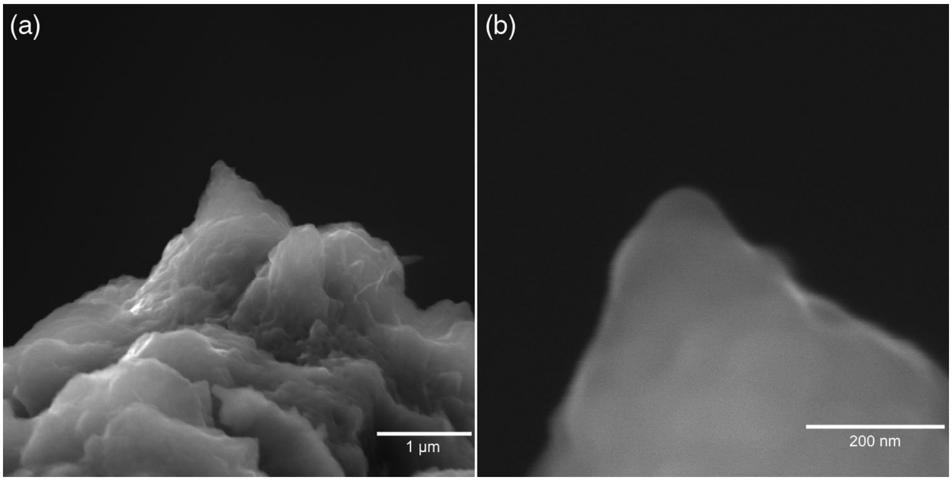

would be determined by required tip smoothness, apex sharpness, and even expected chemical composition of the sample (Figures 8 and 9). These requirements differ with intended use.

The EDX spectra of 0.3 mm thick pencil lead follows a steady progress over the different NaOH concentrations, as seen in Figure 8. While the presence of carbon stays approximately the same, presence of oxygen and natrium increases with etching agent concentration. The thicker, 0.7 mm pencil leads behave quite differently though (Figure 9). Presence of oxygen and natrium decreases with increasing etchant concentration, a reverse phenomenon from the 0.3 mm thick pencil lead. At the highest concentration there is a visible drop in the presence of carbon, and a significant increase of oxygen and natrium

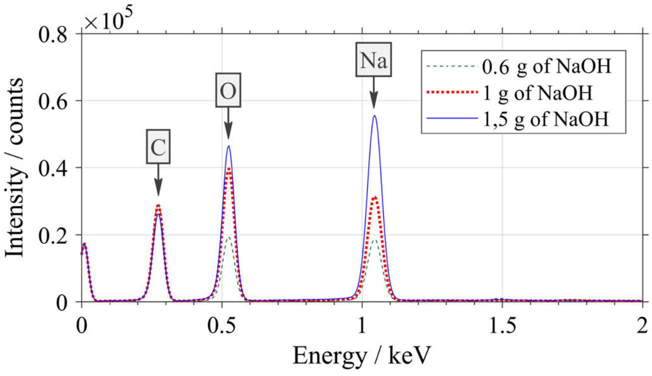

FIGURE 8 Energy-dispersive X-ray spectroscopy (EDX) spectra comparison of the 0.3 mm thick pencil lead in different NaOH solution concentrations [Color figure can be viewed at wileyonlinelibrary.com]

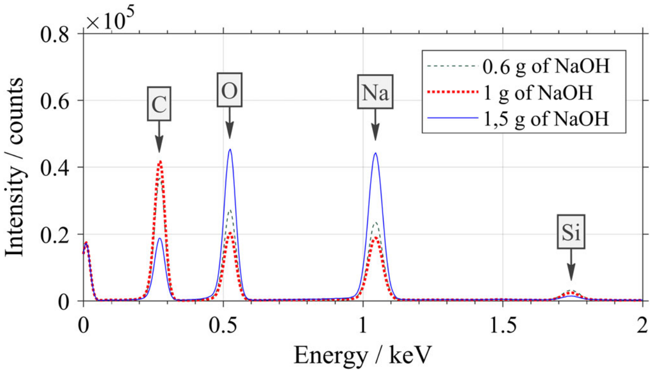

FIGURE 9 Energy-dispersive X-ray spectroscopy (EDX) spectra comparison of the 0.7 mm thick pencil lead in different NaOH solution concentrations [Color figure can be viewed at wileyonlinelibrary.com]

as well. This corresponds with the deposition of dissolved material mixed with the etching agent at the surface of the tip, which is responsible for the rough and uneven appearance of the tip, as seen in Figure 2 and described at the start of this chapter. Trace presence of silicon in the pencil lead composition can be attributed to clays used to form the pencil lead itself.

The issue with deposition of etching agent and dissolved pencil lead material back on the tip makes using the thicker pencil lead suboptimal in the presented method. This is the reason, why images of etching progression (Figure 4) and tip closeups (Figures 5–7) are of 0.3 mm thick pencil lead only.

4 | CONCLUSION

Concentration of the etching agent directly affects the overall shape of resulting tip and apex of the samples. The smallest concentration, 0.6 g NaOH in 10 ml of demi water does produces rough and uneven tips unsuitable for most uses. Tips etched in 1 g of NaOH in 10 ml demi water and those etched in 1.5 g NaOH in 10 ml demi water reach high enough sharpness and smoothness for potential use, but the specifics depend on the intended use, as every method requires components of different properties. Higher concentrations of etching agent leave greater deposits on the pencil leads, as demonstrated by EDX, and must therefore be properly cleaned before potential use. Under methodology specified here it is possible to achieve smooth and sharp tips because of the bubble membrane electrochemical etching, but samples of greater diameter (in this case 0.7 mm thick pencil lead) are unsuitable. The extra material that needs to be removed to form a tip is dissolved into the etching membrane and is redeposited onto the surface of the tip, thus reducing the final quality and usability of the resulting sample.

ACKNOWLEDGMENTS

Research described in this paper was financed by the National Sustainability Program under grant LO1401. For the research, infrastructure of the SIX Center was used.

ORCID

Dinara Sobola https://orcid.org/0000-0002-0008-5265
Pavel Kaspar https://orcid.org/0000-0003-1757-2382

REFERENCES

Cain, S., Cantu, A., Brunelle, R., & Lyter, A. (1978). A scientific study of pencil lead components. *Journal of Forensic Sciences*, *23*, 643–661. https://doi.org/10.1520/JFS10720J

Cataldo, F., Graovac, A., & Ori, O. (Eds.). (2011). *The mathematics and topology of fullerenes* (4th ed.). Dordrecht: Springer.

Khairnar, R. S., Dharmadhikari, C. V., & Joag, D. S. (1989). Pencil lead tips: A field ion and field electron emission microscopic study. *Journal of Applied Physics*, *65*, 4735–4738. https://doi.org/10.1063/1.343225

Knapek, A., Sobola, D., Tomanek, P., Pokorna, Z., & Urbanek, M. (2017). Field emission from the surface of highly ordered pyrolytic graphite. *Applied Surface Science*, *395*, 157–161. https://doi.org/10.1016/j.apsusc.2016.05.002

Kurra, N., & Kulkarni, G. U. (2013). Pencil-on-paper: Electronic devices. *Lab on a Chip*, *13*, 2866–2873. https://doi.org/10.1039/C3LC50406A

Lin, C.-W., Zhao, Z., Kim, J., & Huang, J. (2014). Pencil drawn strain gauges and chemiresistors on paper. *Scientific Reports*, *4*, 3812–3817. https://doi.org/10.1038/srep03812

Marchand, D., Fretigny, C., Lagues, M., Legrand, A. P., McRae, E., Mareche, J. F., & Lelaurain, M. (1984). Surface structure and electrical conductivity of natural and artifical graphites. *Carbon*, *22*, 497–506. https://doi.org/10.1016/0008-6223(84)90082-4

Navrátil, R., Kotzianova, A., Halouzka, V., Opletal, T., Triskova, I., Trnkova, L., & Hrbac, J. (2016). Polymer lead pencil graphite as electrode material: Voltammetric, XPS and Raman study. *Journal of Electroanalytical Chemistry*, *783*, 152–160. https://doi.org/10.1016/j.jelechem.2016.11.030

Popov, V. N. (2004). Carbon nanotubes: Properties and application. *Material Science and Engineering: R*, *43*, 61–102. https://doi.org/10.1016/j.mser.2003.10.001

Quang-Khang, P., Minh-Dung, N., Matsumoto, K., & Shimoyama, I. (2015). Acoustic emission sensor using liquid-on-beam structure. In *18th international conference on solid-state sensors, actuators and* *microsystems* (pp. 1137–1139). IEEE Conference Location: Anchorage, AK, USA. https://doi.org/10.1109/TRANSDUCERS.2015.7181128

Ţălu, Ş. (2015). *Micro and nanoscale characterization of three dimensional surfaces. basics and applications*. Cluj-Napoca, Romania: Napoca Star Publishing House.

Voice, E. H. (1949). The history of the manufacture of pencils. *Transactions of the Newcomen Society*, *27*, 131–141. https://doi.org/10.1179/tns.1949.012

How to cite this article: Sobola D, Kaspar P, Tofel P, Holcman V. Scanning electron microscopy and energy-dispersive X-ray spectroscopy analysis of electrochemically etched graphite tips created from pencil lead. *Microsc Res Tech*. 2020;83:196–201. https://doi.org/10.1002/jemt.23402

Received: 20 June 2019 | Revised: 31 July 2019 | Accepted: 9 August 2019
DOI: 10.1002/jemt.23370

RESEARCH ARTICLE

MICROSCOPY RESEARCH & TECHNIQUE WILEY

Analysis of color shift on butterfly wings by Fourier transform of images from atomic force microscopy

Pavel Kaspar | **Dinara Sobola** | **Petr Sedlák** | **Vladimír Holcman** | **Lubomír Grmela**

Department of Physics, Faculty of Electrical Engineering and Communication, Brno University of Technology, Brno, Czech Republic

Correspondence
Pavel Kaspar, Department of Physics, Faculty of Electrical Engineering and Communication, Brno University of Technology, Technická 2848/8, 616 00 Brno, Czech Republic.
Email: kasparp@feec.vutbr.cz

Review Editor: Alberto Diaspro

Funding information
National Sustainability Program, SIX, Grant/Award Number: LO1401

Abstract

Butterfly wings have complex structure lending it several interesting properties. Coloration of the wing is one of the first things to encounter and the overall visual effect is in fact influenced by several factors. Chemical pigments set the base color of the wing, topographical structures on the wing scales cause color shift by interference and their arrangement into diffraction grating causes iridescence. The thin film interference can be attributed to microscopic ridges covering wing scales. Observation and calculation of the color shift on wings of *Euploea mulciber* species using Fourier transform of images obtained by atomic force microscopy is the focus of this article.

By using Fourier transform infrared spectroscopy it was established that both top and bottom sides of the wing of *Euploea mulciber* have the same chemical composition, even though they have different color. This change of color can be attributed to thin film interference, which was analyzed and calculated by using Fourier transform of images acquired by atomic force microscopy.

KEYWORDS
AFM, butterfly wing, Fourier transform, FTIR

1 | INTRODUCTION

Materials and structures of biological nature, created by evolution, always fascinated scientists, who looked to them for inspiration, finding behavior, structures and patterns, measuring them and adapting them for use in their own inventions. With the shift of science toward nanoscale, several biological materials have already found use, like bacteria (Zhou, Fan, Zhang, Guo, & Ogawa, 2007), pollen (Fadiran & Meredith, 2014), or even spider silk (Singh, Hede, & Sastry, 2007) and others. Butterfly wings were a subject of many scientific theories and papers, exploring the properties and effects of their shape, color, and inevitably with the improvements in scientific tools, their structure (Kronforst, 2015; Singer et al., 2016). Their unique morphology, a periodical arrangement of protein/chitin hybrids with varied shape, arranged in overlapping roof tile pattern (Han, Su, Zhang, Chen, & Chen, 2009; Prum, Quinn, & Torres, 2006), has several functions. It enables flight, provides them with several interesting properties like self-cleaning, fluorescence, and superhydrophobicity (Liu & Jiang, 2011), and at the same time bestows them with colorful patterns. These assist in controlling temperature, attracting potential mates, or camouflaging against predators. Natural coloration might be caused by chemical properties—combination, ratio and thickness of chemical pigments, or by physical structure and topography, showing a dependence of the color on the observation angle (Mika, Matějková-Plšková, Jiwajinda, Dechkrong, & Shiojiri, 2012; Niu et al., 2015).

Numerical methods applied to the propagation of light wave in dependence on structure provided the opening into optical structural analysis of biological nanostructures (Alieva & Agullo-Lopez, 1996). Studies of butterfly wings themselves were performed with the focus on the geometrical structure measured by atomic force microscopy with further data analysis (Garczyk, Stach, Talu, Sobola, & Wróbel, 2017) and by applying mathematical formulae of fractal analysis to the structure (Sobola, Talu, Sadovsky, Papez, & Grmela, 2017; Ţălu, 2015; Talu, Morozov, Sobola, & Škarvada, 2018). Very interesting approach to topology analysis was also done on moiré from scanning electron microscopy (Kishimoto, Wang, Xie, & Zhao, 2007).

The purpose of this article is to subject the same samples of butterfly wings of the *Euploea mulciber* species to several measurement methods using different principles and use acquired results to examine the properties determining changes in color of the wing.

2 | MATERIALS AND METHODS

Samples for the measurement were prepared from wings of *E. mulciber* (striped blue crow), main focus being on microscopic scales covering them. This species was chosen for the properties of its wings' surface topography, and the specific patterns on wing scales.

The first measurement was performed using an optical microscope capable of 2D and 3D measurement. Same locations on the sample were viewed under two different angles, under which the eye is able to perceive brown (base) and blue (changed) color. Topographical structure was observed from optical point of view and the influence of sample topography and incident angle on resulting image was evaluated.

Atomic force microscopy (AFM) in semi-contact mode with phase imaging was used to acquire data as the second method of measurement. When vibration is introduced to the cantilever, first proposed by Binning, Quate, and Gerber (1986), effect of force gradients influences its frequency shift (Martin, Williams, & Wickramasinghe, 1987; Meyer & Amer, 1998) and gives the option of noncontact scanning measurement. When the vibrating tip touches the sample, it is affected by adhesive, repulsive, and even capillary forces to some extent (Korayem, Kavousi, & Ebrahimi, 2011). The sample–tip interaction results then in change of both frequency and phase shift as well. For example, inhomogeneity of the sample results in inhomogeneous phase shift change (hence the name, phase imaging mode). Resolution is affected mainly by material of the cantilever used for measurement and size of the tip and the speed of scanning (Sobola, Talu, Solaymani, & Grmela, 2017). In the case of this article, cantilever was of the Silicon Cantilevers NSG01 type and the tip curvature radius was 10 nm.

Fourier transform infrared spectroscopy (FTIR) was used to acquire data about chemical composition of the samples and mainly to compare the top with the bottom side of the wing, to ensure that the changes in color are only caused by topography and not by pigments or other components of different chemical nature for each of the sides. Excitation of molecules from ground to excited state by illumination (near infrared in this case) is connected with change in vibrational and rotational energy of bonds in the molecule (Berthomieu & Hienerwadel, 2009). Since each bond absorbs different wavelength of light, spectrogram of absorbed light provides a unique fingerprint for specific molecule, thus allowing for an effective chemical identification. Measurement described in this article was performed in reflection mode to analyze only one side with each measurement (since transmission mode would inevitably be affected by the structure of the other side as well) with resolution 1 cm^{-1} and in pressure > 1 hPa.

3 | RESULTS AND DISCUSSION

The wing samples were subjected to two sets of optical measurements, each set done under different illumination angle to observe the effect it had on wing color perceived by human eye. Roof-tile pattern organization is apparent on both top and bottom side of the wing (Figure 1). While this affects the overall colorful patterns and other properties of the wing, the change in the color itself occurs much deeper into the scale structure. More thorough analysis of the individual scale structure requires magnifications not achievable by means of optical microscopy, and therefore further exploration of structural properties was done by AFM. FTIR analysis was performed beforehand to determine chemical composition of both top and bottom sides of the wing. Same (or highly similar) chemical composition would mean that the changes in color are caused by structure, rather than pigment difference, and therefore making AFM measurement viable, even though it is a nonoptical method describing an optical phenomenon. Figure 2 shows the topography of top and bottom scales taken by AFM, ridges and grooves that participate in colorization of the wing. Ridges on the individual scales participate in the thin-film interference, boosting a specific range of wavelengths and changing the base color of the wing, while simultaneously functioning as a diffraction grating (Giraldo & Stavenga, 2016), creating iridescence.

FTIR of the measured sample returned chemical composition spectra (Figure 3). It needs to be pointed out that spectra for both top and bottom part of the wing appear virtually identical, even their magnitude. The peak at 3,286 cm^{-1} represents stretching vibrations of N-H bond and hydrogen bonded O-H stretch 2,918 cm^{-1} and 2,850 cm^{-1} peaks correspond with $-CH_2$ and $-CH_3$, respectively. Peak at 1,652 cm^{-1} belongs to C=O stretch of an amide band. N-H bending of secondary amide produced the peak at 1,543 cm^{-1}. Band appearing at 1,076 cm^{-1} corresponds with stretching of the C-O bond of a secondary OH group (Mekahlia & Bouzid, 2009).

Several chemical pigments are commonly found in insects, some of them even in *lepidoptera* (Bankar, Dar, & Pandit, 2018; Shamim, Ranjan, Pandey, & Ramani, 2014). They share some of the bonds identified by FTIR peaks with the polysaccharides and proteins of the wing itself (i.e., chitin), and they could be attributed with the presence of a number of smaller peaks in the FTIR spectrum. Difference in presence of these pigments should be visible on FTIR analysis though. While quantitative analysis was not used, relative sizes of the peaks and their position from both top and bottom part of the wing are so similar that it can be said that there is no difference in chemical composition of either side of the wing. Therefore, the difference in colors observed is caused entirely by different structure, and not by chemical differences or presence of different pigments. With this information the structural properties were explored in detail by AFM and SEM, focusing purely on the effect of the topography on the incident (and reflected) light.

As can be seen in Figures 4 and 5, the ridges form a quasiperiodic structure. Light incident on this structure is subject to film interference, passing from the surrounding medium (air) into the ridge on a

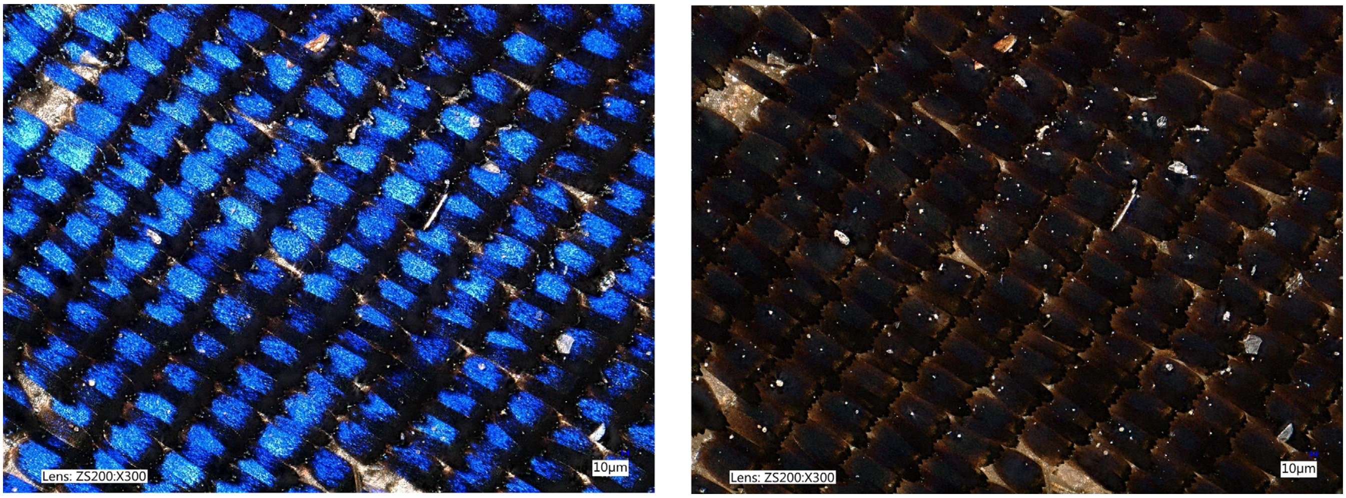

FIGURE 1 Scales on wings forming a roof-tile pattern, top (left) and bottom (right) [Color figure can be viewed at wileyonlinelibrary.com]

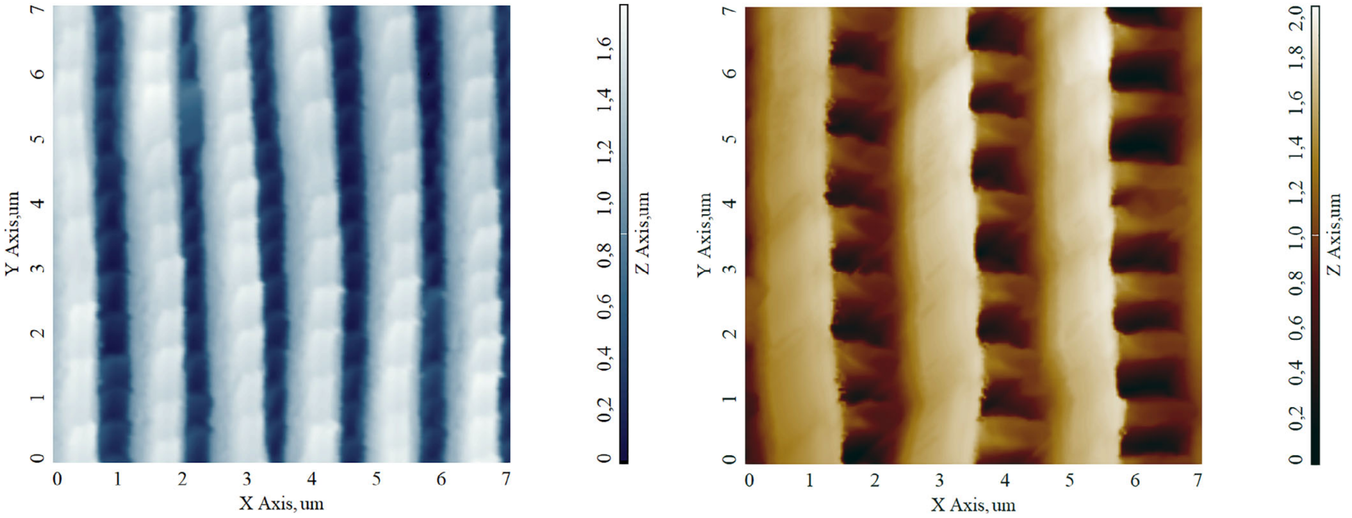

FIGURE 2 Deep AFM scale detail taken from top (left) and bottom (right) of the wing. AFM, atomic force microscopy [Color figure can be viewed at wileyonlinelibrary.com]

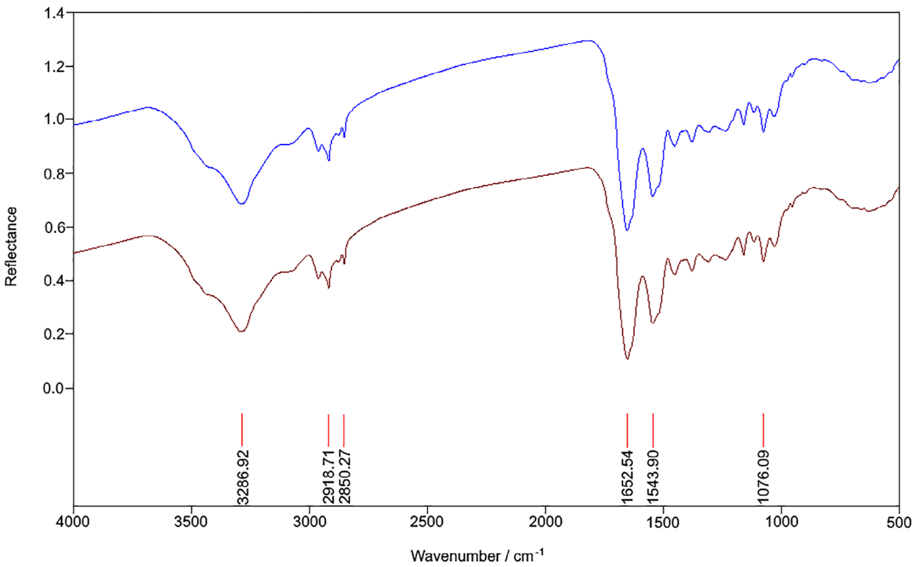

FIGURE 3 FTIR spectra of wing scales, blue (top) and brown (bottom). FTIR, Fourier transform infrared spectroscopy [Color figure can be viewed at wileyonlinelibrary.com]

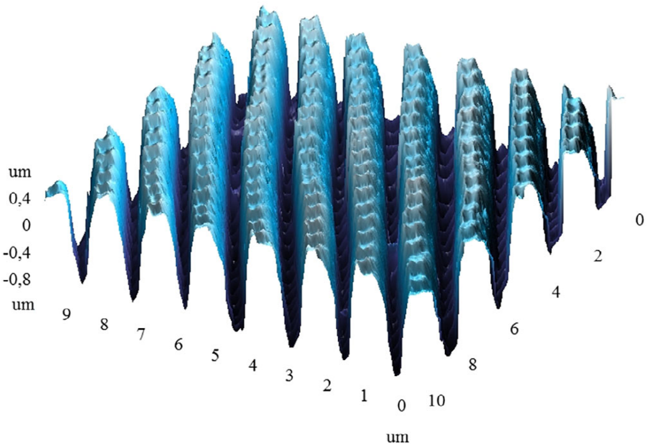

FIGURE 4 3D AFM representation of wing topography taken from the top scale. AFM, atomic force microscopy [Color figure can be viewed at wileyonlinelibrary.com]

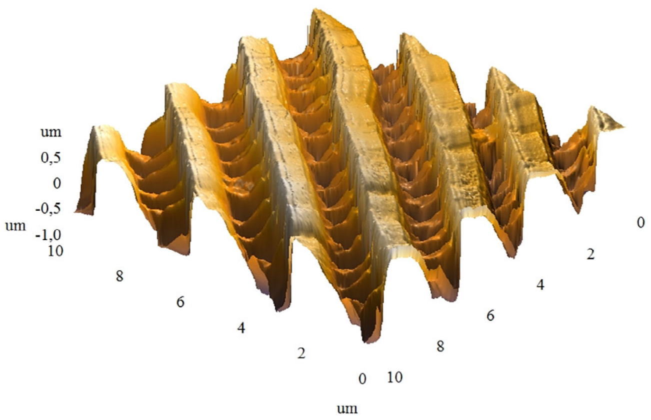

FIGURE 5 3D AFM representation of wing topography taken from the bottom scale. AFM, atomic force microscopy [Color figure can be viewed at wileyonlinelibrary.com]

scale with higher refractive index, causing phase shift, and the subsequent reflection off the back side of the ridge, allowing for the interference to occur. If the interference is constructive, it can boost a specific wavelength. In the case of the upper side of the wing, the boosted wavelengths belong to the band of the color blue. To ensure that the emergence of blue color on the top of the wing and no color change on the bottom is caused in this way, an equation derived from Fresnel equation for phase shift at interface (Hecht, 2001) needs to be solved:

$$\begin{aligned} 2nd &= m\lambda + \frac{\lambda}{2} \\ d &= (2m+1)\frac{\lambda}{4n} \\ \lambda &= \frac{4dn}{2m+1}, \end{aligned} \tag{1}$$

where n is the refractive index of the medium (n_{chitin} = 1.57 for λ = 420 nm) (Leertouwer, Wilts, & Stavenga, 2011), m is a positive integer, λ is wavelength of the interfering wave, and d is the thickness of the ridge.

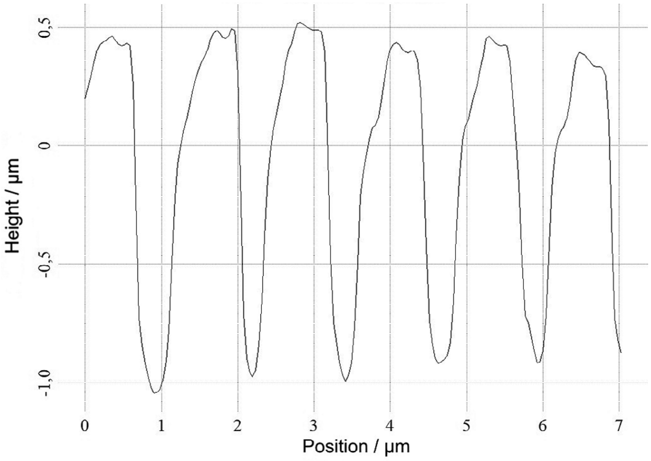

FIGURE 6 Cross-section of a scale from top of the wing, acquired by AFM. AFM, atomic force microscopy

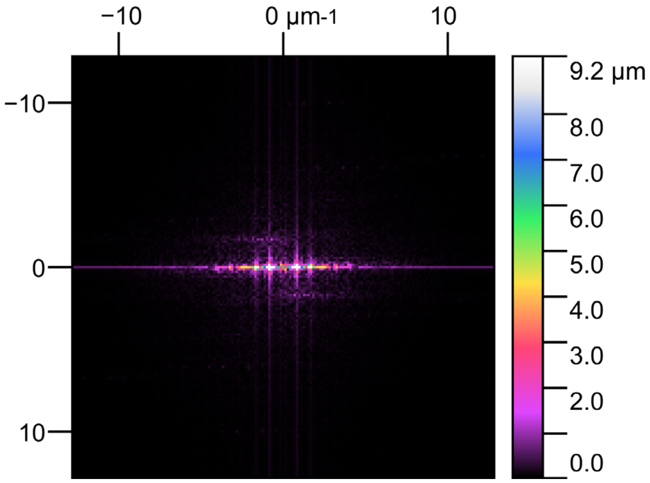

FIGURE 7 0,0 shifted Fourier 2D spectrum of the top scale [Color figure can be viewed at wileyonlinelibrary.com]

Because the blue color on the top of the wing corresponds to wavelength about 420 nm, it is possible to apply it to Equation (1) to find out the thickness of the ridge. This calculation yielded the thickness at d = 0.602 μm. This number corresponds to measured width of the upper parts of the ridge by diagnostical tools of Gwyddion software used for AFM image processing. Therefore, result could be assumed to be reasonably correct due to the scale topography, since the light participating in the constructive interference could only be incident at the upper portion of the ridge, as shown by the cross-section of scale topography (Figure 6). As the structure is not strictly periodical (since it is of organic origin) and precise measuring of each ridge on its own by AFM image processing tools would be impractical, if not downright impossible, a better way to find the mean width of the effective parts of the ridge needed to be found.

Images acquired from AFM were subjected to 2D Fourier transform to define the periodicity of the ridges and grooves of the scale (Figures 7 and 8). Cross sections of Fourier spectra from both top and

FIGURE 8 0,0 shifted Fourier 2D spectrum of the bottom scale [Color figure can be viewed at wileyonlinelibrary.com]

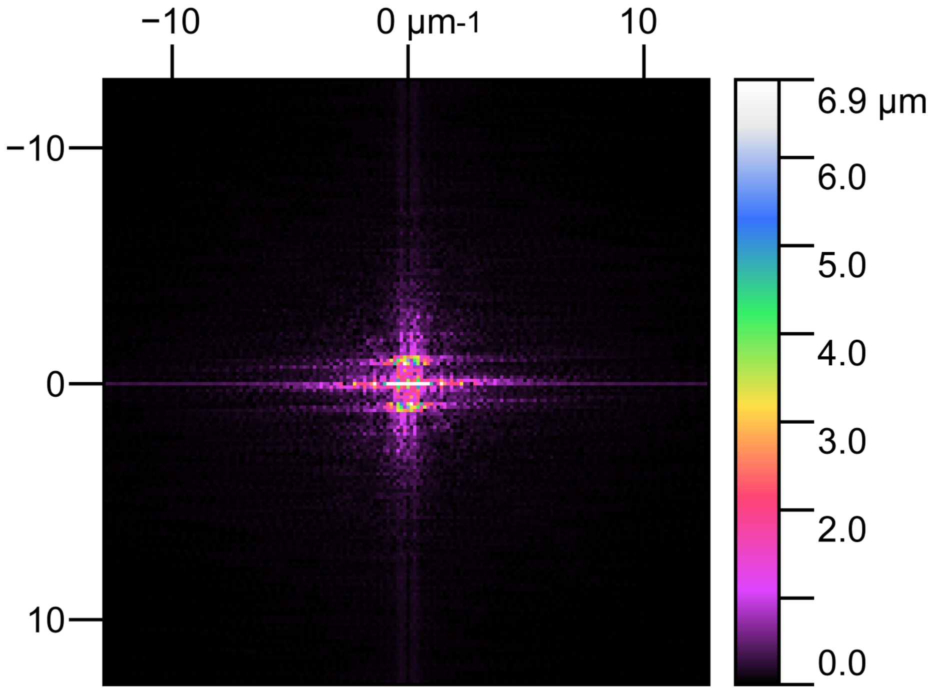

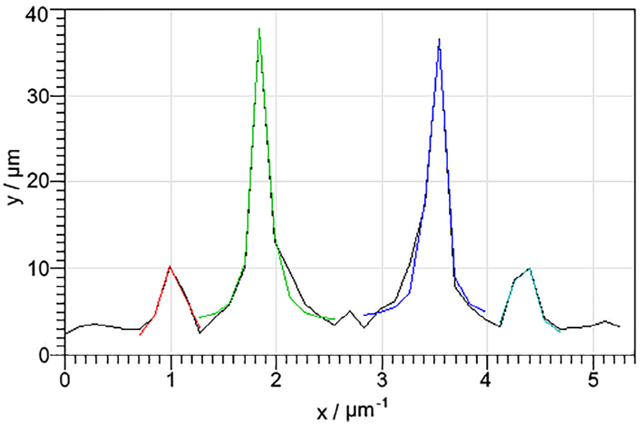

FIGURE 9 Cross-section of Fourier spectrum of the top scale with Lorentzian fitting for each important peak, horizontal axis [Color figure can be viewed at wileyonlinelibrary.com]

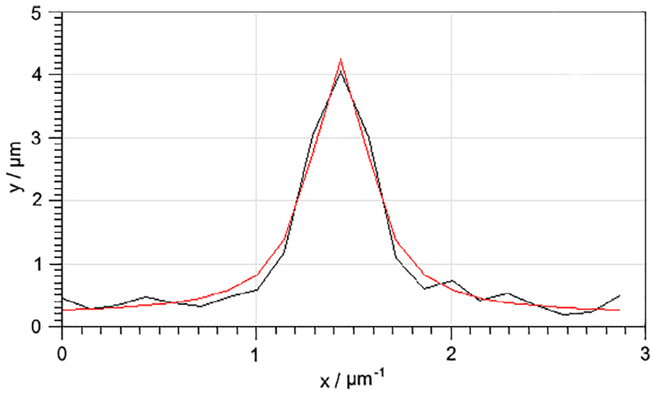

FIGURE 10 Cross-section of Fourier spectrum of the top scale with Lorentzian fitting for each important peak, vertical axis [Color figure can be viewed at wileyonlinelibrary.com]

bottom side of the wing were taken along the *x* and *y* axes in the middle of the 0,0 shifted spectrum, and the peaks were fitted with Lorentzian function to mitigate any deviations caused by sampling spatial frequency. Lorentzian allows for the best fitting of symmetric functions with the emphasis on peak location (Hollas, 2004).

Top scale returned dominant periodicity in one direction—horizontal only (Figure 9), across the ridges.

Fourier transform provided the length of one spatial period at 1.2056 μm, which corresponds with mean distance between the same points of two ridges. Taking into consideration that in order for light to participate, it has to hit the upper part of the ridge, and the width of the ridge increases closer to the base, the result gained from Equation (1) corresponds with the one gained from analysis of Fourier transform and the adjustment for varying size depending on the position on the ridge.

Vertical direction shows no detectable periodicity (Figure 10). While there are secondary ridges set in the valleys between the primary ones, the valleys are far too thin and deep to allow AFM probe to display them properly, and they receive only a small amount of light because of it, making their contribution to color change negligible.

This is, however, the result for the top side of the wing, where the change in color is easily visible. Because the bottom side of the wing has very similar structures (Figure 2), it was subjected to the same analysis using Fourier transform.

Resulting periodicity in horizontal direction (Figure 11) provided the mean distance between ridge centers at 2.1254 μm. Because there is larger space between them, than in the top side scales, light can hit lower portions of the ridge and therefore the adjustment for position will not be as great as with the top side scale. Fortunately, the ridge does not increase as quickly toward its base, and therefore

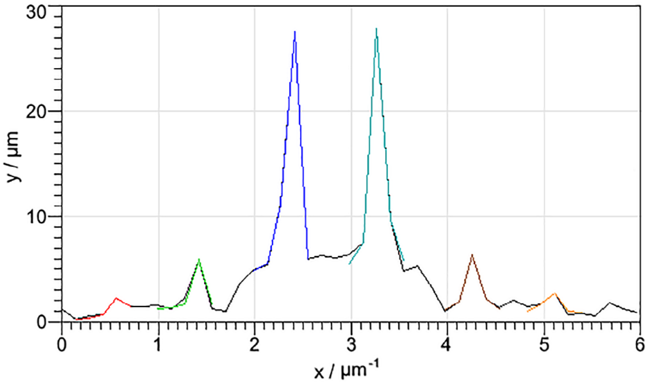

FIGURE 11 Cross-section of Fourier spectrum of the bottom scale with Lorentzian fitting for each important peak, horizontal axis [Color figure can be viewed at wileyonlinelibrary.com]

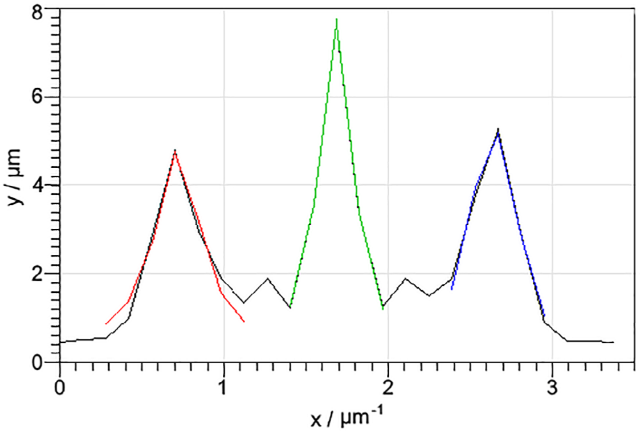

FIGURE 12 Cross-section of Fourier spectrum of the bottom scale with Lorentzian fitting for each important peak, vertical axis [Color figure can be viewed at wileyonlinelibrary.com]

the simpler option of the whole ridge reachable by light being uniform in size can be considered. Equation (1) provided resulting wavelength of constructive interference of light beyond the end of visible spectrum on the red side, which would explain why there is no visible color shift. Also, since the resulting wavelength is into the direction of infrared, it supports the theory of butterflies using their wings for temperature management. Scales on both top and bottom sides of the wing have not only the vertical (primary) ridges, which are being taken into consideration, but also horizontal (secondary) ones (Figure 2), set deeper into the structure into the valley. On top side these horizontal ridges are much more difficult for light to access, let alone to influence reflected light in easily measurable way. The bottom side scales have greater distances between vertical ridges, making it more possible for light to interact with them the same way it does with the vertical ones. Interval of periodicity gained by Fourier transform analysis (Figure 12) was 1.0378 μm. When the considerations for size and location are applied, resulting thickness of these secondary ridges is about 0.4 μm, which would yield wavelength beyond violet, and therefore again outside of visible spectrum. The fact that these secondary formations receive far less illumination, than the primary ones, although still more than the secondary ridges on the top side of the wing, also plays an important part.

4 | CONCLUSION

Coloration of butterfly wings is caused by pigmentation and structural properties. Scales on the top side of the wing have a different color, than the ones on the bottom side, while having the same chemical composition. This color change is caused by structural properties of the scale, mainly the ridges and grooves. Light incident on the scale is subject to thin film interference, which causes color of reflected light to change. This color change depends on thickness of the ridges, which are arranged in semi-periodic structure in both horizontal and vertical direction. By using Fourier transform on AFM images gained from the scales it is possible to determine the overall mean periodicity interval of these semi-periodic structures in horizontal and vertical direction. The periodicity interval can then be used to determine mean thickness of the ridges and therefore to calculate wavelengths boosted by the interference. Results of these calculations correspond with visual observations of the color patterns and confirm the utility of butterfly wings for light interactions outside of visual range.

ACKNOWLEDGMENTS

Research described in this article was financed by the National Sustainability Program under grant LO1401. For the research, infrastructure of the SIX Center was used.

ORCID

Pavel Kaspar https://orcid.org/0000-0003-1757-2382
Dinara Sobola https://orcid.org/0000-0002-0008-5265

REFERENCES

Alieva, T., & Agullo-Lopez, F. (1996). Optical wave propagation of fractal fields. *Optics Communications*, *125*, 267–274. https://doi.org/10.1016/0030-4018(95)00702-4

Bankar, T. N., Dar, M. A., & Pandit, R. S. (2018). Diversity and functions of chromophores in insects: A review. In: M. M. Shah & U. Sharif (Eds.), *Insect science diversity, conservation and nutrition*, *IntechOpen* (pp. 1–16). https://doi.org/10.5772/intechopen.74480

Berthomieu, C., & Hienerwadel, Æ. R. (2009). Fourier transform infrared (FTIR) spectroscopy. *Photosynthesis Research*, *101*, 157–170. https://doi.org/10.1007/s11120-009-9439-x

Binning, G., Quate, C. F., & Gerber, C. (1986). Atomic force microscope. *Physical Review Letters*, *56*(9), 930–933. https://doi.org/10.1103/PhysRevLett.56.930

Fadiran, O. O., & Meredith, J. C. (2014). Surface treated pollen performance as a renewable reinforcing filler for poly(vinyl acetate). *Journal of Materials Chemistry A: Materials for Energy and Sustainability*, *2*, 17031–17040. https://doi.org/10.1039/C4TA03219E

Garczyk, Z., Stach, S., Talu, S., Sobola, D., & Wróbel, Z. (2017). Stereometric parameters of butterfly wings. *Journal of Biomimetics*, *Biomaterials and Biomedical Engineering*, *31*, 1–10. https://doi.org/10.4028/www.scientific.net/JBBBE.31.1

Giraldo, M. A., & Stavenga, G. D. (2016). Brilliant iridescence of Morpho butterfly wing scales is due to both a thin film lower lamina and a multilayered upper lamina. *Journal of Comparative Physiology A*, *202*, 381–388. https://doi.org/10.1007/s00359-016-1084-1

Han, J., Su, H., Zhang, D., Chen, J., & Chen, Z. (2009). Butterfly wings as natural photonic crystal scaffolds for controllable assembly of CdS nanoparticles. *Journal of Materials Chemistry*, *19*, 8741–8746. https://doi.org/10.1039/b911101h

Hecht, E. (2001). *Optics* (4th ed.). Boston, MA: Addison-Wesley.

Hollas, J. M. (2004). *Modern spectroscopy* (4th ed.). Hoboken, NJ: John Wiley & Sons Ltd.

Kishimoto, S., Wang, Q., Xie, H., & Zhao, Y. (2007). Study of the surface structure of butterfly wings using the scanning electron microscopic moiré method. *Applied Optics*, *46*(28), 7026–7034. https://doi.org/10.1364/AO.46.007026

Korayem, M. H., Kavousi, A., & Ebrahimi, N. (2011). Dynamic analysis of tapping-mode AFM considering capillary force interactions. *Scientia Iranica*, *18*(1), 121–129. https://doi.org/10.1016/j.scient.2011.03.014

Kronforst, M. R. (2015). Exploring the molecular basis of monarch butterfly color pattern variation. *Pigment Cell & Melanoma Research*, *28*(2), 127–130. https://doi.org/10.1111/pcmr.12353

Leertouwer, H. L., Wilts, B. D., & Stavenga, D. G. (2011). Refractive index and dispersion of butterfly chitin and bird keratin measured by polarizing interference microscopy. *Optics Express*, *19*, 24061–24066. https://doi.org/10.1364/OE.19.024061

Liu, K., & Jiang, L. (2011). Bio-inspired design of multiscale structures for function integration. *Nano Today*, *6*, 155–175. https://doi.org/10.1016/j.nantod.2011.02.002

Martin, Y., Williams, C. C., & Wickramasinghe, H. K. (1987). Atomic force microscope – force mapping and profiling on a sub 100-Å scale. *Journal of Applied Physics*, *61*, 4723–4729. https://doi.org/10.1063/1.338807

Mekahlia, S., & Bouzid, B. (2009). Chitosan-Copper (II) complex as antibacterial agent: Synthesis, characterization and coordinating bond-activity correlation study. *Physics Procedia*, *2*, 1045–1053. https://doi.org/10.1016/j.phpro.2009.11.061

Meyer, G., & Amer, N. M. (1998). Novel optical approach to atomic force microscopy. *Applied Physics Letters*, *53*, 1045–1047. https://doi.org/10.1063/1.100061

Mika, F., Matějková-Plšková, J., Jiwajinda, S., Dechkrong, P., & Shiojiri, M. (2012). Photonic crystal structure and coloration of wing scales of butterflies exhibiting selective wavelength iridescence. *Materials*, *5*, 754–771. https://doi.org/10.3390/ma5050754

Niu, S., Mu, Z., Yang, M., Zhang, J., Han, Z., & Ren, L. (2015). Excellent structure-based multifunction of morpho butterfly wings: A review. *Journal of Bionic Engineering*, *12*(2), 170–189. https://doi.org/10.1016/S1672-6529(14)60111-6

Prum, R. O., Quinn, T., & Torres, R. H. (2006). Anatomically diverse butterfly scales all produce structural colours by coherent scattering. *The Journal of Experimental Biology*, *209*, 748–765. https://doi.org/10.1242/jeb.02051

Shamim, G., Ranjan, S. K., Pandey, D. M., & Ramani, R. (2014). Biochemistry and biosynthesis of insect pigments. *European Journal of Entomology*, *111*(2), 149–164. https://doi.org/10.14411/eje.2014.021

Singer, A., Boucheron, L., Dietze, S. H., Jensen, K. E., Vine, D., Mcnulty, I., … Shpyrko, O. G. (2016). Domain morphology, boundaries, and topological defects in biophotonic gyroid nanostructures of butterfly wing scales. *Science Advances*, *2*(6), 1–6. https://doi.org/10.1126/sciadv.1600149

Singh, A., Hede, S., & Sastry, M. (2007). Spider silk as an active scaffold in the assembly of gold nanoparticles and application of the gold – silk bioconjugate in vapor sensing. *Bioconjugate Sensors*, *411045*, 466–473. https://doi.org/10.1002/smll.200600413

Sobola, D., Talu, S., Sadovsky, P., Papez, N., & Grmela, L. (2017). Application of AFM measurement and fractal analysis to study the surface of natural optical structures. *Applied Physics*, *15*, 569–576. https://doi.org/10.15598/aeee.v15i3.2242

Sobola, D., Talu, S., Solaymani, S., & Grmela, L. (2017). Influence of scanning rate on quality of AFM image: Study of surface statistical metrics. *Microscopy Research and Technique*, *80*, 1328–1336. https://doi.org/https://doi.org/10.1002/jemt.22945

Ţălu, Ş. (2015). *Micro and nanoscale characterization of three dimensional surfaces. Basics and applications*. Cluj-Napoca, Romania: Napoca Star Publishing House.

Talu, S., Morozov, I. A., Sobola, D., & Škarvada, P. (2018). Multifractal characterization of butterfly wings scales. *Bulletin of Mathematical Biology*, *80*(11), 2856–2870. https://doi.org/https://doi.org/10.1007/s11538-018-0490-7

Zhou, H., Fan, T., Zhang, D., Guo, Q., & Ogawa, H. (2007). Novel bacteria-templated sonochemical route for the in situ one-step synthesis of ZnS hollow nanostructures. *Chemistry of Materials*, *19*, 2144–2146. https://doi.org/10.1021/cm0629311

How to cite this article: Kaspar P, Sobola D, Sedlák P, Holcman V, Grmela L. Analysis of color shift on butterfly wings by Fourier transform of images from atomic force microscopy. *Microsc Res Tech*. 2019;1–7. https://doi.org/10.1002/jemt.23370

BRING YOUR CAREER TO THE NEXT LEVEL IN 2020...

We've expanded our course selection...again!
We now have even more offerings, led by our certified faculty. Maximize your skill and knowledge sets with our...

- Educational Workshops
- Corporate Training
- Group Training
- Private Training
- Equipment Demonstrations

See our website for more information...
www.emsmicroscopyacademy.com


JAN 14-16, 2020
Biological TEM Workshop

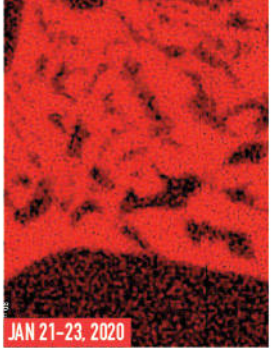
JAN 21-23, 2020
X-Ray Microanalysis Workshop

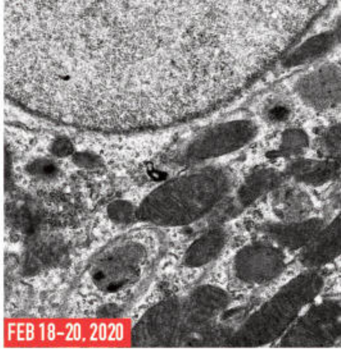
FEB 18-20, 2020
Automated and Rapid Specimen Processing for Electron Microscopy Workshop


FEB 25-27, 2020
Materials Ultramicrotomy
Preparatory Session on FEB 24 for those unfamiliar with microtomy.

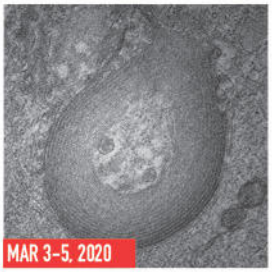
MAR 3-5, 2020
Introduction to Microscopy Techniques Workshop

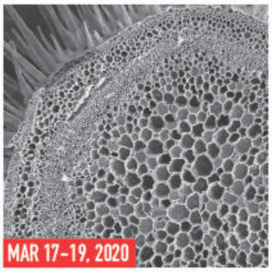
MAR 17-19, 2020
Biological SEM Workshop


MAR 24-26, 2020
Cryo SEM Workshop

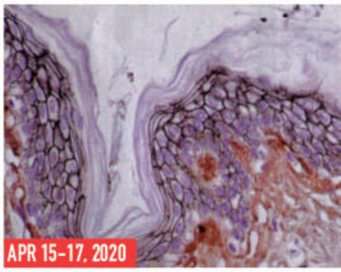
APR 15-17, 2020
Aurion Immunogold Silver Staining

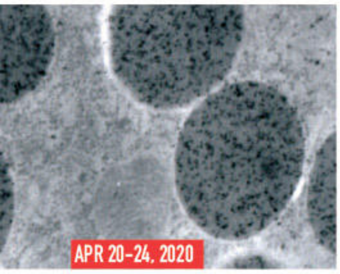
APR 20-24, 2020
Cryosectioning/Immunogold Workshop


MAY 19-21, 2020
Introduction to Microscopy Techniques Workshop

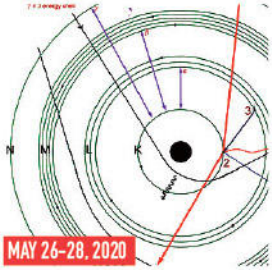

MAY 26-28, 2020
X-Ray Microanalysis Workshop

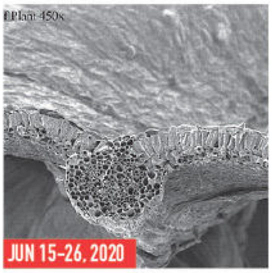
JUN 15-26, 2020
Microscopy: The Complete Image
June Session

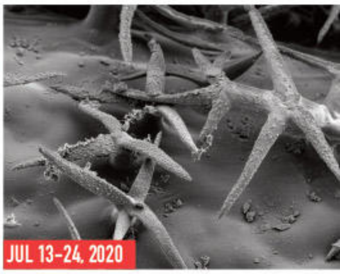
JUL 13-24, 2020
Microscopy: The Complete Image
July Session

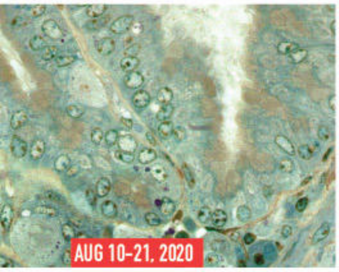
AUG 10-21, 2020
Microscopy: The Complete Image
August Session

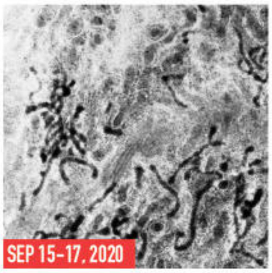
SEP 15-17, 2020
Introduction to Microscopy Techniques Workshop

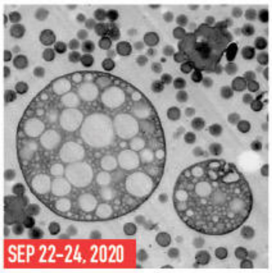
SEP 22-24, 2020
Materials Ultramicrotomy
Preparatory Session on SEP 21 for those unfamiliar with microtomy.

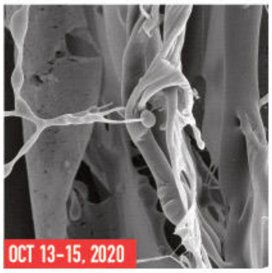
OCT 13-15, 2020
Cryo SEM Workshop

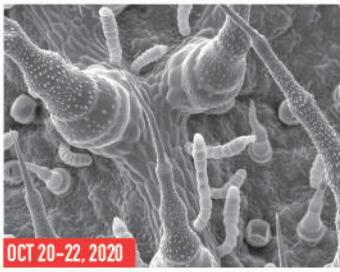
OCT 20-22, 2020
Biological SEM Workshop

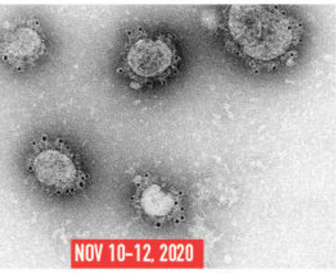
NOV 10-12, 2020
Aurion Immunogold Silver Staining

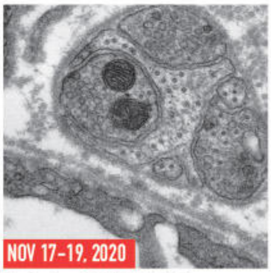
NOV 17-19, 2020
Biological TEM Workshop

SIGN UP FOR A CLASS TODAY, OR SUGGEST A COURSE THAT YOU WANT...

EMS Microscopy Academy

...ENDLESS POSSIBILITIES

www.emsmicroscopyacademy.com

PATENTOVÝ SPIS

(11) Číslo dokumentu:

307 498

(13) Druh dokumentu: **B6**

(51) Int. Cl.:

G01V 3/10	(2006.01)
G01N 27/72	(2006.01)
G01R 33/00	(2006.01)

(19)
ČESKÁ
REPUBLIKA

ÚŘAD
PRŮMYSLOVÉHO
VLASTNICTVÍ

(21) Číslo přihlášky: **2018-33**
(22) Přihlášeno: **23.01.2018**
(40) Zveřejněno: **17.10.2018**
(Věstník č. 42/2018)
(47) Uděleno: **05.09.2018**
(24) Oznámení o udělení ve věstníku: **17.10.2018**
(Věstník č. 42/2018)

(56) Relevantní dokumenty:

WO 2017042968 A1; US 2009021251 A1; JP S564083 A; GB 2499239 A; EP 2433159 A1; EP 2629121 A1; US 2013049745 A1.

(73) Majitel patentu:
Konštrukta-TireTech, 911 01 Trenčín, SK

(72) Původce:
Ing. Vladimír Holcman, Ph.D., Brno, CZ
Ing. Robert Macků, Ph.D., Brno, CZ
Ing. Pavel Škarvada, Ph.D., Brno, CZ
Ing. Štefan Kišac, Trenčín, SK
Ing. Ján Dugáček, Trenčianske Teplice, SK

(74) Zástupce:
Rott, Růžička & Guttmann
Patentové, známkové a advokátní kanceláře, Ing.
Jiří Andera, Vinohradská 37/938, 120 00 Praha 2

(54) Název vynálezu:

Detektor a lokalizátor feromagnetických inkluzí v kontinuálně procházejícím mediu

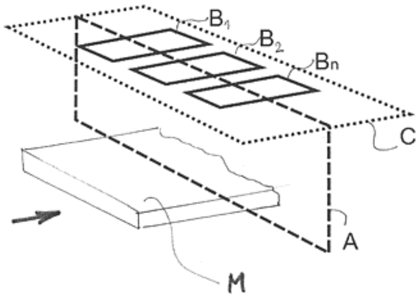

CZ 307498 B6

Detektor a lokalizátor feromagnetických inkluzí v kontinuálně procházejícím mediu

Oblast techniky

Vynález se týká detektoru a lokalizátoru feromagnetických inkluzí v kontinuálně procházejícím mediu, zahrnující primární budicí cívku, skrz kterou medium prochází a dále zahrnuje alespoň dvě snímací cívky.

Dosavadní stav techniky

Systém liniové detekce kovových či nekovových částic je známý a využívá elektromagnetických polí k detekci částic v prostoru (v jedné linii). V rámci těchto systémů je důležité uvažovat citlivost a velikost detekční oblasti. Pro systémy umožňující lokalizaci je nutné definovat navíc maximální detekční vzdálenost a přesnost lokalizace. Tyto parametry jsou úzce svázány a nelze je posuzovat nezávisle. Přenosné lokátory a systémy pro lokalizaci kovových předmětů, spadajících do jiné aplikační oblasti, jsou založeny na posuvu detekční soustavy do místa s charakteristickou odezvou systému. Díky vlastním rozměrům, detekčním parametrům a nutností pohybu v detekčním prostoru nejsou vhodné ke kontinuální detekci např. na pásových dopravnících.

Z evropského patentu EP 2 433 159 je znám systém na lokalizaci kovových objektů, zejména detektor kovů provozovaný v Pl-módu, s několika vysílacími cívkami a nejméně jednou přijímací cívkou, které jsou spolu spojené indukčně a pro potlačení vzájemného působení jsou uspořádané tak, že se částečně překrývají, přičemž je dosažitelný bod optimálního vyrušení vzájemného působení. Systém dále zahrnuje snímačovou elektroniku pro proudové napájení vysílacích cívek a pro vyhodnocení přijímaného signálu přijímací cívky. Vysílací cívky alespoň částečně překrývají nejméně jednu přijímací cívku. Vysílací cívky při stejném proudovém napájení působí na tuto nejméně jednu přijímací cívku, přičemž vzniká lokální bod optimálního vyrušení. Při proudovém napájení první vysílací cívky se bod optimálního vyrušení pohybuje do prvního směru, zatímco při proudovém napájení další vysílací cívky se bod optimálního vyrušení pohybuje do druhého směru. Regulační zapojení pro regulaci proudů k částem vysílací cívky vede k pohybu lokálního bodu optimálního vyrušení, které způsobí vyrušení přijímacího signálu.

Detektory kovu pro výrobní línky se většinou sestávají z minimálně jedné budicí a nejméně jedné primární snímací a nejméně jedné sekundární snímací cívky. Snímací cívky jsou vinuty opačným směrem, a tudíž se jejich příspěvek nuluje, pokud se uvnitř detekční oblasti nenachází kovová částice. Například z evropského patentu EP 2 629 121 je znám detektor kovu, zahrnující kovový uzavřený prostor se vstupním otvorem a výstupním otvorem, jehož plochy příčného průřezu se liší od sebe navzájem co do velikosti. Dále zahrnuje uvnitř uzavřeného prostoru cívkový systém hraničící s detekční zónou, která se rozprostírá mezi vstupním otvorem a výstupním otvorem a skrz kterou se mohou kontrolované předměty pohybovat podél trasy pohybu tak, že vstupují do detektoru kovu skrz vstupní otvor a opouštějí detektor kovu skrz výstupní otvor. Detekční zóna má profil příčného průřezu, který se mění podél trasy pohybu. Systém cívek zahrnuje nejméně jednu vysílací cívku a nejméně jednu první a nejméně jednu druhou přijímací cívku. Cívky se vzájemně liší co do velikosti, přičemž nejméně jedna vysílací cívka, když je napájena energií střídavým elektrickým proudem, generuje primární elektromagnetické pole, které zase indukuje první napětí v nejméně jedné první přijímací cívce a druhé napětí v nejméně jedné druhé přijímací cívce. Nejméně jedna první přijímací cívka a nejméně jedna druhá přijímací cívka jsou umístěny relativně k nejméně jedné vysílací cívce v nestejné vzdálenosti, takže první napětí a druhé napětí se navzájem ruší, pokud není přítomen kov v kontrolovaných předmětech.

Pásový dopravník prostupuje těmito cívkami, takže takovéto uspořádání není vhodné pro účely lokalizace. K omezení vlivu okolních kovových předmětů a rušení se celé zařízení umisťuje do kovové stínicí komory. V jiných uspořádáních se využívá vázaný rezonanční obvod tvoření budicí a snímací cívkou, avšak ani tato uspořádání nejsou pro účely lokalizace vhodná (viz např. US 8841903 B2).

Podstata vynálezu

Nevýhody stavu techniky odstraňuje detektor a lokalizátor feromagnetických inkluzí v kontinuálně procházejícím mediu, zahrnující primární budicí cívku, skrz kterou medium prochází a dále zahrnující alespoň dvě snímací cívky, podle vynálezu, jehož podstata spočívá v tom, že snímací cívky jsou uspořádány v rovině kolmé k rovině primární budicí cívky. Všechny snímací cívky jsou vinuty v libovolném smyslu. V rovině snímacích cívek je uspořádána alespoň jedna sekundární budicí cívka.

Detektor a lokalizátor feromagnetických inkluzí podle vynálezu je schopen odhalit feromagnetické inkluze v kontinuálně procházejícím mediu z magneticky transparentních materiálů daleko přesněji než známá zařízení.

Podle výhodného provedení mohou být další snímací cívky uspořádány po celém obvodu primární budicí cívky.

Detektor podle vynálezu může být připojen na jakékoliv známé vyhodnocovací zapojení. Podle výhodného provedení jsou snímací cívky přes první zesilovače, pásmové propusti a obvody signálového zpracování připojeny k řídicí jednotce. Řídicí jednotka je dále přes první generátor harmonického průběhu a druhý zesilovač připojena k primární budicí cívce. Řídicí jednotka je též přes druhý generátor harmonického průběhu a zesilovač nf signálu připojena k sekundární budicí cívce.

Objasnění výkresů

Na obr. 1 je zobrazen pohled na uspořádání cívek detektoru a lokalizátoru podle vynálezu. Na obr. 2 je blokové schéma detektoru a lokalizátoru podle vynálezu.

Příklady uskutečnění vynálezu

Příklad provedení detektoru a lokalizátoru feromagnetických inkluzí v kontinuálně procházejícím mediu $\underline{M}$ podle obr. 1 a 2 zahrnuje primární budicí cívku $\underline{A}$, skrz kterou medium $\underline{M}$ prochází a dále zahrnuje několik snímacích cívek $\underline{B_1}$ až $\underline{B_n}$, které jsou uspořádány v rovině kolmé k rovině primární budicí cívky $\underline{A}$. Všechny snímací cívky $\underline{B_1}$, $\underline{B_n}$ jsou vinuty v libovolném smyslu. Schopnost lokalizace feromagnetických inkluzí v kontinuálně procházejícím mediu $\underline{M}$ je úměrná počtu snímacích cívek $\underline{B_1}$, $\underline{B_n}$. Snímací cívky $\underline{B_1}$, $\underline{B_n}$. mohou být mechanicky nebo jinými způsoby nastaveny tak, aby byl signál na jejich výstupu minimalizován.

V rovině snímacích cívek $\underline{B_1}$ až $\underline{B_n}$ je uspořádána alespoň jedna sekundární budicí cívka $\underline{C}$, která slouží k vytvoření zázněje, ale také ke kalibraci. Zpracováním výstupních amplitudově-fázových signálů jednotlivých cívek $\underline{B_1}$ až $\underline{B_n}$ lze získat informaci o přítomnosti (detekce) a pozici (lokalizace) feromagnetické částice/částic.

Podle neznázorněného provedení mohou být další snímací cívky $\underline{B_n}$ uspořádány po celém obvodu primární budicí cívky $\underline{A}$.

Primární budicí cívka $\underline{A}$ je víceřadé/sloupcové vinutí realizované válcovým nebo pásovým vodičem schopným přenést hodnoty elektrického proudu v řádech jednotek až desítek ampér.

Snímací cívky B_1 až B_n jsou snímací elementy, které jsou pohyblivé ve směru kolmém k primární budicí cívce A a jsou realizované geometricky pravidelnou skladbou válcových nebo pásových vodičů.

Sekundární budicí cívka C je geometricky pravidelnou skladbou válcových nebo pásových vodičů.

Snímací cívky B_1 až B_n jsou přes první zesilovače 4_1 až 4_n, pásmové propusti 5_1 až 5_n a obvody 6_1 až 6_n signálového zpracování připojeny k řídicí, vyhodnocovací a zobrazovací jednotce 1, dále označované zkráceně jako řídicí jednotka 1.

Řídicí jednotku 1 tvoří uživatelské rozhraní s výpočetní jednotkou, kterou může být počítač, mikrokontrolér, signálový procesor s displejem a ovládacími prvky, případně dotykovým displejem. Uživatelské rozhraní také poskytuje běžná komunikační rozhraní používaná u osobních počítačů a průmyslových systémů.

První zesilovače 4_1 až 4_n jsou přístrojové, nebo diferenciální, případně signálové předzesilovače, kdy podmínkou je precizní nízkošumové provedení s nízkým zkreslením a na pracovním kmitočtu laděným vstupním obvodem.

Každou pásmovou propust 5_1 až 5_n může tvořit soustava pásmových propustí, která může být pasivním i aktivním filtrem např. typu „Sallen Key“, nebo rezonanční obvod/soustava vázaných rezonančních obvodů. Podmínkou je precizní nízkošumové provedení a monotónní fázová charakteristika v propustné oblasti.

Obvody 6_1 až 6_n signálového zpracování mohou být v analogové nebo digitální variantě. Může jít o kombinaci softwarově nebo hardwarově řešených obvodů realizujících: napěťové reference, obvodů pro přechod do spektrální komplexní oblasti, zesilovačů odchylky, výřezových filtrů spektrálních složek, obvodů analogově-digitální konverze a obvodů digitálního signálového zpracování DSPa výpočetní jednotky PLC, hradlového pole, mikrokontroléru.

Dále je řídicí jednotka 1 přes první generátor 2 harmonického průběhu a druhý zesilovač 3 připojena k primární budicí cívce A.

První generátor 2 harmonického průběhu je oscilátor generující harmonický signál, kterým může být generátor produkující harmonický signál případně kmitočtová syntéza s dobrou spektrální čistotou, střednědobou kmitočtovou stabilitou a dobrou fázovou stabilitou.

Druhý zesilovač 3 je výkonový zesilovač s nízkým zkreslením a schopností pracovat do nízkoimpedanční zátěže, nebo audiozesilovač, případně zesilovač s proudovým výstupem.

Řídicí jednotka 1 je též přes druhý generátor 7 harmonického průběhu a zesilovač 8 nf signálu připojena k sekundární budicí cívce C.

Druhý generátor 7 harmonického průběhu může zahrnovat zlomkovou kmitočtovou syntézu odvozenou od prvního generátoru 2 harmonického průběhu, nebo to může být generátor produkující harmonický signál případně kmitočtová syntéza s dobrou spektrální čistotou, střednědobou kmitočtovou stabilitou a dobrou fázovou stabilitou.

Zesilovač 8 nf signálu zahrnuje obvody výkonného zesilovače nf signálu například diskrétní zapojení v „pracovní třídě A“, monolitický audiozesilovač, proudově posílené zapojení s operačními zesilovači, schopné proudového buzení sekundární budicí cívky C.

Detektor a lokalizátor feromagnetických inkluzí podle vynálezu využívá principu snímání deformací střídavého budicího magnetického pole, způsobených feromagnetickým předmětem uvnitř detektoru a převodu na fázově-amplitudový signál lokalizující feromagnetickou inkluze.

Primární budicí cívka A vymezuje rozměr detekční-lokalizační oblasti ve dvou směrech, přičemž primární budicí cívkou A kontinuálně prochází lokalizované medium M (viz obr. 1).

Řídicí jednotka 1 nastaví na výstupu přesného a frekvenčně čistého prvního generátoru 2 harmonického průběhu pracovní frekvenci a povolí jeho výstup. Harmonický signál je dále zesílen druhým zesilovačem 3 a veden do budicí cívky A. Odezva snímacích cívek B_1 až B_n je zesílena prvními zesilovači 4_1 až 4_n a filtrována strmými pásmovými propustmi 5_1 až 5_n.

Filtrované signály jsou individuálně zpracovány a simultánně vzorkovány obvody 6_1 až 6_n signálového zpracování. Výstupy těchto obvodů 6_1 až 6_n signálového zpracování jsou vedeny řídicí jednotky 1, která signály vyhodnotí a nad detekovanými signály provede lokalizaci částice/částic. Výsledek a komunikace s uživatelem, případně vazba s nadřazeným systémem se také děje skrze řídicí jednotku 1, který obsahuje i vstupně výstupní rozhraní a zobrazovací jednotkou.

Kalibrace systému může být jednorázová, nebo průběžná. Při jednorázové kalibraci nastaví řídicí jednotka 1 frekvenci přesného a frekvenčně čistého druhého generátoru 7 harmonického průběhu na frekvenci lehce odlišnou od pracovní frekvence a povolí výstup druhého generátoru 7. Harmonický signál je dále zesílen zesilovačem 8 nf signálu a veden do sekundární budicí cívky C. Magnetickou vazbou jsou následně ovlivněny snímací cívky B_1 až B_n což je využito pro kalibraci v obvodech 6_1 až 6_n signálového zpracování.

V případě potřeby může být použita průběžná kalibrace, to znamená, že je signál sekundární budicí cívky C přítomen po celou dobu měření, aniž by zhoršil citlivost či jiné parametry detektoru, naopak zaručí adaptivitu systému na okolní podmínky.

PATENTOVÉ NÁROKY

1. Detektor a lokalizátor feromagnetických inkluzí v kontinuálně procházejícím mediu (M), zahrnující primární budicí cívku (A), skrz kterou prochází medium (M), a dále zahrnující alespoň dvě snímací cívky (B_1 až B_n), **vyznačující se tím**, že snímací cívky (B_1 až B_n) jsou uspořádány v rovině kolmé k rovině primární budicí cívky (A) a všechny snímací cívky (B_1 až B_n) jsou vinuty v libovolném smyslu, přičemž v rovině snímacích cívek (B_1 až B_n) je uspořádána alespoň jedna sekundární budicí cívka (C).

2. Detektor podle nároku 1, **vyznačující se tím**, že další snímací cívky (B_n) jsou uspořádány po celém obvodu primární budicí cívky (A).

3. Detektor podle nároku 1 nebo 2, **vyznačující se tím**, že snímací cívky (B_1 až B_n) jsou přes první zesilovače (4_1 až 4_n), pásmové propusti (5_1 až 5_n) a obvody (6_1 až 6_n) signálového zpracování připojeny k řídicí jednotce (1) a řídicí jednotka (1) je přes první generátor (2) harmonického průběhu a druhý zesilovač (3) připojena k primární budicí cívce (A) a řídicí jednotka (1) je též přes druhý generátor (7) harmonického průběhu a zesilovač (8) nf signálu připojena k sekundární budicí cívce (C).

2 výkresy

Seznam vztahových značek:

A	budicí cívka
B_1 až B_n	snímací cívky
C	sekundární budicí cívka
M	medium
1	řídicí jednotka
2	první generátor harmonického průběhu
3	druhý zesilovač
4_1 až 4_n	první zesilovače
5_1 až 5_n	pásmové propusti
6_1 až 6_n	obvody signálového zpracování
7	druhý generátor harmonického průběhu
8	zesilovač nf signálu

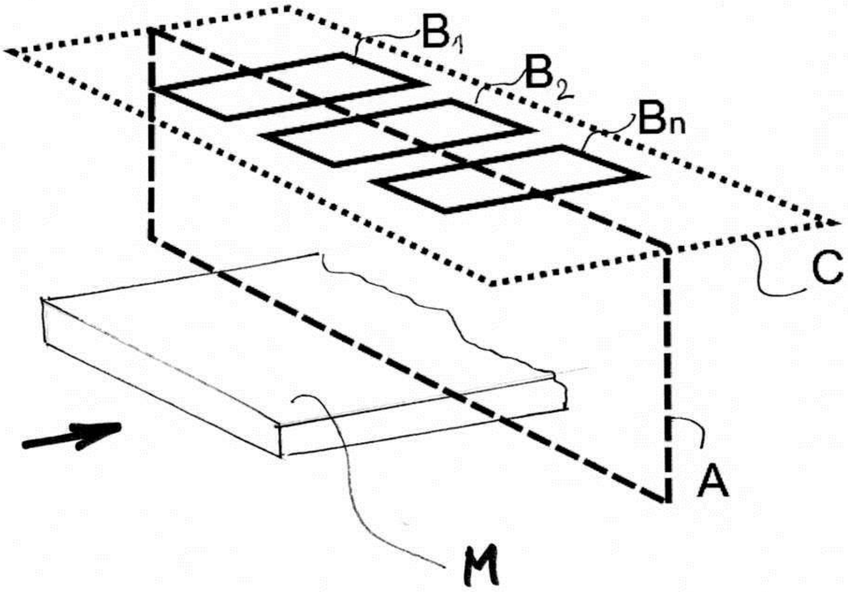

Obr. 1

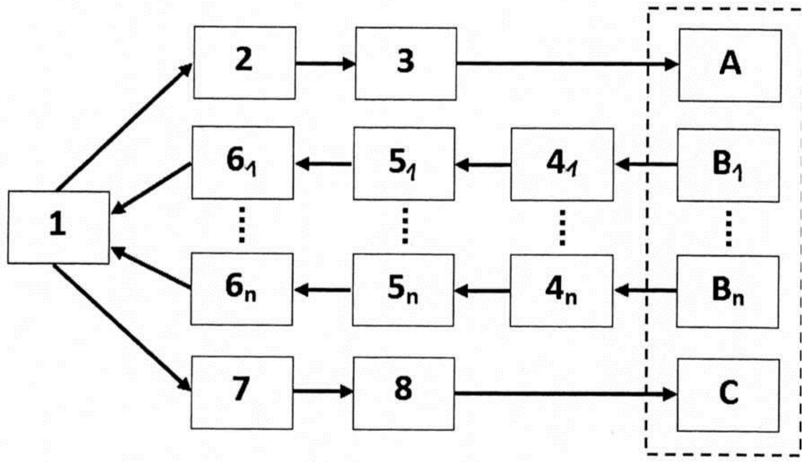

Obr. 2

Konec dokumentu